



**HAL**  
open science

# Structure of exotic nuclei. Nuclear moments of excited states

Konstantin Stoychev

► **To cite this version:**

Konstantin Stoychev. Structure of exotic nuclei. Nuclear moments of excited states. Nuclear Experiment [nucl-ex]. Université Paris-Saclay, 2023. English. NNT : 2023UPASP096 . tel-04721184

**HAL Id: tel-04721184**

**<https://theses.hal.science/tel-04721184v1>**

Submitted on 4 Oct 2024

**HAL** is a multi-disciplinary open access archive for the deposit and dissemination of scientific research documents, whether they are published or not. The documents may come from teaching and research institutions in France or abroad, or from public or private research centers.

L'archive ouverte pluridisciplinaire **HAL**, est destinée au dépôt et à la diffusion de documents scientifiques de niveau recherche, publiés ou non, émanant des établissements d'enseignement et de recherche français ou étrangers, des laboratoires publics ou privés.

Structure of exotic nuclei.  
Nuclear moments of excited states  
*Structure de noyaux exotiques.*  
*Moments nucléaires d'états excités*

Thèse de doctorat de l'université Paris-Saclay

École doctorale n°576, Particules, hadrons, énergie et noyau:  
instrumentation, imagerie, cosmos et simulation (PHENIICS)

Spécialité de doctorat: Physique Nucléaire

Graduate School: Physique

Référent: Faculté des sciences d'Orsay

Thèse préparée dans l'unité de recherche

**IJCLab** (Université Paris-Saclay, CNRS),

sous la direction de **Georgi GEORGIEV**, Directeur de Recherche,

et la co-direction de **Johan LJUNGVALL**, Directeur de Recherche

Thèse soutenue à Paris-Saclay, le 19 septembre 2023, par

**Konstantin STOYCHEV**

**Composition du jury**

Membres du jury avec voix délibérative

**Araceli LOPEZ-MARTENS**

Directrice de Recherche, Université Paris-Saclay, IJCLab

Présidente

**Emmanuel CLÉMENT**

Directeur de Recherche, Université Caen Normandie, GANIL

Rapporteur & Examineur

**Theodoros MERTZIMEKIS**

Professeur, University of Athens

Rapporteur & Examineur

**Giacomo DE ANGELIS**

Professeur, University of Padua, LNL Legnaro

Examineur

**Luis Mario FRAILE**

Professeur, University Complutense Madrid

Examineur

**Title:** Structure of exotic nuclei. Nuclear moments of excited states.

**Keywords:** Nuclear structure, magnetic moments, exotic nuclei

**Abstract:** Magnetic moments of excited nuclear states are a unique probe of nuclear structure. Experimentally obtained values of magnetic moments are useful to constrain theoretical models. Measurements of magnetic moments in exotic nuclei are sensitive to how nuclear structure evolves far from the line of stability. Different experimental techniques have been developed to measure magnetic moments of excited states depending on their half-lives. The Time-Differential Recoil-In-Vacuum (TDRIV) method is applied on excited states with picosecond half-lives. For isomeric states with half-lives in the order of hundreds of nanoseconds a suitable method is the Time-Dependent Perturbed Angular Distribution (TDPAD) method. The main topic of this thesis relates to the application of these methods to measure magnetic moments of excited states in exotic nuclei through the use of radioactive ion beams (RIBs).

The first application of the TDRIV method on a RIB is presented in the first part of the current work. The experi-

ment to measure the magnetic moment of the  $2_1^+$  state in  $^{28}\text{Mg}$  was performed at the MINIBALL setup at HIE-ISOLDE, CERN. The analysis of the obtained data is presented, alongside that of a calibration TDRIV measurement of the magnetic moment of the  $2_1^+$  state in  $^{22}\text{Ne}$ .

In the next part of the thesis the possibilities to extend the range of applicability of the TDRIV method to higher- $Z$  nuclei is discussed. A charge state measurement of titanium ions was performed at JYFL, Finland, in preparation for a future experiment to determine the magnetic moment of the  $2_1^+$  state in  $^{46}\text{Ti}$ . The analysis of the obtained data and simulations of the planned experiment are discussed.

Finally, the magnetic moments of isomeric states around  $^{68}\text{Ni}$  were measured in an experiment at NSCL, MSU, USA, using the TDPAD method following a projectile-fragmentation reaction. A detailed account of the data analysis is provided and the obtained results are compared with shell-model calculations.

**Titre:** Structure de noyaux exotiques. Moments nucléaires d'états excités

**Mots clés:** Structure nucléaire, moments magnétiques, noyaux exotiques

**Résumé:** Les moments magnétiques des états nucléaires excités sont une sonde très sensible de la structure nucléaire. Les valeurs des moments magnétiques obtenues expérimentalement sont extrêmement utiles pour contraindre les modèles théoriques. Les mesures des moments magnétiques dans les noyaux exotiques sont utiles pour explorer comment la structure nucléaire évolue loin de la ligne de stabilité. Différentes techniques expérimentales ont été développées pour mesurer les moments magnétiques des états excités en fonction de leur demi-vie. La méthode Time-Differential Recoil-In-Vacuum (TDRIV) est appliquée sur des états excités avec des demi-vies picosecondes. Pour les états isomères avec des demi-vies de l'ordre de centaines de nanosecondes, une méthode appropriée est la méthode Time-Dependent Perturbed Angular Distribution (TDPAD). Le sujet principal de cette thèse concerne l'application de ces méthodes pour mesurer les moments magnétiques des états excités dans les noyaux exotiques grâce à l'utilisation de faisceaux d'ions radioactifs (RIB).

La première application de la méthode TDRIV sur un RIB est présentée

dans la première partie du présent travail. L'expérience pour mesurer le moment magnétique de l'état  $2_1^+$  dans  $^{28}\text{Mg}$  a été réalisée dans l'installation MINIBALL à HIE-ISOLDE, CERN. L'analyse des données obtenues est présentée, parallèlement à celle d'une mesure TDRIV d'étalonnage du moment magnétique de l'état  $2_1^+$  dans  $^{22}\text{Ne}$ .

Dans la partie suivante de la thèse, les possibilités d'étendre le domaine d'application de la méthode TDRIV aux noyaux supérieurs à  $Z$  sont discutées. Une mesure de l'état de charge des ions titane a été réalisée à JYFL, Finlande, en préparation d'une future expérience visant à déterminer le moment magnétique de l'état  $2_1^+$  dans  $^{46}\text{Ti}$ . L'analyse des données obtenues et les simulations de l'expérience prévue sont discutées.

Enfin, les moments magnétiques des états isomères autour de  $^{68}\text{Ni}$  ont été mesurés dans une expérience au NSCL, MSU, USA, en utilisant la méthode TDPAD à la suite d'une réaction de fragmentation du projectile. Un compte rendu détaillé de l'analyse des données est fourni et les résultats obtenus sont comparés aux calculs du modèle en couches.

На дядо Петьо



# Acknowledgements

First of all, I would like to thank to my supervisors, Georgi and Joa, for giving me this opportunity and for helping me along the way. Thank you for your general support, whether it was fighting against the French administration or fighting bad programming practices, I could always count on you. Thank you also for the frequent reminders to stop focusing on tiny details that to my inexperienced eye seemed much more relevant than they actually were. I've learnt a great deal from both of you and for that I am grateful. I am looking forward to working with you in the future on the many projects we have left to finish, and on the new ones not materialized yet.

Thank you also to Dr. Araceli Lopez-Martens, Dr. Emmanuel Clément, Prof. Theodoros Mertzimekis, Prof. Giacomo De Angelis and Prof. Luis Mario Fraile for accepting to be members of my thesis jury, for taking the time to read this entire thesis and for your thoughtful comments on how to improve it.

I am thankful to Prof. Andrew Stuchbery for his dedication to the craft of g-factor measurements that ultimately led to the ideas behind a large part of my thesis work, for his valuable feedback on my analysis, and for the interesting and educational discussions on possible and impossible experiments. I owe thanks also to the people from the Nuclear Spectroscopy group at JYFL who made our measurement there possible - Dr. Jan Saren, Dr. Juha Uusitalo, Dr. Panu Ruotsalainen, Dr. Kalle Auranen, Dr. Andres Illana, Dr. Andrew Briscoe, Henna Joukainen and Ville Bogdanoff. Further, I want to thank Dr. Kamila Sieja for introducing me to shell-model calculations and Dr. Ivan Kojouharov for teaching me most of what I know about handling HPGe detectors.

Thank you to the SDF group of IJCLab for welcoming me and for providing an English-speaking refuge in a French world. In particular, a big thank you to Dave, Waely and Karl for lending a hand when needed and for their great sense of humor.

This journey was made more pleasant by all the friends I met along the way. Thank you, Jing and Praveen, for the table tennis afternoons and the great vegetarian nights out in Paris. And thank you, Joshua and Gianmarco, for our continued friendship despite the geographical distance, I very much enjoy our times together.

An honourable mention goes to Dr. Martin Djongolov who guided the development of my scientific writing style in the long and painful process of publishing my first publication. Hopefully some of the good practices you tried to teach me can also be found within this thesis. I'd like to also thank Prof. Georgi Rainovski who first invited me into the nuclear physics business which eventually led me to this point.

Няма как да пропусна да благодаря и на моите родители, сестра ми и цялото ми семейство за безрезервната им подкрепа по изборния от мен път, който ме отведе надалеко.

И за финал най-много искам да благодаря на Деси за всичко през изминалите три години. Невъзможно е да се опише с думи всичко преживяно, но ти благодаря за помощта, за оптимизма ти, за безкрайното ти търпение, за разходките на преливници, езера, морета, океани и други случайни водоеми, за нашите пътешествия по света, за всички хубави моменти, които сме прекарвали заедно, и за подкрепата ти в трудните такива. Радвам се, че имах възможността да споделя това приключение с теб.



# Contents

<b>Introduction</b>	<b>3</b>
<b>1 Magnetic dipole moments</b>	<b>5</b>
1.1 Definitions . . . . .	5
1.1.1 Schmidt lines . . . . .	6
1.1.2 Additivity relations . . . . .	7
1.2 Methods for measuring magnetic moments of excited states . . . . .	8
1.2.1 The TDPAD method . . . . .	8
Angular distributions and nuclear orientation . . . . .	9
Perturbed angular distribution . . . . .	11
Spin orientation in projectile fragmentation reactions . . . . .	12
Initial phase of spin orientation . . . . .	15
Gamma-ray detection and extraction of the g factor . . . . .	15
1.2.2 The TDRIV method . . . . .	17
Coulomb excitation . . . . .	18
Attenuation coefficients . . . . .	19
The RIV method . . . . .	20
The Time-Differential RIV method . . . . .	23
TDRIV for radioactive ion beams . . . . .	26
1.2.3 The transient field method . . . . .	27
<b>2 Magnetic moment of the <math>2_1^+</math> state in <math>^{28}\text{Mg}</math></b>	<b>31</b>
2.1 The $N = 20$ island of inversion . . . . .	31
2.2 Experimental setup . . . . .	33
2.2.1 Isotope production . . . . .	33
2.2.2 Ion source and mass separation . . . . .	34
2.2.3 Post-acceleration: REX- and HIE-ISOLDE . . . . .	35
REXTRAP . . . . .	35
REXEBIS . . . . .	35
REXLINAC and HIELINAC . . . . .	36
2.2.4 The MINIBALL setup . . . . .	36
CD DSSSD . . . . .	38
Miniball plunger device . . . . .	38
2.3 Data taking and analysis . . . . .	38
2.3.1 Doppler correction . . . . .	39
2.3.2 The TDRIV analysis code . . . . .	46
2.3.3 Calibration with $^{22}\text{Ne}$ . . . . .	51
2.3.4 $^{28}\text{Mg}$ . . . . .	54
2.4 Discussion . . . . .	57
2.5 $^{22}\text{Ne}$ TDRIV experiment at GANIL . . . . .	63

<b>3</b>	<b>Magnetic moment of the <math>2_1^+</math> state in <math>^{46}\text{Ti}</math></b>	<b>67</b>
3.1	Motivation . . . . .	67
3.2	Charge-state measurement of $^{48}\text{Ti}$ . . . . .	69
3.2.1	Experimental setup . . . . .	70
3.2.2	Data taking . . . . .	73
3.2.3	Analysis . . . . .	75
3.2.4	Discussion . . . . .	85
3.3	Simulations . . . . .	87
<b>4</b>	<b>Magnetic moments of isomeric states around <math>^{68}\text{Ni}</math></b>	<b>93</b>
4.1	The region around $^{68}\text{Ni}$ . . . . .	93
4.2	Experimental setup and data taking . . . . .	96
4.3	Analysis . . . . .	99
4.3.1	$^{67}\text{Ni}$ . . . . .	99
4.3.2	$^{69}\text{Ni}$ . . . . .	106
4.3.3	$^{70}\text{Ni}$ . . . . .	109
4.3.4	$^{71}\text{Cu}$ . . . . .	113
4.3.5	Alignment . . . . .	113
4.4	Discussion . . . . .	115
4.4.1	$^{67}\text{Ni}$ . . . . .	115
4.4.2	$^{69}\text{Ni}$ . . . . .	120
4.4.3	$^{70}\text{Ni}$ . . . . .	122
4.4.4	$^{71}\text{Cu}$ . . . . .	124
<b>5</b>	<b>Summary and outlook</b>	<b>125</b>
5.1	$^{22}\text{Ne}$ , $^{28}\text{Mg}$ and the $N = 20$ island of inversion . . . . .	125
5.2	$^{46}\text{Ti}$ and the TDRIV method for higher- $Z$ nuclei . . . . .	126
5.3	The region around $^{68}\text{Ni}$ and g factors of isomeric states . . . . .	127
<b>A</b>	<b>Résumé en Français</b>	<b>129</b>

# Introduction

The atomic nucleus is a quantum many-body system made up of two types of nucleons - protons and neutrons. The nucleus is bound together by the short-range strong nuclear interaction which acts on the nucleons at the femtometer scale. A description of this complex system based on first principles is beyond our current capabilities. Instead, different theoretical models are employed to explain the various observed properties of nuclei. Such properties are the binding energies, nuclear radii, spins and parities, excited level structure, magnetic dipole and electric quadrupole moments, etc.

Soon after the exploration of nuclear structure began in the 20th century some systematic behaviours of these properties were discovered. For example, nuclei with certain proton numbers  $Z$  and neutron numbers  $N$  were found to have higher binding energies per nucleon compared to the neighboring nuclei. These numbers are referred to as "magic" numbers and correspond to filled shells of protons and neutrons, in similarity to the atomic shell structure. Many of the properties of nuclei can be described by the nuclear shell model through the filling of proton and neutron orbitals. The ordering of the shell-model orbitals begins to change as one goes to more exotic and unstable nuclear systems, both neutron-rich and neutron-deficient. This can lead to the vanishing of some established magic numbers and the appearance of new ones in certain regions of the nuclear chart. In order to understand these changes in nuclear structure the existing theoretical models are revised and new models are proposed. Their validity has to be tested by comparison with experimental measurements of nuclear properties.

In recent years the properties of such exotic nuclei have become experimentally accessible at radioactive beam facilities. One particular line of research is the study of magnetic dipole moments of nuclear states. The magnetic moment is especially sensitive to the single-particle nature of a nuclear state and can provide insight into the nuclear wave function. Information on the relative ordering of the shell-model orbitals and their occupations by the nucleons can also be obtained through the measurement of the magnetic moments, which provides a stringent test of the theoretical predictions.

The main objectives of the current work are to obtain nuclear structure information from magnetic moment measurements on excited states in exotic nuclei and to test the methodological approaches that would allow for the study of a wider range of such nuclei. In the first chapter some details about the magnetic dipole moments are presented and the relevant experimental methods for measuring them are reviewed. These are the Time-Differential Recoil-In-Vacuum (TDRIV) and the Time-Dependent Perturbed Angular Distribution (TDPAD) methods. The second chapter gives a detailed account of the first application of the TDRIV method on a  $^{28}\text{Mg}$  radioactive ion beam and the analysis of the obtained experimental data. The third chapter relays the ongoing work on expanding the range of application of the TDRIV method to higher- $Z$  nuclei. In the fourth chapter the measurements of magnetic dipole moments of isomeric states in the region of  $^{68}\text{Ni}$  using the TDPAD method is presented and the results are compared with theoretical calculations. The final part of the thesis contains the summary and outlook.



# 1 - Magnetic dipole moments

## 1.1 Definitions

The magnetic dipole moment of a nuclear state with total angular momentum  $\vec{I}$  is given by:

$$\vec{\mu} = g\vec{I}\mu_N. \quad (1.1)$$

Here  $g$  is the gyromagnetic factor of the state, also referred to as the  $g$  factor of the state. The magnetic moment is typically given in units of the nuclear magneton  $\mu_N = e\hbar/2m_p$ , where  $m_p$  is the proton mass. Below, the  $\mu_N$  units will sometimes be omitted for clarity.

The nuclear magnetic dipole moment is generated by the orbital motion of the protons and by the intrinsic spins of both protons and neutrons. Therefore, the magnetic moment can also be presented as a sum over the contributions from all individual nucleons:

$$\vec{\mu} = \sum_{k=1}^A g_l^{(k)}\vec{l}^{(k)} + g_s^{(k)}\vec{s}^{(k)}. \quad (1.2)$$

Here  $\vec{l}$  and  $\vec{s}$  are the orbital and intrinsic angular momenta of each nucleon,  $g_{l,s}$  are the corresponding orbital and spin gyromagnetic factors. The gyromagnetic factors reflect on the inner structure of the particles. After the discovery of protons and neutrons, the initial expectations for their orbital and spin  $g$  factors were that they should be similar to those of electrons as all three particles are point-like fermions. For the negatively charged electrons the gyromagnetic factors are  $g_l^e = -1$  and  $g_s^e \approx -2$ . The respective values for protons ( $\pi$ ) and neutrons ( $\nu$ ) were thought to be  $g_l^\pi = 1, g_l^\nu = 0$  and  $g_s^\pi = 2, g_s^\nu = 0$ . However, the spin  $g$  factors of free protons and neutrons were measured experimentally to be [1]:

$$g_s^\pi = 5.5856946893(16), \quad g_s^\nu = -3.82608545(90) \quad (1.3)$$

with very high precision. This was explained with the presence of internal structure of the protons and neutrons which we now know to be composed of three quarks.

From a quantum-mechanical standpoint, the magnetic dipole moment of a nuclear state with total angular momentum  $I$  represents the expectation value of the  $z$ -component of the magnetic dipole operator  $\vec{\mu}$  in the highest magnetic substate  $m_I = I$ . Using the  $|Im\rangle$  notation for the nuclear wave function the magnetic dipole moment is given by:

$$\mu = \langle I, m_I = I | \mu_z | I, m_I = I \rangle. \quad (1.4)$$

Using the expression from Eq. (1.2), the evaluation of the magnetic moment would require the expectation values of the  $z$ -components of the angular momentum and spin operators  $\langle l_z \rangle$  and  $\langle s_z \rangle$ :

$$\langle \mu_z \rangle = \sum_{k=1}^A g_l^{(k)} \langle l_z \rangle + g_s^{(k)} \langle s_z \rangle. \quad (1.5)$$

### 1.1.1 Schmidt lines

For even-even nuclei in their ground-state configuration all nucleons are paired to  $I = 0$  and their magnetic dipole moment vanishes. The odd-mass nuclei can be viewed as a single unpaired valence nucleon outside an even-even  $I = 0$  core. Then, in a simplified view, the magnetic dipole moment of the valence nucleon would be responsible for that of the entire nucleus. This is known as the extreme independent particle model. In the  $jj$ -coupling scheme the total angular momentum of the valence nucleon is  $\vec{j} = \vec{l} + \vec{s}$  and Eq. (1.2) can be rewritten as:

$$\vec{\mu} = g_l \vec{j} + (g_s - g_l) \vec{s}. \quad (1.6)$$

The expectation value of the magnetic moment operator becomes:

$$\langle \mu_z \rangle = g_l \langle j_z \rangle + (g_s - g_l) \langle s_z \rangle, \quad (1.7)$$

which should be evaluated for the highest sub-state  $m_j = j$ . Then,  $\langle j_z \rangle = j\hbar$ , however,  $l_z$  and  $s_z$  are not well defined in this case. Through angular momentum algebra and the relation  $\vec{j} = \vec{l} + \vec{s}$  it can be shown that [2]

$$\langle s_z \rangle = \frac{j}{2j(j+1)} [j(j+1) - l(l+1) + s(s+1)] \hbar. \quad (1.8)$$

With this result, Eq. (1.7) can be evaluated for the two cases of  $s = \pm 1/2$ , which yield:

$$\begin{aligned} j = l + \frac{1}{2} : \quad \langle \mu_z \rangle &= g_l \left( j - \frac{1}{2} \right) + \frac{1}{2} g_s, \\ j = l - \frac{1}{2} : \quad \langle \mu_z \rangle &= g_l \frac{j(j+3/2)}{j+1} - \frac{1}{2} \frac{j}{j+1} g_s. \end{aligned} \quad (1.9)$$

These two equations describe curves known as Schmidt lines. Comparing some experimentally measured magnetic moments with the Schmidt lines reveals that almost all values lie in between these lines. This is true for both odd-proton and odd-neutron nuclei, as shown in Fig. 1.1.

The Schmidt lines manage to capture the overall trends of the magnetic moments as a function of  $j$ . However, the experimental values generally lie in between from these lines. This is thought to be due to the use of the free-nucleon spin g factors (Eq. (1.3)). Within the nucleus the individual nucleons interact through the exchange of mesons and meson-exchange current corrections to the magnetic moment are introduced. Another approach that is often used is to introduce effective spin g factors in an attempt to reach better agreement with experimental values. The effective values scale the free-nucleon spin g factor with a coefficient, also known as a quenching factor. The value of this coefficient can be slightly arbitrary but is usually chosen to best reproduce experimental values. In earlier works a quenching factor of 0.6 was suggested [4] while more recently 0.7 [5] and even 0.75 [6] are used. Typically, the quenching factors also differ depending on the valence space of shell-model orbitals that is considered in the calculations. Although the effective spin g factors may help theoretical calculations reach better agreement with experiment in some cases, in general, the quenching factor does not provide any direct physical insight. Instead, the necessity of a quenching factor to reproduce some results indicates that there are interactions or correlations that have not been fully accounted for in the calculations.

Another comment can be made on the large spread of the experimental values visible in Fig. 1.1. It is considered that this spread is due to the oversimplification of the extreme

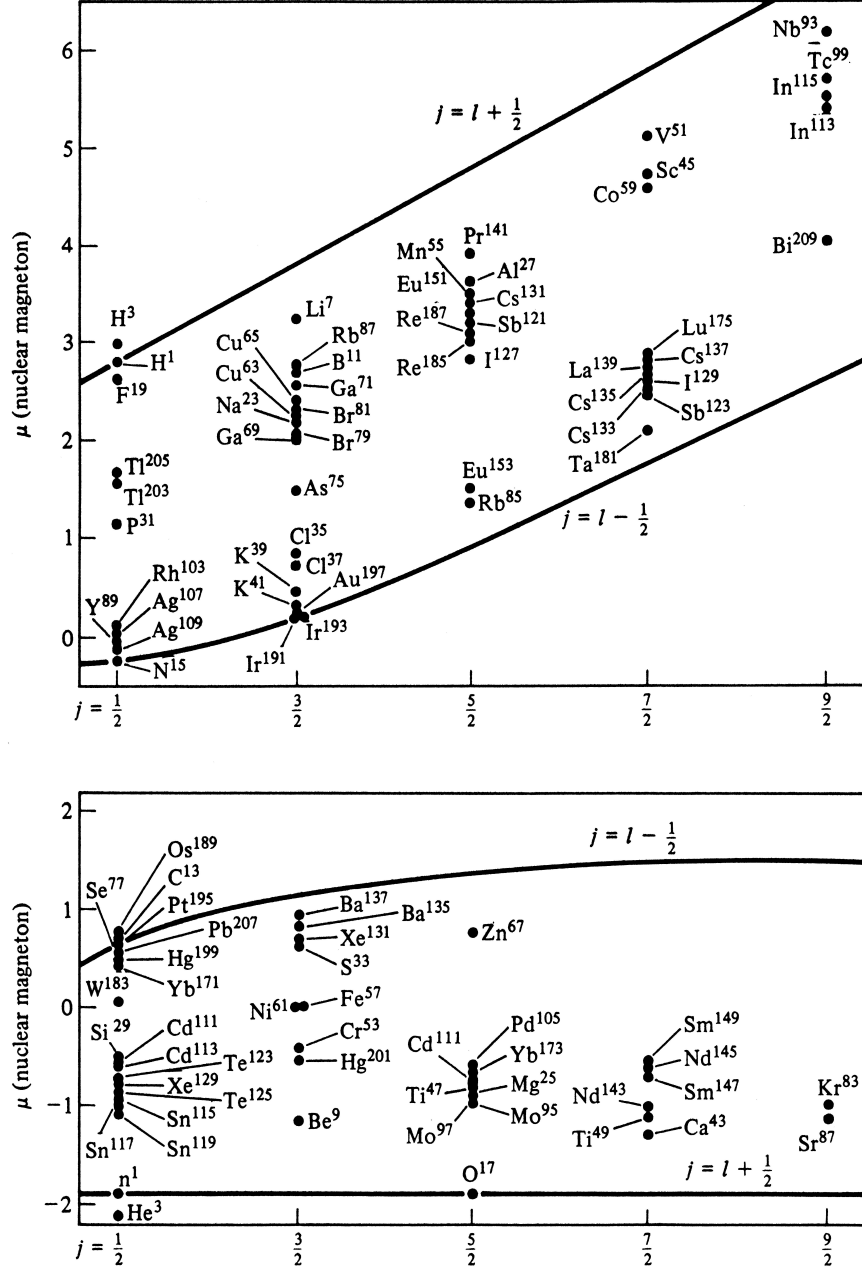


**Figure 1.1:** The calculated Schmidt lines for  $j = l \pm 1/2$  compared to experimentally measured magnetic moments of odd-proton (top) and odd-neutron (bottom) nuclei. Figure adapted from [3].

independent particle model. In a lot of cases considering only one valence nucleon is not enough to correctly describe the nuclear wave function. Additional pairs of nucleons have to be broken and multiple configuration-mixing scenarios have to be taken into account. This implicitly shows that the magnetic dipole moment is a very sensitive probe to the various contributions to the nuclear wave function.

### 1.1.2 Additivity relations

The magnetic dipole moment of a nuclear systems with more than one valence nucleon can be obtained through the following formalism.

Let there be two valence nucleons with angular momenta  $I_A$  and  $I_B$ , respectively, outside

an inert core with  $I = 0$ . The total angular momentum of the nucleus is then  $\vec{I} = \vec{I}_A + \vec{I}_B$  and the magnetic dipole moment is given by:

$$\mu = gI = \langle II | gI_z | II \rangle = \langle II | g_A I_{Az} + g_B I_{Bz} | II \rangle \quad (1.10)$$

Through the generalized Landé formula and the appropriate substitutions, the total g factor of the nucleus can be given as [7]:

$$g = \frac{1}{2}(g_A + g_B) + \frac{1}{2}(g_A - g_B) \frac{I_A(I_A + 1) - I_B(I_B + 1)}{I(I + 1)}. \quad (1.11)$$

Eq. (1.11) is known as the additivity relation and it can be applied in a similar fashion to nuclear systems with more valence nucleons. Note that in the particular case of  $I_A = I_B$  the second term vanishes and the g factor is independent of the total angular momentum of the valence nucleons.

## 1.2 Methods for measuring magnetic moments of excited states

The mean lifetimes of excited nuclear states span a wide range of multiple orders of magnitude. The measurement of these lifetimes requires the use of associated processes with a comparable time-scale. Various methods for lifetime measurements have been developed to target different ranges of lifetimes. Similarly, determining the magnetic dipole moments of these excited states requires different techniques depending on the lifetimes of the states of interest. For long-lived isomeric states with  $T_{1/2} \gtrsim 10^{-2}$  s the magnetic moments can be obtained through laser spectroscopy. For states with lifetimes in the range of 1 ns  $\lesssim T_{1/2} \lesssim 100\mu\text{s}$  two available methods are the Time-Dependent Perturbed Angular Distribution (TDPAD) or Correlation (TDPAC). Considering states with picosecond lifetimes both the Time-Differential Recoil-In-Vacuum (TDRIV) method and the Transient Field (TF) method are applicable. The methods listed above are not at all exhaustive and a more comprehensive list can be found e.g. in Refs. [5, 8]. The methods relevant to the current work are the TDPAD and TDRIV methods which will be presented in more details below. A short overview of the TF method is also included at the end of the chapter to allow for comparisons to be made with the TDRIV method.

### 1.2.1 The TDPAD method

The general principle of operation of the TDPAD method relies on the interaction of a nucleus with a magnetic field  $\vec{B}$ . The magnetic dipole interaction between the magnetic dipole moment  $\vec{\mu}$  and the magnetic field is given by the Zeeman Hamiltonian:

$$H_B = -\vec{\mu} \cdot \vec{B}. \quad (1.12)$$

The eigenvalues of the Hamiltonian are given by:

$$E_m = \langle Im | H_B | Im \rangle = \omega_L m \hbar, \quad (1.13)$$

where

$$\omega_L = -\frac{g\mu_N B}{\hbar} \quad (1.14)$$

is the Larmor angular frequency and the minus sign denotes that for a positive  $g$  factor the angular velocity  $\vec{\omega}_L$  is anti-parallel to the magnetic field  $\vec{B}$ . The interaction lifts the degeneracy of the magnetic substates  $m_I$  and the resulting hyperfine splitting of the energy levels is given by

$$\Delta E_m = \omega_L \hbar. \quad (1.15)$$

In a semi-classical view, the magnetic field exerts a torque on the magnetic dipole moment, which results in a precession of the nuclear spins around the magnetic field axis with the Larmor frequency. For a spin-oriented ensemble of nuclei the orientation axis will precess around the magnetic field axis with the same frequency. In turn, the angular distribution of  $\gamma$  rays depopulating the state of interest will also exhibit an oscillatory behaviour as the orientation axis rotates. Therefore, measuring the changes of  $\gamma$ -ray intensities at a given angle as a function of time can be directly linked to the  $g$  factor of the state of interest through the Larmor frequency. The key concepts of the TDPAD method, namely the spin-orientation of the nuclear ensemble, the angular distribution of emitted  $\gamma$  rays, the perturbation factors and the experimental implementation, are discussed below.

## Angular distributions and nuclear orientation

Let us consider a nuclear ensemble in a given initial excited state  $I_i$  with randomly-oriented spins. The excited state decays to a final state  $I_f$  through  $\gamma$ -ray emission. The angular distribution  $W(\theta, \phi)$  of the  $\gamma$  rays depopulating the state is isotropic due to the random orientation of the spins. If the ensemble in the initial state has been spin-oriented, this introduces an anisotropy in the angular distribution. The initial orientation of the spins is viewed relative to the  $z$  axis and is typically described by the orientation tensor  $B_{kn}$ . The orientation parameters are related to the statistical tensor  $\rho_{kn}$  by:

$$B_{kn}(I_i) = \sqrt{2I_i + 1} \rho_{kn}(I_i). \quad (1.16)$$

The statistical tensor is given by

$$\rho_{kn}(I_i) = \sqrt{2k + 1} \sum_{m, m'} (-1)^{I_i + m} \begin{pmatrix} I_i & I_i & k \\ -m' & m & n \end{pmatrix} \langle I_i m | \rho | I_i m' \rangle, \quad (1.17)$$

where  $\rho$  is the density matrix of the initial state. In the more general case, the oriented ensemble is in a parent state with spin  $I_0$  that decays through several unobserved transitions to the initial state with spin  $I_i$ . Then, additional deorientation parameters  $U_k(I_0, I_i)$  have to be taken into account as the orientation in the state  $I_i$  cannot exceed that of its parent state  $I_0$ . The deorientation parameters are multiplicative in case of cascades of multiple transitions between the oriented state with spin  $I_0$  and the observed  $\gamma$ -decaying state with spin  $I_i$ . Then, the angular distribution of the  $\gamma$  ray emitted from the initial state is:

$$W(\theta, \phi) = \sqrt{4\pi} \sqrt{2I_i + 1} \sum_{k, n} \frac{\rho_{kn}(I_i) A_k(I_i, I_f, \lambda) U_k(I_0, I_i) Y_{kn}(\theta, \phi)}{\sqrt{2k + 1}}. \quad (1.18)$$

Here  $A_k(I_i, I_f, \lambda)$  are the angular distribution coefficients, with  $\lambda$  being the transition multipolarity, and  $Y_{kn}(\theta, \phi)$  are the spherical harmonics.

For axially-symmetric orientation of the nuclear spins only the  $n = 0$  elements of  $\rho_{kn}$  remain

non-zero and Eq. (1.18) can be simplified to:

$$W(\theta) = \sum_k B_k(I_i) A_k(I_i, I_f, \lambda) U_k(I_0, I_i) P_k(\cos \theta), \quad (1.19)$$

where  $P_k(\cos \theta)$  are the Legendre polynomials and we introduce the notation  $B_k(I_i) \equiv B_{k0}(I_i)$ . When the orientation axis is used as the reference axis for the density matrix, the matrix is diagonal. The diagonal matrix elements represent the relative populations of each substate  $P(m)$ :

$$P(m) = \langle I_i m | \rho | I_i m \rangle, \quad (1.20)$$

and

$$\sum_m P(m) = 1. \quad (1.21)$$

Then, for axially-symmetric orientation, the  $B_k(I_i)$  parameters are given by:

$$B_{k0}(I_i) \equiv B_k(I_i) = \sqrt{2k+1} \sqrt{2I_i+1} \sum_{m,m'} (-1)^{I_i+m} \begin{pmatrix} I_i & I_i & k \\ -m & m & 0 \end{pmatrix} P(m). \quad (1.22)$$

from where it follows that  $B_0 = 1$ . From the relation of  $B_k$  to the populations of the substates  $P(m)$  in Eq. (1.22) several distinct types of orientation can be defined.

First, let us consider again the case of no initial orientation and randomly-oriented spins. This corresponds to an equal population of all substates:

$$P(m) = \frac{1}{2I+1}; \text{ and } B_k = 0, \quad k > 0, \quad (1.23)$$

and leads to  $W(\theta) = 1$  and isotropic  $\gamma$ -ray emission as mentioned at the beginning of this Section. The second scenario we can consider is that of an axially-symmetric orientation where the population of substates is also mirror-symmetric about the plane, perpendicular to the orientation axis. In that case we have:

$$P(m) = P(-m); \text{ and } B_k = 0, \quad k = 1, 3, \dots, \quad (1.24)$$

which is referred to as alignment of the nuclear spins. Alignment can be either prolate ( $B_2 > 0$ ) with spins oriented along the symmetry axis, or oblate ( $B_2 < 0$ ) with spins oriented perpendicular to the symmetry axis. Finally, the type of nuclear orientation, for which the substate populations are not mirror-symmetric is known as polarization:

$$P(m) \neq P(-m); \text{ and } B_k \neq 0, \quad k > 0. \quad (1.25)$$

The different modes of nuclear orientation are schematically shown in Fig. 1.2.

For a spin-aligned ensemble the degree of normalized alignment  $A$  is defined as:

$$A \equiv \frac{\sum_m \alpha_2(m) P(m)}{|\alpha_2(m_{max})|}, \quad (1.26)$$

where  $m_{max}$  denotes the substate(s) with the highest population and

$$\alpha_2(m) = 3m^2 - I(I+1). \quad (1.27)$$

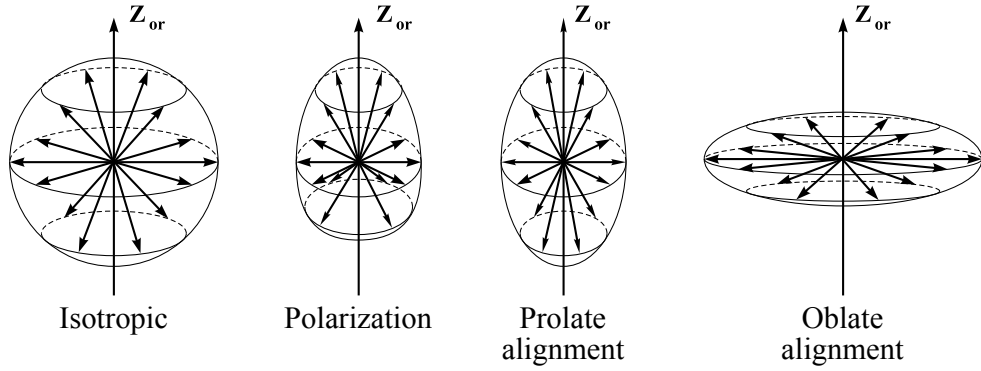


**Figure 1.2:** Schematic representation of the different spin-orientation types, adapted from Ref. [9].

The definition in Eq. (1.26) guarantees that  $-1 \leq A \leq 1$ . There are three possible cases for the value of the normalization factor  $\alpha_2(m_{max})$  based on the type of alignment (prolate or oblate) and the spin  $I$  of the state (integer or half-integer):

$$|\alpha_2(m_{max} = I)| = I(2I - 1); \quad A > 0, \quad (1.28)$$

$$|\alpha_2(m_{max} = 0)| = I(I + 1); \quad A < 0, I = 0, 1, \dots \quad (1.29)$$

$$|\alpha_2(m_{max} = \pm 1)| = I(I + 1) - 3/4; \quad A < 0, I = 1/2, 3/2, \dots \quad (1.30)$$

The alignment is also related to the orientation parameters  $B_k$ . A frequently made assumption for the angular distribution of  $\gamma$  rays in Eq. (1.19) is that the terms for  $k \geq 4$  are negligible and are not considered. Then, the alignment can be calculated using:

$$A = \frac{\sqrt{I(I+1)(2I+3)(2I-1)}}{\sqrt{5}|\alpha_2(m_{max})|} B_2. \quad (1.31)$$

## Perturbed angular distribution

The description of the angular distribution in the previous section assumes a static system with an initial spin orientation. In the presence of a time-dependent perturbation, such as the induced precession of the nuclear spin, one has to solve the time-dependent Schrödinger equation for the total Hamiltonian to obtain the time-evolution of the wave functions  $|\Phi_I(i)\rangle$ :

$$i\hbar \frac{\partial}{\partial t} |\Phi_I(i)\rangle = H |\Phi_I(i)\rangle. \quad (1.32)$$

If we consider that the density matrix is a representation of the density operator  $\rho$  in the basis  $|Im\rangle$ :

$$\rho_{mm'} = \langle Im | \rho | Im' \rangle = \frac{1}{N} \sum_i \langle Im | \Phi_I(i) \rangle \langle \Phi_I(i) | Im' \rangle \quad (1.33)$$

we can solve instead the von Neumann equation for the time-evolution of the density operator:

$$i\hbar \frac{\partial \rho}{\partial t} = [H, \rho]. \quad (1.34)$$

Using the solution of Eq. (1.34) the time-dependent density matrix can be written as:

$$\begin{aligned}\rho_{mm'}(t) &= \langle Im | \rho(t) | Im' \rangle = \\ &= \sum_{\substack{\mu, \mu' \\ N, N'}} \langle Im | N \rangle \langle N | I\mu \rangle \langle Im' | N' \rangle^* \langle N' | I\mu' \rangle^* e^{-\omega_L(N-N')t} \langle \mu | \rho(0) | \mu' \rangle.\end{aligned}\quad (1.35)$$

Considering the above, the evolution of the orientation tensor  $B_{kn}(t)$  is given by:

$$B_{kn}(t) = \sum_{k', n'} G_{kk'}^{mn'}(t) B_{k'n'}(t=0).\quad (1.36)$$

Here  $G_{kk'}^{mn'}(t)$  is the perturbation factor which in the general case can be written as:

$$\begin{aligned}G_{kk'}^{mn'}(t) &= \sqrt{2k+1}\sqrt{2k'+1} \sum_{\substack{m, \mu \\ N, N'}} (-1)^{m-\mu} \begin{pmatrix} I & I & k \\ -m & m' & n \end{pmatrix} \begin{pmatrix} I & I & k' \\ -\mu & \mu' & n' \end{pmatrix} \\ &\quad \times e^{-\omega_{NN'}t} \langle Im | N \rangle \langle N | I\mu \rangle \langle Im' | N' \rangle^* \langle N' | I\mu' \rangle^*.\end{aligned}\quad (1.37)$$

Using the orthogonality of the Wigner  $3j$  symbols Eq. (1.37) is simplified to:

$$G_{kk'}^{mn'}(t) = \delta_{kk'} e^{-in\omega_L t}, \quad n = m - m',\quad (1.38)$$

which gives the following expression for the orientation tensors:

$$B_{kn}(t) = e^{-in\omega_L t} B_{kn}(t=0).\quad (1.39)$$

For simplicity in the notations up to this point we have omitted the use of several different reference frames. The orientation tensors are regarded in the orientation reference frame, the perturbation factors are in the principle axis system of the nucleus and the angular distribution is in the laboratory frame. In the general case, these three reference frames do not coincide. Moreover, the orientation reference frame is rotating with the Larmor frequency  $\omega_L$  around the magnetic field axis. Transformations using Euler angles are used to convert everything to the laboratory frame.

Combining Eq. (1.18) with Eq. (1.39) and applying the reference-frame transformations we obtain the following expression:

$$W(\theta, t) = \sum_k B_k(I_i; t=0) A_k(I_i, I_f, \lambda) U_k(I_0, I_i) P_k[\cos(\theta - \omega_L t)].\quad (1.40)$$

The above expression gives the time-dependent perturbed angular distribution of  $\gamma$  rays emitted from an axially-symmetric spin-oriented nuclear ensemble in the laboratory frame.

## Spin orientation in projectile fragmentation reactions

The spin-oriented nuclear ensemble can be produced by various means. Nowadays, the most commonly used methods are those in which the reaction mechanism produces the nuclear state of interest with some degree of orientation. Orientation of the nuclear spins has been observed following Coulomb excitation, fusion-evaporation, transfer reactions, projectile-fragmentation reactions, etc. The mechanism of spin orientation relevant to the application of the TDPAD method in the current work is that after projectile-fragmentation reactions, which is outlined

below.

In projectile-fragmentation reactions a projectile nucleus impinges on a target with an energy typically in the tens to hundreds of MeV/A. As a result, there are a number of nucleons abraded from the projectile and a heavy fragment remains. Two regimes of the reactions are usually differentiated based on the initial beam energy - intermediate or relativistic. Energies between 20 MeV/A and 200 MeV/A are considered intermediate while energies higher than 200 MeV/A are considered relativistic. In both regimes the peripheral collisions with abrasion of nucleons is the main process. However, for the lower energy range of the intermediate regime transfer reactions can compete with the fragmentation reactions.

A description of the fragmentation process is obtained through kinematic considerations using the participant-spectator model, also known as the abrasion-ablation model [10]. The model does not take into account many of the parameters that are expected to play some role in the outcome of the reaction. The effects of the projectile and target spins, the target thickness are not considered. Nevertheless, using this model Asahi *et al.* [11] were able to qualitatively reproduce the experimentally-deduced spin orientation from the  ${}^9\text{Be}({}^{18}\text{O}, {}^{14}\text{B})$  reaction at 60 MeV/A.

The general idea of the participant-spectator model is that during the peripheral collisions there is only a small overlap between the projectile and target nuclei. The group of nucleons that are abraded from the projectile are called the “participant” as they actively take part in the reaction. Due to the large velocity of the projectile, the model assumes that the heavy reaction fragment remains undisturbed by the collision and it is referred to as the “spectator”. The fragments are forward focused and the distribution of reaction yields as a function of momentum follows a specific Gaussian distribution known as a Goldhaber or momentum distribution. The mean of the distribution of fragment yields corresponds to equal momenta of the fragment and the projectile:

$$\vec{p}_{frag} = \vec{p}_{proj} \equiv \vec{p}_0. \quad (1.41)$$

The yields are normally distributed around this center value with a width:

$$\sigma = \sigma_0 \sqrt{\frac{A_{frag}(A_{proj} - A_{frag})}{A_{proj} - 1}}, \quad (1.42)$$

where  $A_{proj,frag}$  is the mass number of the projectile/fragment and  $\sigma_0 \approx 90$  MeV/c [12]. The variation of  $\vec{p}_{frag}$  around the mean value is due to the momentum  $\vec{p}_{part}$  that has been transferred to the participant. In the reference frame of the projectile, the participant is described with the radius-vector  $\vec{r}_{part}$ . After the collision, the acquired momentum  $\vec{p}_{part}$  generates an angular momentum:

$$\vec{I}_{part} = \vec{r}_{part} \times \vec{p}_{part}. \quad (1.43)$$

In its initial state, the projectile does not have angular momentum relative to its rest-frame. Then, from conservation of angular momentum it follows that after the collision the fragment has angular momentum:

$$\vec{I}_{frag} = -\vec{I}_{part} = -\vec{r}_{part} \times \vec{p}_{part}. \quad (1.44)$$

From here, two extreme cases can be examined - if the momentum of the participant is parallel or perpendicular to the momentum of the projectile. First, when  $\vec{p}_{part} \parallel \vec{p}_{proj}$  we have:

$$|\vec{p}_{frag}| = |\vec{p}_{proj}| \pm |\vec{p}_{part}|, \quad (1.45)$$

where the sign depends on whether  $\vec{p}_{part}$  is parallel or anti-parallel to  $\vec{p}_{proj}$ . These two instances

describe the far-right and far-left wings of the Goldhaber distribution, respectively. In both of these cases the angular momentum  $\vec{I}_{frag}$  is perpendicular to the beam axis, which corresponds to oblate ( $A < 0$ ) spin-alignment, as defined in the previous Section. Therefore, for fragments in the wings of the Goldhaber distribution a negative alignment is obtained.

In the second extreme case of  $\vec{p}_{part} \perp \vec{p}_{proj}$  we have:

$$|\vec{p}_{frag}| = |\vec{p}_{proj}|, \quad (1.46)$$

which corresponds to the mean of the Goldhaber distribution. The orientation of the angular momentum  $\vec{I}_{frag}$  is along the beam axis, which defines a prolate ( $A > 0$ ) alignment for the center of the Goldhaber distribution.

From these considerations it follows that any other relative orientation of  $\vec{p}_{part}$  and  $\vec{p}_{proj}$  would correspond to the slopes of the Goldhaber distribution. Another conclusion is that at some value of  $|\vec{p}_{frag}|$  the sign of the alignment has to change from positive in the center to negative in the wings. A schematic representation of the above arguments is shown in Fig. 1.3.

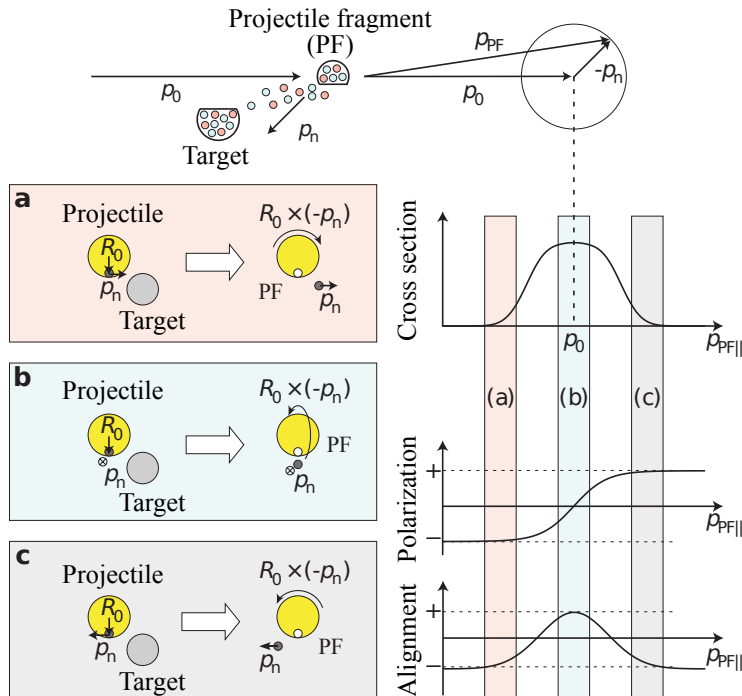


**Figure 1.3:** Production principle of spin-orientation in projectile-fragmentation reactions according to the participant-spectator model. The three panels on the left show the extreme cases of the relative orientation of the momentum of the participant and projectile described in the text for oblate (a,c) and prolate alignment (b). The corresponding reaction cross section, polarization and alignment are shown on the right. The following notations are used:  $\vec{p}_0 \equiv \vec{p}_{proj}$ ,  $\vec{p}_{PF} \equiv \vec{p}_{frag}$  and  $\vec{p}_n \equiv \vec{p}_{part}$ . Figure adapted from Ref. [13].

As visible in Fig. 1.3, some degree of spin polarization is also expected in the wings of the momentum distribution. In order to obtain a spin-polarized ensemble, the fragments from the reaction have to be extracted at an angle, relative to the initial direction of the projectile. This can be done e.g. with beam-swinger magnets placed before the fragmentation target [14].

Finally, it should be taken into account that the spin-oriented fragments can interact with various beam-line detectors e.g. for particle identification or time-of-flight measurements. It is possible for the fragments to capture one or more electrons when passing through the material. The coupling of the nuclear spin to the electron spin through the hyperfine interaction can

significantly reduce the spin alignment of the ensemble. An additional multiplicative electron pick-up correction  $f$  to the orientation parameter  $B_2$  should be included in the angular distribution of Eq. (1.40). This correction is expected to be  $f = 1$  for the higher-energy intermediate and relativistic regime of projectile-fragmentation. For lower-energy intermediate fragmentation reactions the value of  $f$  might decrease as the probability to capture an electron becomes non-negligible.

## Initial phase of spin orientation

A practical consideration when using projectile fragmentation as the process to orient the nuclear ensemble is the use of a mass spectrometer to select the fragments of interest. The mass spectrometers typically utilize several deviating dipole magnets for  $A/Q$  selection. When the spin-oriented fragments pass through the dipole magnets in-flight they interact with the magnetic field, which exerts a Lorentz force:

$$\vec{F}_L = Qe\vec{v} \times \vec{B}. \quad (1.47)$$

Here  $Qe$  is the charge of the nucleus,  $\vec{v}$  is its velocity. The momentum of the nucleus precesses under the influence of the Lorentz force with the cyclotron frequency:

$$\omega_C = -\frac{QeB}{Am_N}, \quad (1.48)$$

where  $Am_N$  is the mass of the fragment and the minus sign again denotes that  $\vec{\omega}_C$  is anti-parallel to  $\vec{B}$ . Independently, the interaction of the magnetic field with the nuclear dipole moment forces a precession of the orientation axis of the spin ensemble relative to the magnetic field axis with the Larmor frequency.

After passing through the mass-spectrometer the direction of the momentum  $\vec{p}$  has deviated by an angle  $\theta_C$  from its original direction. Analogously, the orientation axis has rotated by an angle  $\theta_L$  from its original direction. These two angles are related through their respective frequencies:

$$\theta_L = \theta_C \frac{\omega_L}{\omega_C} = \theta_C \frac{gA}{2Q}. \quad (1.49)$$

From here we can find an expression for the relative difference between the directions of the momentum and the orientation axis at the end of the spectrometer:

$$\alpha = \theta_L - \theta_C = -\theta_C \left(1 - \frac{gA}{2Q}\right). \quad (1.50)$$

The  $\alpha$  angle gives the initial phase of the precession of the orientation axis in the TDPAD measurement. Considering this, the perturbed angular distribution from Eq. (1.40) is modified to:

$$W(\theta, t) = \sum_k B_k(I_i; t=0) A_k(I_i, I_f, \lambda) U_k(I_0, I_i) P_k[\cos(\theta - \omega_L t - \alpha)]. \quad (1.51)$$

## Gamma-ray detection and extraction of the g factor

At the end of the mass spectrometer the selected fragments are implanted into a foil. An external magnetic field is applied in the vertical direction and several  $\gamma$ -ray detectors are placed in the horizontal plane. Depending on the mean lifetime of the excited nuclear state of interest either fast scintillator detectors or HPGe detectors are typically used.

The  $\gamma$ -ray intensity measured by a detector at an angle  $\theta$  is given by:

$$I(\theta, t) = I(t = 0)e^{-t/\tau}W(\theta, t), \quad (1.52)$$

where  $I(t = 0)$  is the initial intensity of the  $\gamma$  ray at the time of implantation of the fragments,  $\tau$  is the mean lifetime of the excited state of interest and  $W(\theta, t)$  is the perturbed angular distribution from Eq. (1.51).

The size of a detector and its distance from the implantation foil impact its sensitivity to the angular distribution of the registered  $\gamma$  rays. A geometrical correction factor  $Q_k$  is introduced to account for this effect. For a cylindrical detector with a radius  $r$  at a distance  $h$  from the implantation point the correction factor for  $k = 2$  can be approximated by [15]:

$$Q_2 = \frac{1}{2} \cos(\delta)(1 + \cos(\delta)), \quad (1.53)$$

where

$$\delta = \tan^{-1}(r/h). \quad (1.54)$$

With the addition of the geometrical factor the angular distribution becomes:

$$W(\theta, t) = \sum_k f B_k A_k U_k Q_k P_k [\cos(\theta - \omega_L t - \alpha)], \quad (1.55)$$

where the spin-dependencies have been omitted for clarity and the electron pick-up correction  $f$  has been included.

The goal of the TDPAD method is to obtain the  $g$  factor of the excited state of interest through measuring the Larmor precession frequency. This is achieved by constructing the ratio function:

$$R(\theta, t) = \frac{I(\theta, t) - \epsilon I(\theta + \frac{\pi}{2}, t)}{I(\theta, t) + \epsilon I(\theta + \frac{\pi}{2}, t)} = \frac{W(\theta, t) - \epsilon W(\theta + \frac{\pi}{2}, t)}{W(\theta, t) + \epsilon W(\theta + \frac{\pi}{2}, t)}, \quad (1.56)$$

where  $\epsilon$  is the relative efficiency of two detectors placed at angles  $\theta$  and  $\theta + \frac{\pi}{2}$  from the beam axis. For a spin-aligned ensemble the odd- $k$  orientation parameters  $B_k$  vanish. Additionally, all  $k \geq 4$  constituents of the sum in the perturbed angular distribution can be neglected in most cases. Then, only the  $k = 0$  and  $k = 2$  terms are used in the summation. Substituting Eq. (1.55) in Eq. (1.56) we obtain:

$$R(\theta, t) = \frac{2(1 - \epsilon) + 3f B_2 A_2 U_2 Q_2}{2(1 + \epsilon) + f B_2 A_2 U_2 Q_2} \cos[2(\theta - \omega_L t - \alpha)]. \quad (1.57)$$

Finally, if we assume that the two detectors are identical, their relative efficiency would be  $\epsilon = 1$  and Eq. (1.57) simplifies to:

$$R(\theta, t) = \frac{3f B_2 A_2 U_2 Q_2}{4 + f B_2 A_2 U_2 Q_2} \cos[2(\theta - \omega_L t - \alpha)]. \quad (1.58)$$

This expression is typically used in analysing TDPAD experimental data. The experimental  $\gamma$ -ray intensities are used to construct an experimental ratio function, which is fitted with Eq. (1.58). The Larmor frequency, and by extension the  $g$  factor and its sign, are extracted from the fit. The orientation factor  $B_2$  is also obtained from the amplitude of the oscillations in the experimental ratio function and the initial alignment  $A$  can be calculated using Eq. (1.31).

It should be noted that the ratio function can be constructed for detectors placed at any

angles  $\theta_1$  and  $\theta_2$ . However, it can be shown that the highest sensitivity of the method is obtained for  $\theta_1 - \theta_2 = \pi/2$ . At such values the anisotropy of the perturbed angular distribution is the highest. Also, in a lot of TDPAD experiments four detectors are used at  $\pi/2$  angles between each other. In that case the  $\gamma$ -ray intensities of each pair of opposite detectors ( $\theta_1 - \theta_2 = \pi$ ) can be summed. This could only modify the relative efficiency and/or the  $Q_2$  factor in Eq. (1.58) and not the observed frequency.

Another important point is that there are certain configurations of the experimental setup that render the ratio function insensitive to the sign of the  $g$  factor. This can be shown by re-writing Eq. (1.58) with the explicit forms of  $\omega_L$  (Eq. (1.14)) and the deviation angle  $\alpha$  (Eq. (1.50)):

$$R(\theta, t) = R_0 \cos \left[ 2(\theta + \theta_C) - 2g \left( \frac{\theta_C A}{2Q} - \frac{\mu_N B t}{\hbar} \right) \right], \quad (1.59)$$

where  $R_0$  is the amplitude. Let us consider the case of  $\theta + \theta_C = n\pi/2$  for any integer  $n$ . Then, from the properties of the cosine function, the  $2(\theta + \theta_C) = n\pi$  term can simply be removed from the argument of the cosine function in Eq. (1.59). In such a case the argument of the cosine is proportional to  $-2g$ . However, the cosine is an even function and thus, the ratio function would not be sensitive to the sign of the  $g$  factor. Therefore it is imperative to consider the angles at which the detectors are placed in combination with the deviation angles of the utilized mass spectrometer of the facility.

Finally, it is possible to perform a TDPAD measurement using a single detector by changing the direction of the applied magnetic field, which reverses the direction of the spin precession. The ratio function then takes the form:

$$R(\theta, t) = \frac{I(\omega_L, t) - I(-\omega_L, t)}{I(\omega_L, t) + I(-\omega_L, t)} = \frac{3fB_2A_2U_2Q_2 \sin [2(\theta - \alpha)] \sin (2\omega_L t)}{4 + fB_2A_2U_2Q_2 \cos [2(\theta - \alpha)] \cos (2\omega_L t)}, \quad (1.60)$$

and its amplitude has a maximum when the detector is placed at  $\theta = \alpha \pm 45^\circ$  or  $\theta = \alpha \pm 135^\circ$ .

## 1.2.2 The TDRIV method

The Time-Differential Recoil-In-Vacuum (TDRIV) method is a modification based on the Recoil-In-Vacuum (RIV) method. Both methods are based on the hyperfine interaction between the nucleus and an external magnetic field. In this case the projectile nuclei impinge on a target foil and undergo Coulomb excitation, which produces a spin-oriented ensemble in an excited nuclear state. The projectiles recoil out of the target into vacuum as ions. The electrons orbiting the nucleus in configurations with atomic spin  $J > 0$  generate a hyperfine magnetic field  $B_{hf}$ . The hyperfine field couples the nuclear spin  $\vec{I}$  and the atomic spin  $\vec{J}$  to a total spin  $\vec{F}$ . The interaction of the nuclear magnetic moment with the hyperfine field is again given by the Hamiltonian:

$$H_B = -\vec{\mu} \cdot \vec{B}. \quad (1.61)$$

Using the Wigner-Eckart theorem it can be shown that the corresponding eigenvalues are:

$$E_F = \frac{1}{2} \frac{g\mu_N B_{hf}}{J} (F(F+1) - I(I+1) - J(J+1)), \quad (1.62)$$

where  $B_{hf}$  is the strength of the hyperfine field at the site of the nucleus. The hyperfine splitting of the energy levels is given by:

$$\Delta E_{FF'} = \omega_{FF'} \hbar \quad (1.63)$$

where

$$\omega_{FF'} = \frac{1}{2} \frac{g\mu_N B_{hf}}{J\hbar} (F(F+1) - F'(F'+1)), \quad (1.64)$$

Here  $\omega_{FF'}$  represents the frequency which corresponds to a transition between the two substates  $F$  and  $F'$ . The hyperfine interaction gives rise to a precession of the nuclear spin around the total spin with the frequency  $\omega_{FF'}$ . This can again be treated as a time-dependent perturbation that modifies the angular distribution of  $\gamma$  rays depopulating the excited nuclear state of interest while the ions recoil in vacuum. Either the recoiling ions or the scattered target nuclei are registered in coincidence with the  $\gamma$  rays in a particle detector to produce particle- $\gamma$  angular correlations. The time-evolution of these angular correlations gives information on the nuclear excited state  $g$  factor through Eq. (1.64).

Although the general principle behind the RIV and TDRIV methods is the same, one is a time-integral measurement while the other is time-differential. In both methods the excited states of interest are populated through Coulomb excitation of the projectile nuclei and the reaction mechanism will be briefly outlined below. Then, the RIV method will be presented to introduce the relevant concepts, followed by an exposition of the TDRIV method. Finally, a more recent modification of the TDRIV method for use with radioactive ion beams (RIBs) will be discussed.

## Coulomb excitation

The process of Coulomb excitation is very well known and a description of it can be found in most nuclear physics textbooks. Here, only a few notes on the topic will be given. A comprehensive review can be found in Ref. [16].

Coulomb excitation is a reaction process in which a projectile nucleus interacts with a target nucleus via the electromagnetic field resulting in an excitation of one of the two involved nuclei. The Coulomb force between two nuclei with charges  $Z_1e$  and  $Z_2e$  is given by:

$$F_{Coul} = \frac{Z_1 Z_2 e^2}{R^2}, \quad (1.65)$$

where  $R$  is the distance of closest approach between the two nuclei, calculated from the center of each nucleus. A projectile nucleus impinging on a target nucleus is inelastically scattered due to the Coulomb force. The scattered nucleus can be described through the nuclear statistical tensor  $\rho_{kq}(I)$ . Moreover, the description is exact and is calculable from first principles as it is derived from the theory of electromagnetism. This is also the reason why Coulomb excitation is a widely used reaction mechanism in nuclear structure experiments.

Coulomb excitation is a very useful reaction mechanism for magnetic moments studies as it produces a spin-oriented nuclear ensemble. The experimental methods that employ Coulomb excitation to extract the transitional and diagonal matrix elements of excited states typically employ Cline's "safe" criterion [17]. The criterion states that if the minimal distance between the surfaces of the projectile and target nuclei is at least 5 fm, the effects of the strong nuclear interaction are expected to be negligible. From this a range of scattering angles can be defined as either "safe" or "unsafe", depending on the distance of closest approach between the two nuclei. At separation distances above 5 fm, the Coulomb-nuclear interference term for calculating the excitation cross sections is negligible. At smaller separation distances, the importance of this term increases. In Coulomb-excitation experiments the main observables are most often the de-excitation  $\gamma$ -ray yields in coincidence with the scattered particle in a particular angular range. These particle- $\gamma$  yields are directly related to the excitation cross sections for populating the

excited states. Therefore the “safe” criterion is necessary to guarantee that the interaction of the projectile and target nuclei is purely electromagnetic. In contrast, what is important for magnetic moments studies is that the nuclear ensemble is spin-oriented after the reaction, which is true for Coulomb excitation. It is assumed that the Coulomb-nuclear interference does not alter the spin-orientation and, hence, the “safe” criterion is not followed. If the nuclear interaction has some effect on the spin orientation, it would most likely lead to an overall reduction in the degree of orientation at “unsafe” angles, which would not hinder the measurements significantly.

## Attenuation coefficients

As mentioned above, the Coulomb-excited projectiles recoil out of the target in vacuum as ions. The spin-oriented nuclear system with spin  $\vec{I}$  is described by the Coulomb-excitation statistical tensor  $\rho_{kq}(I)$ . Analogously, the atomic system with a randomly-oriented spin  $\vec{J}$  can be described by a statistical tensor  $\rho_{kq}(J)$ . When the ions recoil into vacuum the hyperfine interaction couples the nuclear and atomic spins to a total spin  $F$ . The statistical tensors also couple to form the total statistical tensor  $\rho_{kq}(F)$ , given by:

$$\rho_{kq}(FF') = \sum_{\substack{k_i, k_j \\ q_i, q_j}} \rho_{k_i q_i}(I) \rho_{k_j q_j}(J) (2F+1)(2F'+1)(2k_i+1)(2k_j+1) \langle k_i k_j q_i q_j | kq \rangle \left\{ \begin{array}{ccc} I & J & F \\ I & J & F' \\ k_i & k_j & k \end{array} \right\}, \quad (1.66)$$

where  $\langle k_i k_j q_i q_j | kq \rangle$  is a Clebsch-Gordan coefficient and the curly brackets indicate a Wigner 9j symbol.

The interaction of the nucleus with the hyperfine field introduces a time-dependent perturbation, which can be treated similarly to the TDPAD method in the previous Section. The time-evolution of the statistical tensor is given by:

$$\rho_{kq}(FF', t) = e^{-i\omega_{FF'}t} \rho_{kq}(FF', t=0), \quad (1.67)$$

where  $\omega_{FF'}$  is taken from Eq. (1.64). Every transition between two substates  $F$  and  $F'$  corresponds to a precession of the nuclear spin around the total spin with the frequency  $\omega_{FF'}$ . For  $J > 1/2$  there are multiple possible transitions with their own precession frequencies. When considering the nuclear ensemble, all of the possible frequencies will be observed and the overall effect would be a superposition of these frequencies weighted by the probabilities for the respective transitions to occur. The case of  $J = 1/2$  relates to a single electron in an  $s$  orbital. In this particular case only two substates are available -  $I + 1/2, I - 1/2$ , and there is just one possible transition, leading to a single observable frequency, given by [18]:

$$\omega_{I+1/2, I-1/2} = \frac{g\mu_N(2I+1)B_{hf,s}}{\hbar} \quad (1.68)$$

The presence of multiple precession frequencies leads to an attenuation of the nuclear spin orientation over time. At the time the ions exit the target material ( $t = 0$ ) the nuclear spins are oriented in the same direction with the same initial phase. At any given flight time  $t_f$  the different frequencies will result in phase shifts between parts of the nuclear ensemble, which reduces the observed total orientation. Using the properties of the Coulomb-excitation

statistical tensor  $\rho_{kq}(I)$ , the attenuation coefficient  $G_k(t)$  can be written as:

$$G_k(t) = \sum_{F,F'} C_{IJ}^{FF'}(k) \cos(\omega_{FF'}t), \quad (1.69)$$

where

$$C_{IJ}^{FF'}(k) = \frac{(2F+1)(2F'+1)}{2J+1} \left\{ \begin{matrix} F & F' & k \\ I & I & J \end{matrix} \right\}^2 \quad (1.70)$$

If we consider a dynamic atomic system in which transitions between atomic states are possible the expression in Eq. (1.69) must be modified. The loss of orientation due to unobserved atomic transitions is described by the deorientation coefficients  $U_k$ , which act on the atomic statistical tensor  $\rho_{kq}(J)$ . For a transition between atomic states  $J_i$  and  $J_f$  with multipolarity  $L$  we have:

$$\rho_{kq}(J_f, t + \Delta t) = \rho_{kq}(J_i, t) U_k(J_i, J_f, L), \quad (1.71)$$

with

$$U_k(J_i, J_f, L) = (-1)^{J_i+J_f+L+k} \sqrt{2J_i+1} \sqrt{2J_f+1} \left\{ \begin{matrix} J_i & J_f & k \\ J_f & J_f & L \end{matrix} \right\}. \quad (1.72)$$

The final atomic state with  $J_f$  is associated with its own attenuation coefficients due to its coupling to the nuclear spin. The attenuation coefficients for successive atomic states are multiplicative, similar to the deorientation parameters  $U_k$ . For a cascade of atomic transitions the final attenuation coefficient is given by:

$$G_k^A(t_N) = G_{k,1}(t_1) \prod_{i=2}^N G_{k,i}(t_i - t_{i-1}), \quad (1.73)$$

where  $A$  denotes the sequence of atomic transitions,  $t_i$  is the time at which the the state  $i$  has decayed and  $N$  is the total number of states in the cascade.

Finally, it must also be considered that the recoiling ions have different charge states  $Q$ . The charge-state distribution of an ion exiting a foil depends only on  $Z$  of the projectile,  $Z$  of the foil material and the ion velocity when exiting the material. Atomic cascades are then possible in each of the ionic species. Combining Eq. (1.73) with the charge-state distribution we obtain the expected average attenuation factor for the entire ensemble:

$$G_k(t) = \sum_Q c_Q \sum_A^{N_A} G_k^{QA}(t) / N_A. \quad (1.74)$$

Here  $N_Q$  is the number of charge states with their fractional population  $c_Q$ ,  $N_A$  is the number of cascades  $A$  for each individual charge state  $Q$ . The fractional population of ionic species is normalized to unity:

$$\sum_Q c_Q = 1 \quad (1.75)$$

For simplicity, the summation on the atomic cascades and the ionic species will be omitted in the following sections, although it must always be taken into account in practice.

## The RIV method

In the RIV method the scattered projectile ions are not directly registered and the nuclear state of interest de-excites via  $\gamma$ -ray emission in flight. The  $\gamma$  rays are registered in an array of

HPGe detectors characterized by the angles  $\theta_\gamma, \phi_\gamma$ . Scattered light target nuclei are detected in a particle detector at  $\theta_p, \phi_p$  in coincidence with the  $\gamma$  rays. Here we assume that a particle detector without azimuthal symmetry is used, as shown in Fig. 1.4. The particle detection allows for full kinematic reconstruction of the Coulomb-excitation process. The velocity of the recoils can be extracted, which is needed to correct for the Doppler shift of the  $\gamma$  rays emitted in flight. The velocity of the ions at the time of exiting the target is also needed to determine the charge-state distribution of the ions.

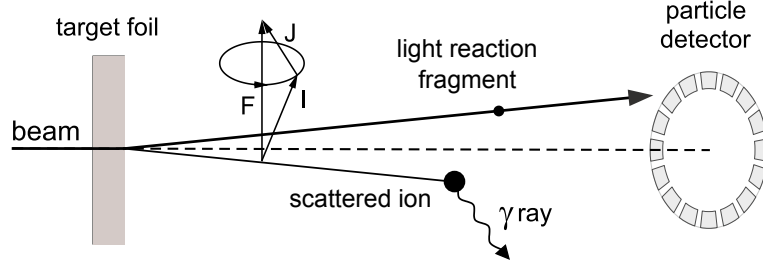


**Figure 1.4:** Schematic of a setup for a RIV experiment.

The unperturbed particle- $\gamma$  angular correlations observed after Coulomb excitation are given by:

$$W(\theta_p, \theta_\gamma, \Delta\phi) = \sum_{k,q} B_{kq} A_k Q_k D_{q,0}^{k*}(\Delta\phi, \theta_\gamma, 0), \quad (1.76)$$

where  $\Delta\phi = \phi_p - \phi_\gamma$ ,  $B_{kq}$  are the orientation tensors, related to the statistical tensors through Eq. (1.16),  $A_k$  are the angular distribution coefficients and  $Q_k$  are the geometrical correction factors. The Wigner  $D$ -matrix accounts for the relative directions of the  $\gamma$  ray and the recoiling ion and contains the spherical harmonics  $Y_k^q(\theta_\gamma, \phi_\gamma)$ . For particle detectors that retain azimuthal symmetry, the spherical harmonics are reduced to the Legendre polynomials. All spin-dependencies of the tensors, coefficients and factors have been omitted for simplicity.

When the time-dependent attenuation coefficients  $G_k(t)$  and the  $U_k$  de-orientation coefficients are included Eq. (1.76) becomes:

$$W(\theta_p, \theta_\gamma, \Delta\phi, t) = \sum_{k,q} G_k(t) B_{kq} A_k U_k Q_k D_{q,0}^{k*}(\Delta\phi, \theta_\gamma, 0). \quad (1.77)$$

Here the attenuation coefficients from Eq. (1.69) can be rewritten to [18]:

$$G_k(t) = 1 - 2 \sum_{F>F'} C_{IJ}^{FF'}(k) [1 - \cos(\omega_{FF'} t)], \quad (1.78)$$

where we have also incorporated a sum over all charge states.

In RIV experiments the recoils are not stopped and the interaction time of the hyperfine field and the nuclear magnetic moment extends to the limit of infinity. Thus, the experimentally measured quantity is the integral over time of the particle- $\gamma$  angular correlations. Since all other terms in Eq. (1.77) can be calculated from first principles, the measured quantity is essentially the integral of the  $G_k(t)$  coefficients. Taking into account the finite mean lifetime  $\tau$  and  $\lambda = 1/\tau$  of the nuclear excited state of interest, the average attenuation coefficient can be expressed as [18]:

$$G_k(\infty) = \int_0^\infty G_k(t) e^{-\lambda t} \lambda dt. \quad (1.79)$$

Substituting  $G_k(t)$  from Eq. (1.78) yields:

$$G_k(\infty) = 1 - 2 \sum_{F>F'} C_{IJ}^{FF'}(k) \frac{\omega_{FF'}^2 \tau^2}{1 + \omega_{FF'}^2 \tau^2}. \quad (1.80)$$

Two conclusions can be drawn from the above expression. First, the RIV method is not sensitive to the sign of the  $g$  factor of the nuclear state as  $G_k(\infty) \propto \omega_{FF'}^2 \propto g^2$ . Second, the attenuation coefficient depends on the product of the  $g$  factor and the mean lifetime of the state -  $g\tau$ . Therefore, the precision of the mean lifetime impacts the level of precision that is achievable for the  $g$  factor.

For experiments with axially-symmetric particle detectors only the even- $k$  terms of the angular correlation remain non-zero and the terms with  $k > 4$  are neglected. The experimentally obtained perturbed angular correlations are fitted to obtain  $G_2(\infty)$  and  $G_4(\infty)$ . Additional calibration measurements on isotopes with known  $g$  factors are needed to calibrate the hyperfine interaction. The calibration  $G_{2,4}(\infty)$  values are extracted and plotted as a function of  $|g|\tau$ . Then, they are approximated by a function to deduce the  $G_k(|g|\tau)$  dependence. From the obtained dependence the  $g$  factor of the state of interest can be extracted using its known lifetime and the experimental  $G_k$  values.

More recently, Stone, Stone and Jönsson [19] suggested an almost *ab initio* approach for the analysis of RIV data. The General Relativistic Atomic Structure Package (GRASP) [20] software is able to perform atomic-structure calculations based on first principles. The hyperfine field strengths for all relevant atomic states can be calculated and used to extract the respective precession frequencies. Using the lifetimes of the atomic states, a full simulation of atomic cascades and the resulting attenuation factors can be achieved. The important distinction from a real *ab initio* approach is that the initial populations of atomic excited states are unknown. An initial distribution of excited states has to be assumed to begin the simulations of atomic transitions. Similarly, some assumptions about the charge-state distribution of ionic species are needed. Nevertheless, the approach allows for a detailed description of the attenuation factors of the ensemble of ions recoiling in vacuum without the need for calibration measurements with known  $g$  factors. The largest uncertainty in this approach is in the time just after the ions have exited the target. There can be a large number of very fast cascades of transitions that are difficult to observe experimentally, and therefore difficult to include in the modelling of the process.

A first practical application of the proposed technique was used by Chen *et al.* [21] to re-analyse the RIV data for Te isotopes from Ref. [22]. A somewhat good agreement was achieved with experiment for most of the experimental values. Further developments of this approach to RIV data analysis were presented by Dr. Brendan McCormick, ANU, as part of his doctoral thesis [23]. He developed a software package RIVSimulate that incorporates the more recent GRASP2018 [24] atomic structure data and the needed experimental parameters to simulate the  $G_k(t)$  attenuation factors. The software package also has the capabilities to fit experimental attenuation factors.

One important general point to be made is that there is a minimum “hard core” residual orientation of the ensemble that is independent of the strength of the hyperfine interaction. Taking the limit of Eq. (1.80) for  $\omega_{FF'}\tau \rightarrow \infty$  it can be shown that:

$$G_k(h.c.) = \sum_F C_{IJ}^{FF}(k) \quad (1.81)$$

## The Time-Differential RIV method

The time-differential modification of the RIV method was used in the 1970s and 1980s to measure several  $g$  factors of short-lived excited state in nuclei up to  $^{24}\text{Mg}$ , e.g. Refs. [25, 26, 27, 28, 29, 30, 31]. It allows for the Larmor precession frequency to be sampled directly, rather than through the attenuation coefficients  $G_k(t)$ . The method employs a plunger device, consisting of two parallel foils and an apparatus that can change and control the distance between them. The plunger device was developed for lifetime measurements of excited nuclear states with lifetimes in the order of picoseconds. Later it was also employed for  $g$ -factor measurements of excited state in the same range of lifetimes. A brief overview of the plunger method for lifetime measurements is deemed necessary before continuing with the TDRIV method.

A nuclear reaction between the projectile nuclei and the first foil (target) populates the excited state of interest. The state can decay via  $\gamma$ -ray emission either in flight or at rest, after implantation in the second foil (stopper). The energy of the  $\gamma$  rays emitted in flight is shifted by the Doppler effect compared to the energy of  $\gamma$  rays emitted at rest. The ratio of shifted and unshifted  $\gamma$  rays depends on the lifetime of the state, the velocity of the recoiling nuclei and the target-stopper distance, also referred to as the plunger distance. Changing the plunger distance modifies the flight time of the recoils and so the ratio between the shifted and unshifted  $\gamma$  rays. Experimentally, the lifetime of the excited state can be extracted from the changes of the intensity of the shifted and unshifted  $\gamma$ -ray peaks in the detector energy spectra. This is the basis of the Recoil Distance Doppler-Shift (RDDS) method. A detailed overview of the method can be found in Ref. [32].

Coming back to the TDRIV method, the first foil is the target in which the beam nuclei undergo Coulomb excitation. The recoiling ions are described in the exact same way as in the RIV method. The second foil is the stopper foil, where the ions are implanted. The hyperfine interaction is interrupted when the nucleus enters the stopper foil and the nuclear and atomic spins de-couple. The time-dependent perturbation stops and so does the precession of the nuclear spin. The orientation of the spin ensemble is then fixed in a certain direction which defines the angular distribution of the  $\gamma$  rays emitted at rest. The scattered light fragments from the Coulomb-excitation reaction are not stopped by the stopper foil and are registered in a particle detector, as shown in Fig. 1.5. Similar to the RIV method, the particle- $\gamma$  angular correlations from Eq. (1.77) are observed.

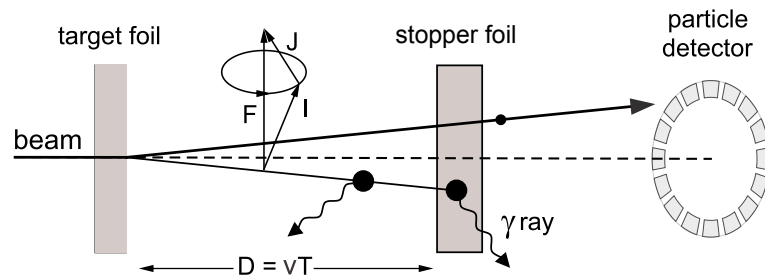


**Figure 1.5:** Schematic of a setup for a TDRIV experiment. The de-excitation  $\gamma$  rays can be emitted either in flight or at rest after implantation in the stopper foil. Light reaction fragments are registered in a particle detector to construct the particle- $\gamma$  angular correlations. The distance  $D$  between the two foils is controlled by the plunger device.

The flight time of the nucleus between the two foils defines the time in which the hyperfine interaction has acted on the nuclear spin. For a recoiling nucleus with velocity  $v$  and a distance between the foils  $D_1$  the flight time is  $T_{f1} = D_1/v$ . Increasing the plunger distance to  $D_2 > D_1$  gives a longer flight time  $T_{f2} > T_{f1}$ . During the added flight time  $\Delta T = T_{f2} - T_{f1}$  the

orientation of the nuclear spin has rotated around the total spin by an angle  $\Delta\theta = \omega_L \Delta T$ . As a consequence, when the recoils are implanted into the stopper the orientation of the spins, and so the particle- $\gamma$  angular correlations, will be slightly different. The plunger device allows to experimentally sample the Larmor frequency of precession of the nuclear spin ensemble through the dependence of the angular correlations on the flight time of the recoils.

The excited nuclear state can de-excite either in flight or at rest, implanted in the stopper. This results in two components of the particle- $\gamma$  angular correlations and the corresponding attenuation coefficients  $G_k(t)$ . The “flight” component refers to decays that have occurred in flight and the “stopped” component is due to decays at rest. The in-flight decays can occur at any point of the flight time which would correspond to different levels of attenuation. Therefore, an average “flight” attenuation coefficient is weighted by the possibility for the decay of the nuclear state [18]:

$$G_k^{\text{flight}}(T) = \frac{\int_0^T G_k(t) e^{-\lambda t} \lambda dt}{\int_0^T e^{-\lambda t} \lambda dt}. \quad (1.82)$$

The “flight” attenuation factors lead to a diminishing amplitude of the oscillation pattern over time. This results in a loss of anisotropy in the particle- $\gamma$  angular correlations as a function of flight time.

The attenuation coefficient for the “stopped” ions is simply [18]:

$$G_k^{\text{stopped}}(T) = G_k(t = T), \quad (1.83)$$

where  $T$  is the time at which the ions have reached the stopper foil. The  $G_k^{\text{stopped}}(T)$  represents a stable oscillation pattern with no loss of amplitude over time due to attenuation. This behaviour translates to the particle- $\gamma$  angular correlations as well.

The  $\gamma$  rays emitted in flight or at rest result in a shifted and unshifted peak in the detector energy spectra, respectively. The Doppler shift depends on the angles of emission of the  $\gamma$  ray relative to the direction of the nucleus. Depending on the particular detector configuration the Doppler shift could be small enough so that the shifted and unshifted  $\gamma$ -ray peaks may not be resolved in the energy spectra. In that case, the attenuation coefficient of the observed particle- $\gamma$  angular correlations is given by [18]:

$$G_k^{\text{total}}(t) = (1 - e^{-t/\tau}) G_k^{\text{flight}}(t) + e^{-t/\tau} G_k^{\text{stopped}}. \quad (1.84)$$

The combined effect of the “flight” and “stopped” component is such that the attenuation of the “flight” component reduces the amplitude of the “stopped” component over time. However, the frequencies that make up the oscillation pattern are identical for the “stopped”, “flight” and “total” cases.

Considering the particle- $\gamma$  angular correlations, the oscillatory pattern of  $G_k(t)$  would result in a periodic gain and reduction of anisotropy of the angular correlations. Therefore the frequency, and by extension the nuclear g factor, can be probed by measuring the changes of anisotropy of  $W(\theta_p, \theta_\gamma, \Delta\phi, t)$  as a function of flight time or plunger distance.

Experimentally, this is achieved by designating the particle-gamma detector combinations that exhibit the highest initial anisotropy of their angular correlations at  $t = 0$ . These combinations are separated in two groups - those for which the anisotropy initially increases as a function of flight time ( $W^\uparrow$ ) and those for which it initially decreases ( $W^\downarrow$ ). A ratio function is

then constructed by:

$$R(t) = \left( \prod_{i=1}^n \frac{W^\uparrow(t)}{W^\downarrow(t)} \right)^{1/n}, \quad (1.85)$$

where  $n$  is the number of considered particle- $\gamma$  detector combinations. The ratio function largely factors out detector efficiencies for both  $\gamma$  rays and particles. It exhibits an oscillatory pattern that is directly related to the precession frequency. Thus, the g factor of the state of interest can be extracted by fitting the experimentally-constructed  $R(t)$  function.

If the number of particle- $\gamma$  combinations  $n$  in Eq. (1.85) is too high, the combinations with lower anisotropy will decrease the overall sensitivity of the  $R(t)$  function. Instead, several groups of combinations can be defined with varying degrees of anisotropy to form several independent  $R(t)$  functions. These can be fitted simultaneously to obtain a consistent value for the g factor.

The optimal conditions for a TDRIV g-factor measurement would require a large fraction of ions with a single  $s$ -shell electron. They exhibit the largest hyperfine field strengths, given by:

$$B_{ns} = 16.7 \frac{Z^3}{n^3} \left[ 1 + \left( \frac{Z}{84} \right)^{5/2} \right], \quad (1.86)$$

where  $n$  is the major shell number. For H-like ions with a  $1s$  electron the hyperfine field strength increases rapidly with  $Z$ . At around  $Z \approx 20$  the precession frequency associated with the H-like ions would become too large to be experimentally measurable. To access higher- $Z$  nuclei with the TDRIV method Li-like ( $n = 2$ ) and Na-like ( $n = 3$ ) ions could be utilized to counteract the  $Z^3$  dependence.

One important experimental detail is related to the use of a plunger device. In general, the two plunger foils are stretched and kept parallel to each other. A voltage is applied to each one and the two parallel foils act as a capacitor. The capacitance of the system is a function of the distance between the foils and is measured in real time. In modern plunger devices, a piezo-electric motor is used to control the distance between the foils. It attempts to compensate any fluctuations based on the capacitance readings to keep the distance constant. Small defects or particles on the surfaces of the two foils limit the minimal distance between them. If the two foils come into contact the capacitance measurement fails and the control over the distance is lost. The absolute distance at which the two foils come into contact is referred to as the plunger zero-offset distance. Its absolute value is not easy to determine. For lifetime measurements with the RDDS method the absolute distance is not necessary as the relative changes of intensities are enough to extract the lifetime of interest. However, for the TDRIV method the zero-offset distance shifts the entirety of the obtained  $R(t)$  function along the time-axis. This introduces a large systematic uncertainty in the final g factor. Therefore, it is imperative that the zero-offset distance is determined in each experiment.

Several approaches exist to measure this distance. If the lifetime of the state of interest is known and the shifted and unshifted  $\gamma$ -ray peaks are resolved, the distance can be inferred from the ratio of the two areas of the peaks. Another alternative is to perform a calibration TDRIV measurement on a state with a well-known g factor. Yet another method used back in the 1970s and 1980s was to shine a light between the target and foil at the closest distance and measure the width of the passed light with a precision ruler [27]. The measured distance was then confirmed from the fits of the  $R(t)$  function. Lastly, a laser interferometer measurement has also been utilized in TDRIV measurements in the 1970s and 1980s [27, 28] to measure the zero-offset of the plunger device.

## TDRIV for radioactive ion beams

With the technical advancements in accelerators for nuclear physics, radioactive ion beams (RIBs) have become available at multiple facilities. Since most of the known nuclides are radioactive they can provide a great amount of information on nuclear structure. It is imperative that experimental methods are developed to accommodate experiments that utilize RIBs. One of the main problems with regard to RIB experiments are the low beam intensities. The achieved intensities, independent of production methods, are usually several orders of magnitude lower than those of stable beams. The RIV method has already been applied successfully to measure  $g$  factors of short-lived excited states in radioactive isotopes [22, 33, 34]. An issue related to the low beam intensity is the efficiency of the detection setup. The RIV and TDRIV methods have a clear advantage over other methods as they are able to make use of a full  $4\pi$  angular coverage if it is available. In contrast, other methods such as TDPAD and the transient field method only utilize detectors in one plane, which significantly reduces the  $\gamma$ -ray efficiency.

Another possible difficulty with RIB experiments is the build-up of  $\gamma$ -ray activity. The implanted radioactive nuclei undergo one or more  $\beta$  decays and large amounts of  $\gamma$  rays are produced from transitions in the daughter nuclei. During the running time of an experiment the intensity of these parasitic  $\gamma$  rays increases and can completely overwhelm even modern detectors, electronics and data acquisition systems. The RIV method partly circumvents this problem as the thin target allows for the unreacted radioactive beam to move out of view of the detection system. Some beam nuclei are scattered and remain within the vacuum chamber, yet they are orders of magnitude less than the total unreacted beam. The TDRIV method, on the other hand, becomes impossible to use as all projectiles are stopped by the thick stopper foil.

To overcome this drawback of the TDRIV method Stuchbery, Mantica and Wilson [35] proposed a modification to the method that would enable its use in RIB experiments. They suggested to exchange the thick stopper foil for a thin foil which only resets the electron configuration of the recoiling ions. The thinner foil would allow for the scattered beam particles to be directly registered in the particle detector, while the unreacted beam is deposited away from the detector setup (see Fig. 1.6).

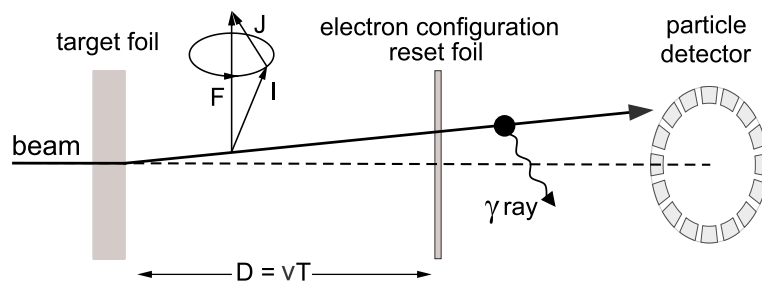


**Figure 1.6:** Schematic of the modified setup for a TDRIV experiment on RIBs. The stopper foil is exchanged for a thin reset foil so that the unreacted RIB nuclei can be deposited away from the detector setup. The scattered beam nuclei are directly registered in a particle detector to construct the particle- $\gamma$  angular correlations. The de-excitation  $\gamma$  rays are emitted in flight either before or after the reset foil.

In this case, the attenuation factor for ions between the target and reset foil is the same as in the original formulation of the TDRIV method (see Eq. (1.82)). The attenuation factor after the reset foil is given by [35]:

$$G_k^{\text{reset}}(T) = G_k(T)G_k(\infty), \quad (1.87)$$

where  $G_k(\infty)$  is the average attenuation coefficient for decays after passing through the reset foil. Simulations performed by the authors showed that the observed oscillation frequency in the  $R(t)$  function remains the same in the modified method, at the cost of a diminished amplitude.

The feasibility of the proposed TDRIV method for use with RIBs was tested in an experiment performed at the ALTO facility in Orsay, France. The goal of the experiment was to measure the g factor of the  $2_1^+$  state in stable  $^{24}\text{Mg}$ , which was already known from literature  $g_{lit}(2_1^+, ^{24}\text{Mg}) = 0.51(2)$  [27]. The measurement yielded a very accurate and precise result of  $g(2_1^+, ^{24}\text{Mg}) = 0.538(13)$  [36] which showed that the modified TDRIV method is viable. A comparison between the simulated  $G_k(t)$  coefficients for  $^{24}\text{Mg}$  for the standard and modified TDRIV methods is shown in Fig. 1.7.

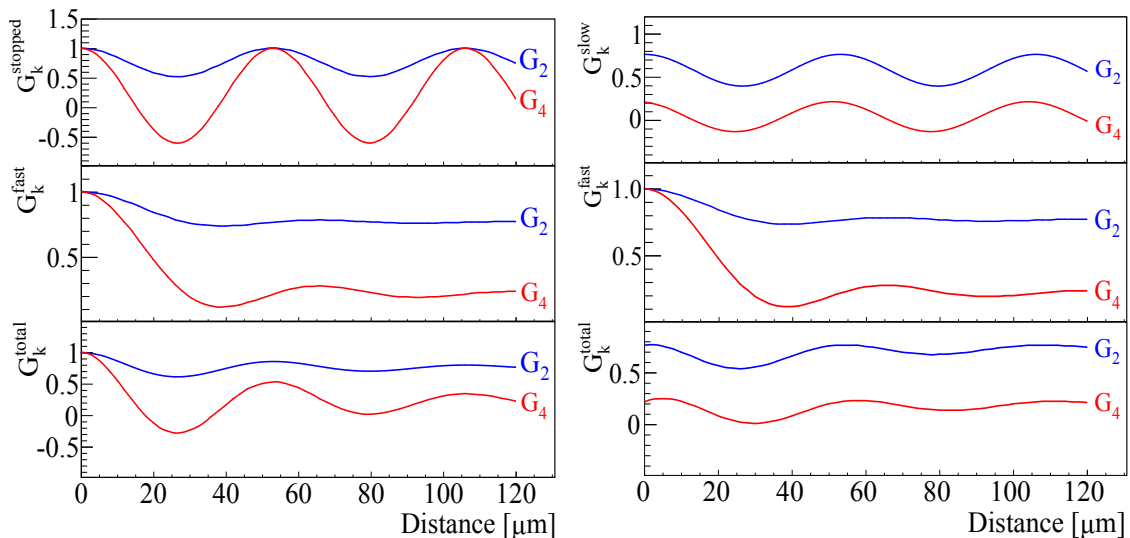


**Figure 1.7:** Comparison between the attenuation factors for the original (left) and the modified (right) TDRIV method. The notations  $G_k^{\text{fast}} \equiv G_k^{\text{flight}}$  and  $G_k^{\text{slow}} \equiv G_k^{\text{reset}}$  are used. Figure adapted from Ref. [37].

The first application of the new TDRIV technique on a RIB was an experiment to measure the g factor of the  $2_1^+$  state in  $^{28}\text{Mg}$ . The analysis of the obtained data is part of the current work and is described in detail in Chapter 2.

### 1.2.3 The transient field method

One of the available alternative methods for measuring g factors of short-lived excited states is the transient field method. A very brief overview will be provided below mainly to provide context for comparison with the TDRIV method. A more extensive review of the method can be found in Ref. [38].

The TF method is based on the hyperfine interaction of ions recoiling through solids. The beam nuclei impinge on a multi-layered target. The nuclear reaction which populates the excited state of interest and produces a spin-oriented ensemble occurs in the first layer of the target, facing the beam. Most often Coulomb excitation is used. The second layer is made of a ferromagnetic material such as iron or gadolinium. An external magnetic field is applied to polarize the ferromagnetic material. This polarization also affects and orients the spins of some of the electrons in the material. When a high-velocity ion passes through a solid it captures and releases electrons very rapidly multiple times. At each step, the hyperfine interaction couples the oriented nuclear spin to the atomic spin and gives rise to a precession of the nuclear spin around the total spin  $F$ . Most of the electrons in the ferromagnetic material are not polarized

by the external magnetic field and their spins are isotropic. The net effect of the precession of the nuclear spin from coupling to electron spins with isotropic orientation would be zero. However, every interaction of the nucleus with an electron with a polarized spin would always lead to a precession with the same direction and with a frequency that depends on the orbital in which the electron was captured. Although the fraction of polarized electrons in the material is small, the net effect of a large amount of interactions with such electrons would be a small shift in the orientation of the nuclear spin. This shift can again be described through attenuation coefficients  $G_k(t)$ . The projectiles are usually stopped in a third layer of the target, which is not ferromagnetic.

The perturbed particle- $\gamma$  angular correlations are measured to determine the shift in the orientation and obtain the g factor of the nuclear state. Only light scattered target nuclei are registered in a particle detector. The highest sensitivity to the angular correlations is in a plane perpendicular to the orientation of the external magnetic field and the polarization of the ferromagnetic material. Similar to the TDPAD method, the optimal configuration consists of four detectors in a compact configuration around the target. In the case of the TF method, the detectors are not at  $90^\circ$  angles with respect to each other. They are placed at the positions which correspond to the largest slope in the particle- $\gamma$  angular correlations, where the small change in orientation would yield the largest visible effect.

The transient field is the net magnetic field at the site of the nucleus during its passage through the ferromagnetic host. Although in principle it consists of a sequence of hyperfine fields that could be calculated, no analytic expression exists for the TF strength  $B_{TF}$ . It has been shown that the TF strength depends on the ferromagnetic material, the degree of polarization of the electrons, the atomic number  $Z$  of the recoiling ion and its velocity  $v$ . The velocity dependence has been linked to the Bohr velocity-matching criterion. The criterion states that the highest probability to capture an electron is expected when the Bohr velocity of the bound electron is similar to the ion velocity in the medium. This has been shown to be the case for light nuclei [38].

Over the last several decades several parametrizations of the TF strength have been suggested [39, 40, 41, 42]. Each parametrization contains several free parameters that are fitted to available experimental data, usually for a limited range of ion velocities and  $Z$ . Some general conclusions that have been reached are that the  $Z$ -dependence is generally smooth yet not necessarily monotonous. Without a specific measurement of the TF strength for a given  $Z$  it cannot be guaranteed that its strength would be similar to that for  $Z \pm 1$ . No  $N$  dependence has been observed and the velocity dependence of the TF strength has been shown to remain identical along an isotopic chain. This allows for multiple relative g-factor measurements in neighboring isotopes to be performed relative to a single absolute g-factor value. The absolute reference value is usually a g factor that has been measured by a different method. This type of relative measurements use the same parametrization for  $B_{TF}$ , which allows for the results to be scaled accordingly at a later date if the reference g-factor value is found to be erroneous or the parametrization itself is modified. However, the free-fitted parameters of each parametrization are a source of systematic uncertainties.

Since the 1970s, a lot of the low-lying short-lived excited states in stable isotopes have been measured using the TF method. Several measurements on RIBs have also been performed [43, 44, 45, 46]. More recently, the High-Velocity Transient Field (HVTF) method was proposed for applications to RIBs. The higher velocity of the ions aims to increase the capture of  $1s$  electrons as the H-like hyperfine fields are the strongest. This would result in a higher frequency and a larger net rotation of the nuclear spin orientation. Two HVTF measurements have been performed, both on RIBs [47, 48, 49, 50]. The main issue with applying the TF method on

RIBs is that the projectiles are stopped in the target and activity builds up over time. This sets some limitations on the beam intensity that can be utilized in such experiments as to not deteriorate the detector performance from the high  $\gamma$ -ray rates.



# 2 - Magnetic moment of the $2_1^+$ state in $^{28}\text{Mg}$

## 2.1 The $N = 20$ island of inversion

The region of deformation in Ne, Na and Mg isotopes at  $N \approx 20$  was first discovered in the 1970s. A direct mass measurement of Na isotopes by Thibault *et al.* [51] found indications for a sudden onset of deformation in  $^{31,32}\text{Na}$  from the two-neutron separation energies  $S_{2n}$ . A similar shape transition had already been described in the region  $N = 88 - 92$  when approaching the rare-earth nuclei, well known for their deformed rotational structure. A theoretical explanation for this phenomenon, proposed by Campi *et al.* [52], was that the deformation arises due to filling of the  $f_{7/2}$  orbital. The authors point out that this can be understood in terms of Nilsson's diagrams due to the crossing of the  $1f_{7/2}$  and  $1d_{3/2}$  subshells at large prolate deformations. They performed Hartree-Fock calculations with a modified Skyrme interaction and were able to reproduce the results of Ref. [51]. A follow-up mass measurement of  $^{31,32}\text{Mg}$  [53] confirmed the shape transition is also observed in the Mg isotopes. A laser spectroscopy measurement of Na isotopes reported a continuous increase of the mean square charge radii up to  $^{34}\text{Na}$  [54]. Two  $\beta$ -decay studies of Na isotopes [55, 56] confirmed the deformation in  $^{32}\text{Mg}$  through  $\gamma$ -ray spectroscopy. The observed drop in excitation energy of the first  $2^+$  state from 1483 keV in  $^{30}\text{Mg}$  to 885 keV in  $^{32}\text{Mg}$  was attributed to a large deformation. All of the aforementioned works established the region around  $^{32}\text{Mg}$  as a new region of nuclear deformation, that was referred to as an "island of inversion" (IoI).

Later studies attempted to obtain more information about the region from transition probabilities. The first intermediate-energy Coulomb-excitation experiment on  $^{32}\text{Mg}$  was performed at RIKEN [57]. The authors obtained a  $B(E2, 0_1^+ \rightarrow 2_1^+)$  value much larger than predicted by pure  $sd$ -shell calculations for a semi-magic nucleus. Their results, however, were in very good agreement with previously published calculations in the  $sdpf$  valence space [58]. Further experiments at NSCL/MSU [59], GANIL [60] and RIKEN [61] extended the limits of the IoI to Ne isotopes and more exotic Mg isotopes. Conflicting results for the transition probabilities in  $^{30}\text{Mg}$  and  $^{32}\text{Mg}$  prompted several experiments to be performed also at ISOLDE, CERN [62, 63, 64]. The results for  $^{30}\text{Mg}$  are in agreement with a pure- $sd$  shell-model view and the authors state that it is located outside of the IoI. In contrast, the  $^{31}\text{Mg}$  results indicate that the intruder  $fp$  configurations dominate over the spherical  $sd$  ones in the ground-state band [64]. This is interpreted as  $^{31}\text{Mg}$  being the first Mg isotope inside the IoI. Although these two studies describe a sharp boundary of the IoI, this is still a topic of debate. A recent experiment of single-neutron removal from  $^{31}\text{Mg}$  was performed at GANIL to investigate  $^{30}\text{Mg}$  and the transition towards the IoI [65]. The results were not conclusive but favored a smooth transition into the IoI rather than a clear transition at  $^{31}\text{Mg}$ . This view is also supported by recent theoretical calculations by Tsunoda *et al.* [66] in the  $sdpf$  model space. The calculations predict a gradual increase of the number of particle-hole excitations in the ground state of even-even Mg isotopes up to  $^{28}\text{Mg}$ . This is followed by an abrupt increase in two steps - from  $^{28}\text{Mg}$  to  $^{30}\text{Mg}$  and then another reaching  $^{32}\text{Mg}$ . Specifically for  $^{30}\text{Mg}$ , it is predicted that  $2p - 2h$  excitations will dominate the ground-state wave functions, followed by equal amounts of  $0p - 0h$  and  $4p - 4h$

excitations. In the case of  $^{32}\text{Mg}$ , the contribution of  $4p - 4h$  excitations is expected to surpass that of  $2p - 2h$ , with an additional small fraction of  $6p - 6h$  and virtually no  $0p - 0h$  excitations. The authors of the study argue that the increase in  $4p - 4h$  and  $6p - 6h$  configurations is the main driver of the nuclear deformation in this region.

Direct information about the relevant configurations of the nuclear wave functions can be obtained through g-factor measurements. We performed shell-model calculations with the ANTOINE code [67] using the USDB interaction [68] to calculate the expected g factors of the first  $2_1^+$  states in even-even Mg isotopes. Note that the effective nucleon g factors proposed in Ref. [69] were used in the calculations. The results are shown in Fig. 2.1 and compared with Monte Carlo Shell Model calculations from Ref. [70] in the *sdpf* model space. Analogous calculations with the *J*-coupled code NATHAN [71] were performed by Dr. Kamila Sieja, IPHC Strasbourg, to obtain the decomposition of these states in pure proton or neutron configurations. The g factor of the  $2_1^+$  state in  $^{24}\text{Mg}$  is calculated to be just above 0.5, as expected for an  $N = Z$  nucleus. The protons and neutrons play an equal role in the  $2_1^+$  excitation with 25.6% of the wave function being  $\pi(2^+) \otimes \nu(0^+)$  and 25.6% being  $\pi(0^+) \otimes \nu(2^+)$ . At  $^{26}\text{Mg}$ , the  $\nu d_{5/2}$  sub-shell closure reduces the neutron contribution ( $\pi(0^+) \otimes \nu(2^+) = 17.1\%$ ) and the higher proton contribution ( $\pi(2^+) \otimes \nu(0^+) = 52.4\%$ ) increases the g-factor value. A similar, yet diminished, effect is present in  $^{28}\text{Mg}$  where the  $\nu s_{1/2}$  sub-shell closure is reached, with 26.6% pure neutron and 42.8% pure proton contributions. Then, the g factors from the USDB calculations increase towards the  $N = 20$  shell closure in  $^{32}\text{Mg}$  where the  $2_1^+$  configuration is determined entirely by proton excitations as no cross-shell excitations are allowed for the neutrons.

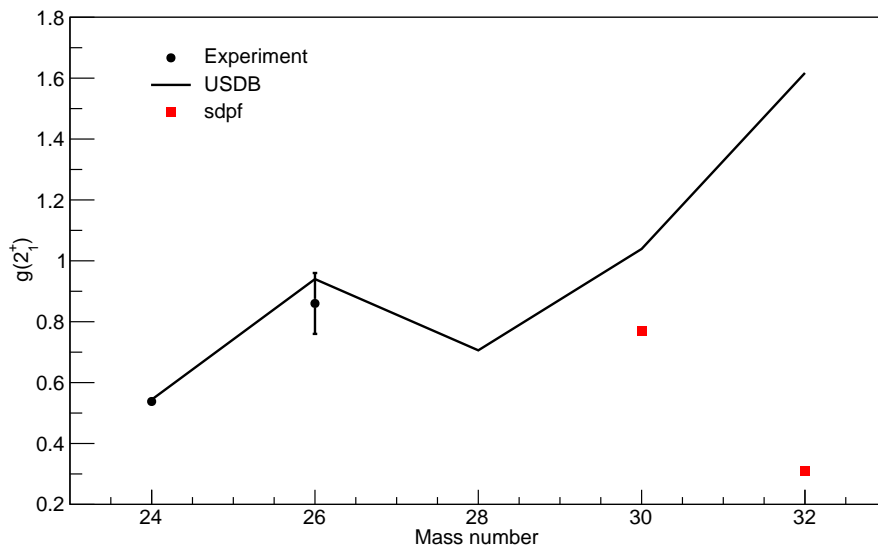


**Figure 2.1:** Experimental and calculated g factors for even-even Mg isotopes. Uncertainty of  $^{24}\text{Mg}$  result is smaller than the point. Our USDB calculations use the effective g factors while the *sdpf* calculations [70] used the free-nucleon g factors, hence, the comparison is strictly qualitative.

In contrast, the *sdpf* calculations by Otsuka *et al.* [70] predict a deviation from the pure *sd*-shell behaviour at  $^{30}\text{Mg}$  due to neutron excitations to the  $f_{7/2}$  orbital. It must be stressed, however, that the calculations by Otsuka *et al.* [70] are possibly outdated, as their predictions for the relative fractions of  $np - nh$  configurations in Mg isotopes differ significantly from the more recent calculations by Tsunoda *et al.* [66]. For comparison, the fractions of  $np - nh$ ,  $n = 0, 2, 4$  excitations in  $^{28}\text{Mg}$  are approximately 96%, 4% and 0% (Ref. [70]) and 64%, 33% and 3% (Ref. [66]), respectively. The same comparison for  $np - nh$ ,  $n = 0, 2, 4, 6$  excitations in  $^{32}\text{Mg}$  yields 9%, 63%, 29% and 0% (Ref. [70]) and 2%, 36%, 52% and 10% (Ref. [66]), respectively. One could expect that the *sdpf* g factors shown in Fig. 2.1 could possibly decrease further when

the additional neutron  $p - h$  excitations to the  $f_{7/2}$  are considered. Such a decrease would be more pronounced for the more neutron-rich nuclei, within the IoI.

From the experimental point of view, the lifetimes of the  $2_1^+$  states in these Mg isotopes vary from about 0.7 ps in  $^{26}\text{Mg}$  to around 16 ps in  $^{32}\text{Mg}$ . The  $g$  factors of excited states with such lifetimes are accessible for the RIV, the TDRIV and the TF methods. However,  $^{28-32}\text{Mg}$  isotopes are radioactive, which adds to the complexity of such a measurement. Up to now, there have been only three RIV measurements [22, 33, 34] and six transient field measurements [43, 47, 48, 44, 50, 45, 46] on radioactive ion beams. Although a modification of the TDRIV method for RIB applications was introduced by Stuchbery, Mantica and Wilson [35], it has not been tested experimentally on a radioactive ion beam. Its first application on a stable beam was the measurement of  $g(2_1^+)$  in  $^{24}\text{Mg}$  using H-like ions by Kusoglu *et al.* [36]. The obtained result is in agreement with the USDB calculations as seen from Fig. 2.1. Further, the result shows the exceptional precision and accuracy that can be achieved with the TDRIV method. A later TF measurement of  $g(2_1^+, ^{26}\text{Mg})$  [72], performed relative to the precise value of  $g(2_1^+, ^{24}\text{Mg})$ , resolved a discrepancy between several previous measurements and is also in agreement with the USDB calculations. However, this measurement also exhibits a lack of precision, inherent to the TF method. An experiment to measure  $g(2_1^+)$  in  $^{28}\text{Mg}$  was performed in 2017 at ISOLDE, CERN. The first goal of the experiment was to apply the modified TDRIV method [35] to a radioactive ion beam for the first time. The second, equally important goal was to use the  $^{28}\text{Mg}$  measurement as a stepping stone on the way to measure  $g(2_1^+, ^{32}\text{Mg})$  in the IoI, which would provide a stringent test for the theoretical models in this region. The details of the  $^{28}\text{Mg}$  experiment, the data analysis and the obtained results are presented in this chapter.

## 2.2 Experimental setup

The ISOLDE facility at CERN is specialized in the production of radioactive ion beams through the Isotope Separation On-Line (ISOL) technique. This technique can be implemented in various ways. Usually, it requires a thick target that is bombarded with high-energy particles that induce fission, fragmentation and spallation processes to produce radioactive isotopes. These isotopes are extracted from the target, ionized, mass separated and then the isotope of interest is transported to the experimental setup. A schematic of the ISOLDE experimental hall is shown in Fig. 2.2

### 2.2.1 Isotope production

The ISOL method at ISOLDE is implemented via a pulsed beam of 1.4-GeV protons from the Proton Synchrotron Booster. The protons impinge on a cylindrical target container with a 2-cm diameter and 20-cm length. The target, placed inside the container, can be chosen from a number of materials (Pb, Ta, Sn, Nb, etc.) or compounds ( $\text{UC}_x$ ,  $\text{ZrO}_2$ ,  $\text{SiO}_2$  etc.). Optimization of the target material and its properties can lead to higher yields of the desired isotopes or improved purity of the beam. Some of the target properties that have to be considered before an experiment include its density, production cross sections, release characteristics, etc.

Neutron-rich nuclei are produced through fission and spallation processes, while neutron-deficient nuclei are produced from fragmentation reactions. The beam purity for some neutron-rich isotopes may be improved if neutron-induced fission is used as opposed to proton-induced fission. In such cases a proton-to-neutron converter is placed parallel to the target container. The proton beam impinges on the converter, typically made of tungsten, and induces spallation reactions. The spallation generates neutrons that in turn induce fission in the ISOLDE target.

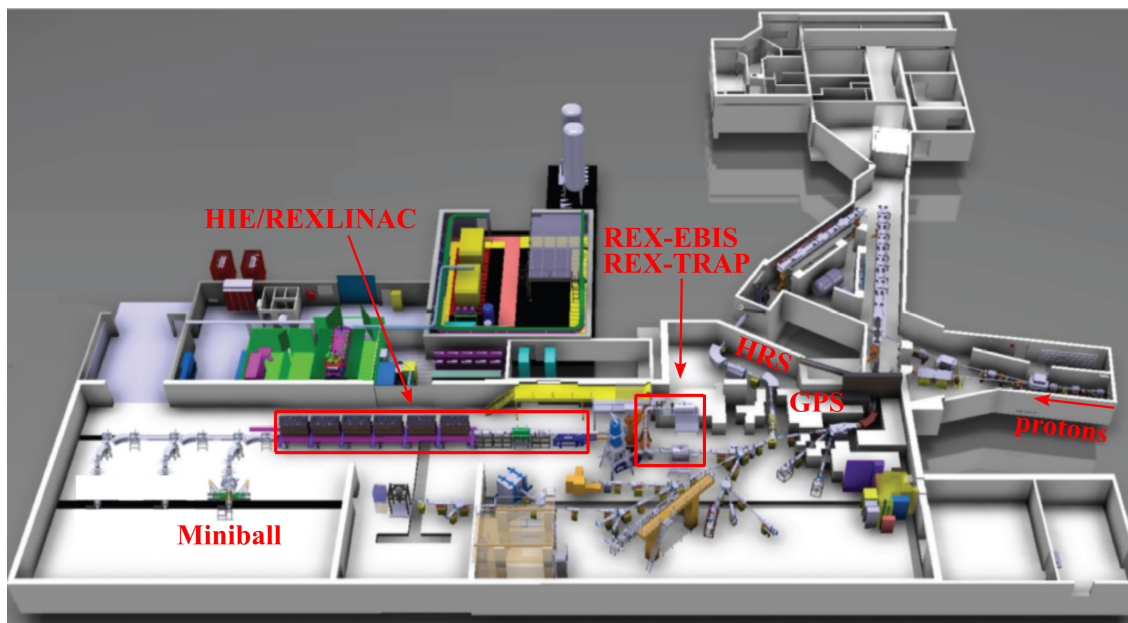


**Figure 2.2:** A schematic view of the ISOLDE experimental hall, adapted from [73]. Some of the infrastructure relevant to the present work is marked in red.

A wide range of isotopes can be produced by the ISOL method via different reaction mechanisms. However, the method has some limitations on which of these isotopes can be extracted and prepared as a beam for experiments. The extraction of the various isotopes produced in the target is achieved through the processes of diffusion and effusion. The target is electrically heated to around  $2000^{\circ}\text{C}$  to increase the mean free path of the isotopes in the material and aid these processes. One major limitation of the ISOL technique is that isotopes of refractory elements, such as W, Re, Os, Zr, etc., with very high boiling temperatures are impossible to extract from the target due to their low mobility in the material. The second important limitation of the ISOL method is related to the half-lives of the desired isotopes. In general, if the half-life of a given isotope is shorter than a few ms, the efficiency of its extraction and utilization as a beam is heavily reduced. This is due to the time required for its extraction, ionization, mass separation and transport to the experimental setup, which can vary between a few ms and several seconds.

### 2.2.2 Ion source and mass separation

The isotopes that successfully exit the target material do so as neutral atoms. They have to be ionized in order to be manipulated with electric and magnetic fields and transported towards the experimental setup. The extracted atoms are guided through an electrically heated cavity. Collisions of the extracted atoms with the walls of the hot cavity can cause them to lose an electron and become ionized. The cavity is typically made of a material with a high work function such as tungsten. If the ionization potential of the extracted atoms is lower than the work function of the cavity, the surface ionization becomes very efficient. However, this is not a selective process - atoms of multiple isotopes are ionized at the same time. Thus, even after mass separation the beam would contain the isotope of interest and multiple isobaric contaminants.

A more advanced method to selectively ionize the atoms of the desired isotope is through laser ionization. The Resonance Ionization Laser Ion Source (RILIS) [74, 75] is based on the fact that the atomic structure of each element is unique. It utilizes a combination of two or

three tunable, pulsed lasers to excite an electron to a high-lying excited state and subsequently ionize it. The laser pulses are directed along the axis of the hot cavity. The material of the cavity is also modified to have a lower work function (e.g. Nb, TaC) to decrease the probability for parasitic surface ionization. A laser ionization scheme is devised separately for atoms of different elements and the exact cascade of atomic transitions is chosen to optimize the ionization efficiency. The efficiency of RILIS can be up to several orders of magnitude larger than surface ionization [75]. In addition, RILIS significantly reduces the amount of isobaric contaminants in the beam. However, RILIS is element-specific and not isotope-specific, hence, ions of multiple isotopes of the same element are produced simultaneously. The singly-charged ions are guided out of the hot cavity via an extraction electrode to be mass separated.

There are two mass separators available at ISOLDE, each with its own primary target and ion source. These are the General Purpose Separator (GPS) and the High Resolution Separator (HRS). Per their specifications, the GPS has a mass resolving power of  $M/\Delta M = 2400$ , while the HRS has a mass resolving power of up to  $M/\Delta M = 15000$  [76], however, the resolving power of both separators can be significantly lower in experimental conditions. Both separators are connected to the beam line that supplies the majority of experimental setups in the ISOLDE hall.

### 2.2.3 Post-acceleration: REX- and HIE-ISOLDE

The energy of the radioactive ion beam after mass separation is typically in the 30- to 60-keV range. These energies are suitable for low-energy experiments such as studies of  $\beta$ -decay, ground-state properties, mass measurements, laser spectroscopy, etc. Experiments aiming at investigating the excited-state structures of the radioactive beam nuclei require much larger beam energies in the order of several MeV/A. This is achieved through post-acceleration of the radioactive ion beam. The first project for post-accelerated beams at ISOLDE was the Radioactive beam EXperiment (REX) [77]. It was later upgraded to High Energy and Intensity (HIE)-ISOLDE [78]. The entire post-acceleration setup at ISOLDE consists of four stages - REXTRAP, REXEBIS, REXLINAC and HIELINAC.

#### REXTRAP

The incoming semi-continuous beam of ions from the mass separator is injected into the REXTRAP Penning trap [77, 78], designed inside a 3 T cylindrical superconducting magnet. Electrodes at the entrance and exit of the trapping volume generate the entry and exit potential barriers of the trap. The incoming ions are electrostatically decelerated by the entry barrier of the trap. Once inside the trap volume, the ions oscillate longitudinally between the entry and exit potential barriers. The ions are further cooled down by collisions with a buffer gas inside the trap volume, typically Ne, Ar or both. The magnetic field induces a combination of a magnetron and a reduced cyclotron motions that lead to a radial expansion of the ion orbits. A radio frequency field is applied to a split-ring electrode in the center of the trap for radial cooling. As a result of the applied fields and cooling the ions are accumulated in the potential minimum of the trap. After sufficient cooling the exit potential barrier of the trap is lowered and the bunched ions are extracted.

#### REXEBIS

At this stage, the incoming ions are singly-charged. However, it is very inefficient to accelerate singly-charged ions and it requires a large amount of space for the acceleration stage.

Due to the limited space available at the ISOLDE hall it was deemed that an intermediate charge-breeding station would be the most efficient solution. The bunches of singly-charged ions from REXTRAP are sent towards REXEBIS (Electron-Beam Ion Source) [77, 78] for charge-breeding. This is achieved by trapping the ion bunch in a cylindrical trap inside a superconducting solenoid magnet with a field of 2 T. Inside the trapping region it is ionized by an intense beam of 3- to 6-keV electrons produced by an electron gun. The mass-to-charge ratio of the ions after charge breeding is in the range  $2.5 < A/Q < 4.5$ , where the upper limit is imposed by the acceptance of the REXLINAC. The charge-breeding time depends on the requested  $A/Q$  value for post-acceleration and the mass of the ions. For light ions ( $A < 10$ ) it is in the order of a few ms and reaches hundreds of ms for heavy ions ( $A > 200$ ). After sufficient charge-breeding time the extraction potential is lowered to allow the ions to escape the trap. The potential can be modulated to perform a fast or slow extraction of the ion bunch. Residual gasses from REXTRAP (Ne and Ar) are usually also present in REXEBIS. An additional  $A/Q$  selection is installed between REXEBIS and REXLINAC for the radioactive ion beam. A scan over  $A/Q$  values is performed before each measurement to determine the optimal  $A/Q$  value that maximizes beam intensity and minimizes the amount of contaminants. The contamination at this stage could be any stable isobaric contaminant from the secondary beam or the Ne and Ar.

Although the Ne gas from REXTRAP is typically considered a beam contamination, it is also used as a stable beam for detector tests in the experimental setups after the post-acceleration stage. In this case the presence of Ne in REXEBIS is considered an advantage as such detector tests can be performed independently while a radioactive ion beam is delivered to other low-energy experiments at ISOLDE.

## REXLINAC and HIELINAC

The REXLINAC [77, 78] is a compact linear accelerator operating at room temperatures. It was installed in 2001 with a maximum beam energy of 2.2 MeV/A, increased to 3 MeV/A in 2004 with the addition of another accelerating cavity. The successful experiments performed with REX-ISOLDE in the early 2000s prompted the development of the HIE-ISOLDE project to attain higher beam energies. A set of six cryomodules with a total of 32 superconducting radio-frequency (RF) cavities is envisaged to reach a maximum beam energy of 10 MeV/A [78]. The first two cryomodules of the HIELINAC were installed in the beginning of 2017 and placed after the REXLINAC. They allowed the radioactive beams to be accelerated up to 5.5 MeV/A. A second pair of cryomodules was installed in 2018. The last two cryomodules will replace some of the REXLINAC cavities.

The post-accelerated beam is delivered to one of three experimental areas - the MINIBALL  $\gamma$ -ray spectrometer, the ISOLDE Solenoidal Spectrometer (ISS) or the area dedicated to movable setups.

### 2.2.4 The MINIBALL setup

The MINIBALL  $\gamma$ -ray spectrometer [79, 80] was designed in parallel with and specifically for experiments at REX-ISOLDE. As such, its characteristics are adapted to tackle the difficulties entailed by experiments with post-accelerated radioactive ion beams. One of these difficulties is the lower beam intensity compared to that of stable beams, especially for nuclei far away from stability. In addition, the post-accelerated nuclei typically have a velocity of a few percent of the speed of light, reaching more than 10% for lighter nuclei. All  $\gamma$ -rays emitted in flight by these nuclei will exhibit a significant Doppler shift that has to be corrected for. This requires

precise knowledge of the velocity and direction of the nuclei, as well as the direction in which the  $\gamma$ -ray was emitted. Moreover, the presence of background radiation from the decay of the radioactive beam has to be considered as a possible contamination in the  $\gamma$ -ray spectra.

To tackle these challenges, the MINIBALL detector setup was developed and put into operation in 2001. It consists of eight triple clusters of encapsulated large-volume  $n$ -type HPGe detectors. The clusters are mounted on movable arc-shaped arms allowing for flexible placement of the detectors. The secondary target is placed inside a vacuum chamber at the center of the detector setup (see Fig. 2.3). In a compact configuration, at the shortest possible distance from the target position, the full MINIBALL setup covers about 60% of the  $4\pi$  solid angle. In this configuration, a photopeak efficiency of about 8% is achieved for 1.3-MeV  $\gamma$ -rays, and a high energy resolution of 2.3 keV is obtained at this  $\gamma$ -ray energy. The outer contact of each individual HPGe crystal is electronically six-fold segmented to reduce the effective solid angle and allow for precise corrections for the Doppler shift. The signals of each segment are read out separately, as is the core signal - equivalent to the sum of all segment signals within uncertainties.

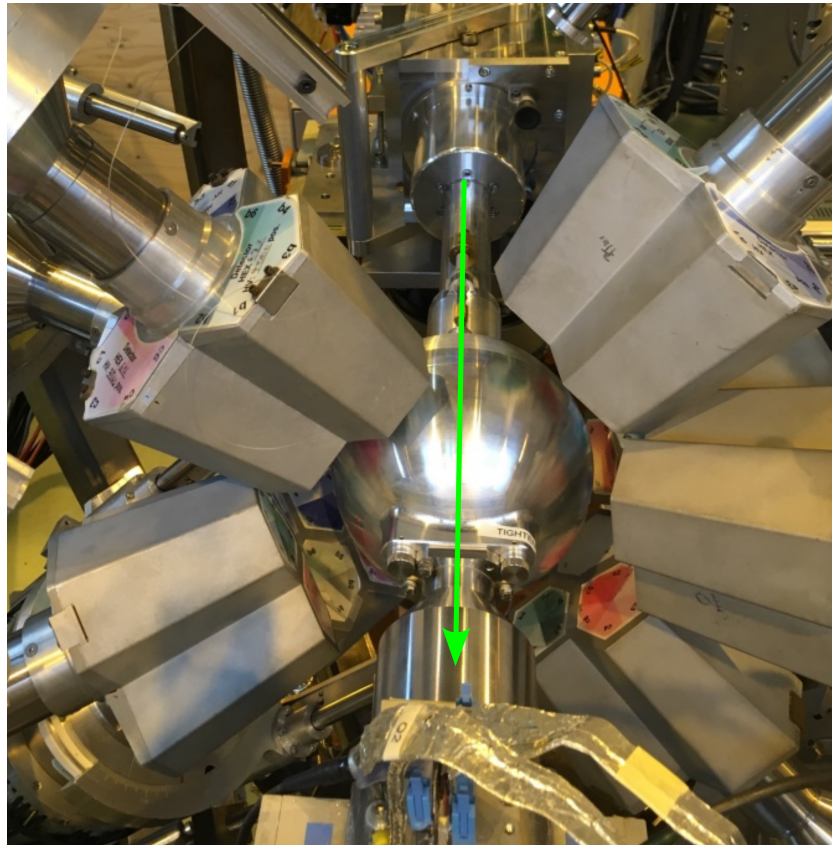


**Figure 2.3:** The configuration of the MINIBALL clusters in the present experiment with the beam direction shown with the green arrow. Photo courtesy of Dr. Liam P. Gaffney.

Although the interaction point of the  $\gamma$  ray is important, the direction and velocity of the emitting nucleus is equally important for a precise Doppler correction procedure. Typically, the radioactive ion beams at MINIBALL are used in Coulomb-excitation or transfer-reaction experiments. In both cases the beam nuclei impinge on a stable target at the center of the MINIBALL setup. The HPGe detectors then register the  $\gamma$  rays emitted in flight by the scattered nuclei. Ancillary particle detectors are placed inside the vacuum chamber to measure the direction and energy of these nuclei. The data from the particle detectors is used for the Doppler correction of the coincident  $\gamma$  rays on an event-by-event basis.

## CD DSSSD

The Compact Disk (CD) Double-Sided Silicon Strip Detector (DSSSD) [81] is a particle detector developed for Coulomb-excitation experiments at MINIBALL. It has an inner and outer active diameter of 16 and 84 mm, respectively, and is comprised of four identical quadrants. The front face of each quadrant is divided into 16 annular strips (rings) with a width of 1.9 mm and a 2-mm pitch (see Fig. 2.4). The back face of each quadrant contains 24 sector strips with a pitch of  $3.4^\circ$ . As per its specifications, the azimuthal angular coverage of each quadrant is limited to about  $82^\circ$  due to the space needed for the signal readouts of all channels. This will be discussed further in Chapter 2.3.1. The segmentation of the front and back faces of the CD detector provides a very precise simultaneous determination of the direction ( $\phi_p, \theta_p$ ) and velocity ( $E_p$ ) of the incident particles.

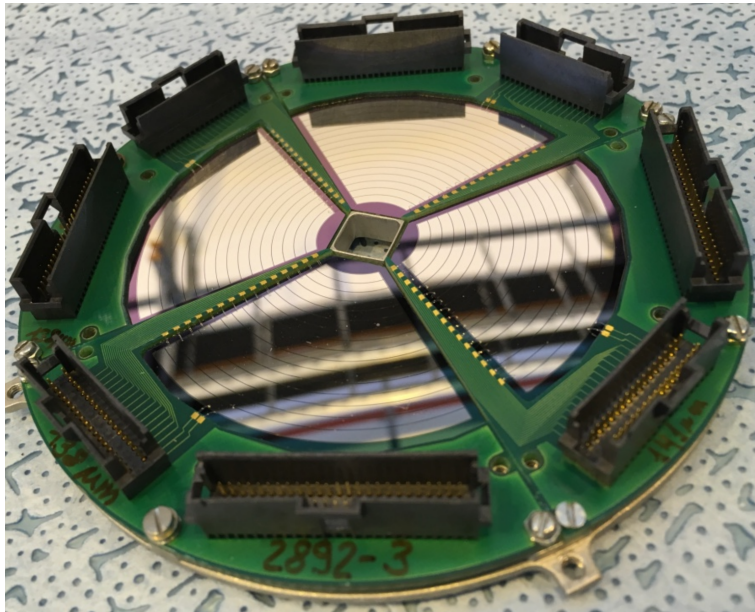


**Figure 2.4:** The front face of the CD DSSSD with the segmentation in annular rings visible. Photo courtesy of Dr. Liam P. Gaffney.

## Miniball plunger device

To increase the capabilities of the MINIBALL setup a plunger device was developed to enable lifetime measurements of excited nuclear states via the Recoil Distance Doppler Shift (RDDS) method. The design of the plunger device and the modified vacuum chamber was accomplished by the Institute of Nuclear Physics at the University of Cologne, Germany.

## 2.3 Data taking and analysis

The experiment to measure the  $g$  factor of the  $2_1^+$  state in  $^{28}\text{Mg}$  using the TDRIV method was performed at ISOLDE in November 2017. The Mg nuclei were extracted from a  $\text{SiO}_2$  primary target and ionized using the RILIS. After mass separation with the GPS, the  $^{28}\text{Mg}$  beam was post-accelerated to 5.5 MeV/A and delivered to the MINIBALL setup. The setup consisted of the eight MINIBALL triple clusters of HPGe detectors, the CD DSSSD particle detector and the MINIBALL plunger device. A  $3.9 \text{ mg/cm}^2$   $^{93}\text{Nb}$  foil and a  $1.1 \text{ mg/cm}^2$   $^{181}\text{Ta}$  foil were used as a plunger target and electron configuration reset foil, respectively.

It has to be noted that the  $^{28}\text{Mg}$  experiment was the first one to utilize the MINIBALL plunger. As such, special care was taken to calibrate the system with an additional TDRIV g-factor measurement performed on the  $2_1^+$  state in stable  $^{22}\text{Ne}$ , easily available from REX-TRAP/REXEBS. The adopted value for this g factor  $|g(2_1^+, ^{22}\text{Ne})| = 0.326(12)$  was measured by Horstman *et al.* [28] with very good precision. Therefore this complementary TDRIV measurement could be used to test the MINIBALL plunger. In addition, by applying the TDRIV analysis procedure on the well-known  $^{22}\text{Ne}$   $g(2_1^+)$  value, the zero-offset distance of the plunger device could be extracted. Then, the zero-offset could be fixed for the TDRIV analysis of the  $^{28}\text{Mg}$  data to significantly decrease the systematic uncertainty.

The calibration run with a  $^{22}\text{Ne}$  beam was performed at the beginning of the experiment. Data was collected at 18 different plunger distances between 0.7 and 720  $\mu\text{m}$ . These values do not include the plunger zero-offset, which was to be deduced from the data analysis. Afterwards, the first run with a radioactive  $^{28}\text{Mg}$  beam was started. The average proton current on the primary  $\text{SiO}_2$  target was initially about 2  $\mu\text{A}$ . The  $^{28}\text{Mg}$  singly-charged ions were charge bred to a 9+ charge state ( $A/Q = 3.11$ ) before post-acceleration. The beam intensity on the MINIBALL target was about  $4 \times 10^6$  pps. A fraction of the incoming beam nuclei were Rutherford scattered within the vacuum chamber. Of those, only the  $\gamma$  rays emitted by Coulomb-excited nuclei, registered in the CD detector, were of interest for the experiment. Most of the scattered nuclei simply contributed to increase the overall  $\gamma$ -ray activity. The  $\gamma$  rays emitted after the  $\beta^-$  decay of  $^{28}\text{Mg}$  ( $T_{1/2} = 20.915(9)$  h) and that of its daughter nucleus,  $^{28}\text{Al}$  ( $T_{1/2} = 2.245(2)$  min), were detrimental to the experiment. The accumulating activity increased the rate at which  $\gamma$  rays were registered by the HPGe detectors to more than 10 kHz, which deteriorated their performance. This forced a reduction of the initial proton beam to 0.5  $\mu\text{A}$  to decrease the post-accelerated beam intensity to  $1.6 \times 10^6$  pps. After collecting data for three plunger distances with the  $^{28}\text{Mg}$  beam the activity had once again increased to problematic levels. The beam was changed back to the stable  $^{22}\text{Ne}$  until the parasitic activity had dissipated. Data was taken for seven more plunger distances with the  $^{22}\text{Ne}$  beam. Then the experiment switched back to the  $^{28}\text{Mg}$  beam to acquire data at seven additional plunger distances. Overall, measurements were performed at 25 plunger distances for  $^{22}\text{Ne}$  and 10 plunger distances for  $^{28}\text{Mg}$ , between 0.7 and 27.1  $\mu\text{m}$ , not taking into account the zero-offset distance.

The initial data sorting, energy calibration, gain alignment, etc., was performed by Dr. A. Boukhari using the MiniballCoulexSort software package, developed by Dr. Liam P. Gaffney, University of Liverpool. A preliminary Doppler correction and TDRIV analysis of the acquired  $^{22}\text{Ne}$  data are presented in his doctoral thesis [82]. The obtained preliminary result of  $|g(2_1^+, ^{22}\text{Ne})| = 0.421(36)$  shows a significant discrepancy with the adopted value.

In the current work, the detailed analysis of the experimental data for  $^{22}\text{Ne}$  and  $^{28}\text{Mg}$  is discussed, starting with the Doppler correction. Then, the software used for the TDRIV analysis is introduced, followed by the obtained results and a short discussion.

### 2.3.1 Doppler correction

A correction for the Doppler shift of the  $\gamma$ -ray energy is required in various  $\gamma$ -spectroscopy experiments in which the nuclei of interest are in flight. The energy  $E_\gamma$  that a  $\gamma$  ray, emitted from a nucleus in flight, deposits in a detector is modified by the Doppler effect, following the relation:

$$E_\gamma = E_{\gamma,0} \frac{\sqrt{1 - \beta^2}}{1 - \beta \cos(\theta_{\gamma-p})}. \quad (2.1)$$

Here  $E_{\gamma,0}$  is the energy of the  $\gamma$  ray in the rest frame of the nucleus,  $\beta = v/c$  is the velocity of the nucleus, normalized to the speed of light, and  $\theta_{\gamma-p}$  is the angle of emission of the  $\gamma$  ray relative to the direction of the nucleus. The angle  $\theta_{\gamma-p}$  depends on the  $\theta_\gamma$ ,  $\phi_\gamma$  and  $\theta_p$ ,  $\phi_p$  angles, at which the  $\gamma$  ray and the scattered nucleus were detected, respectively, through the relation:

$$\cos(\theta_{\gamma-p}) = \sin(\theta_\gamma) \sin(\theta_p) \cos(\phi_p - \phi_\gamma) + \cos(\theta_\gamma) \cos(\theta_p). \quad (2.2)$$

Experimental methods such as TDRIV or Coulomb excitation require the total yield of the  $\gamma$ -ray transitions of interest (in coincidence with scattered particles) for the data analysis. Without correcting for the Doppler effect, the total intensity of the  $\gamma$ -ray transition is spread over a large apparent energy range and cannot be properly accounted for. A good reconstruction of the rest-frame  $\gamma$ -ray energy  $E_{\gamma,0}$  can be achieved only when the  $\theta_{\gamma,p}$ ,  $\phi_{\gamma,p}$  angles and the velocity  $\beta$  are determined precisely. This has to be done on an event-by-event basis, separately for each particle- $\gamma$  coincidence.

The determination of the HPGe detector positions at the MINIBALL setup is usually done using the  $^{22}\text{Ne}(d,n)^{23}\text{Na}$  reaction on a  $\text{CD}_2$  target. In this reaction, the  $^{23}\text{Na}$  products are scattered at very small  $\theta_p$  angles and are not registered in the particle detector. Therefore, the exact velocity of the scattered nuclei cannot be used in the Doppler correction. Instead, the positions of the Doppler-shifted 441-keV transition in  $^{23}\text{Ne}$  are determined for each individual segment of all HPGe detectors by an automated script. An approximation is made that the  $^{23}\text{Ne}$  nuclei are scattered at zero degrees. A minimization procedure is then utilized to find the optimal 3D coordinates of the HPGe clusters that reproduce the positions of the Doppler-shifted peaks. However, in the current experiment a different approach was used. The TDRIV calibration measurement with  $^{22}\text{Ne}$  on a Nb target can also be used to determine the HPGe detector positions. In this case the  $^{22}\text{Ne}$  nuclei scatter at larger angles into the CD detector and their kinetic energy can be measured. The procedure becomes slightly more complicated than the  $(d,n)$  reaction as the accuracy of the CD detector coordinates impacts the precision on the extracted HPGe detector coordinates. Thus we first consider the relevant parameters from the CD detector -  $\theta_p$ ,  $\phi_p$ , and the velocity  $\beta$ .

The direction of the scattered nucleus is obtained from the CD detector hits. The impinging nucleus enters the active volume of the detector through one of the annular strips (rings) on the front-face of the detector, which provides the  $\theta_p$  information. The nucleus deposits its total kinetic energy in the silicon. This can be read out either from the front-face annular strips, or from the corresponding back-face sector strips, from which we obtain  $\phi_p$  information. The determination of the exact angles  $\theta_p$  and  $\phi_p$  is done during the sorting of the data by taking into account the distance between the target and the CD detector, the inner radius of the CD detector, the width of each ring, as well as the orientation of the CD detector in the vertical plane. All of these values are provided as parameters to the sorting code. The inner radius and the width of each strip are known from the detector specifications [81]. The target-CD distance was determined to be 33.3 mm in the preliminary analysis [82]. In the current analysis this value was modified to 29.2 mm after comparison of the experimental particle spectra and kinematic simulations performed with the LISE++ software package [83]. The rotation of the CD detector in  $\phi$  in the vertical plane was determined to be  $243.8^\circ$  at the time of the experiment. With this information provided, the code calculates the  $\theta_p$  and  $\phi_p$  of the ring and sector in which a particle has been registered. A schematic representation of the CD detector, showing the individual  $\theta - \phi$  pixels arising from its segmentation, is presented in Fig. 2.5.

The velocity of the particles is calculated from the energy  $E_p$  deposited in the detector. Both beam-like and target-like nuclei are scattered into the CD detector and they are clearly

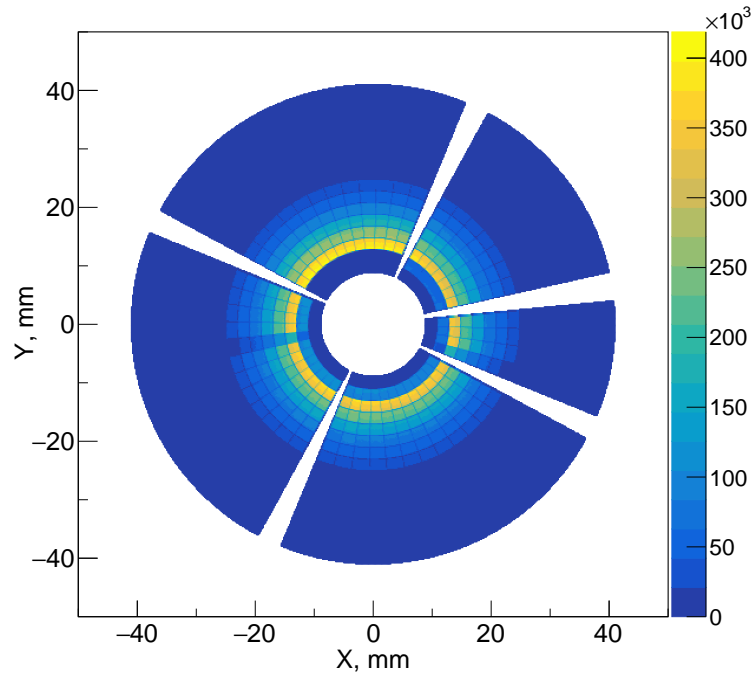


**Figure 2.5:** Schematic view of the CD particle detector and its segmentation in  $\theta$  and  $\phi$  in polar coordinates. The Z axis depicts the total number of registered particles in each pixel from the entire  $^{22}\text{Ne}$  data set. The innermost two rings were shielded due to radiation damage incurred in the previous experiments, as well as an expected rate of incident particles that was deemed too high for the detector’s capabilities. The four gaps between the quadrants are visible, as well as one sector strip which was not operational.

distinguished based on their energy. In addition, the beam-like nuclei can elastically or inelastically scatter from both the Nb target foil and the Ta reset foil. Kinematics calculations were performed with LISE++ to ascertain the origin of the different structures seen in the energy spectra of the CD detector. The  $E_p$  vs.  $\theta_p$  matrix from one of the CD quadrants is shown in Fig. 2.6 and is compared to the LISE++ calculations. The innermost annular strip (ring 1) is omitted from the plot as it is entirely shielded. The shielding also covered most of the ring 2, as evidenced by the severely reduced statistics compared to ring 3. The particles with energy lower than the LISE++ calculations are attributed to incomplete charge collection in the CD detector due to defects in the silicon lattice from radiation damage accumulated during the previous experiments. These events cannot be used in the analysis as the velocity  $\beta$  will be wrongly reconstructed due to the lower measured particle energy.

Separate 2D particle cuts were prepared in the analysis to select events with the desired type of particle. The velocity of the selected particles is calculated from their known mass and energy. The region of interest in  $E_p$  vs.  $\theta_p$  matrix is the target-scattered beam-like nuclei. The inclusion of degrader-scattered events is detrimental to the TDRIV analysis as they only contribute to the  $G_k(\infty)$  component. This will be elaborated upon in the following sections. The used particle cut for  $^{22}\text{Ne}$  is shown in Fig. 2.6.

The  $\gamma$  rays in coincidence with the target-scattered particles are utilized to determine the positions of the HPGe detectors. Due to the dependence of Eq. (2.1) on  $\theta_p$  only the innermost rings with the highest statistics were considered. The overall procedure was the same as for the  $(d, n)$  reaction. The position of the Doppler-shifted  $2_1^+ \rightarrow 0_{g.s.}^+$  transition in  $^{22}\text{Ne}$  (1275 keV) in the  $\gamma$ -ray energy spectra was automatically determined for all individual HPGe detector segments. Then, another script performed a minimization procedure to obtain the positions

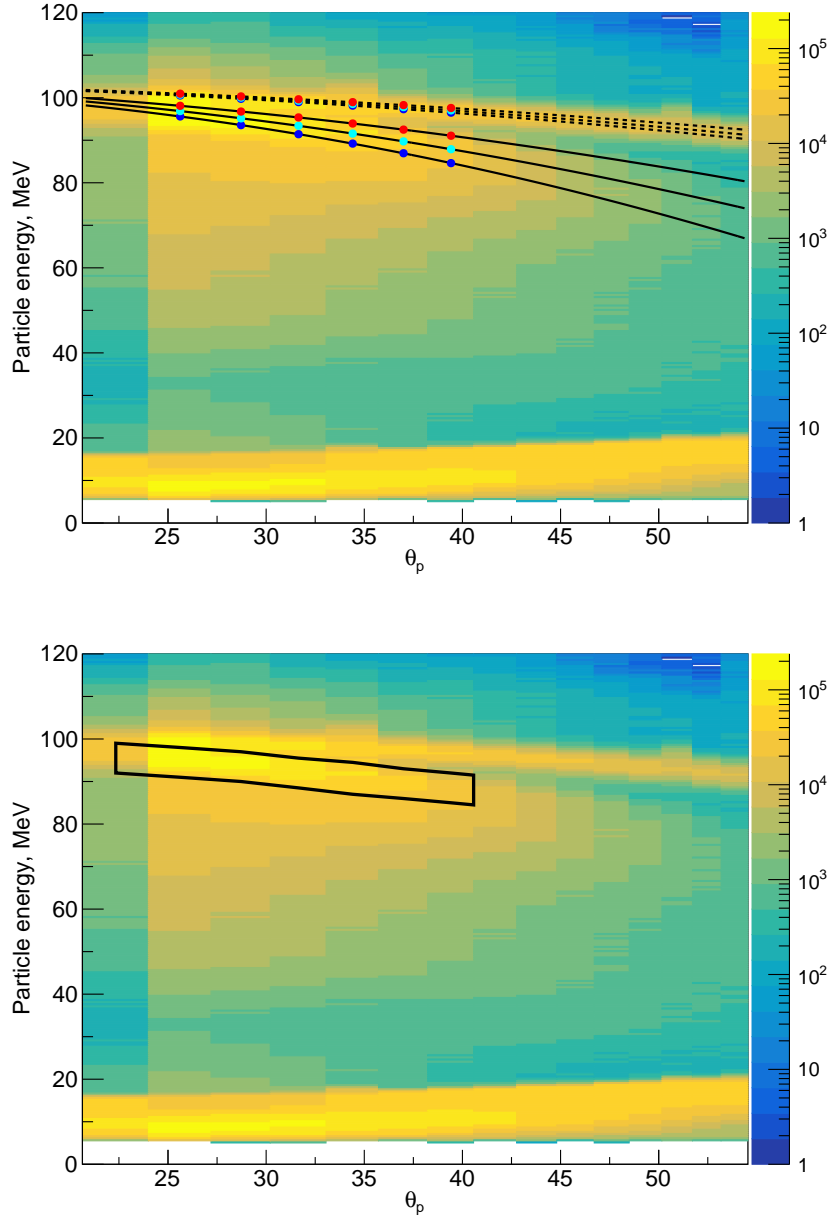


**Figure 2.6:** (Top) Particle energy as a function of  $\theta_p$  of the CD annular rings for the full  $^{22}\text{Ne}$  data set. Kinematic calculations performed with LISE++ show the expected energy of the  $^{22}\text{Ne}$  ions after undergoing Coulomb excitation on the  $^{93}\text{Nb}$  target (solid lines) or on the  $^{181}\text{Ta}$  degrader (dashed lines). The red, cyan and blue circles denote the calculations performed for a reaction at the entrance, middle or exit of the target/degrader foil, respectively. Scattered target-like particles are clearly distinguished at particle energies below  $\approx 20$  MeV.

(Bottom) Plot of the particle energy as a function of  $\theta_p$  for the entire  $^{22}\text{Ne}$  data set. The used particle cut for  $^{22}\text{Ne}$  nuclei scattered from the  $^{93}\text{Nb}$  target is shown in black. The particles with incomplete charge collection below the particle cut are not included as the kinematic reconstruction of  $\beta$  would be inaccurate. Annular rings at higher  $\theta_p$  angles are not utilized in the analysis as the contribution of useful events is negligible.

of the MINIBALL triple clusters. The positions of the triple clusters are described by four coordinates -  $R, \phi, \theta, \alpha$ , defined as shown in Fig. 2.7. Each two clusters are attached to the same vertical arc and have almost identical  $\phi$  angles. The original script tackled the minimization for these pairs of clusters at the same time by using the same  $\phi$  angle for both. In the current work the script was modified to perform the minimization over all clusters simultaneously.

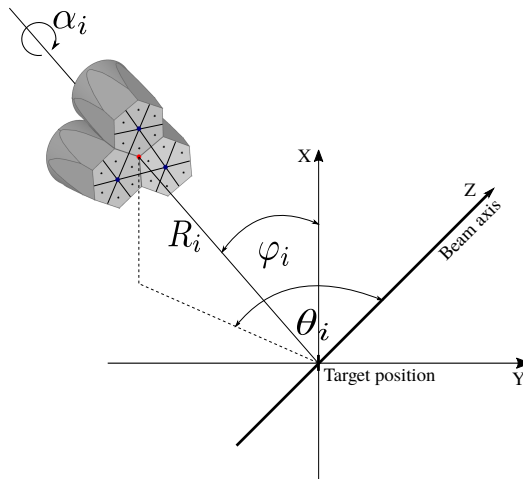


**Figure 2.7:** Schematic definition of the MINIBALL intrinsic coordinates  $R, \theta, \phi, \alpha$ . The individual coordinates of all HPGe detector segments are calculated from the coordinates of the centre of the triple cluster. Figure taken from Ref. [84].

The minimization procedure attempts to find the set of coordinates that best reproduce the measured peak positions. The obtained coordinates are input in the analysis code to check the FWHM of the Doppler-corrected peak. The resulting FWHM of 21 keV for the 1275-keV peak was a significant improvement over the 33-keV FWHM from the preliminary analysis [82]. At this point in the analysis an attempt was made to further improve the Doppler correction by considering the effects of the required coincidences with the CD detector, which, as mentioned above, is not the typical procedure at MINIBALL. When the particle coincidences were restricted only to the innermost active ring (ring 3) to limit the influence of  $\theta_p$ , the Doppler correction was found to be nearly identical. However, it was observed that  $\phi_p$  has a much larger influence on the procedure. Fig. 2.8 shows the non-Doppler-corrected spectrum for a single segment of a HPGe crystal. It shows two distinct Doppler-shifted peaks that are part of a distribution of counts resulting from coincidences with particles with different  $\phi_p$ . While  $\phi_\gamma$  is fixed for the selected HPGe detector segment,  $\phi_p$  covers the entire range from 0 to  $2\pi$  for the different CD sectors. Therefore, the  $\cos(\phi_p - \phi_\gamma)$  term in Eq. (2.2) reaches its extreme values of  $\approx \pm 1$  for some particle- $\gamma$  combinations, giving rise to the structure in Fig. 2.8. Consequently, obtaining the non-Doppler-corrected peak positions for each HPGe segment to be used in the minimization procedure becomes a non-trivial task.

To overcome this, each of the four CD detector quadrants was separated in half to define eight sections in  $\phi_p$ . Although this significantly reduced the statistics in each combination between a HPGe segment and a CD  $\phi_p$  section, the Doppler-shifted peak positions were determined. The minimization script was modified further to treat the eight  $\phi_p$  sections for every HPGe segment with the  $\phi_p$  angles of the centres of each of these sections fixed. Again, only the innermost active ring of the particle detector (ring 3) was considered. The newly obtained HPGe detector positions still did not result in an improved Doppler correction. The eight  $\phi_p$  angles of the CD detector sections were then set as free parameters in the minimization. The resulting  $\phi_p$  values, obtained from the minimization, showed that the claimed  $\phi_p$  coverage of

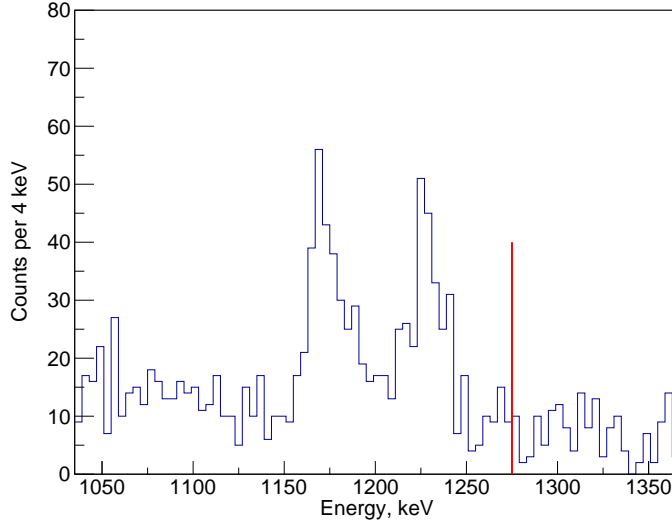


**Figure 2.8:** Non-Doppler-corrected energy spectrum of one HPGe detector segment in coincidence with CD annular ring 3. The energy of the  $\gamma$ -ray transition is indicated by a red line. Two shifted peaks are observed with a continuous distribution of counts in between them due to the influence of  $\phi_p$  on the Doppler shift.

the CD detector quadrants was not correct. The reported coverage of  $82^\circ$  for a single quadrant would entail a difference of  $41^\circ$  between the centers of its two halves, as originally used in the minimization. However, the  $\Delta\phi$  between the two adjacent sections of a quadrant was found to be approximately  $35^\circ$  for all quadrants. Such a large difference was unexpected and all possible explanations had to be considered. One probable explanation was an error in the minimization code. An entirely new minimization code was written by Dr. Johan Ljungvall which independently reproduced the apparent reduced  $\phi_p$  coverage. To ultimately confirm these results, a photo of one CD detector quadrant was used to visually measure the  $\phi$ -coverage of the active region of the annular rings, as shown in Fig. 2.9. Two strips of inactive material are present on both sides of the active annular strips. These dead strips have a fixed geometrical width which covers a different angular range with increasing  $\theta_p$  leading to a smaller active region at low  $\theta_p$ . The measured angular coverage was in agreement with the values obtained from the minimization procedure.

The  $\phi_p$  coverage was then measured for all rings and parametrized as a function of the annular ring. Two new functions were added to the analysis code to more accurately determine the  $\phi_p$  of detected particles and improve the Doppler correction. After implementing these modifications a FWHM of 15 keV was obtained for the Doppler-corrected 1275-keV line, as shown in Fig. 2.10. The large improvement in FWHM compared to the preliminary analysis is both due to the improved description of the particle detector, and due to the more precise particle selection (Fig. 2.6) and target-CD distance.

The obtained MINIBALL coordinates are given in Table 2.1. A map of the HPGe detectors in the laboratory frame is shown in Fig. 2.11. Eight triple clusters with a total of 23 crystals were operational in this experiment. Multiple segments were disabled or not operational as is visible in Fig. 2.11. The MINIBALL clusters were positioned close to  $\theta_\gamma = 90^\circ$  as the amplitude of the particle- $\gamma$  angular correlations is expected to be the highest.

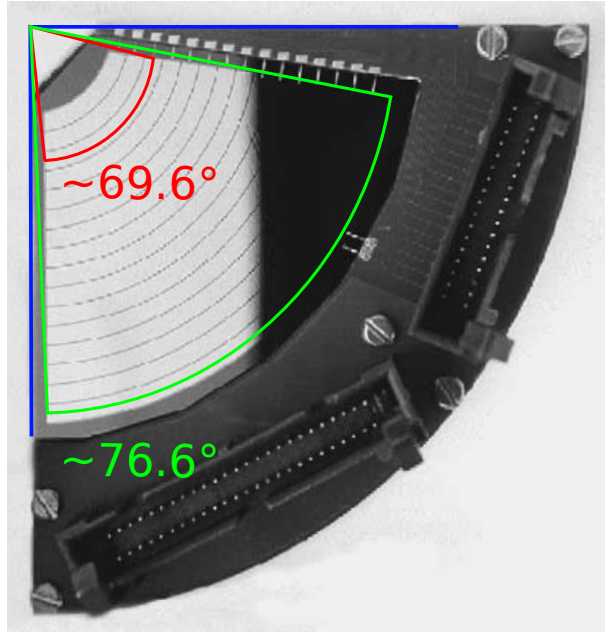


**Figure 2.9:** Photograph of a CD detector quadrant, taken from Fig. 2 in Ref. [81]. The measured  $\phi_p$  angular coverage of ring 3 (red) of the detector is significantly lower than the coverage of ring 16 (green) and both are below the expected  $82^\circ$ , quoted in Ref. [81]. The strip of dead material on the top of the photograph is used for the readout signals of each ring.

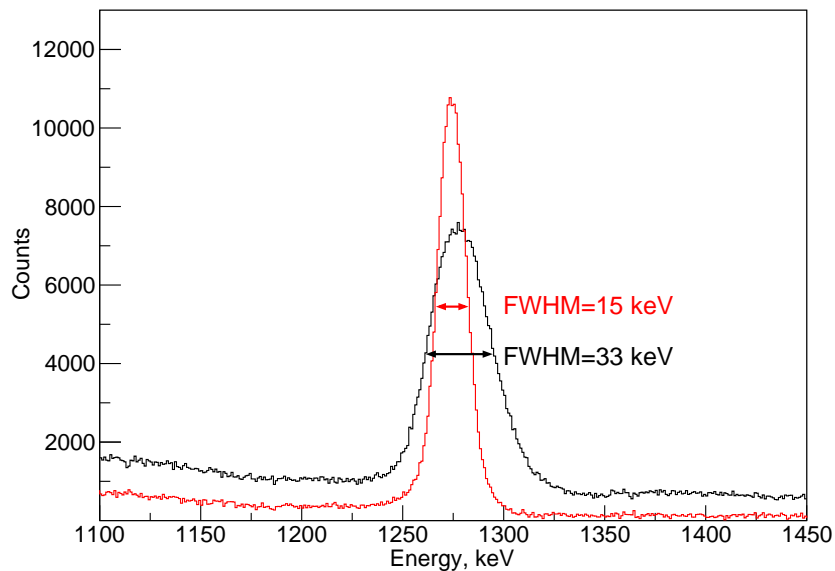


**Figure 2.10:** Comparison of the Doppler-corrected HPGe energy spectra from the preliminary analysis (black, Ref. [82]) and the current work (red) for the 1275-keV line of the  $2_1^+ \rightarrow 0_{g.s.}^+$  transition in  $^{22}\text{Ne}$ . The improvement in the FWHM is due to the combination of the modified target-CD distance, the improved geometrical description of the CD detector and the new particle cut. The reduced level of the  $\gamma$ -ray background in the red spectrum is a result from the different particle cut applied on the CD detector.

**Table 2.1:** Coordinates of the MINIBALL clusters within the intrinsic MINIBALL coordinate system, obtained from the minimization procedure.

Cluster	r, mm	$\theta$	$\phi$	$\alpha$
17	169.8	104.8	139.7	330.5
12	99.0	92.5	36.2	263.9
16	125.2	76.6	107.0	260.3
13	85.8	131.8	77.3	65.5
22	102.6	122.9	256.9	249.9
18	120.2	91.1	218.2	77.9
14	108.6	120.0	323.5	290.0
23	124.1	77.0	282.1	71.7

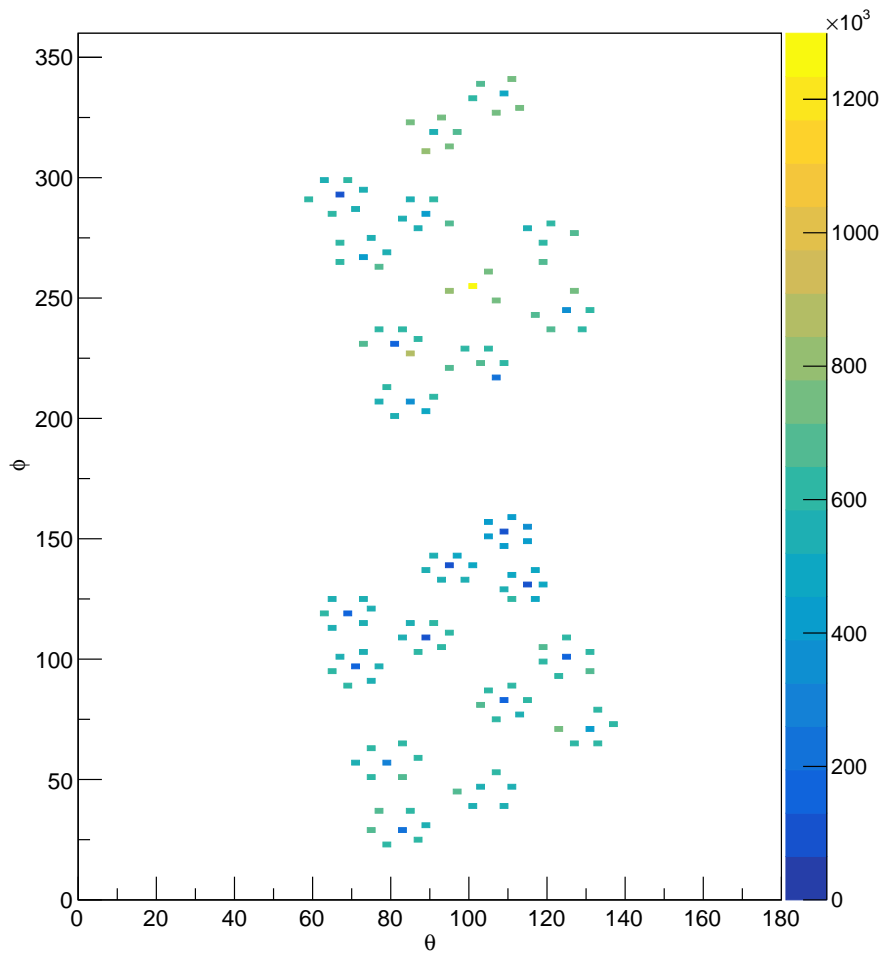


**Figure 2.11:** Map of HPGe detector coordinates in the laboratory frame showing the positions of each crystal segment and core.

### 2.3.2 The TDRIV analysis code

The analysis of the TDRIV data is performed with the TDRIV\_MODEL program, written originally by Prof. A.E. Stuchbery, ANU, with some later modifications by Dr. Georgi Georgiev. The TDRIV code, as it will be referred to in this text, is written entirely in FORTRAN and represents a collection of subroutines that are used for simulations and analysis of TDRIV data.

The overall mode of operation, input data and some details for the relevant subroutines will be discussed below. The subroutines are designated by four-letter names, which will be used in the text for clarity.

Upon starting the TDRIV program the user is prompted to either manually enter the various input parameters and files (subroutine EDIT), or read them from a file from the previous session (subroutine LSET). The first input parameters are the beam nuclei, their energy, the target and reset foil materials and thickness. Two input files are also provided, structured as input files for the Winther-de Boer COULEX code [16], which has been implemented in the TDRIV program. These are used for calculating the Coulomb-excitation cross sections for the beam impinging on each of the two foils. The target and degrader foils are separated in a given number of layers that are used in the calculations.

Following this, the mean lifetime of the nuclear state of interest is given, along with an initial guess for its  $g$  factor. Initial  $G_{2,4}(\infty)$  values are also provided. These values are used for simulating angular correlations,  $G_k$  attenuation factors or  $R(t)$  functions. Next, a list of all relevant electron configurations is provided which contains the atomic spin, the hyperfine field strength at the nucleus and the fraction of each configuration. It should be noted that the electron configurations are static and no atomic decays are considered.

Then the particle and HPGe detectors information is provided. The type of particle detector is chosen and all its geometric properties are described to define the number of pixels and their positions. The number of HPGe detectors is also given, which in this case is the number of HPGe crystals (23), rather than individual segments. Another detector geometry input file is provided, which contains a table with the  $\theta_\gamma$ ,  $\phi_\gamma$ ,  $\phi_p$ ,  $\Delta\phi$  of each particle- $\gamma$  combination. An additional parameter that describes the “strength” of each of these combinations is also given. This parameter will be discussed in detail below.

With this information provided, the user is required to run the TENS subroutine that calculates energy losses, Rutherford-scattering and Coulomb-excitation cross sections, and sets up the statistical tensors  $\rho_{kq}$  for the particle detector. The code takes the number of layers that the two foils are divided in and calculates the energy losses in each layer. Then the Rutherford-scattering and Coulomb-excitation cross sections are evaluated at each step for the corresponding energy and for each annular ring of the particle detector. The code also determines whether the Coulomb excitation is “safe” by checking if the nuclear surfaces touch, rather than by applying Cline’s criterion of 5-fm separation, as mentioned in Chapter 1.2.2. The more lenient criterion is used as the influence of the nuclear interaction in the excitation process is not a problem for the TDRIV method as it does not change the spin alignment of the nuclei.

At this point, the user is free to choose any of the remaining subroutines which can calculate perturbed or unperturbed angular correlations (CTEN), simulate  $G_k(t)$  curves (PLTG) or  $R(t)$  functions (RTRI). The WSET/WSED subroutines take the  $\theta_\gamma$  and  $\Delta\phi$  for a selected particle- $\gamma$  combination as inputs and calculate the expected angular correlations  $W(\theta_\gamma, \Delta\phi, t)$  as a function of flight time of the nuclei or the equivalent flight distance. This type of plot is used to determine whether  $W(\theta_\gamma, \Delta\phi, t)$  initially increases ( $W^\uparrow$ ) or decreases ( $W^\downarrow$ ) for the selected particle- $\gamma$  combination, which is relevant for the construction of the  $R(t)$  function. The amplitude of  $W(\theta_\gamma, \Delta\phi, t)$  is used to distinguish more sensitive particle- $\gamma$  combinations from the less sensitive ones. In the TDRIV analysis of  $g(2_1^+)$  in  $^{24}\text{Mg}$  [36, 37] the particle- $\gamma$  combinations were separated in four groups: “strong”, “intermediate”, “weak” and “null” combinations. The “strong” combinations exhibit  $W(\theta_\gamma, \Delta\phi, t)$  oscillations with high amplitude and the “null” combinations barely exhibit a visible oscillatory pattern at all. The assignments of more and less sensitive combinations is done independently for the increasing ( $W^\uparrow$ ) and decreasing ( $W^\downarrow$ )

combinations. Examples of these  $W(\theta_\gamma, \Delta\phi, t)$  curves are shown in Fig. 2.12.

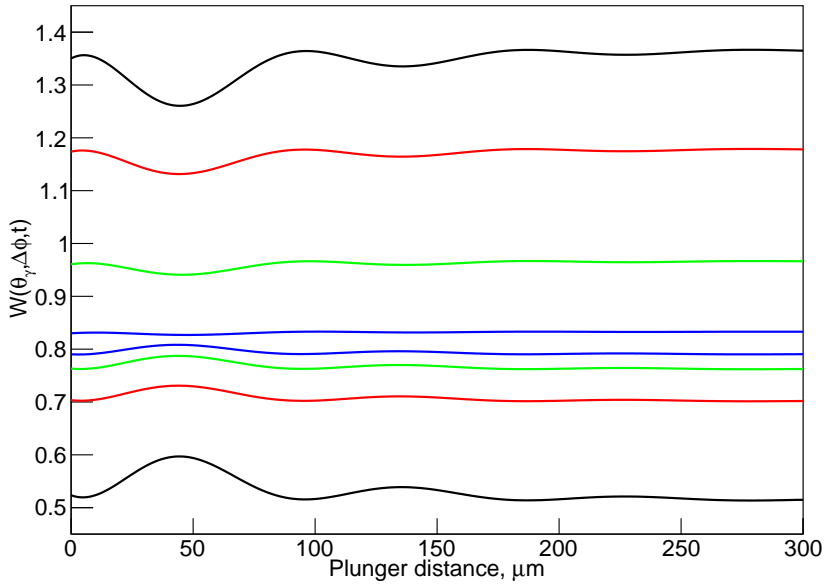


**Figure 2.12:** Calculated angular correlations for particle- $\gamma$  combinations between one HPGe crystal (17C) and selected CD detector  $\phi_p$  sectors as a function of plunger distance. The top four curves represent  $W^\downarrow$  combinations and the bottom four curves -  $W^\uparrow$  combinations. Combinations identified as “strong” (black) exhibit larger amplitudes compared to “intermediate” (red), “weak” (green) and “null” (blue) combinations.

The amplitude of a  $W(\theta_\gamma, \Delta\phi, t)$  curve for particle- $\gamma$  combination is quantified by:

$$\frac{W(D_1) - W(D_2)}{W(D_1) + W(D_2)}. \quad (2.3)$$

Here  $W(D_{1,2})$  are the  $W(\theta_\gamma, \Delta\phi, t)$  values, calculated at two distances  $D_{1,2}$ . Typically, these distances are chosen to be the first minimum and first maximum of  $W(\theta_\gamma, \Delta\phi, t)$ . In the  $^{24}\text{Mg}$  study the total number of particle- $\gamma$  combinations was 104 and it was possible to manually select the “strong”, “intermediate”, “weak” and “null” combinations. In the current study there are 23 HPGe crystals  $\times$  47 CD detector  $\phi_p$  sectors = 1081 particle- $\gamma$  combinations. Therefore some existing subroutines were modified and several entirely new subroutines were added to the TDRIV program to automate this procedure. A brief outline of the logic of the process is as follows. First, using Eq. (2.3) the amplitude for every particle- $\gamma$  combination is calculated. The user is then prompted to input the desired percentage distribution of “strong”, “intermediate”, “weak” and “null” combinations, which is applied to both  $W^\uparrow$  and  $W^\downarrow$  combinations. The full list of combinations is then sorted by the amplitude and the “strength” parameter, starting from 1 (“strong  $\uparrow$ ”) to 4 (“null  $\uparrow$ ”), then from -4 (“null  $\downarrow$ ”) to -1 (“strong  $\downarrow$ ”), is printed out in an additional column according to the desired fractions. The resulting file is used to generate a new detector geometry input file. The user has to run the EDIT and TENS subroutines to change the previous detector geometry file to the newly generated one and complete the procedure.

Another useful subroutine (PLTG) calculates and prints out the  $G_2(t)$  and  $G_4(t)$  curves as a function of flight time. It is used to evaluate the  $G_k(\infty)$  values to be used later in the fitting procedure. The subroutine is also used to identify the oscillatory patterns that each electron configuration would contribute to the overall oscillations by considering them one at a time. This can also be achieved by the RTRI subroutine which simulates the total  $R(t)$

function as a function of flight time or plunger distance. Note that the simulations of  $G_k(t)$  factors and the  $R(t)$  functions utilize the initial g-factor value provided at the initialization of the code. These simulations should be performed for several values of the initial g factor to observe how much that influences the results. Nevertheless, by simulating the  $R(t)$  function it is possible to make a decision on the percentage of “strong” particle- $\gamma$  combinations to include in the detector geometry input file. If the percentage is large, that would include combinations with lower amplitudes, which would decrease the overall amplitude of the  $R(t)$  function. A smaller percentage of “strong” combinations would maximize the  $R(t)$  amplitude. However, the statistics in the experimental HPGe detector spectra for a smaller fraction of “strong” combinations would be low and their uncertainty would increase. A balance between  $R(t)$  amplitude and experimental statistical uncertainty has to be considered.

The last relevant subroutine is the FIT3 subroutine, which is used to fit the experimental  $R(t)$  function. The fitting procedure is based on a  $\chi^2$  grid search over all relevant parameters: the g factor, the attenuation coefficients  $G_{2,4}(\infty)$ , the geometrical factor  $Q_2$ , the plunger zero-offset distance  $D_0$ , the target excitation fraction and the H- and He-like fraction of the ions. The user provides the lower and upper boundaries for each parameter, as well as the step the code should increment them with. The  $\chi^2$  value is calculated for each individual point on the full parameter grid and the minimum is found from the available grid points. This approach is not fully optimized and is very time consuming for fine grids and/or a large number of parameters. In reality, most of these parameters are calculated or estimated beforehand and kept fixed in the fit in order to extract the g factor. The geometric factor  $Q_2$  was estimated for all individual HPGe crystals, taking into account their distance from the target, obtained from the minimization procedure in the previous Section. Then the value  $Q_2^{avg}$ , averaged over all crystals, was fixed in the fitting procedure. As mentioned above, the attenuation factors  $G_{2,4}(\infty)$  are simulated from the PLTG subroutine, however, they depend on the g-factor value. The simulations with PLTG are performed for different initial g factors to determine the range of possible  $G_{2,4}(\infty)$  values which should be considered in the minimization.

The plunger zero-offset distance  $D_0$  is usually determined from the experimental data. Typically, if there are HPGe detectors at forward or backward angles it is possible to distinguish between the Doppler-shifted and unshifted component of the  $\gamma$ -ray peak of interest. In the present case where a degrader foil is used, instead of a stopper foil, these would correspond to fast and slow components of the peak of interest. The known lifetime of the state can be used to extract  $D_0$  directly from the ratio of the areas of the fast and slow components for the shortest plunger distance. If the lifetime is not known, the RDDS method can be applied to measure the lifetime from the TDRIV data and then use it to obtain  $D_0$ . In the current experiment this approach was not possible as the HPGe detectors were positioned close to  $90^\circ$  where the fast and slow peaks are not resolved. Therefore, the calibration TDRIV measurement of the known g factor of the  $2_1^+$  state in  $^{22}\text{Ne}$  was planned to be used to obtain the zero-offset distance, as already mentioned.

The next parameter is the target excitation fraction, which represents the fraction of nuclei which underwent Coulomb excitation on the target foil, rather than on the degrader foil. Depending on the used particle detector these two types of events could be differentiated by the energy of the scattered particle. Special care was taken when selecting the cuts on the particle energy in the CD detector to minimize the contribution of excitations on the degrader foil (see Fig. 2.6). This was achieved by considering separately the energy spectrum for each CD detector ring in coincidence with the  $2_1^+ \rightarrow 0_{g.s}^+$   $\gamma$  ray for  $^{22}\text{Ne}$  or  $^{28}\text{Mg}$ . Then, from the kinematics calculations with LISE++, the energies of the target- and degrader-scattered nuclei were used to fit two Gaussian distributions. The lower and upper boundaries of the particle

cut for each CD ring were modified until the calculated areas of the two fitted Gaussian distributions within the cut were optimized to suppress the degrader-excitation fraction. The total target-excitation fraction was calculated as the weighted average of the corresponding fractions for the individual rings. An example is shown in Fig. 2.13.

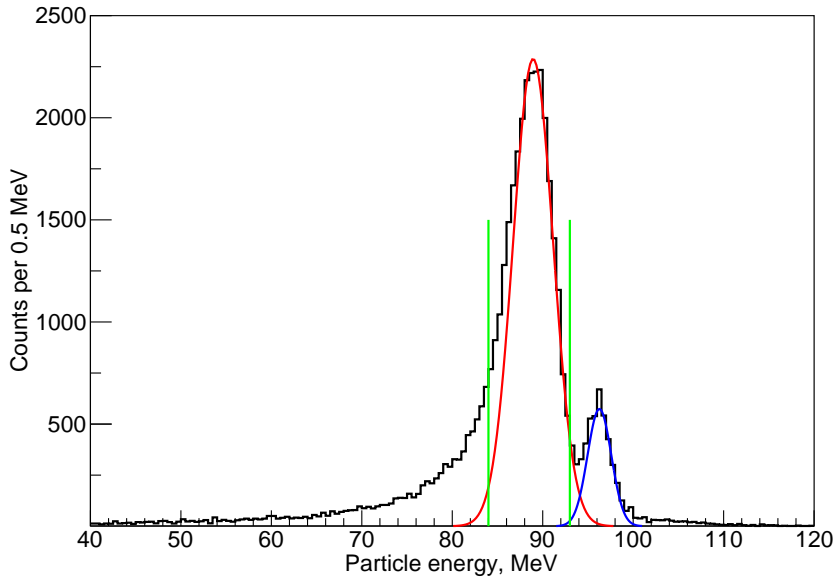


**Figure 2.13:** Energy spectrum of CD detector ring 7 in coincidence with the 1275-keV  $\gamma$  ray in  $^{22}\text{Ne}$ , summed over all plunger distances. The two peaks correspond to the Coulomb excitation of  $^{22}\text{Ne}$  on the Nb target and the Ta degrader. The Gaussian distributions simultaneously fitted to the two peaks are used to select the particle cut for this CD ring (green lines). A linear background was used in the fitting procedure and is not shown here. The tailing on the left of the target-scattered events is due to the events with incomplete charge collection in the CD detector, which have to be excluded.

In the TDRIV code, the H-like fraction of ions refers to H-like ions in their atomic ground state. This value can be taken from the input table of electron configurations but it can also be modified for the purposes of the fit. The He-like fraction in the fitting procedure refers to the sum of all other electron configurations from the input table - excited H-like, excited He-like and any Li-like ions. Modifying the so-called He-like fraction in the fit scales up or down the corresponding electron configurations while keeping their relative populations fixed. This is introduced mostly for ease of operation of the fitting subroutine. Varying several electron configurations, among other parameters of the fit, can make the full scan of the  $\chi^2$  grid extremely time consuming.

After all parameter ranges and steps are provided to the code, it performs an individual fit of the experimental  $R(t)$  function for all possible combinations of parameter values - a grid search. The code calculates the  $\chi^2$  value for each combination and the combination with the lowest overall  $\chi^2$  represents the fit result. Before fitting for the g factor, usually a series of fits are performed to optimize the values of  $G_{2,4}$  and the electron configuration fractions. These parameters are obtained from simulations and some degree of inaccuracy could be expected. When fitting with more than one free parameter, the code produces a separate plot of the  $\chi^2$  value as a function of each parameter. These are used to fine-tune the values of the parameters before fixing them for the final fit of the g factor.

### 2.3.3 Calibration with $^{22}\text{Ne}$

The Doppler-corrected  $\gamma$ -ray energy spectra for beam-like nuclei from the full  $^{22}\text{Ne}$  data set are shown in Fig. 2.14.

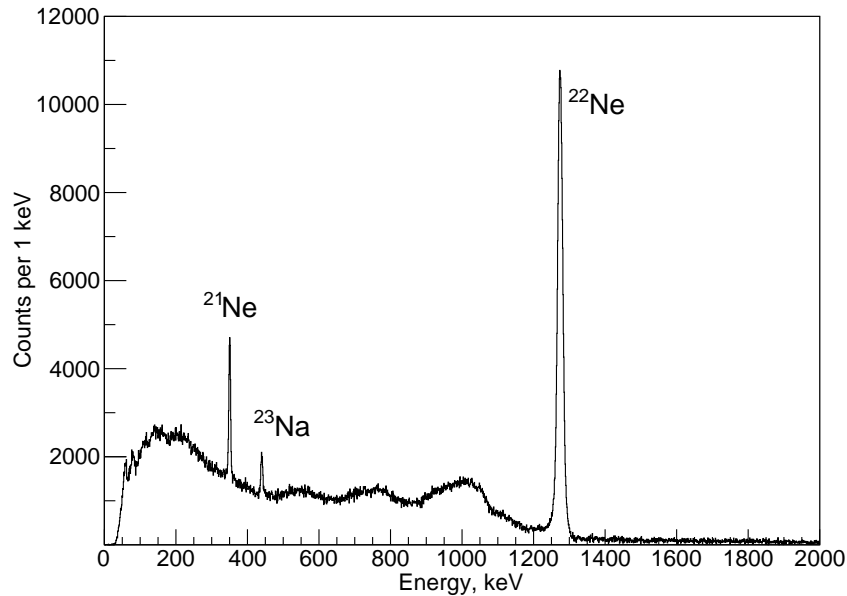


**Figure 2.14:** HPGe detector energy spectrum Doppler corrected for beam-like nuclei, registered in the CD detector from the complete  $^{22}\text{Ne}$  data set. The bumps visible between 500 and 1100 keV correspond to stopped  $\gamma$  rays or  $\gamma$  rays emitted in flight by target-like nuclei which are broadened from the Doppler correction for beam-like nuclei.

A new detector geometry file was generated for the  $^{22}\text{Ne}$  case following the procedure outlined in the previous Section, based on the adopted g-factor value of 0.326(12) [28]. A total of 231 particle- $\gamma$  combinations ( $231/1081 \approx 21.3\%$ ) were designated as “strong  $\uparrow$ ” and the same amount as “strong  $\downarrow$ ”. The “intermediate”, “weak” and “null” combinations were not utilized in the TDRIV analysis as will be discussed below. The detector geometry file was included in the MINIBALL analysis code and individual  $\gamma$ -ray energy spectra were defined for the combinations with different labels. All particle- $\gamma$  coincidences with a particle in the selected particle cut (Fig. 2.6) were Doppler-corrected and sorted in the appropriate  $\gamma$ -ray spectrum based on the corresponding labels. This was done separately for the data collected at each plunger distance. The 1275-keV peak in the “strong  $\uparrow$ ” and “strong  $\downarrow$ ” energy spectra was fitted with a Gaussian distribution plus a linear background to obtain the area of the peak. The ratio of the two areas and its associated uncertainty were calculated and printed out in a file for each plunger distance to obtain the experimental  $R(t)$  function, shown in Fig. 2.15. The experimental  $R(t)$  file is then provided to the TDRIV program to begin the fitting procedures.

The target-excitation fraction for the  $^{22}\text{Ne}$  beam particle cut was calculated to be 98% and this value was fixed in the FIT3 subroutine. Next, the geometric factor  $Q_2 = 0.97$  was calculated using the RIVSimulate package [23]. Some of the functionalities that exist in the TDRIV code have not yet been fully implemented in RIVSimulate, therefore the TDRIV code was utilized for fitting the  $R(t)$  function in the current analysis.

The electron configurations that were initially considered to be relevant for the TDRIV measurement included a 45% H-like fraction and a 12% He-like fraction. The remaining 43% of ions were expected to be bare nuclei or He-like ions in the atomic ground state ( $J = 0$ ) for which there is no hyperfine field and spin coupling. The He-like fraction of ions included one excited H-like configuration, four excited He-like configurations and the Li-like atomic ground-state

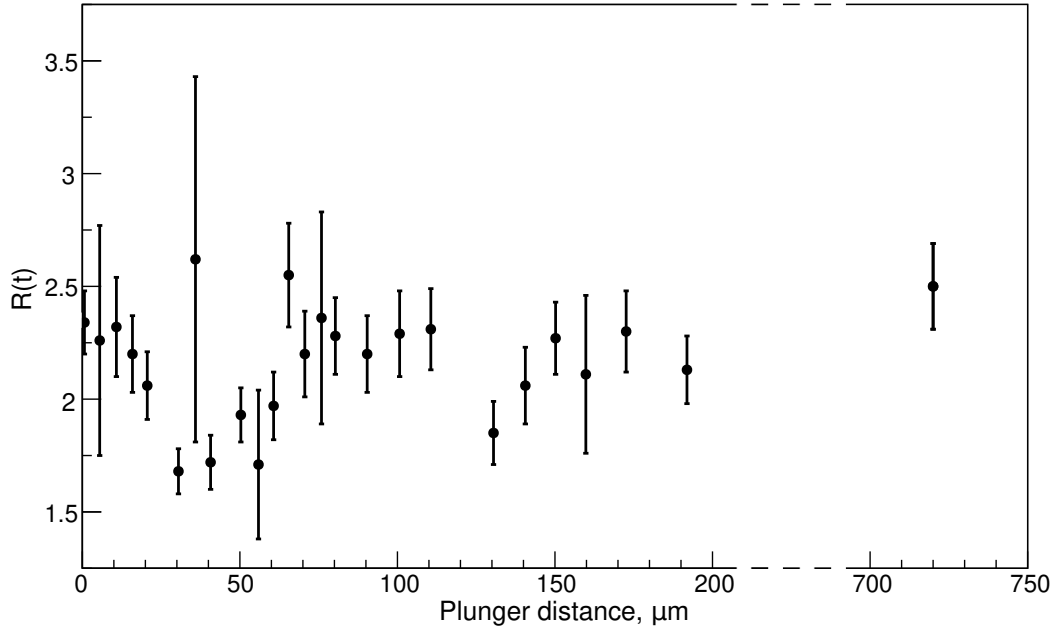


**Figure 2.15:** Experimental  $R(t)$  function obtained from the  $^{22}\text{Ne}$  data.

configuration, listed in Table 2.2. The initial fits performed on the experimental  $R(t)$  function showed that due to the rather large uncertainties in Fig. 2.15 the minimization procedure has no sensitivity to the presence of the He-like fraction. Therefore, the He-like fraction was set to 0% for all following fits. Then, fitting the H-like fraction produced a minimum in the  $\chi^2$  surface at 46(2)% and this value was fixed in the subsequent fits.

**Table 2.2:** Electron configurations provided in the initial input for the minimization procedure for the  $^{22}\text{Ne}$  data. The atomic spin, hyperfine field strength and fraction are given for each configuration. The H-like minimization parameter modifies the initial input value for the H-like ground-state fraction (45.1%). The He-like minimization parameter value modifies the sum of fractions of all other interacting configurations (11.9%) and the individual fractions are scaled accordingly.

Electron configuration	J, $\hbar$	$B_{HF}$ , kT	Fraction, %
H-like g.s.	1/2	16.81	45.1
H-like exc.	1/2	2.11	4.1
He-like exc. 1	1	18.41	0.8
He-like exc. 2	2	16.80	1.3
He-like exc. 3	1	9.21	0.8
He-like exc. 4	1	0.15	0.8
Li-like g.s.	1/2	1.48	4.1
Bare, He-like g.s.	0	0	43.1

Although the  $^{22}\text{Ne}$  g-factor measurement was supposed to be used as calibration for that of  $g(2_1^+, ^{28}\text{Mg})$ , the preliminary results in Ref. [82] showed a discrepancy with the literature value. Therefore multiple fits were performed with a very large grid, covering a wide range of g-factor values and their corresponding  $G_{2,4}(\infty)$  factors, as well as the unknown plunger offset  $D_0$ . The results showed that, indeed, the  $\chi^2$  minimum is consistently found to be at g-factor values above 0.4, much higher than the adopted value of 0.326(12) [28]. Therefore, in most following minimizations, the range of allowed g-factor values was set between 0.4 and 0.5.

These restrictions were also used to set limitations on the possible ranges of the  $G_{2,4}(\infty)$ . This allowed for smaller steps to be used in the grid for the free parameters ( $g, G_2(\infty), G_4(\infty), D_0$ ) while keeping the overall computation time reasonable, in the order of 1-2 days.

Note that changing the range of possible values for the  $g$  factor also implies changes to the observed angular correlations  $W(\theta_\gamma, \Delta\phi, t)$  (see Fig. 2.12). The initial  $g$  factor, given in the starting EDIT subroutine, modifies the distances  $D_1$  and  $D_2$  of the first minimum/maximum in  $W(\theta_\gamma, \Delta\phi, t)$  and alters the “strength” assignments from Eq. (2.3) of some combinations. Therefore, the fitting procedure is iterative - for a given range of  $g$ -factor values a new detector geometry file is generated e.g. for the average allowed  $g$  factor. The  $^{22}\text{Ne}$  data are re-sorted with the new particle- $\gamma$  combination labels to generate a new experimental  $R(t)$  function. This new  $R(t)$  function is provided to the TDRIV code to perform the fit. If the minimization finds a  $\chi^2$  minimum at a different value of  $g$ , a new detector geometry file is generated for that value. This process is repeated until convergence is reached, after which the fit becomes less sensitive to changes in the  $G_{2,4}(\infty)$  parameters compared to changes in the plunger zero-offset distance  $D_0$ . The values of  $G_{2,4}(\infty)$  are then fixed and the final minimizations are performed only for  $g$  and  $D_0$ .

Following this procedure, the global  $\chi^2$  minimum was found to be at  $g(2_1^+, ^{22}\text{Ne}) = 0.45(4)$  and  $D_0 = 2(4) \mu\text{m}$  with  $\chi^2/\text{ndf} = 1.02$  ( $\text{ndf} = 23$ ). The fit of the experimental  $R(t)$  function is presented in Fig. 2.16. The uncertainties given for  $g$  and  $D_0$  are taken as the  $\chi^2 \pm 1$  intervals for the projections of the  $\chi^2$  surface on these parameters. The large uncertainty of our result using only the most sensitive “strong” particle- $\gamma$  combinations determined that the “intermediate” and “weak” combinations cannot contribute to the results as their associated uncertainties are even larger. A figure of merit for the  $R(t)$  function is its amplitude. It is defined as the difference between the first maximum and minimum of the curve, normalized to the baseline at infinity. The obtained amplitude of the fit shown in Fig. 2.16 is about 38%.

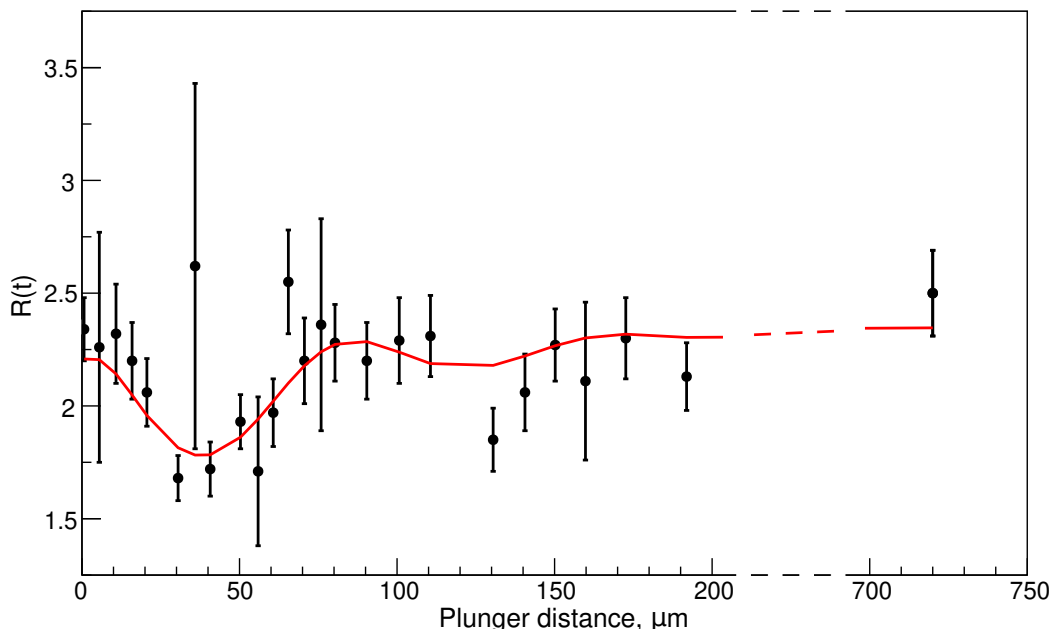


**Figure 2.16:** The best fit of the experimental  $R(t)$  function for  $^{22}\text{Ne}$  obtained from the TDRIV analysis.

Multiple sets of minimizations were performed to test the robustness of the obtained result with respect to changes in some experimental parameters. Several detector geometry files were produced with a varying percentage of “strong” combinations between 10% and 25% of the

total number of combinations for  $\uparrow$  and  $\downarrow$ . The observed differences in the resulting  $g$  factor were well within the statistical uncertainty of our result. Further, fits were performed for experimental  $R(t)$  functions obtained with different particle cuts to study the influence of the target-excitation fraction. Again, the differences were within the statistical uncertainty of the  $g$  factor result. Finally, a C++/ROOT macro was prepared to randomly remove several points from the experimental  $R(t)$  input file for the TDRIV code to test how stable the result is to changes in the data set. This was done for two cases - removing five or seven experimental points out of the 25 available. The  $g$ -factor results remained within the statistical uncertainties, although with a larger spread of the mean values.

The aforementioned tests provide some level of confidence in the obtained result, although it leads to an even larger discrepancy with the adopted value 0.326(12) [28], compared to the preliminary result 0.421(36) [82]. The disagreement between our current result and the literature value shows that the intended use of the  $^{22}\text{Ne}$   $g$  factor for calibration is not feasible and thus hinders the analysis of the  $^{28}\text{Mg}$  data. The obtained zero-offset distance  $D_0 = 2(4) \mu\text{m}$  from the minimization has a large uncertainty that extends to unphysical negative values. In addition, a zero-offset of  $2 \mu\text{m}$  is very difficult to achieve in practice and is thus considered unlikely, while a larger offset would result in a smaller  $g$ -factor value. Without additional information for at least one of these two parameters, no firm conclusions can be drawn for either one from the current data set.

### 2.3.4 $^{28}\text{Mg}$

The same analysis techniques used in the  $^{22}\text{Ne}$  case were applied on the  $^{28}\text{Mg}$  data set. A beam contamination of  $^{28}\text{Si}$  was identified already at the time of the experiment. The attempts to quantify the contamination from the particle energy spectra, as well as from the  $\gamma$ -ray energy spectra with calculations of the excitation cross section, indicate between 30% and 50% of  $^{28}\text{Si}$  in the beam. The  $\gamma$ -ray energy spectrum Doppler-corrected for beam-like nuclei is shown in Fig. 2.17. The particle energy vs.  $\theta_p$  matrix with a comparison to LISE++ calculations is shown in Fig. 2.18 together with the selected particle cut.

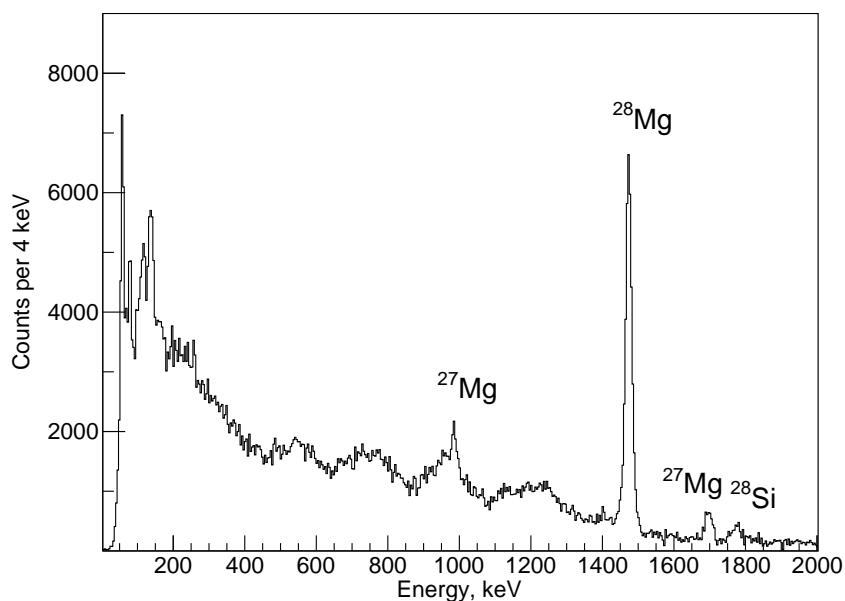


**Figure 2.17:** HPGe detector energy spectrum Doppler-corrected for the beam-like nuclei registered in the CD detector from the complete  $^{28}\text{Mg}$  data set.

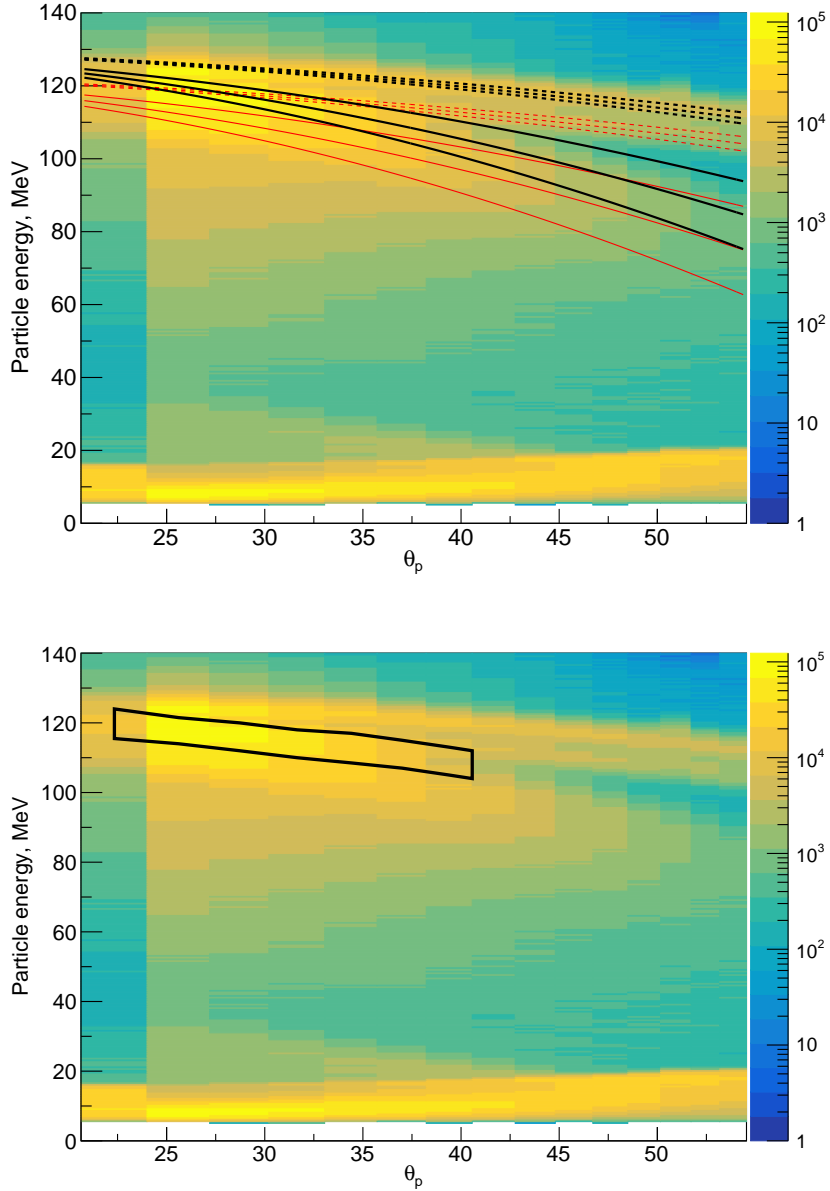


**Figure 2.18:** (Top) Particle energy as a function of  $\theta_p$  of the CD annular rings for the full  $^{28}\text{Mg}$  data set. The LISE++ calculations of the expected energy of the  $^{28}\text{Mg}$  (black) or  $^{28}\text{Si}$  (red) ions after undergoing Coulomb excitation on the  $^{93}\text{Nb}$  target (solid lines) or the  $^{181}\text{Ta}$  degrader (dashed lines) are shown.

(Bottom) The used particle cut for  $^{28}\text{Mg}$  scattered from the  $^{93}\text{Nb}$  target is presented in black. Annular rings at higher  $\theta_p$  angles are not utilized in the analysis as the contribution of useful events is negligible.

The next step in the analysis was to begin the iterative procedure of fitting the experimental  $R(t)$  function. A starting detector geometry file for the TDRIV code was generated with an initial guess for the  $g$  factor. The same fraction of “strong” particle- $\gamma$  combinations was used as for the  $^{22}\text{Ne}$  data. This geometry file was implemented in the MINIBALL analysis codes to produce the “strong  $\uparrow$ ” and “strong  $\downarrow$ ” energy spectra for each of the ten plunger distances. The intensity of the 1474-keV line in these spectra was determined and the resulting experimental  $R(t)$  function, shown in Fig. 2.19, was introduced in the TDRIV code to begin the fitting iterations.

The target-excitation fraction for  $^{28}\text{Mg}$  was calculated to be 99% for the beam cut shown

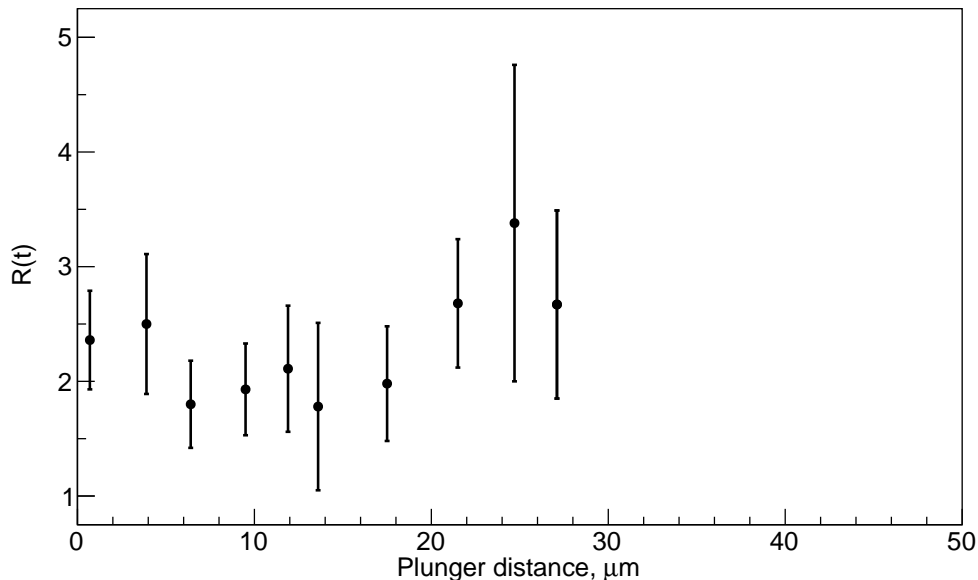


**Figure 2.19:** Experimental  $R(t)$  function for  $^{28}\text{Mg}$ . The plunger zero-offset distance is not included.

in Fig. 2.18. The value of the geometric factor  $Q_2$  was again kept fixed at  $Q_2 = 0.97$ . The H-like fraction of ions was also exactly the same as in the  $^{22}\text{Ne}$  measurement - 46%, due to the same beam energy and similar  $Z$  ( $Z = 10$  for Ne and  $Z = 12$  for Mg). Simulations in LISE++ with the Schiwietz-Grande model [85] also indicate very similar H-like fractions for the two cases. Considering the large statistical uncertainties in the experimental  $R(t)$  points no sensitivity towards small changes in the H-like fraction percentage was expected. The hyperfine field strength of the H-like ground-state configuration of  $^{28}\text{Mg}$  was calculated to be 29.1 kT. No sensitivity to the He-like fraction of ions was observed and the fraction was again fixed at 0%.

Two possible approaches to fitting the  $^{28}\text{Mg}$   $R(t)$  function were explored with regards to the plunger zero-offset  $D_0$ . Tests with slightly different particle cuts and varying percentages of “strong  $\uparrow, \downarrow$ ” combinations were performed for both approaches and the results were rather stable to such changes. The first approach is the same as for the  $^{22}\text{Ne}$  case - fitting for both the g factor and  $D_0$  simultaneously. Following the iterative procedure, described in the previous Section, this resulted in a g-factor value  $|g(2_1^+, ^{28}\text{Mg})| = 0.8(4)$  with a rather large uncertainty. The obtained offset of  $D_0 = 2(5) \mu\text{m}$  is in agreement with the  $D_0 = 2(4) \mu\text{m}$  obtained from the  $^{22}\text{Ne}$  fit. However, the reduced  $\chi^2$  value of the global minimum is 0.4 (ndf= 8), which is interpreted as over-fitting of the data and does not give confidence in the result. The obtained fit of the  $R(t)$  data points is shown in Fig. 2.20.

In the second approach the zero-offset distance can be fixed at  $D_0 = 2 \mu\text{m}$ , taken from the  $^{22}\text{Ne}$  results, to constrain the fit. Again, following the iterative procedure, the  $\chi^2$  minimum for  $g(2_1^+, ^{28}\text{Mg})$  was found to be at  $|g| = 0.8(2)$ . However, the reduced  $\chi^2$  value of this fit is 0.35 which is again interpreted as over-fitting of the data. Further, the systematic uncertainty of the plunger zero-offset value from the  $^{22}\text{Ne}$  fit is not considered in this fit, leading to a reduced final uncertainty. In order to properly take this uncertainty into account, the  $D_0$  parameter has to be set free in the minimization and the following additional term:

$$\left[ \frac{\left( D_0^{\text{fit}} - D_0^{\text{Ne}} \right)}{\sigma(D_0^{\text{Ne}})} \right]^2 \quad (2.4)$$

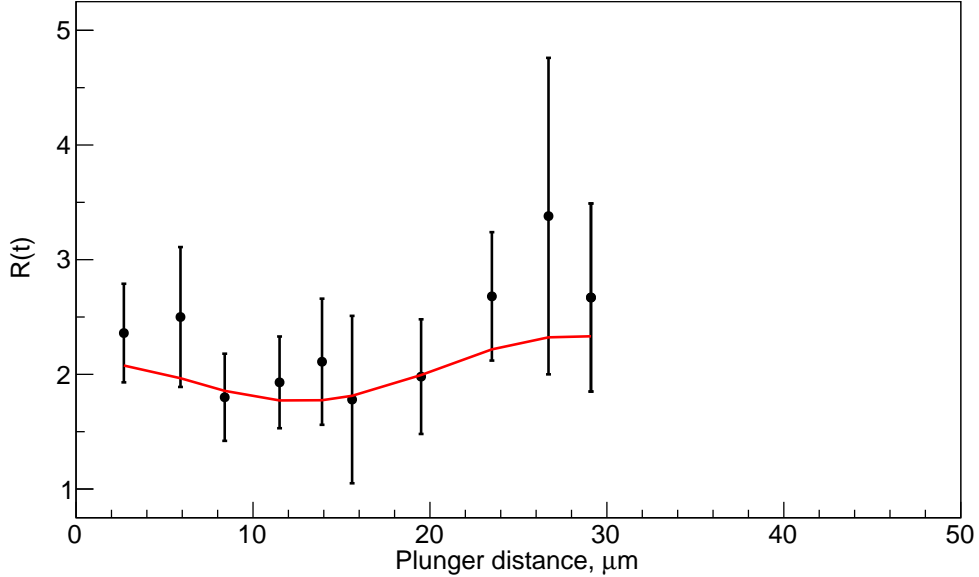


**Figure 2.20:** Fit of the  $R(t)$  function. Note that the experimental points have been shifted with the obtained zero-offset distance of  $2 \mu\text{m}$ .

has to be included in the  $\chi^2$  function. This term forces the fit value  $D_0^{fit}$  to approach  $D_0^{Ne}$  while taking into account its uncertainty  $\sigma(D_0^{Ne})$ . After implementing this change, the fit result for the g factor was  $|g(2_1^+, {}^{28}\text{Mg})| = 0.8(3)$ .

Still, without the precise calibration from the  ${}^{22}\text{Ne}$  g factor, the zero-offset value is questionable and so is any result for the g factor in  ${}^{28}\text{Mg}$ . With two available data sets ( ${}^{22}\text{Ne}$ ,  ${}^{28}\text{Mg}$ ) and three unknown parameters ( $g(2_1^+, {}^{22}\text{Ne})$ ,  $g(2_1^+, {}^{28}\text{Mg})$ ,  $D_0$ ) it is impossible to obtain concrete results. Valuable information could still be extracted through factoring out one of the parameters ( $D_0$ ) and considering the correlation between the other two parameters ( $g(2_1^+, {}^{22}\text{Ne})$ ,  $g(2_1^+, {}^{28}\text{Mg})$ ). This was achieved in the following manner.

The  $g(2_1^+, {}^{22}\text{Ne})$  value is fixed at a certain value in the minimization procedure and the  ${}^{22}\text{Ne}$  data set is fitted for the plunger offset  $D_0$ . The uncertainty on the resulting  $D_0^{Ne}$  value is taken as the  $\chi_{min}^2 \pm 1$  interval of the fit. Next, a fit of the  ${}^{28}\text{Mg}$  data is performed for both the g factor and  $D_0$  with the term from Eq. (2.4) included in the  $\chi^2$  function. This way the systematic uncertainty in the plunger offset value is taken into account at the same time as the statistical uncertainty of the  ${}^{28}\text{Mg}$  data points. Repeating this process for multiple initial  $g(2_1^+, {}^{22}\text{Ne})$  values allows for the correlation between the  ${}^{22}\text{Ne}$  and  ${}^{28}\text{Mg}$  g factors to be constructed. The obtained correlation curve is shown in Fig. 2.21.

## 2.4 Discussion

The discrepancy between the obtained result for  $g(2_1^+, {}^{22}\text{Ne})$  and its adopted value is striking. It is certain that either the measurement of Horstman *et al.* [28] or the current one is erroneous in some way, or both. When compared to theory neither of the results is reproduced. In Ref. [72] shell-model calculations were performed for the  $N = Z + 2$  nuclei in the  $sd$ -shell using the code ANTOINE and the USDB interaction with effective nucleon g factors. The comparison of the calculated and experimental g-factor values is shown in Fig. 2.22. The measurements for  ${}^{18}\text{O}$  and  ${}^{22}\text{Ne}$  differ significantly from the shell-model predictions, while  ${}^{26}\text{Mg}$ ,  ${}^{30}\text{Si}$  and  ${}^{34}\text{S}$  are in agreement with the calculations. The result for  ${}^{38}\text{Ar}$  is higher than the experimental value,

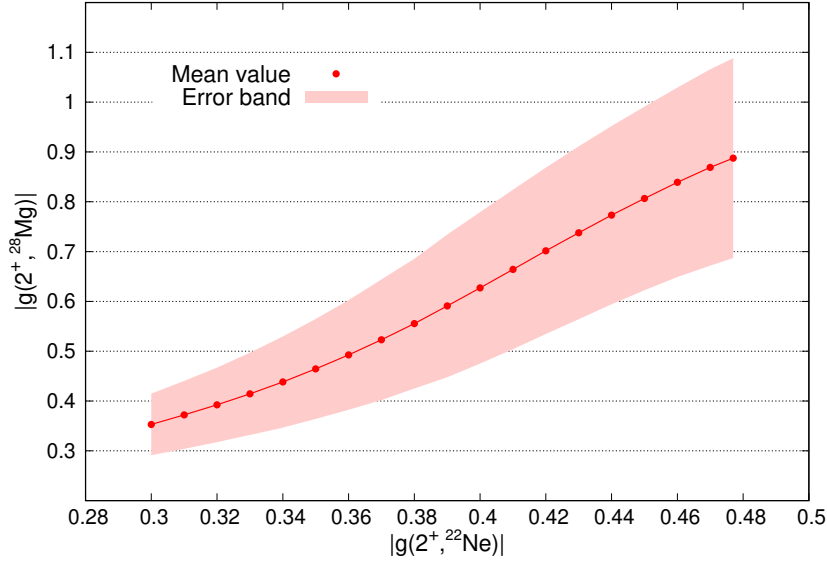


**Figure 2.21:** Correlation between  $g(2_1^+, {}^{22}\text{Ne})$  and  $g(2_1^+, {}^{28}\text{Mg})$ . The lower cut-off value of 0.3 for  $g(2_1^+, {}^{22}\text{Ne})$  is arbitrary while the upper cut-off value at 0.477 stems from the fit of  $D_0^{Ne}$  reaching a minimum at  $0 \mu\text{m}$ .

however, the authors of the experimental study in Ref. [86] achieve good agreement within the  $sd$  shell using the WBT interaction and the free-nucleon  $g$  factors. Overall, it seems that the shell-model is able to reproduce the  $g$  factors for these nuclei but agreement breaks down for  ${}^{22}\text{Ne}$  and  ${}^{16}\text{O}$ .

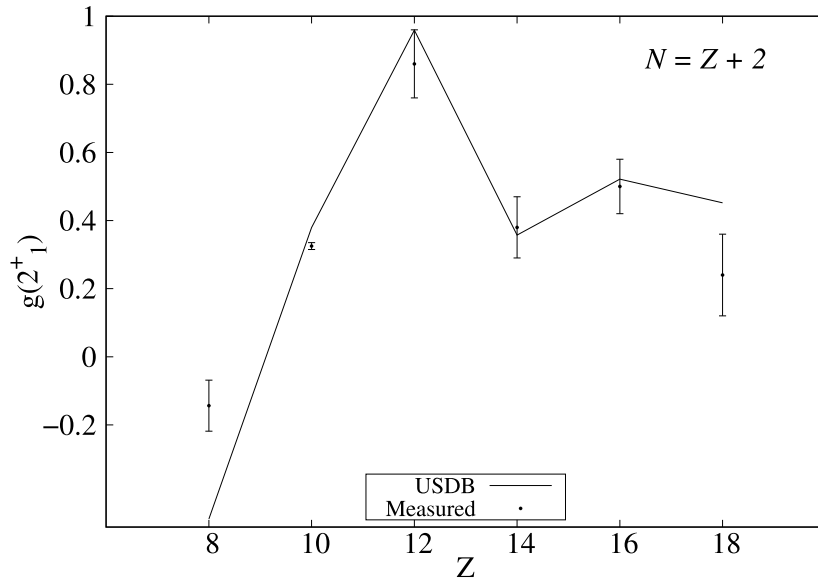


**Figure 2.22:** Experimental and theoretical values of  $g(2_1^+)$  for all  $N = Z + 2$  nuclei in the  $sd$  shell. Figure taken from Ref. [72].

Looking more in depth at the Ne isotopes, the only stable even-even Ne isotopes are  ${}^{20}\text{Ne}$  ( $N = Z$ ) and  ${}^{22}\text{Ne}$  ( $N = Z + 2$ ). Shell-model calculations were performed for these two isotopes using the code ANTOINE and the USDA and USDB interactions. The  $g$ -factor values obtained from the calculations are shown in Fig. 2.23 and compared with the respective adopted  $g$ -factor values. While very good agreement is observed between experiment and theory for  ${}^{20}\text{Ne}$ , that is not the case for  ${}^{22}\text{Ne}$ . Recent ab-initio calculations for the  $g$  factor of the  $2_1^+$  state in  ${}^{22}\text{Ne}$  are also in agreement with the shell-model calculations [87]. The adopted  $g$ -factor value is

around  $4\sigma$  away from the USD predictions. Note that for both  $^{20}\text{Ne}$  and  $^{22}\text{Ne}$  the adopted  $g$  factors originate from TDRIV measurements performed by Horstman *et al.* [27, 28]. Although the same experimental technique and setup were used in the two measurements by the same collaboration, an important distinction can be made from the used target foils. A short account of the two studies is deemed necessary and is presented below.

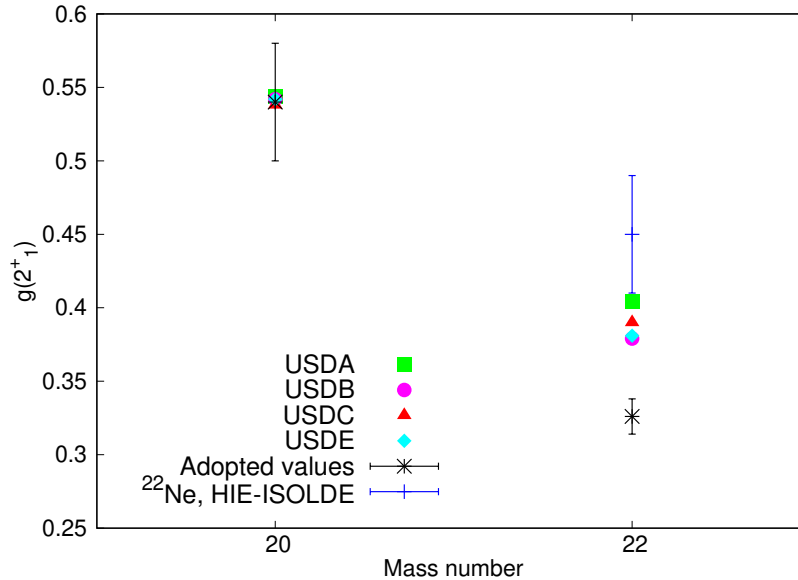


**Figure 2.23:** Shell-model predictions for  $g(2_1^+)$  in  $^{20,22}\text{Ne}$  compared with experimental results. The USDA and USDB calculations were performed with the ANTOINE code. The USDC [88] and USDE [89] calculations were performed by Prof. A. E. Stuchbery, ANU, using the NuShellX code [90]. All USD calculations for  $^{20}\text{Ne}$  are in agreement with each other and with the experimental result of 0.54(4) from Ref. [27]. For  $^{22}\text{Ne}$  the predictions of the various USD calculations are consistent with small deviations between the different interactions. The adopted value for  $g(2_1^+)$  of  $^{22}\text{Ne}$  is more than  $4\sigma$  away from the shell-model predictions. The value obtained in the current work is less precise than the adopted one but lies within  $2\sigma$  of all listed theoretical predictions.

The  $g$ -factor measurement of the  $2_1^+$  state in  $^{20}\text{Ne}$  was performed at the Utrecht 7-MV EN Tandem accelerator. A beam of 36.7-MeV  $^{12}\text{C}^{5+}$  ions was impinged at an angle of  $30^\circ$  on the target foil. The target consisted of three layers:  $500 \mu\text{g}/\text{cm}^2$  Ni,  $300 \mu\text{g}/\text{cm}^2$  Ag and about  $200 \mu\text{g}/\text{cm}^2$  C. The  $^{12}\text{C}(^{12}\text{C}, \alpha)^{20}\text{Ne}$  reaction was used to populate the  $2_1^+$  state in  $^{20}\text{Ne}$ . The C layer of the target was positioned facing the plunger stopper foil and therefore determined the charge-state distribution of the ions recoiling out of the target. The energy of the  $^{20}\text{Ne}$  ions exiting the target is estimated to be around 1.5-1.6 MeV/A. Over the course of the measurement an additional carbon build-up of up to  $13 \mu\text{m}/\text{cm}^2$  on the plunger foils was determined. This is not considered to have played a significant role in this experiment as it can only slightly modify the charge-state distribution due to additional energy losses. Moreover, the authors assume a 50% uncertainty on the thickness of the  $200 \mu\text{g}/\text{cm}^2$  layer and the observed carbon build-up is well within these uncertainties. The plunger distance was controlled with a screw micrometer and the zero-offset distance was precisely measured with a He-Ne laser interferometer. Four large-volume NaI scintillator detectors were used for registering the emitted  $\gamma$  rays. An annular Si surface-barrier detector was placed at backward angles to detect the  $\alpha$ -particles from the reaction. Two separate measurements were performed for  $^{20}\text{Ne}$  with identical targets. Data was taken at around 30 different plunger distances in both measurements. The applied analysis procedure was in essence the same as the TDRIV analysis described in the current work. The two  $g$ -factor values, 0.53(4) and 0.58(8), extracted from fitting the two  $^{20}\text{Ne}$  datasets were

averaged to obtain the final value 0.54(4) which is the current adopted value for  $g(2_1^+, {}^{20}\text{Ne})$ .

An important part of the  ${}^{20}\text{Ne}$  TDRIV analysis of Horstman *et al.* was the assessment of the relevant ionic species, their relative fractions and the populations of the respective atomic ground-state or excited-state configurations. The fractions of all electron configurations that contributed to the observed oscillations in the  $R(t)$  function were first determined directly from the fits of the  $R(t)$  functions. Then, an integral RIV measurement was performed using the same reaction and utilizing a magnetic spectrograph. The fully-stripped, H-like, He-like and Li-like ions were separated with the magnetic spectrograph and diverted to four different particle detectors. Three NaI scintillator detectors were placed at appropriate angles around the setup and another particle detector was placed at backward angles to register the  $\alpha$ -particles. A simultaneous fit of the particle- $\gamma$  angular correlations was performed. The fitting procedure included several parameters to determine the relative populations of the ground and excited states for the different ionic species as well as normalization factors. The fractions of each electron configuration obtained from the magnetic spectrograph measurement were in reasonable agreement with those from the direct fit of the  $R(t)$  function. Such an independent confirmation of the charge-state distribution and the population of atomic ground and excited states gives more confidence to the  $g(2_1^+, {}^{20}\text{Ne})$  value extracted from the TDRIV analysis. As shown in Fig. 2.23, the obtained result is well reproduced by modern shell-model calculations.

It has to be noted that a  $g(2_1^+)$  measurement for  ${}^{24}\text{Mg}$  was also performed as part of the same experiment and is described in the same publication [27]. In this case a 41.7 MeV  ${}^{16}\text{O}^{6+}$  beam was used to induce the  ${}^{12}\text{C}({}^{16}\text{O}, \alpha){}^{24}\text{Mg}$  reaction on the same Ni-Ag-C target. The energy of the  ${}^{24}\text{Mg}$  ions recoiling out of the target was around 1.5 MeV/A. The magnetic spectrograph analysis was not applied on  ${}^{24}\text{Mg}$  and the fractions of the relevant electron configurations were extracted from the fit of the  $R(t)$  function. The obtained g factor 0.51(2) is only marginally lower than the 0.538(13) value from the recent TDRIV measurement of Kusoglu *et al.* [36]. Overall, the measurements performed by Horstman *et al.* on  ${}^{20}\text{Ne}$  and  ${}^{24}\text{Mg}$  show that they had good control over all experimental parameters needed for the analysis. However, that seems to not have been the case in the following  ${}^{22}\text{Ne}$  measurement.

The experiment to measure  $g(2_1^+, {}^{22}\text{Ne})$  was performed with the exact same experimental setup. A 40.6 MeV  ${}^{19}\text{F}^{6+}$  beam was delivered on a  ${}^4\text{He}$ -implanted Ni-Ag target to induce the  ${}^4\text{He}({}^{19}\text{F}, p){}^{22}\text{Ne}$  reaction. The Ni and Ag layers were of the same thickness as in the targets from the previous experiment - 500  $\mu\text{g}/\text{cm}^2$  and 300  $\mu\text{g}/\text{cm}^2$ , respectively. The  ${}^4\text{He}$  implantation was done on the Ni layer, which was positioned to face the stopper foil. The energy of the recoiling ions is estimated to be around 1.1 MeV/A from the observed Doppler shift of the  $\gamma$ -ray energy. The authors note that the problem of carbon build-up on the targets was once again present. Four independent measurements were performed with separate targets that had different thickness of the carbon layers. Two of these measurements utilized more than one target to reduce the overall carbon build-up on any one target. This was deemed necessary by the authors as they observed protons and  $\gamma$  rays from the  ${}^{12}\text{C}({}^{19}\text{F}, pn){}^{29}\text{Si}$  reaction. The first excited state of  ${}^{29}\text{Si}$  decays to the ground state via a 1.273-MeV  $\gamma$  ray, which coincides with the 1.275 MeV  $2_1^+ \rightarrow 0_{g.s.}^+$  transition in  ${}^{22}\text{Ne}$ . A background subtraction procedure was applied to remove the contamination from  ${}^{29}\text{Si}$ . However, the main problem arising from the build-up of carbon on the target is related to some assumptions by the authors about its influence on the charge-state distribution. It must be stressed that the authors did not perform a separate magnetic spectrograph measurement and relied mainly on the fitting procedure of the  $R(t)$  function to obtain the fractions of the different ions. The results for the g factors and the used fractions of ionic species for the performed four independent measurements are shown in Table 2.3 and are discussed below.

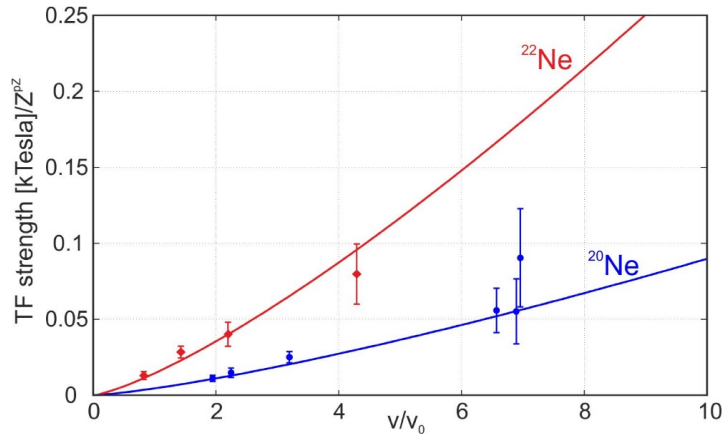
**Table 2.3:** The  $g$  factor of the  $2_1^+$  state in  $^{22}\text{Ne}$  and the electronic populations as measured in four separate experiments. Adapted from Table 1 in Ref. [28].

Experiment	C layer $\mu\text{g}/\text{cm}^2$	Populations of electronic states (%)			$\chi^2$	$ g $
		H-like	excited He-like	Li-like		
1	15	31(6)	8(9)	20	1.15	0.303(20)
2	4	7(5)	25(5)	30	1.07	0.351(32)
3	5	7(5)	28(8)	39	1.00	0.352(30)
4	10	12(5)	22(4)	20	0.79	0.329(23)
Average						0.326(12)

First, the fraction of Li-like ions was kept fixed to 20% or 30%, based on the thickness of the carbon layer, with these values taken from Ref. [91]. Although such a large change in the Li-like fraction is possibly not expected from the addition of around  $10 \mu\text{g}/\text{cm}^2$  of carbon, it is not too crucial for the measurement. Horstman *et al.* comment that the  $g$  factors obtained from fitting without the Li-like fraction are within the uncertainties of the results in Table 2.3. Simulations with LISE++ and the Schiwietz-Grande model for  $^{22}\text{Ne}$  ions exiting a  $^{12}\text{C}$  foil predict a Li-like fraction of around 30%, in agreement with the assumed fraction. Regarding the He- and H-like fractions, the authors assume a varying amount of each, somewhat correlated with the thickness of the carbon layer. They offer a possible explanation that some of the electrons from excited He-like configurations could be stripped by a sufficiently thick carbon layer, resulting in a higher H-like fraction. Such an effect is questionable as the charge-state distribution of ions passing through a foil depends only on  $Z_{\text{ion}}$ ,  $Z_{\text{foil}}$  and the exit energy of the ions. This proposition implies that the addition of several  $\mu\text{g}/\text{cm}^2$  of carbon is sufficient to drastically change the charge-state distribution, shifting 20% of the ions from He-like to H-like ions. The Schiwietz-Grande simulations from LISE++ predict about 40% of He-like and 15% of H-like ions which is more in line with the assumed fractions in measurements 2-4. Note that in the first measurement, in which the authors assume a 31(6)% fraction of H-like ions and a negligible 8(9)% fraction of He-like ions, the resulting  $g$  factor is significantly lower than those from measurements 2-4. This first measurement also has the lowest uncertainty on the  $g$  factor, which is factored in when the authors average the  $g$  factors from the four measurements to obtain the final result  $|g| = 0.326(12)$ . In the discussion the authors compare the results to the theoretical calculations available at the time. Most of the calculations predict a value within  $2\sigma$  of the experimental result, with the only exception being a calculation by Chung and Wildenthal in the full  $sd$  space that obtained  $g = +0.38$ , which is in agreement with the modern calculations in Fig. 2.23. At the end of Ref. [28], the authors comment that an identical experiment to measure  $g(2_1^+, ^{22}\text{Ne})$  was performed by Böhm *et al.* [92]. The result of that experiment was  $|g| = 0.36(3)$ , in agreement with the result of Horstman *et al.*, but less precise. It should be noted that the individual measurements 2 and 3 by Horstman *et al.* are in good agreement with the value by Böhm *et al.* and also agree with Chung and Wildenthal's calculations.

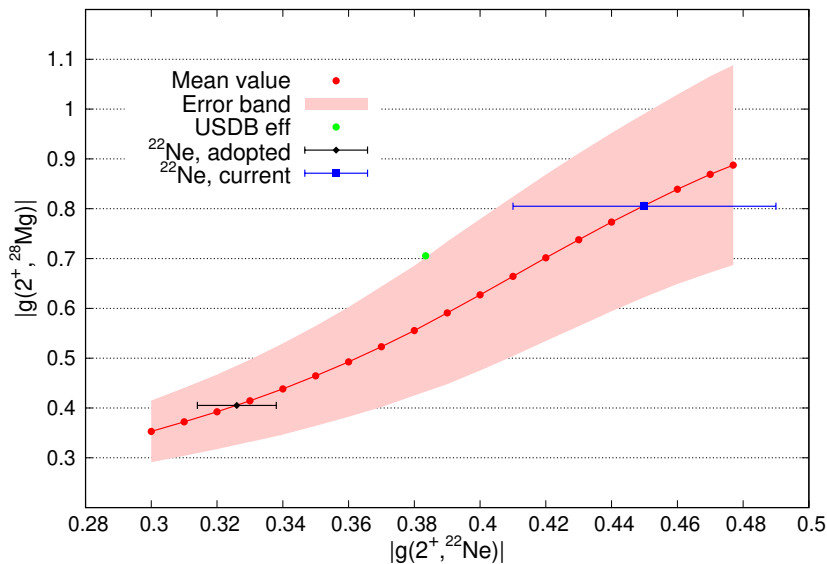
The main conclusion from the above overview of Ref. [28] is that, unlike the  $^{20}\text{Ne}$  measurement, the authors did not have good control over the fractions of the relevant electron configurations. Although the result claims very high precision, its accuracy seems to be doubtful. This is corroborated also from transient field measurements of Ne isotopes. The velocity dependence of the TF strength changes as a function of  $Z$  and should be constant for all Ne isotopes. Using the adopted  $g$  factors of the  $2_1^+$  states in  $^{20,22}\text{Ne}$  to calibrate the TF strengths, a deviation is observed between the velocity dependence for the two isotopes, as shown in

Fig. 2.24. A larger  $g(2_1^+, {}^{22}\text{Ne})$  value would partly or fully compensate this discrepancy.



**Figure 2.24:** Velocity dependence of the transient field strength for  ${}^{20,22}\text{Ne}$  obtained from TF experiments with various ion velocities. The TF strengths are calculated using the respective adopted g-factor values for  ${}^{20,22}\text{Ne}$ . The fits of the two data sets (solid lines) are not in agreement, as would be expected for same- $Z$  isotopes. Plot courtesy of Prof. A. E. Stuchbery.

The discussion on the apparent flaws in the work of Horstman *et al.* and the adopted value for  $g(2_1^+, {}^{22}\text{Ne})$  do not constitute any sort of confirmation of the conflicting result from the current work. As pointed out in Chapter 2.3.3, without a proper measurement of the plunger zero-offset distance, the current result is unconvincing. This applies also to the obtained value of  $g(2_1^+, {}^{28}\text{Mg})$ . However, the obtained correlation between the two g factors (Fig. 2.21) provides valuable insight. We performed shell-model calculations with the USDB interaction for the two g factors and the obtained predicted correlation between them is shown in Fig. 2.25. The effective  $g_s$  and  $g_l$  values from Ref. [69] were used in the calculations:  $g_s^\pi = 5.15$ ,  $g_l^\pi = 1.159$ ,  $g_s^\nu = -3.55$ ,  $g_l^\nu = -0.09$ .



**Figure 2.25:** Correlation between  $g(2_1^+, {}^{22}\text{Ne})$  and  $g(2_1^+, {}^{28}\text{Mg})$ . The  $g(2_1^+, {}^{22}\text{Ne})$  results from Ref. [28] and the current work are shown for reference. The prediction for the g factors of the  $2_1^+$  states in  ${}^{22}\text{Ne}$  and  ${}^{28}\text{Mg}$  from shell-model calculations with the USDB interaction is marked in green.

The first notable point from the correlation plot is that of the adopted  $g(2_1^+, {}^{22}\text{Ne})$  value.

If this value is accurate, the corresponding  $g(2_1^+, {}^{28}\text{Mg})$  would lie much lower than the USDB predictions. For comparison, the intruder-dominated  $g(2_1^+, {}^{32}\text{Mg})$  is predicted to be just below  $g = 0.4$  by calculations within the *sdpf* model space [70]. A scenario in which the structure of  ${}^{28}\text{Mg}$  is already dominated by intruder configurations is highly unlikely. On the other hand, starting from the current result of 0.45(4) for the  ${}^{22}\text{Ne}$  g factor, the uncertainty of the  ${}^{28}\text{Mg}$  g factor would be around 40%. Such a result would be in agreement with the USDB prediction but would not exclude a minor decrease in the g factor due to *pf* admixtures to the wave function. In essence, the uncertainty would be too large to draw any conclusions on the structure of  ${}^{28}\text{Mg}$ .

Additional shell-model calculations for  ${}^{28}\text{Mg}$  within the *sdpf* model space were performed by Dr. F. Nowacki, IPHC Strasbourg. The used effective  $g_l$  and  $g_s$  values were taken from previous calculations for  ${}^{35}\text{Si}$  [93]. The obtained value  $g(2_1^+, {}^{28}\text{Mg}) = 0.7$  is indistinguishable from the pure USDB result of  $g(2_1^+, {}^{28}\text{Mg}) = 0.71$ . From the theoretical point of view, a drop in the g-factor value at  ${}^{28}\text{Mg}$  is not expected due to *pf* admixtures to the wave function. However, the g factors of  $2_1^+$  states in the even-even Mg isotopes are expected to be sensitive to the single-particle energy (SPE) of the  $d_{3/2}$  orbital. Further calculations by F. Nowacki showed that if the SPE of the  $d_{3/2}$  orbital is decreased by 1 MeV, the  ${}^{28}\text{Mg}$  g factor would be reduced to 0.61. In that regard, the fact that the USDB prediction lies just above the error band of the obtained correlation curve is curious. It is reminiscent of the  ${}^{26}\text{Mg}$  g-factor result, shown in Fig. 2.1 where the USDB prediction lies at the upper edge of the experimental uncertainty. Nevertheless, the current experimental uncertainties for both  ${}^{28}\text{Mg}$  and  ${}^{26}\text{Mg}$  are too large to make any claims about the SPEs.

Finally, extracting a meaningful result for  $g(2_1^+, {}^{28}\text{Mg})$  requires a new measurement of  $g(2_1^+, {}^{22}\text{Ne})$  that would resolve the discrepancy between the current result and the adopted value of Horstman *et al.* [28]. A proposal for such a measurement has already been accepted and will be performed at GANIL, France. Simulations of the experimental setup and the expected  $R(t)$  function were performed in preparation for this measurement and are discussed in the following Section.

## 2.5 ${}^{22}\text{Ne}$ TDRIV experiment at GANIL

The planned  ${}^{22}\text{Ne}$  TDRIV experiment at GANIL will make use of the Orsay Universal Plunger System (OUPS) [94], the EXOGAM HPGe detector array [95] and the Orsay Particle Scintillator Array (OPSA). The EXOGAM array is composed of up to 16 clover detectors with four quadruple-segmented HPGe crystals in each clover. Eight of the clovers are placed in a ring around  $\theta = 90^\circ$  and four clovers can be placed at both forward ( $\approx 45^\circ$ ) and ( $\approx 135^\circ$ ). The OPSA particle detector array is being developed at IJCLab in collaboration with GSI, Darmstadt, based on original schematics from the Australian National University. It is based on LYSO scintillators with a SiPM readout. It consists of two rings of 6 mm  $\times$  6 mm LYSO crystals, as shown on the schematic in Fig. 2.26. The first ring has an inner diameter of 12.5 mm and contains 12 crystals, while the second ring has 16 crystal with an outer diameter of 25.6 mm. The OPSA detector was designed specifically for TDRIV experiments. The fast LYSO scintillators allow for high particle rates per crystal and their energy resolution of about 10% is enough to distinguish beam-like from target-like ions. In addition, the beam-like ions scattered into the two rings would have slightly different velocities due to passing through different effective thickness of the target and degrader foils. This will result in slightly different charge state distributions of the ions registered in the two rings. Therefore the data from the two rings can be considered as two independent measurements.

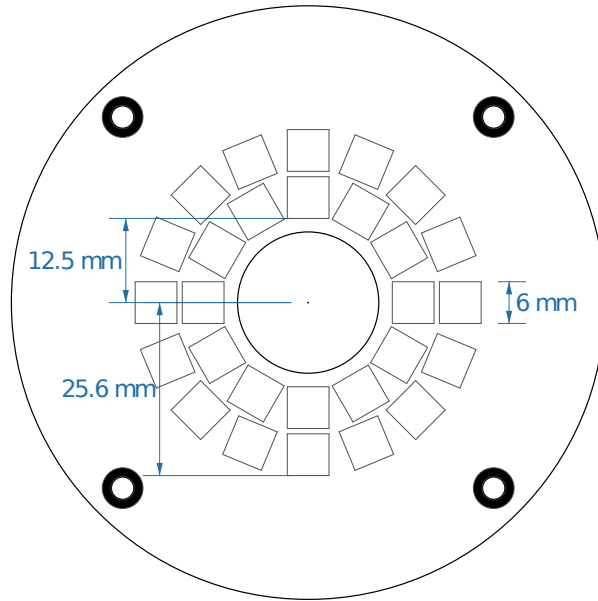


**Figure 2.26:** Schematic of the Orsay Particle Scintillator Array (OPSA) based on  $6 \times 6$  mm LYSO scintillator crystals. The inner radius of the first ring and the outer radius of the second ring are shown.

The target and degrader foils will be of the same materials and similar thickness to the ones used in the HIE-ISOLDE experiment. The beam of  $^{22}\text{Ne}$  ions, provided by the CIME cyclotron, will have the same energy of 5.5 MeV/A as in the HIE-ISOLDE experiment. However, its intensity will be between 2 and 3 orders of magnitude higher -  $\approx 10^9$  pps, compared to  $\approx 10^6$  pps at ISOLDE. The restricting factor for the intensity at ISOLDE is the silicon CD particle detector, which can sustainably handle rates of around 100 pps. The LYSO-scintillator OPSA array is faster and more robust, and can sustain much higher rates of incident particles up to several thousand pps. The higher beam intensity allows for higher statistics obtained in less time. Data can be taken at more plunger distances with lower statistical uncertainty in each data point to obtain a very precise  $R(t)$  function.

As described in the Sections above, the plunger zero-offset distance is an extremely important parameter. In the proposed experiment at GANIL it could be obtained in two ways. First, the EXOGAM Clovers at forward or backward angles will observe a Doppler-shifted 1275-keV  $\gamma$  ray ( $2_1^+ \rightarrow 0_{g.s.}^+$ ). Due to having a degrader, instead of a stopper, there will be a “fast” and a “slow” shifted component, rather than a “shifted” and an “unshifted” component. The lifetime of the  $2_1^+$  state is known with high precision from a recent study of Petkov *et al.* [96] and can also be re-measured from the obtained data with the RDDS method. Then, the plunger zero-offset distance can be obtained from the ratio of the “fast” and “slow” peak areas at the shortest plunger distance. The alternative is to rely on the very high statistics expected in this measurement to directly fit the experimental  $R(t)$  function for both the g factor and  $D_0$ . This approach has been used in the TDRIV measurement of  $^{24}\text{Mg}$  at ALTO and did not impact the overall precision of the g factor. Both approaches are viable and can be applied to obtain independent measurements of the plunger zero-offset.

For the experiment in GANIL it is expected that 12 EXOGAM clover detectors will be available. The ring of eight clovers at  $90^\circ$  and four Clovers at backward angles were included in the simulations. Only the outer ring of OPSA was used in the simulations for simplicity. The array was placed at forward angles, 30 mm away from the target/degrader, leading to an angular coverage of  $33^\circ < \theta_p < 41^\circ$  for the outer ring. The total number of particle- $\gamma$

combinations in this setup is 768. Utilizing the newly implemented subroutines in the TDRIV code a detector geometry input file was generated with 20% of the combinations designated as “strong  $\uparrow$ ” and 20% as “strong  $\downarrow$ ”. A  $3 \text{ mg/cm}^2$   $^{93}\text{Nb}$  target and a  $1 \text{ mg/cm}^2$   $^{181}\text{Ta}$  degrader foils were considered in the simulation. Assuming a  $g(2_1^+, ^{22}\text{Ne})$  value of 0.45, the expected  $R(t)$  function was simulated and is shown in Fig. 2.27. With sufficient statistics it is expected that also the “intermediate” and “weak” combinations can become useful. Their respective  $R(t)$  functions can be fitted simultaneously with the “strong”  $R(t)$  function to obtain a self-consistent result.

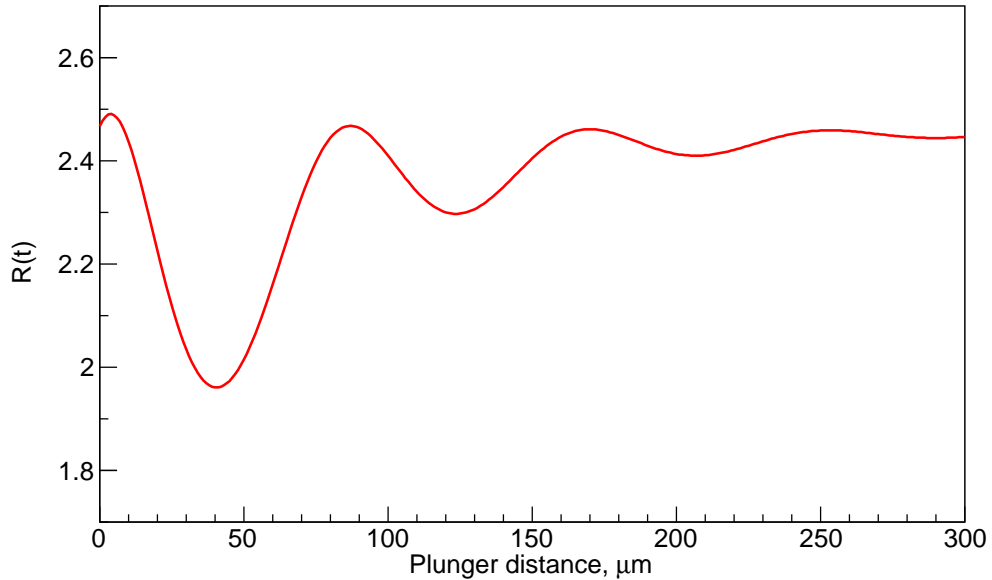


**Figure 2.27:** Simulated  $R(t)$  curve for the planned  $^{22}\text{Ne}$  TDRIV experiment at GANIL.

Based on the simulation and the experience from the HIE-ISOLDE experiment, it is planned that data will be taken for up to 30 plunger distances in the range between 0 and  $180 \mu\text{m}$ . Assuming optimal experimental conditions, the obtained statistical uncertainty in each point should allow for an overall precision of the extracted  $g$  factor of around 2%. Such a measurement would definitively resolve the discrepancy between the available experimental results to this point. It will also allow for a  $g(2_1^+, ^{28}\text{Mg})$  value to be extracted from the correlation plot in Fig. 2.21.



# 3 - Magnetic moment of the $2_1^+$ state in $^{46}\text{Ti}$

## 3.1 Motivation

In the previous Chapter it was described how the TDRIV method is applied on H-like ions. However, the range of nuclei that can be studied through H-like ions is quite limited. The  $(Z/n)^3$  dependence of the hyperfine field strength from Eq. (1.86) sets a limit on the suitable isotopes. For isotopes with  $Z > 20$  the period of the oscillations in the  $R(t)$  function would be too small to be experimentally observed. Charge states with more electrons, reducing the field at the nuclear site, have to be utilized in order to access higher- $Z$  nuclei with the TDRIV method.

The g factors of short-lived excited states in higher- $Z$  nuclei are attainable using the TF method. As mentioned in Chapter 1.2.3, the TF strength cannot be deduced from first principles. Instead, it is extracted from parametrizations, which are calibrated using well-known g factors measured via alternative methods. While the TF method has proven itself as very useful, the scarcity of suitable calibration values in the  $fp$  shell has been a longstanding concern. A consequent issue with the TF measurements, raised by N.J. Stone [97], is the underestimation of the uncertainty of the TF strength. He states that the intrinsic uncertainty of the parameters that enter into the TF parametrizations is often not considered for the overall uncertainty of the reported results. Stone argues that an increase of 15-20% of the reported uncertainties is necessary in most cases.

One of the typically used TF calibration points is the g factor of the  $2_1^+$  state in  $^{56}\text{Fe}$ . However, up until the measurement of East *et al.* [98], the adopted value for  $g(2_1^+, ^{56}\text{Fe})$  was  $g = 0.61(8)$ . This adopted value was itself an average of three previous measurements. In their work East *et al.* show that the latest of the three previous measurements had extracted a result based on the values obtained in the first two measurements. Thus the third value was not independent and should not have been used in obtaining the averaged adopted value. Excluding this problematic value results in an increased uncertainty for the adopted g factor:  $g(2_1^+, ^{56}\text{Fe}) = 0.61(13)$ . In the years before the study of East *et al.* there have been multiple experiments performed using the TF method to measure g factors of nuclei in the  $fp$  shell. Most of these experiments used the adopted  $^{56}\text{Fe}$  g factor to calibrate the TF strength. Therefore East *et al.* argue that the results obtained from these measurements could be uncertain by about 20% [98]. In the same publication East *et al.* performed a g-factor measurement of  $g(2_1^+, ^{56}\text{Fe})$  relative to the precisely known  $g(5/2_1^-; ^{57}\text{Fe})$ , measured by the TDPAD method. The experimental results were averaged with the corrected adopted value to obtain  $g(2_1^+, ^{56}\text{Fe}) = 0.51(5)$  [98].

The TDRIV method can alleviate these concerns of the TF method by providing new accurate and precise measurements of g factors in the  $fp$  shell to be used as calibration points. This in turn can greatly increase the accuracy of the TF strength parametrizations in this region and lower the associated uncertainties. One such example is an experiment that took place at the ALTO facility in Orsay in 2014 as part of the MINORCA campaign. This was a proof-of-principle experiment aiming to apply the TDRIV method on Na-like ions. The goal of the measurement was to determine the g factor of the  $2_1^+$  state in  $^{56}\text{Fe}$ . A detailed account of the analysis can be found in Dr. Brendan McCormick's doctoral thesis (ANU) [23]. The final result from this experiment  $g(2_1^+, ^{56}\text{Fe}) = 0.549(19)$  is in good agreement with the previously

reported value of East *et al.* [98] with precision improved by a factor of two. The precise g-factor value from the TDRIV measurement can now be used to re-calibrate the TF strengths in the previous measurements in the region.

Although the TDRIV method can be applied up to  $Z \approx 50$  by utilizing Na-like ions, the analysis of the  $R(t)$  function is considerably more difficult compared to the cases of H-like ions. Even if the largest fraction of ions is in a Na-like state, there are significant contributions from F-like, Ne-like, Mg-like and Al-like ions. In addition, all of these types of ions can be populated in a number of excited atomic states, introducing a large number of frequencies that influence the  $R(t)$  function. Factoring in the cascades of short-lived excited atomic states within the time frame of the observed oscillations adds to the complexity.

An unexplored alternative to Na-like ions is the use of Li-like ions. The lower number of electrons simplifies the atomic structure and reduces the density of available excited atomic states. Based on the strength of the hyperfine field, the lower bound for applying the TDRIV method on Li-like ions is  $Z \gtrsim 14$  and the upper bound is at  $Z \approx 35$ . This range covers part of the *sd* shell and most of the *fp* shell nuclei. A detailed study on the use of Li-like ions in a TDRIV experiment has not been performed before. As mentioned in Chapter 2.4, the measurement by Horstman *et al.* [28] on  $^{22}\text{Ne}$  assumed a dominant Li-like fraction of ions. However, that is not considered a suitable test for Li-like ions due to the poor control over the charge state distributions of the ions in that experiment. Therefore a proof-of-principle experiment was proposed to examine the viability of Li-like ions for a TDRIV g-factor measurement.

The experiment to be performed at the JYFL facility, University of Jyväskylä, Finland, aims to measure the g factor of the  $2_1^+$  state in  $^{46}\text{Ti}$ . The adopted value for this g factor is taken from a TF measurement [99] performed relative to the value of  $g(2_1^+, ^{56}\text{Fe})$ , later shown to have been problematic [98]. The authors report a high-precision value  $g(2_1^+, ^{46}\text{Ti}) = 0.496(27)$ . However, in the Table of recommended values of magnetic moments [97] Stone assigns an uncertainty to this result increased by a factor of three. Nevertheless, even with a significantly increased uncertainty a discrepancy is observed between the experimental g factor and the theoretical shell-model calculations. In Fig. 3.1 the measured g factors for selected nuclei in the region are compared to shell-model calculations in the full *fp* shell with two different interactions. The calculations succeed in reproducing the overall trends of the g factors and some agreement is achieved for the Fe isotopes and for  $^{50,52}\text{Cr}$ . Nevertheless, there seems to be a systematic underestimation of the Ti g factors. The authors in Ref. [99] attribute this underestimation to excitations of the  $^{40}\text{Ca}$  core, yet it could be due to the adopted TF parametrization.

A similar conclusion was reached by Taylor *et al.* [103] for the neighboring  $^{44}\text{Ca}$ , two protons below  $^{46}\text{Ti}$ . The authors find that the pure  $(f_{7/2})^4$  configuration cannot explain the obtained  $g(2_1^+, ^{44}\text{Ca})$  result, as well as the known  $B(E2, 0_{g.s.}^+ \rightarrow 2_1^+, ^{44}\text{Ca})$  and  $Q(2_1^+, ^{44}\text{Ca})$  values. Instead, they apply a simple model that allows *np* – *nh* excitations for both protons and neutrons. The results from this approach indicate that particle-hole excitations have a large contribution to the wave function (61(6)%). Moreover, the particle-hole component is considered to be mostly due to proton core excitations as there are already four valence neutrons above the full  $N = 20$  shell. The importance of proton excitations is corroborated further by the obtained positive g-factor value  $g(2_1^+, ^{44}\text{Ca}) = +0.12(5)$ . Such an admixture to the wave function could also play a role in the  $2_1^+$  state in  $^{46}\text{Ti}$ .

In the case of  $^{44}\text{Ti}$  with two protons and two neutrons both in the  $f_{7/2}$  orbital, Schielke *et al.* [104] measured the g factor of the  $2_1^+$  state to be 0.52(15). The authors performed shell-model calculations within the *fp* shell using the KB3 and FPD6 effective interactions. They found that the calculations in the full *fp* shell model space agree better with the experimental result compared to a pure  $(f_{7/2})^4$  configuration. This was attributed specifically to a contribution from

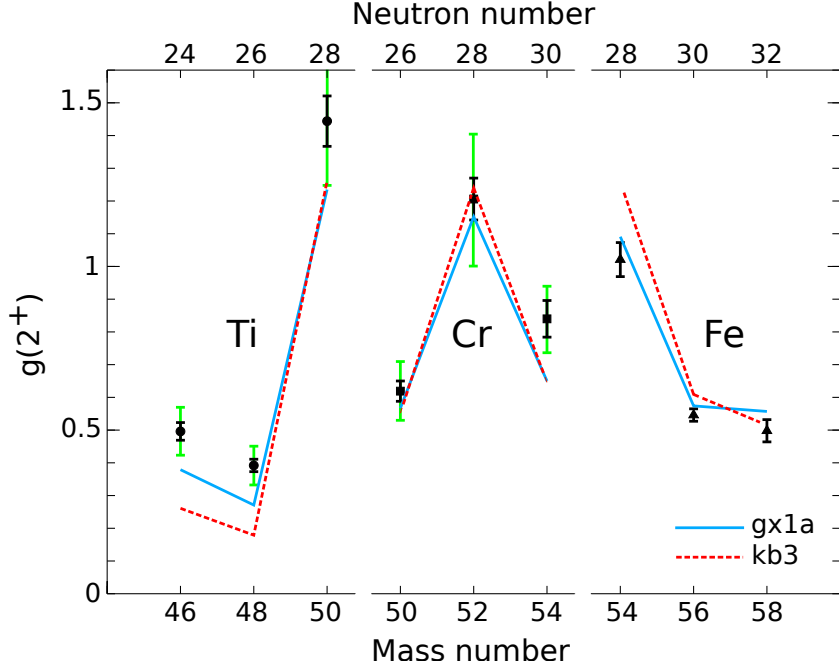


**Figure 3.1:** Experimentally obtained g factors of selected even-even Ti [99, 100], Cr [99, 101] and Fe [98, 102] isotopes compared with shell-model calculations. The uncertainties of the published results are given in black. The corresponding increased uncertainties given by Stone in [97] are shown in green. The value for  $^{56}\text{Fe}$  is obtained with the TDRIV method [98]. The values for  $^{54,58}\text{Fe}$  have been obtained in a measurement relative to the  $^{56}\text{Fe}$  g factor [102] and have already been adjusted for the new TDRIV value. Qualitative agreement with the theoretical predictions is observed. Experimental values for Ti isotopes are not in good agreement with theory. Plot courtesy of Prof. A. E. Stuchbery.

the  $(f_{7/2})^3(p_{3/2})^1$  configuration. However, both the KB3 and the FPD6 interactions provide a g factor for the  $(f_{7/2})^3(p_{3/2})^1$  configuration that is in agreement with the experimental result. The authors comment that to distinguish between the predictions of the two interactions an experimental uncertainty on the level of 1% is needed, which cannot be reached by the TF method.

The sub-5% precision achievable with the TDRIV method is expected to be able to provide insight into the admixtures present in the wave function of the  $2_1^+$  state in  $^{46}\text{Ti}$ . Both the suggested proton core excitation and the importance of the  $(f_{7/2})^3(p_{3/2})^1$  configuration in  $^{46}\text{Ti}$  can be probed through the planned TDRIV measurement. In addition, the exact nature of the presumed particle-hole excitations from the simplistic model in Ref. [103] can be elucidated upon.

### 3.2 Charge-state measurement of $^{48}\text{Ti}$

One of the important input parameters for planning TDRIV measurements and their subsequent analysis is the charge-state distribution of the recoiling ions after exiting the target material. Although there are models, for example in the LISE++ package, that can predict the required values, the various models in the literature can produce significantly different results, which would impact the TDRIV analysis. It is preferable to perform a dedicated charge-state measurement to determine these distributions accurately for the ions of interest before performing a TDRIV experiment. This also allows for several target materials to be tested in order to optimize the experimental conditions - in this case to maximize the Li-like

fraction of ions.

The technical requirements for performing a charge-state measurement are not very high. The charge-state distribution does not change for different isotopes of the same element. It depends only on  $Z_t$  of the target material,  $Z_p$  of the probe ion and the energy of the ions exiting the target. Therefore the charge-state measurement can be performed at a stable beam facility using the most abundant stable isotope even if the isotope of interest is very exotic. The beam must then impinge on a target foil of the studied material and the recoiling ions pass through an analysing magnet to reach a detection system. Varying the current of the analysing magnet allows one to scan through all charge states and observe the changes in intensity in the detection system. Comparing the maximum observed intensity for each charge state yields their relative population. The detection system can be a Faraday cup or any type of detector that can directly or indirectly measure the intensity of incoming ions.

Finally, to obtain the energy dependence of the charge-state distribution, the measurement has to be performed for several different beam energies, which can be achieved in several ways. The obvious solution would be to change the initial beam energy, which is relatively easy at a Tandem accelerator facility, but is time consuming at a cyclotron facility, such as JYFL. Another option is to have a set of target foils with different thicknesses to modulate the exit energy of the ions through energy losses in the target material. However, the preparation of a set of foils can be quite expensive, depending on the target material and the required thickness, and even more so if more than one target material is to be studied. The third possibility is to decrease the initial beam energy using a set of energy degraders of varying thickness placed just before the target foil. This decreases the overall cost as the degraders can be produced from a material that would be less expensive, however, they would introduce more angular straggling of the ions after the target foil due to scattering in the degrader foil. Finally, a combination of all three options was chosen for the charge state measurement of  $^{48}\text{Ti}$  at JYFL.

### 3.2.1 Experimental setup

The charge-state measurement was performed at the JYFL facility of the University of Jyväskylä, Finland. At JYFL, heavy ions are accelerated using a K130 cyclotron. The principle of operation of cyclotrons is based on a combination of a vertical magnetic field  $B$  and a high-frequency electric field. The magnetic field changes the direction of the ion in the horizontal plane while the electric field is used to accelerate the ion. The frequency at which an ion of mass  $m$  and charge  $q$  will orbit under the influence of the magnetic field is the cyclotron frequency:

$$\omega_c = \frac{qB}{m}. \quad (3.1)$$

The K130 cyclotron at JYFL is separated into three sectors and the alternating electric field is applied in the gaps between them. Each time the ions pass through a gap the appropriate electric field is applied to accelerate them. The accelerated ions have a higher velocity which leads to a larger bending radius under the influence of the magnetic field. This results in an outward spiral trajectory of the ions until they exit the cyclotron. Ions with different charge-to-mass ratios have different cyclotron frequencies as follows from Eq. (3.1). The frequency of the alternating electric field is adjusted to the cyclotron frequency of the desired ionic species.

The maximum kinetic energy per unit mass for an ion accelerated in a cyclotron is defined

by its K factor through the relation:

$$\frac{T}{A} = K \left( \frac{Q}{A} \right)^2, \quad (3.2)$$

where  $A$  is the atomic mass number of the ion and  $Q$  is the charge state of the ion. The K factor itself is the maximum kinetic energy to which a proton ( $A = 1, Q = 1$ ) can be accelerated, which is 130 MeV for the JYFL cyclotron. If several ionic species are present with the same charge-to-mass ratio or  $A/Q$  value, they will be accelerated to the same kinetic energy per unit mass (MeV/A). Ions with a different  $A/Q$  value will see a repulsing potential when reaching the sector gaps due to their differing cyclotron frequency and they will be stopped on the inner walls of the cyclotron.

The heavy ions accelerated in the K130 cyclotron are produced using an Electron Cyclotron Resonance (ECR) ion source. The ECR technique utilizes the same cyclotron concept of a superposition of a static magnetic field and a perpendicular high-frequency electrostatic field to accelerate electrons to very high energies in a small volume. When the frequency of the electrostatic field is the electron cyclotron frequency

$$\omega_{ec} = \frac{eB}{m_e}, \quad (3.3)$$

the electrons can resonantly increase their kinetic energy in the plane perpendicular to the magnetic field. The desired material for beam production is introduced into the ECR zone where the high-energy electrons ionize the atoms through collisions. For this measurement, the Ti is introduced to the plasma through the MIVOC method (Metal Ions from Volatile Compounds) [105]. An organic compound of natural Ti (73.72%  $^{48}\text{Ti}$ ) is prepared and placed inside the ECR source. The compound slowly vaporizes at room temperature and the evaporated molecules drift to the ECR zone. The high-energy electrons break the molecules into individual atoms and ionize them. The  $^{48}\text{Ti}$  ions are then extracted through a set of electrodes and are guided to the K130 cyclotron to be accelerated.

After the accelerated  $^{48}\text{Ti}$  ions with the appropriate charge state exit the cyclotron they are diverted by a dipole magnet to the Recoil Ion Transport Unit (RITU) recoil separator [106]. It consists of a target chamber, three focusing quadrupole (Q) magnets and a bending dipole (D) magnet in a QDQQ configurations, and a vacuum chamber at the focal plane. A schematic of the RITU separator is shown in Fig. 3.2. The bending angle of the dipole magnet is  $25^\circ$  with the radius of its curvature being  $\rho = 1.85$  m, giving a maximum rigidity of 2.2 Tm. The angular acceptance of the separator is 10 msr and the dispersion is 10 mm/% [106].

The RITU separator is usually utilized in gas-filled mode to separate primary beam-like reaction products after fusion-evaporation reactions. However, it is also possible to be used in vacuum mode as per its specifications [106]. It has been tested in vacuum conditions during its commissioning but no experiments since then have required this mode of operation. In the case of a charge-state measurement, it is necessary to run in vacuum mode as passing through a gas volume would alter the charge-state distribution of the ions.

The three quadrupole magnets of RITU are for vertical, horizontal and vertical focusing of the beam, respectively. Their current values were calibrated using a standard triple- $\alpha$  source ( $^{239}\text{Pu}$ ,  $^{241}\text{Am}$ ,  $^{244}\text{Cm}$ ) and a position-sensitive DSSSD. The triple- $\alpha$  source was placed in the target chamber at the entrance of the first quadrupole magnet. A square  $16 \times 16$ -segmented DSSSD was placed at the focal plane to register the emitted  $\alpha$  particles. The current of the three quadrupole magnets was then adjusted until the beam spot of the  $\alpha$  particles was

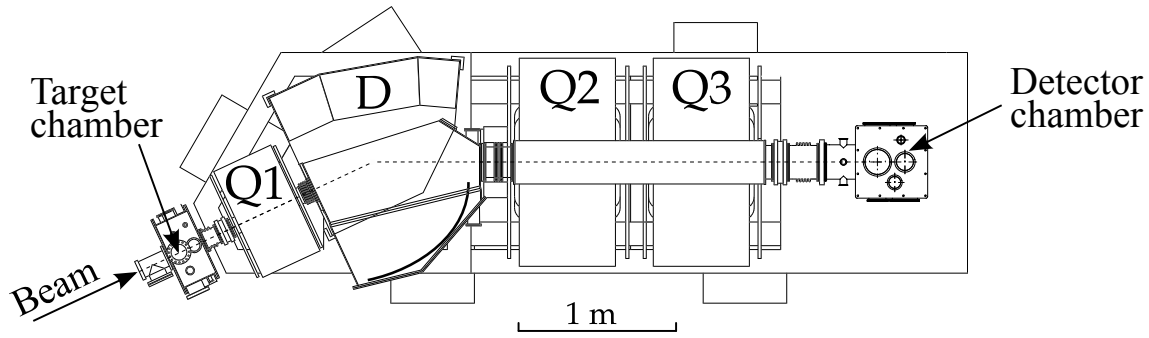


**Figure 3.2:** Schematic top view of the RITU recoil separator at JYFL, adapted from [107].

minimized.

Inside the target chamber there are three available positions for placing a target ladder. In addition, there is an independent target wheel with 12 positions. One of the positions on the target wheel is occupied by a quartz crystal for beam focusing and alignment. When the beam impinges on the quartz crystal, the crystal scintillates in the visible spectrum. A small camera is placed at backward angles in the target chamber to monitor the light emitted from the quartz. The beam is tuned until it passes precisely through a 5-mm opening in the center of the quartz crystal and the scintillation light is decreased to a minimum.

The materials to be studied in the charge state measurement were C, Mg, Nb and Ta. One foil of each C ( $\approx 0.1 \text{ mg/cm}^2$ ), Mg ( $\approx 0.87 \text{ mg/cm}^2$ ) and Ni ( $\approx 1.48 \text{ mg/cm}^2$ ) were prepared and placed in the third target ladder, just before the entrance to the recoil separator. A set of seven Ta foils of varying thickness (between  $\approx 3.6 \text{ mg/cm}^2$  and  $\approx 21.6 \text{ mg/cm}^2$ ) were placed on the target wheel to be used both as beam energy degraders for the measurements of C, Mg and Nb foils, and for a measurement of Ta as a target material.

At the RITU focal plane there is a vacuum chamber where any number of ancillary detectors can be placed depending on the type of experiment taking place. For the purposes of the charge-state measurement, a small detector setup was developed at JYFL to monitor the rates of incoming beam ions. A thick Au foil was placed at the focal plane, tilted by  $45^\circ$  in the vertical plane. Three ZnS scintillators with silicon photomultiplier readout were placed at around  $75^\circ$ ,  $90^\circ$  and  $105^\circ$  angles relative to the beam axis. These scintillators have poor energy resolution and high detection efficiency for heavy ions and are used only as particle counters. The intensity of ions passing through RITU is monitored by the rates of Rutherford-scattered nuclei in each of the ZnS detectors. All scattering reactions of the Ti nuclei with the Au targets would be mostly forward focused and are implanted in a thick Al “beam dump” behind the Au target. Shielding was put in place between the beam dump and the ZnS detectors to exclude the possibility of backward-scattered ions from the beam dump. The complete setup at the focal plane is shown in Fig. 3.3.

The measurement of count rates in the three ZnS detectors in the focal plane heavily depends on the initial beam intensity. However, this can only be directly measured by inserting a Faraday cup in the beam, which stops most of the beam. Therefore if there are any intensity fluctuations during data taking, they cannot be observed. In order to monitor the initial beam intensity during the experiment in a less intrusive manner a thin Ta foil ( $\approx 0.45 \text{ mg/cm}^2$ ) was placed in the second target ladder in the target chamber. A fourth ZnS detector was placed at backward angles in the target chamber to monitor the rates of back-scattered Ti ions from this Ta foil. The goal of the Ta foil and the additional ZnS detector was to provide an online reading of the beam intensity that can be used to normalize the count rates of the ZnS detectors at the focal

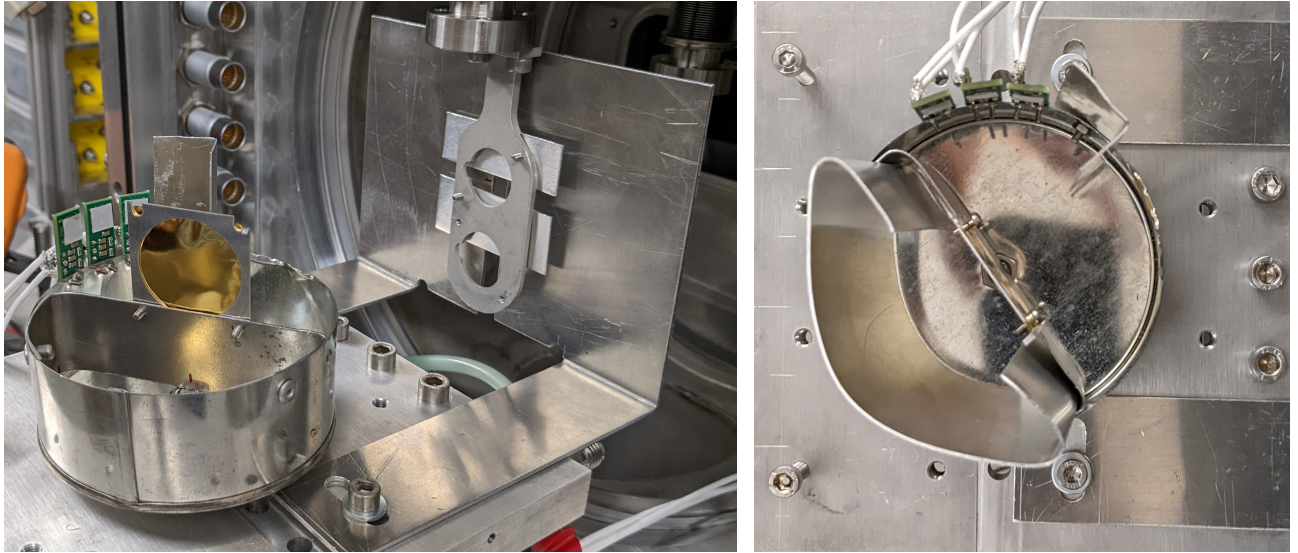


**Figure 3.3:** (Left) Full view of the detection setup at the RITU focal plane. A set of two vertical and two horizontal aluminium plates are placed to act as a collimator for the beam after the dipole magnet. The thick Au foil is positioned to form a  $45^\circ$  angle to the incoming beam. An L-shaped piece of aluminium is used to shield the three ZnS detectors from any beam particles scattered from the collimators. (Right) Top view of the detection setup at the focal plane. Incoming beam would be coming from the right side of the picture. Another piece of aluminium is placed behind the Au foil to act as a beam dump. Its edges are bent inward to shield the ZnS detectors from any backward-scattered ions from the beam dump.

plane. With the same reasoning a fifth ZnS detector was added to monitor forward-scattered ions after the C/Mg/Nb foils in the third target ladder. The inside of the target chamber is shown in Fig. 3.4.

The signals of the five ZnS detectors were sent via coaxial cables to the TDR DAQ system [108]. The Grain software [109] reads a code written in Java that defines the input channels and structures how the incoming data is visualized on-line. In the current measurement, the count rates were accumulated over six seconds and plotted as a function of absolute time since the start of the run. In addition, the traces of each hit on the detectors were also written in the data stream to be used in the offline analysis. An interesting feature of Grain is that once the data has been written to file it can be replayed with a modified version of the Java code to introduce changes to the visualization plots.

### 3.2.2 Data taking

The charge-state measurement of  $^{48}\text{Ti}$  took place in January 2022 over the course of three days. Due to the limited time available the measurement was performed for two initial beam energy settings, which were further modulated through the Ta degraders on the target wheel to obtain multiple data points for each setting. The essential part of the measurement was to scan a wide range of  $B\rho$  values, corresponding to different charge states, by changing the current of the RITU dipole magnet for each combination of initial beam energy, Ta degrader and studied target material.

The current of the dipole magnet was monitored and controlled remotely via a graphical user interface. For convenience, the current value was defined in terms of percentage of the maximum current, although it was also possible to directly define the required magnetic field in

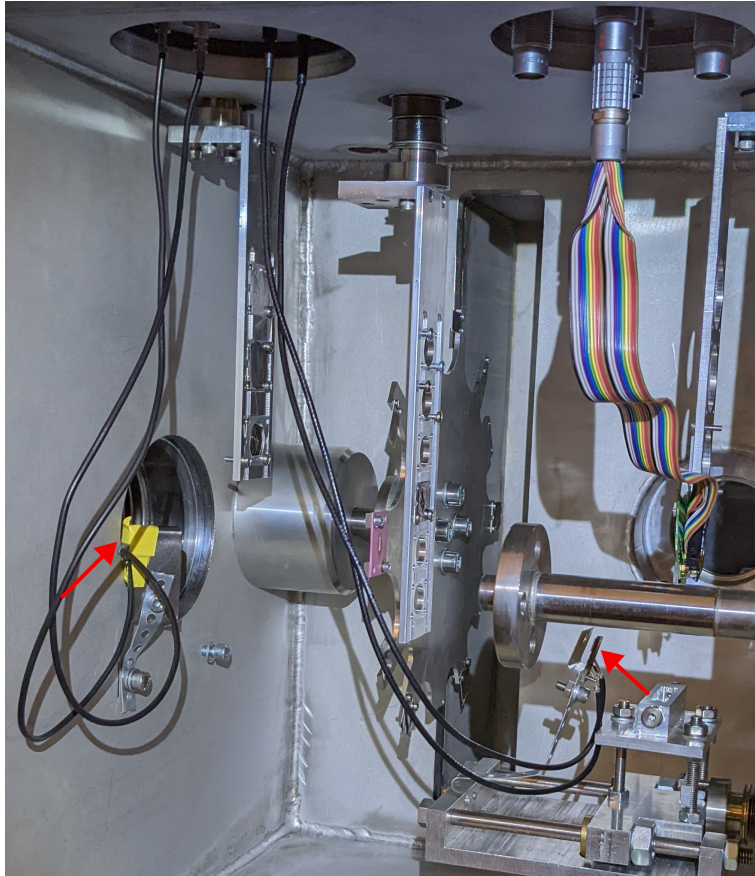


**Figure 3.4:** The RITU target chamber. Beam is coming from right to left. The right-most target ladder holds the 5 mm collimator. The rainbow cable is the readout of the camera for focusing the beam on the quartz. The second target ladder holds the  $0.45 \text{ mg/cm}^2$  Ta foil with the rest of the positions empty. The target wheel is just downstream of the second target ladder. The pink holder contains the small quartz crystal for beam focusing. The C, Mg and Nb foils are placed on the third target ladder just in front of the entrance of the recoil separator. The two ZnS detectors are marked with red arrows.

units of Gauss. In order to maintain the magnet on the same hysteresis curve, its current was set to 80% of the maximum value at the beginning of each measurement. From that starting point, the current was decreased once by a large step of 30-40% to reach the approximate  $B\rho$  values where the charge states are expected to be observed. Then the current was further decreased in smaller steps of 0.2% ( $\approx 25 \text{ Gs}$ ) to scan over the charge states and observe the count rates in the ZnS detectors. It was also taken into account that the magnet requires some time to reach its equilibrium magnetic field value after changing its current. For example, the magnetic field value would stabilize after around 20 seconds for a step of 0.2% in current, but it required at least a few minutes for the reset back to 80% current at the end of a scan before starting the next one.

For the first beam setting -  $^{48}\text{Ti}^{13+}$  at an energy of 418 MeV, the current of the dipole was modified manually and the corresponding magnetic field strength at each step was written down by hand. The manual controls led to some mistakes for parts of some measurements e.g. increasing the current slightly and then continuing the measurement without resetting back to 80% current. Such mistakes made parts of the scans unusable in the analysis. Towards the end of the scans for the first beam setting the control system of the dipole magnet was upgraded so that it would sample the magnetic field value around twice per second. The reading would then be sent to the DAQ system to be recorded with the rest of the data stream and with the

appropriate timestamp.

Overall, there were 13 scans performed during the first beam setting - one scan of the incoming beam and three scans for each studied material (C, Mg, Nb, Ta) with different degrader foils. A full list of the performed scans for this beam setting is given in Table 3.1. It was observed that the angular spread introduced by using the 5.4 mg/cm<sup>2</sup> Ta degrader was already large enough for neighboring charge states to overlap. Therefore the Ta degraders on the target wheel thicker than 5.4 mg/cm<sup>2</sup> were not used in any of the measurements.

**Table 3.1:** A list of all degrader-foil combinations scanned manually with the 418 MeV <sup>48</sup>Ti<sup>13+</sup> beam setting.

Degrader-foil combination				Studied material
N <sup>o</sup>	Second target ladder Ta, mg/cm <sup>2</sup>	Target wheel Ta, mg/cm <sup>2</sup>	Third target ladder C/Mg/Nb, mg/cm <sup>2</sup>	
0	-	-	-	Beam scan
1	0.45	-	-	Ta
2	0.45	3.6	-	Ta
3	0.45	5.4	-	Ta
4	0.45	-	1.48	Nb
5	0.45	3.6	1.48	Nb
6	0.45	5.4	1.48	Nb
7	0.45	-	0.87	Mg
8	0.45	3.6	0.87	Mg
9	0.45	5.4	0.87	Mg
10	0.45	-	0.1	C
11	0.45	3.6	0.1	C
12	0.45	5.4	0.1	C

During these measurements it was observed that the positions of some of the scanned charge states were shifted with respect to the expected  $B\rho$  values. The reason for these unexplained shifts became apparent during the scans in the second beam setting after another upgrade of the dipole magnet control system allowed it to be run automatically using a Python script.

The second beam setting utilized <sup>48</sup>Ti<sup>12+</sup> ions at an energy of 340 MeV. After the addition of automatic scanning, all scans in this beam setting were performed by measuring a dipole current range of 14% in steps of 0.2% for 60 seconds per step. This revealed the origin of the observed shifted charge states to be a contamination in the beam - two distinct charge state distributions were discerned. The contamination was considered to be another ion with the same  $A/Q = 4$  value such as <sup>16</sup>O<sup>4+</sup> or <sup>40</sup>Ca<sup>10+</sup>, which have been observed as contaminants in previous experiments at JYFL.

A total of nine scans were performed with the second beam setting and a detailed list is shown in Table 3.2. Some scans performed in the first beam setting were not repeated for the second beam setting due to lack of time.

After the end of the measurement an automatic scan of the magnetic field values was done from 80% to 0% current in steps of 0.2% to be used as calibration in the data analysis.

### 3.2.3 Analysis

The data obtained during the second beam setting at 340 MeV were much more detailed due to the automatic scanning and were therefore analysed first.

**Table 3.2:** A list of all degrader-foil combinations scanned automatically with the 340 MeV  $^{48}\text{Ti}^{12+}$  beam setting. All of the scans were performed with steps of 0.2% current with the exception of the direct beam scan, where a 0.1% step was used.

Degrader-foil combination				Studied material
N <sup>o</sup>	Second target ladder Ta, mg/cm <sup>2</sup>	Target wheel Ta, mg/cm <sup>2</sup>	Third target ladder C/Mg/Nb, mg/cm <sup>2</sup>	
13	0.45	-	-	Ta
14	0.45	3.6	-	Ta
15	0.45	5.4	-	Ta
16	0.45	-	1.48	Nb
17	0.45	3.6	1.48	Nb
18	0.45	5.4	1.48	Nb
19	0.45	3.6	0.1	C
20	0.45	5.4	0.1	C
21	-	-	-	Beam scan

The simplest charge-state distribution measurement performed was the scan of the incoming beam with no foils. Two charge states were observed in the scanned range of  $B\rho$  values. However, none of them were at the expected position in  $B\rho$  for a  $^{48}\text{Ti}^{12+}$  beam at 340 MeV. The intensity of one of the charge states was much higher and was therefore assigned as the  $^{48}\text{Ti}^{12+}$ . The other charge state was assigned as the  $^{48}\text{Ti}^{13+}$ , resulting from collisions with residual gas in RITU. Based on these assignments a calibration factor of  $\approx 1.07$  was determined for the magnetic field of the dipole magnet. These assignments and the calibration factor were both confirmed in the course of the data analysis. All magnetic field values quoted in the analysis are already corrected with this factor.

The first charge-state measurement in the automatic regime was performed using the 0.45 mg/cm<sup>2</sup> Ta foil. In this measurement the beam passes through the least amount of material and the exiting ions have the least amount of angular straggling leading to well defined charge states in the ZnS spectra. The count rates of one of the ZnS detectors in the focal plane obtained in this measurement are shown in Fig. 3.5.

The observed charge states belong to two separate charge-state distributions and each charge state has been assigned to one of these distributions based on the comparison between the count rates in two of the ZnS detectors at the focal plane. The comparison between the count rates of the most forward and backward ZnS detectors in the focal plane is presented in Fig. 3.6. It shows that some of the charge states have enhanced count rates in the detector at 75°, compared to those in the detector at 105°.

A confirmation of these assignments to the two charge-state distributions comes from the maximum energy deposited in any of the ZnS detectors, as shown in Fig. 3.7. As follows from Eq. (3.2), an ionic species with heavier mass would have higher kinetic energy. Therefore if one of the ions has higher  $A$ , it would explain both the enhanced intensity at forward angles and the higher deposited energy in the ZnS detectors for the respective charge states.

The next step in the analysis is to identify the two ionic species present in the beam and assign them to their corresponding charge-state distribution. This could easily have been accomplished with a single HPGe detector at the focal plane to register  $\gamma$  rays following the Coulomb excitation of the beam ions on the thick Au foil. However, with no spectroscopic information from  $\gamma$  rays, this can only be achieved through the energy losses of the ions in the Ta degraders and the studied target materials as they depend on the  $Z$  of the ions.

The  $B\rho$  value at which a given charge state  $Q$  is observed in the ZnS detector is directly

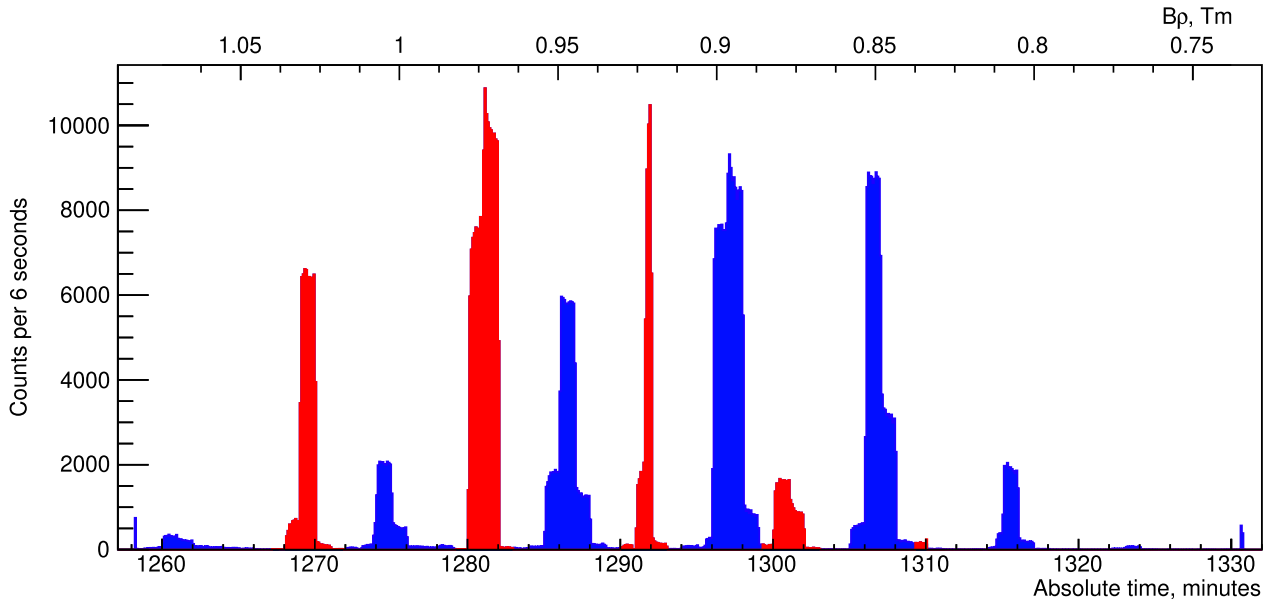


**Figure 3.5:** Count rates in Detector 1 ( $105^\circ$ ) after the  $0.45 \text{ mg/cm}^2$  Ta foil as a function of time (bottom X axis) and magnetic rigidity (top X axis). The charge states from the two distinct charge state distributions are colored in red and blue. The comparatively narrower peak at the 1292 minutes is due to a Faraday cup being inserted into the beam line by the beam operator. This temporarily decreases the intensity of the beam reaching the target chamber. The two small, sharp peaks on the two ends of the spectrum are artifacts of a large change of the dipole magnet current in a short time. The left-most peak results from the initial drop from 80% current to the starting value of the scan. One or more charge states were above the scanned range of  $B\rho$  values and for a short duration the corresponding ions were able to pass through the dipole magnet and reach the ZnS detectors. The right-most peak is from the increase of the current when it is reset back to 80% and passes rapidly through all scanned charge states in reverse.

related to the kinetic energy  $T$  of the ion through the equation

$$B\rho = \frac{mv}{Q} = \frac{\sqrt{2Tm}}{Q}, \quad (3.4)$$

where  $m$  and  $v$  are the mass and velocity of the ion. All ions have approximately the same kinetic energy after exiting the set of degraders and foils and entering the dipole magnet, independent of their charge state. Therefore, if we consider Eq. (3.4) for two neighboring charge states  $Q_1$  and  $Q_2$ ,  $Q_1 = Q_2 - 1$ , taking the ratio of the left and right sides of the equations would result in the following relation:

$$\frac{B_1}{B_2} = \frac{Q_2}{Q_1} = \frac{Q_2}{Q_2 - 1}, \quad (3.5)$$

where  $B_1$  and  $B_2$  are the magnetic field values of the dipole magnet at which the corresponding charge states are observed in the ZnS detectors. From Eq. (3.5) the charge state  $Q_2$  can be extracted using experimentally determined magnetic field values for the two charge states. This procedure can be taken a step further to increase its precision by taking Eq. (3.5) for the next pair of charge states -  $Q_2$  and  $Q_3$ ,  $Q_3 = Q_2 + 1$ . The combination of the resulting equation and Eq. (3.5) can be solved for  $Q_2$  to yield:

$$Q_2 = \frac{B_1 + B_3}{B_1 - B_3}. \quad (3.6)$$

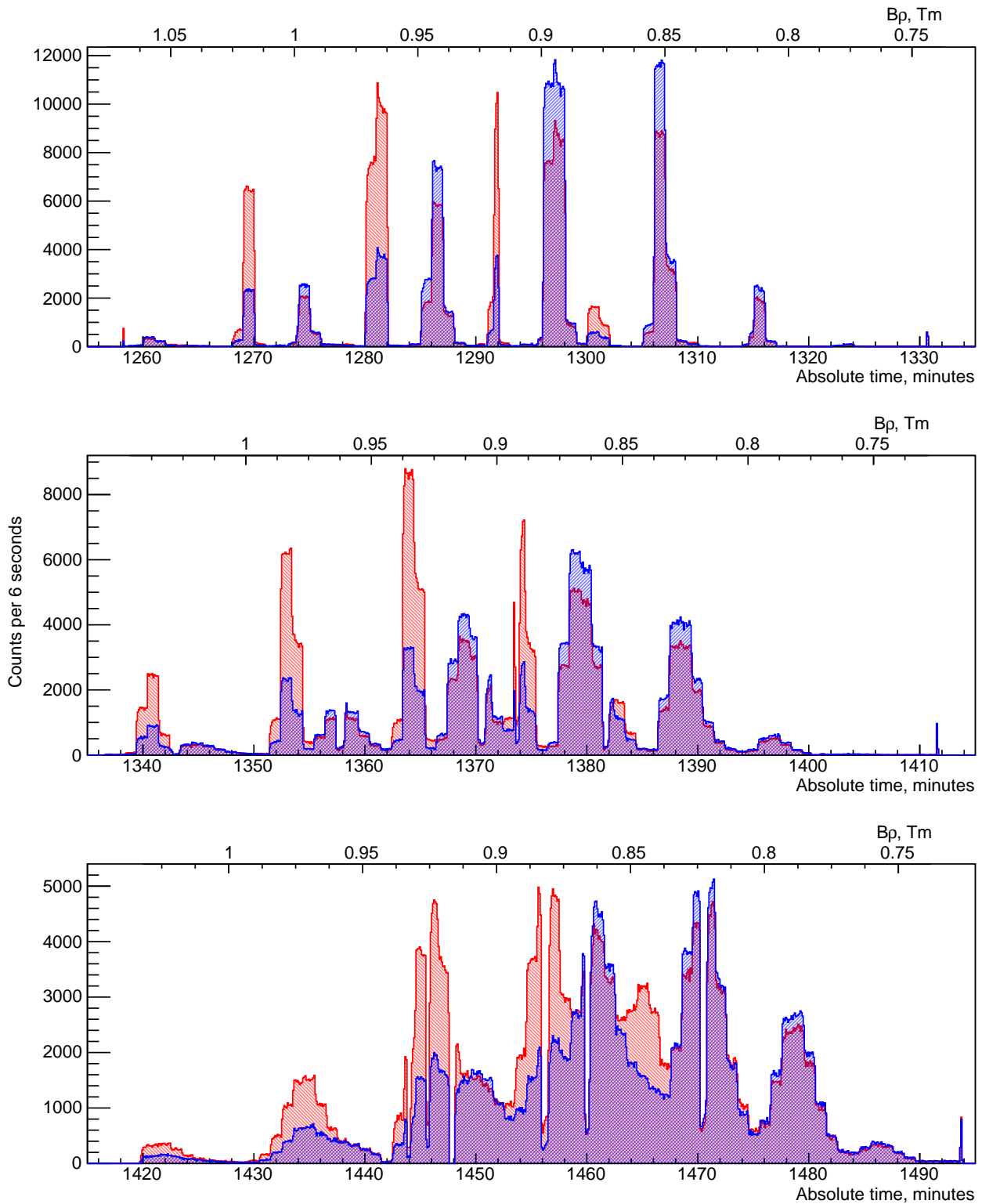


**Figure 3.6:** Count rates in the ZnS detectors at  $75^\circ$  (red) and  $105^\circ$  (blue) after the three Ta degrader combinations. The overall intensity of the two distributions at forward angles is almost the same. At backward angles one of the distributions has its intensity significantly suppressed, while the other distribution is slightly enhanced. The thicker Ta degraders introduce significant angular straggling of the ions leading to overlap between the charge states of the two distributions.

Using Eq. (3.6) the charge states of most of the observed peaks in the ZnS spectra can be calculated from the magnetic field values of the neighboring two peaks from the same charge-state distribution. In the case of the first and last peaks in the ZnS spectra for each distribution

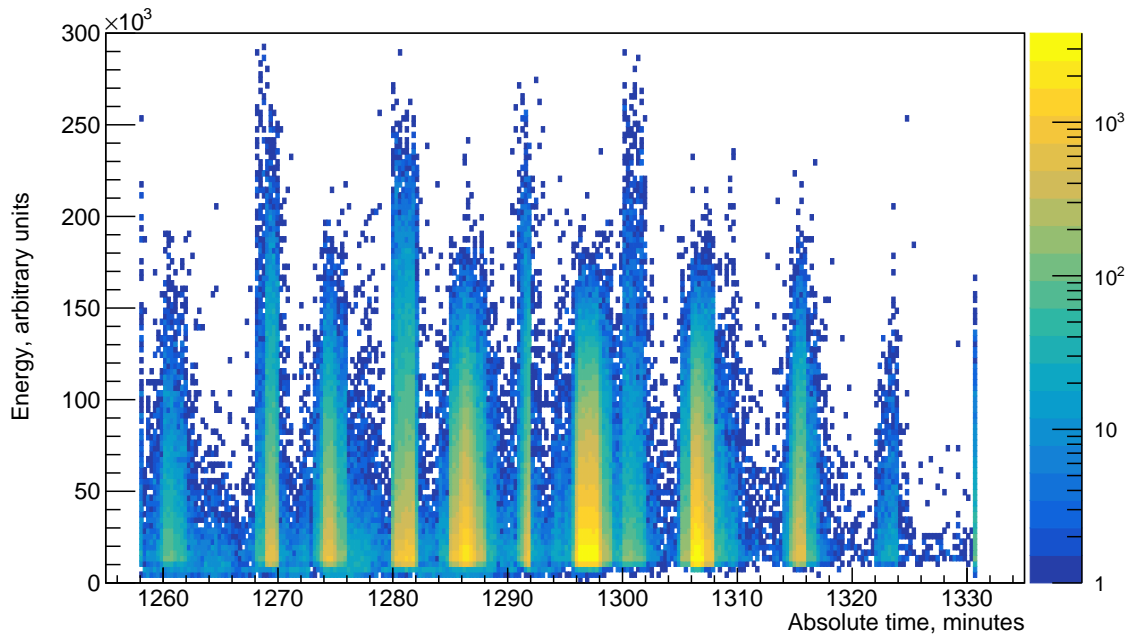


**Figure 3.7:** The uncalibrated energy deposited by the scattered ions in the ZnS detector at  $75^\circ$ . It is visible that the maximum deposited energy is different for the charge states of the two distributions yet remains relatively constant for all charge states of the same charge-state distribution.

Eq. (3.5) has to be used instead.

The equilibrium magnetic field values are extracted from a 2D matrix, a detail of which is shown in Fig. 3.8. Although each step in magnetic field is  $\approx 25$  Gs, some information can also be obtained from the first 15-20 seconds before the field has stabilized to its new value. If the actual peak of the scanned charge state happens to correspond to a magnetic field value in the dynamic region of a step, it results in a very narrow spike in the count rates. Two examples of this behaviour can be seen in two of the higher-intensity peaks in Fig. 3.5. This type of occurrence provides sub-25-Gs accuracy on the extracted magnetic field value.

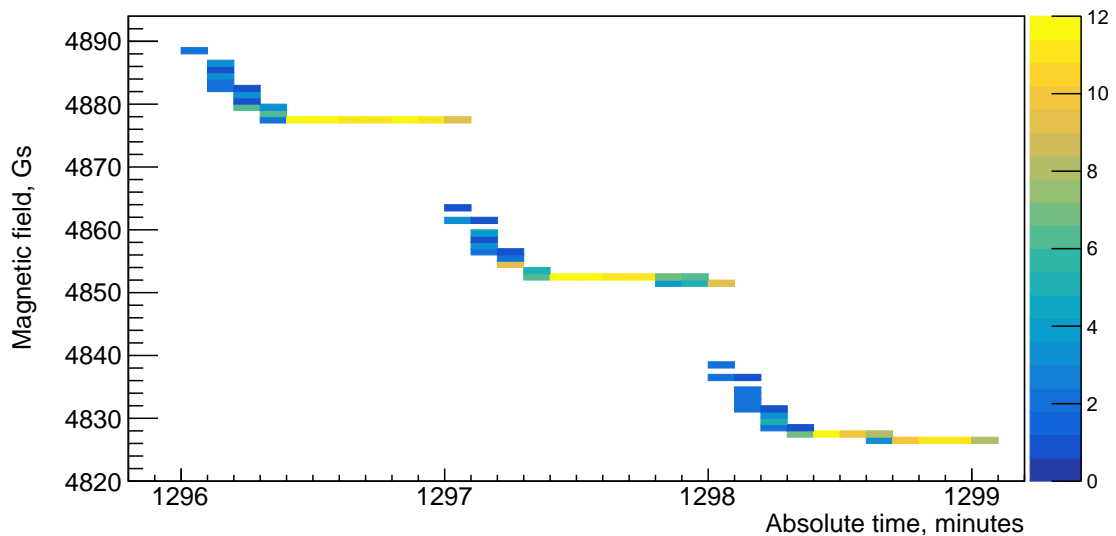


**Figure 3.8:** The magnetic field as a function of absolute run time showing the steps of  $\approx 25$  Gs. The binning on the X axis is set to six seconds per bin to correspond exactly to the time-binning in the count rate spectra (Fig. 3.5). The value on the Z axis is the number of times the dipole magnet control system has sent the given magnetic field value.

After the magnetic field values corresponding to each charge have been extracted a comparison can be made between the expected values and the calculated ones. The highest observed charge states for both distributions in Fig. 3.5 is  $Q = 22$ , which could correspond to a fully stripped  $^{48}\text{Ti}^{22+}$  ion. Therefore the assignments of the charge states from the measurement with the  $0.45 \text{ mg/cm}^2$  Ta degrader are still not enough to distinguish which charge-state distribution belongs to  $^{48}\text{Ti}$  and which - to the contaminant species. Still, these charge-state assignments significantly reduce the list of possible contaminant species. The most probable candidates with the same  $A/Q$  value were considered to be  $^{16}\text{O}^{4+}$ ,  $^{36}\text{Ar}^{9+}$  or  $^{40}\text{Ca}^{10+}$ , based on previous experiments at RITU. However, none of these ions can reach a charge state of 22 and therefore cannot be the observed contaminant species. An  $A/Q$  value of 4 is not achievable for any other stable Ti isotopes ( $Z = 22$ ). This leads to the conclusion that any realistic candidates for the contaminant have to be stable isotopes with  $Z > 22$  and  $A/Q = 4$ . Isotopes that fulfil these conditions are  $^{52}\text{Cr}^{13+}$ ,  $^{56}\text{Fe}^{14+}$ ,  $^{60}\text{Ni}^{15+}$ , etc. These isotopes are all heavier than  $^{48}\text{Ti}$  which from Eq (3.2) requires that their kinetic energy is higher. This suggests that the charge-state distribution exhibiting lower maximum deposited energy in Fig. 3.7 belongs to the Ti ions.

The only way to definitively identify the ionic species producing the observed charge-state distributions is through the energy losses of the ions passing through the different foils. The energy losses depend on the atomic number of both the beam and the foil material, as well as on the energy of the beam particles. They can be estimated with LISE++ using the energy loss model of Ziegler *et al.* [110] and the known thickness of each foil. The expected magnetic field value for each charge state can then be calculated using the exit energy of the ions and Eq. (3.4).

The same procedure of extracting the magnetic field values and determining the charge state of each peak was applied to all measurements from this beam setting. The charge states were separated in two data sets based on which ionic species they belong to as shown in Fig. 3.6. Then, the experimentally obtained  $B$  values for both data sets were compared to the ones calculated for  $^{48}\text{Ti}^{12+}$  ions. The initial energy of the Ti beam was varied in reasonable limits around the expected 340-MeV value. At an initial energy of 342 MeV a good agreement was reached with the data set corresponding to the lower maximum deposited energy in Fig. 3.7. The comparison between experimental and calculated magnetic field values is shown in Fig. 3.9. The contaminant ionic species was found to be  $^{52}\text{Cr}^{13+}$  at an energy of  $\approx 372$  MeV following the same procedure for the second data set of charge states.

Note that the thickness of the  $5.4 \text{ mg/cm}^2$  Ta degrader had to be significantly modified. The difference between the calculated and expected  $B$  values for the three measurements utilizing this degrader were in the order of hundreds of Gs yet in agreement with each other. Therefore the assumed thickness of the foil was deemed not correct and was increased to  $8.3 \text{ mg/cm}^2$  to reach good agreement with the calculations.

The measurements from the first beam setting were analyzed following an identical procedure. Reasonable agreement between the calculated and experimental magnetic field values was obtained for  $^{48}\text{Ti}^{13+}$  ions at an energy of 424 MeV, as shown in Fig. 3.10. The thickness of all foils and degraders was kept the same as for the 342 MeV Ti ions for consistency.

A large discrepancy is visible in Fig. 3.10 for the data points from the  $0.45 \text{ mg/cm}^2$  Ta measurement. This is due to the measurement being the first to be performed, before any contamination was identified and before the calibration factor of the magnetic field was determined. In this measurement only a single scan per charge state was made based on the calculations for their expected positions in  $B\rho$  value. Therefore the scanned  $B\rho$  values did not correspond to the peaks of the expected charge states. Nevertheless, from comparisons such as Fig. 3.6 and Fig. 3.7 it was confirmed that these charge states are produced by the Ti ions.

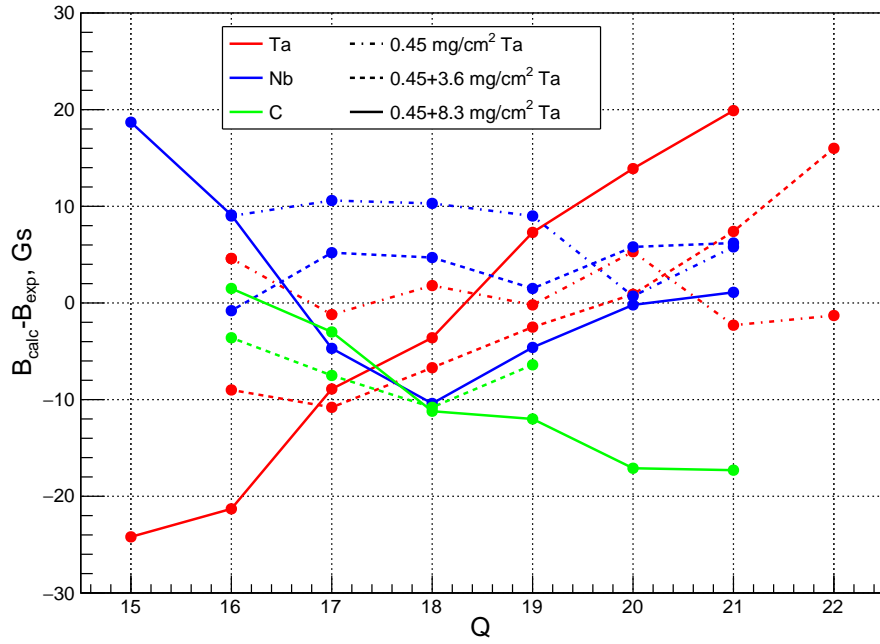


**Figure 3.9:** Difference between the calculated and experimentally obtained magnetic field values for all charge states of  $^{48}\text{Ti}^{12+}$  ions at 342 MeV. The combination of Ta degraders used is denoted by the different line styles. The uncertainty of each data point is  $\approx 13$  Gs and the error bars have been omitted for visibility. Most data points are in agreement with zero within their uncertainty. The largest deviations from zero are present in the measurements with the thickest Ta degrader combination. This is attributed to the overlap between charge states, as shown in Fig 3.6, leading to imprecise determination of the peak position.

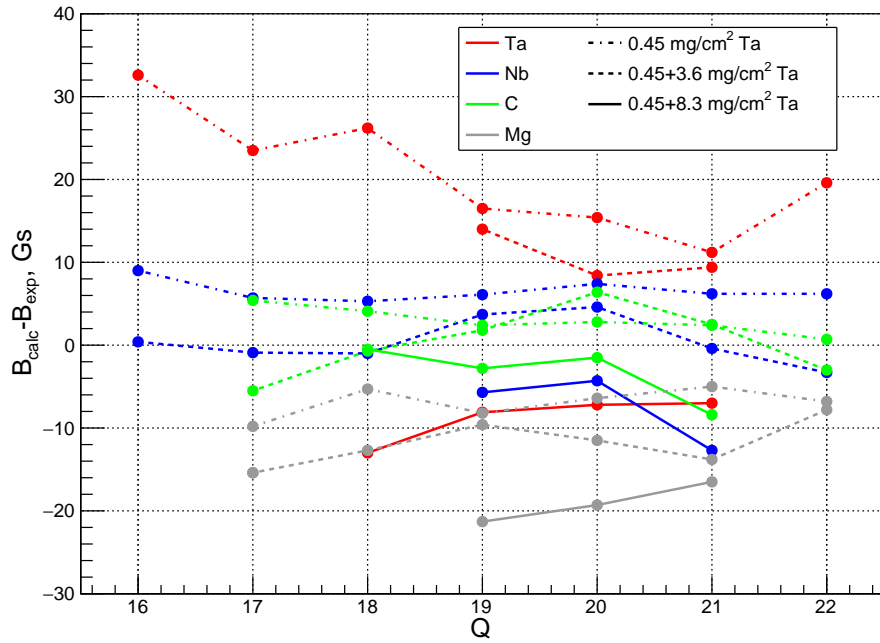


**Figure 3.10:** Difference between the calculated and experimentally obtained magnetic field values for all charge states of the  $^{48}\text{Ti}^{13+}$  ions at 424 MeV. The uncertainty of each data point is  $\approx 13$  Gs and the error bars have been omitted for visibility. All data points from the Mg measurement seem to be systematically below zero, which could indicate that the foil was slightly thicker than expected.

In addition, the observed count rates in the ZnS detectors should be proportional to the count rates at the center of the corresponding charge states. This means that the count rates can be still used to extract a charge-state distribution from this measurement.

After the charge-state distributions of  $^{48}\text{Ti}$  were identified the fraction of Li-like ions were extracted. The shape of the charge-state distribution can usually be described by a normal distribution, as used in the parametrizations of Nikolaev-Dmitriev [111] and Schiwietz-Grande [85]. However, close to atomic shell closures and especially around the extreme cases of fully-stripped ions or neutral atoms the distribution is skewed. Then, the charge-state distribution is better described by a skew-normal distribution.

The probability density function (PDF) of a skew-normal distribution is defined as:

$$f(x) = 2\phi(x)\Phi(\alpha x), \quad (3.7)$$

where  $\alpha$  is the shape parameter,  $\phi(x)$  is the PDF of a standard normal distribution:

$$\phi(x) = \frac{1}{\sqrt{2\pi}}e^{-\frac{x^2}{2}} \quad (3.8)$$

and  $\Phi(x)$  is its corresponding cumulative density distribution:

$$\Phi(x) = \int_{-\infty}^x \phi(t)dt = \frac{1}{2} \left[ 1 + \operatorname{erf} \left( \frac{x}{\sqrt{2}} \right) \right]. \quad (3.9)$$

Here  $\operatorname{erf}(x)$  denotes the Gaussian error function, which can only be evaluated through numerical algorithms.

The shape parameter  $\alpha$  in Eq. (3.7) qualitatively describes the skewness of the distribution. A value of  $\alpha < 0$  and  $\alpha > 0$  results in a left-skewed and right-skewed distribution, respectively, while  $\alpha = 0$  is equivalent to a normal distribution. Usually two more parameters - the location  $\xi$  and scale  $\omega$ , are introduced through the substitution  $x \rightarrow (x - \xi)/\omega$ , leading to the final expression for the skew-normal distribution PDF:

$$f(x) = \frac{2}{\omega} \phi \left( \frac{x - \xi}{\omega} \right) \Phi \left( \alpha \frac{x - \xi}{\omega} \right). \quad (3.10)$$

A C++/ROOT macro was prepared to fit all obtained charge-state distributions using Eq. (3.10). However, for most charge-state distributions from the current measurement some charge states with significant fractions of the total intensity were outside of the scanned  $B\rho$  ranges. Therefore the measured intensities could not be normalized and in order to take this into account an amplitude parameter  $A$  was included in the fitting function. The use of four fit parameters excludes the possibility to extract the Li-like fraction from charge-state distributions with less than four experimental points. This requirement lead to a total of 16 fitted charge-state distributions out of a total of 20 scanned, not considering the two scans of the incoming beam. A comparison of the obtained fits for the charge-state distributions of Ta and Nb foils is shown in Fig. 3.11. The fit results for all charge-state distributions are presented in Table 3.3.

The fractions of Li-like  $^{48}\text{Ti}$  ions are then plotted as a function of the exit energy of the ions in Fig. 3.12.

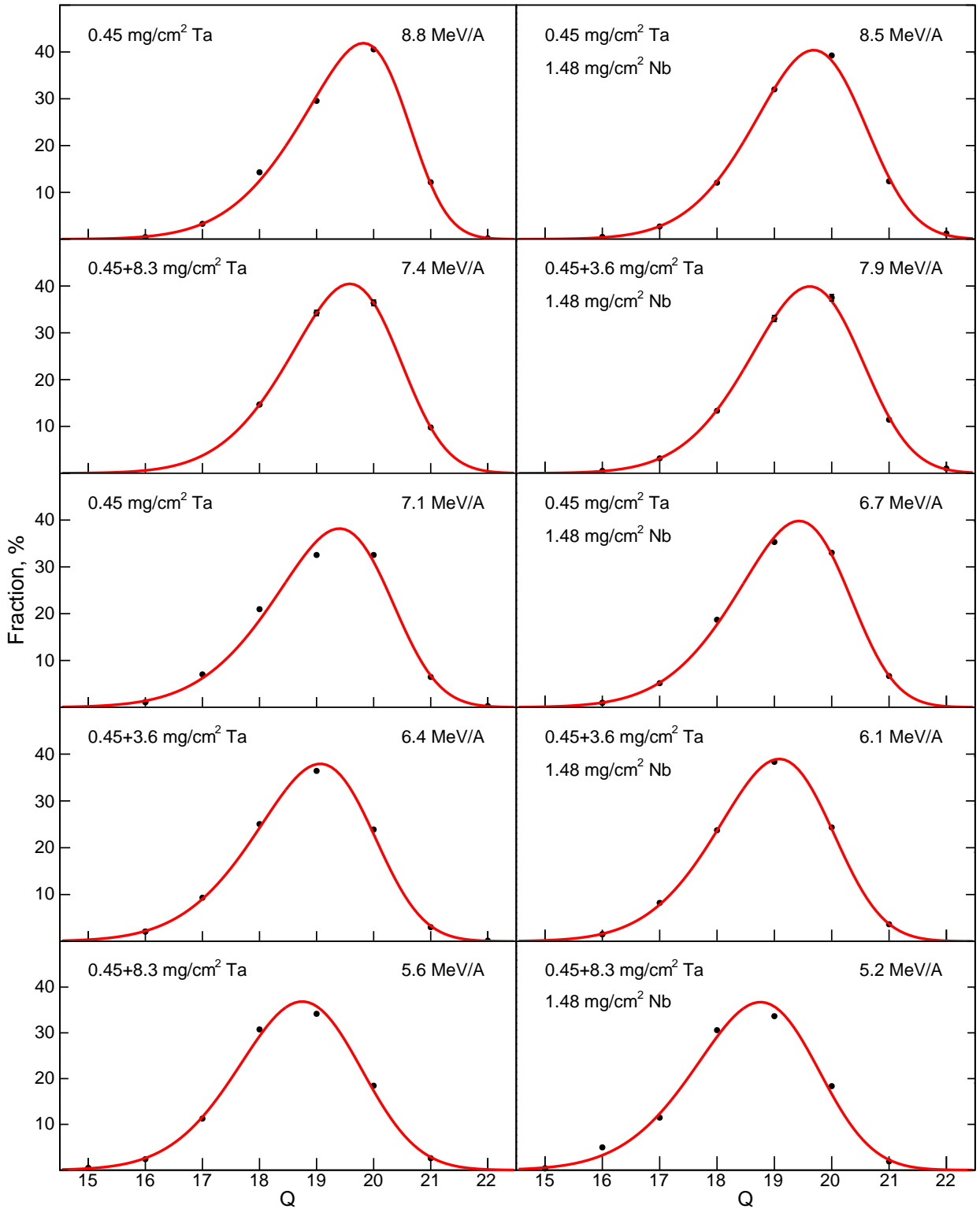


**Figure 3.11:** Comparison between the fitted charge-state distributions from all Ta foil (left) and Nb foil (right) measurements. The maximum of the distribution visibly shifts to lower charge states as the exit energy of the ions decreases.

**Table 3.3:** Summary of the results for all fitted charge-state distributions. The measurements marked by an asterisk contained only four charge states, the same as the number of parameters in the fit function.

Beam energy MeV	$N_e$	Studied material	$\alpha$	$\xi$	$\omega$	$A$ $10^3$	Q=19 %
418	1	Ta	-2.60(6)	20.58(1)	1.52(1)	25.9(2)	30.6(3)
	3*	Ta	-1.93(16)	20.36(4)	1.45(4)	10.2(1)	34.3(6)
	4	Nb	-1.70(6)	20.44(2)	1.40(2)	16.6(1)	32.2(4)
	5	Nb	-1.66(9)	20.38(3)	1.41(2)	7.9(1)	33.2(5)
	7	C	-0.57(10)	20.54(6)	0.94(2)	32.4(2)	18.2(20)
	8	C	-0.85(11)	20.66(5)	1.01(3)	9.5(1)	18.9(4)
	9*	C	-2.08(26)	20.86(3)	1.19(2)	15.9(1)	19.9(4)
	10	Mg	-0.93(5)	20.55(2)	1.23(2)	34.9(2)	19.5(2)
340	11	Mg	-1.26(6)	20.84(3)	1.28(2)	20.5(1)	21.5(3)
	13	Ta	-2.12(5)	20.23(1)	1.58(1)	26.3(2)	35.5(2)
	14	Ta	-1.94(7)	19.89(2)	1.55(2)	17.2(1)	37.9(3)
	15	Ta	-1.29(7)	19.51(3)	1.42(2)	14.6(1)	35.8(4)
	16	Nb	-2.04(6)	20.22(1)	1.50(1)	26.2(2)	36.3(3)
	17	Nb	-1.72(7)	19.87(2)	1.46(2)	16.4(1)	38.8(4)
	18	Nb	-1.61(7)	19.58(3)	1.52(2)	13.1(1)	35.7(4)
	20	C	-1.93(11)	20.55(2)	1.44(2)	13.8(1)	30.4(4)

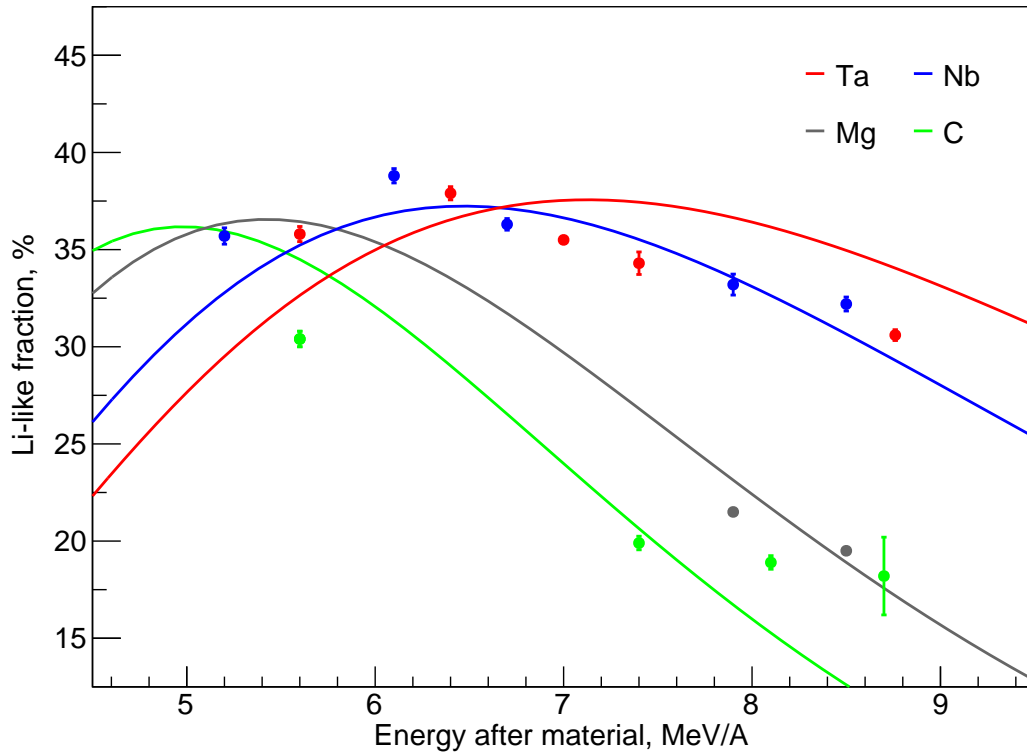


**Figure 3.12:** Comparison between experimentally obtained fraction of Li-like ions and the predictions from the Schiwietz-Grande model in LISE++.

### 3.2.4 Discussion

The main goal of the charge-state measurement was to obtain the energy dependence of the Li-like fraction of Ti ions after different materials, shown in Fig. 3.12. The comparison with the Schiwietz-Grande model predictions shows that there is quantitative and qualitative agreement with the experimental data for Nb. For Ta the agreement is only qualitative as the peak of the experimental points seems to be shifted to lower energies compared to the predicted position. There seems to be some agreement also for Mg, however, that is difficult to be determined based on only two data points. The C data points show significant deviations from the expected behaviour. Similar conclusions were drawn from the comparison to other available charge-state distribution models provided by LISE++. They have been omitted from Fig. 3.12 for clarity as they do not contribute any further insight. Based on the results in Fig. 3.12, it was deemed that a combination of Nb and Ta foils would be used in the  $^{46}\text{Ti}$  TDRIV g-factor measurement. An energy of the scattered  $^{46}\text{Ti}$  particles of about 6 MeV/A after the Nb or Ta target would produce the largest possible fraction of Li-like ions. Nevertheless, the kinetic energy of the ions also has some implications on its electron configuration that have to be taken into account.

The ground-state electron configuration of a Li-like Ti ion is  $1s_{1/2}^2 2s_{1/2}^1$  and the strength of the corresponding hyperfine field can be precisely calculated via Eq. (1.86). This in turn defines the frequency of precession of the total spin  $F$  that should be observed experimentally. However, it is possible that the Li-like ions are produced in an excited atomic state with a different electron configuration. That would result in a different hyperfine field and precession frequency. The experimental signature in the TDRIV method is essentially a weighted average of all contributing precession frequencies. Therefore the relative populations of the electron configurations and their corresponding frequencies can result in either a constructive or a destructive interference. It is necessary to consider what excited atomic states are expected to contribute to the observed signal and to take measures to reduce unwanted frequencies.

Calculations of the excited atomic states of Li-like ions and their properties were performed by Dr. Brendan McCormick (ANU) using the GRASP2018 software package. The results of the calculations for the first few excited states of Li-like Ti ions are presented in Table 3.4. The half-life of the first  $2^+$  state in  $^{46}\text{Ti}$  is 5.3(2) ps [112], hence the contributions from the short-lived higher-lying atomic states ( $3s_{1/2}^1, 3p_{1/2}^1$ ) would be negligible. Only the contributions from the atomic ground state ( $2s_{1/2}^1$ ) and the first two excited states ( $2p_{1/2}^1, 2p_{3/2}^1$ ) will impact the g-factor measurement. In addition, the half-lives of the first two excited atomic states are much longer than the half-life of the  $2^+$  nuclear state. This excludes any possibility of atomic transitions occurring before the nuclear state has decayed. Therefore the relative populations of each electron configuration will be constant throughout the flight time of the ions.

**Table 3.4:** Results of GRASP2018 calculations for the first few excited states of Li-like Ti ions.

Excitation energy eV	Electron configuration	$T_{1/2}$ ps	$B_{HF}$ kT
0	$1s_{1/2}^2 2s_{1/2}^1$	-	20.61
40.5	$1s_{1/2}^2 2p_{1/2}^1$	420.4	6.41
48.2	$1s_{1/2}^2 2p_{3/2}^1$	250.4	3.20
801.6	$1s_{1/2}^2 3s_{1/2}^1$	0.5	5.98

It has been shown in previous studies of H-like ions [113] and Na-like ions [114] that the electron configuration of the ions after passing through a foil heavily depends on their kinetic energy. Both studies compare the population of excited atomic states for two different exit

energies of the ion. They consider ions with an exit energy above and below the empirically known exit energy that maximizes the desired charge state. Their findings indicate that if the energy of the ions after the material is below the energy of the maximum, the atomic ground state is practically not populated. In that case all recoiling ions are initially in an excited atomic state. Contrary, if the exit energy is above that of the maximum for a given charge state, the population of excited atomic states is suppressed and most ions are in the atomic ground state. Therefore, the  $^{46}\text{Ti}$  TDRIV g-factor measurement would require that the energy of the ions scattered from the target foil towards the particle detector is higher than 6 MeV/A. An energy of the scattered ions around 7 MeV/A is envisaged. This is expected to optimize the population of Li-like ions in the atomic ground state and reduce the contribution from excited states.

The relative populations of the atomic excited states can be estimated using the Boltzmann distribution. This approach was first proposed by Stuchbery [34] based on RIV analysis of Ge isotopes. It was later applied by McCormick [23] in the TDRIV analysis of  $g(2_1^+)$  in  $^{56}\text{Fe}$ . In the case of atomic excited states, the probability for a state with an energy  $\varepsilon_k$  to be populated is given by the Boltzmann distribution as

$$p_k = \frac{1}{Q} e^{-\varepsilon_k/T}. \quad (3.11)$$

Here  $T$  is a parameter that functions as the temperature of the system. The value of  $T \approx 25$  eV was found to agree well with the experimental data for Ge isotopes [34], and for  $^{56}\text{Fe}$  [23]. The normalization factor  $Q$  is given by

$$Q = \sum_{i=1}^N e^{-\varepsilon_i/T}. \quad (3.12)$$

A Monte Carlo simulation of the population of excited atomic states during the TDRIV measurement of  $^{46}\text{Ti}$  can be performed using the RIVSimulate software package [23]. Some of the relevant input parameters are the lifetime of the  $2_1^+$  state, the probability distribution to be used, the fraction of each ionic species and the corresponding GRASP2018 files. These files contain the information of their atomic state structure - spin and parity, excitation energy, decay transitions, etc. Performing the Monte Carlo simulation for the Li-like ions with the Boltzmann distribution for the energies relevant to the current measurement yields relative populations of approximately 75%, 15% and 10% for the atomic ground state, the  $2p_{1/2}^1$  and the  $2p_{3/2}^1$ , respectively. These fractions will be used in the simulations below.

Similar considerations apply for the neighboring charge states as well. According to the Schiwietz-Grande simulations in LISE++, the highest fraction of Be-like ions would be achieved at exit energies of  $\approx 4.5$  MeV/A. Thus at exit energies around 7 MeV/A mostly their atomic ground-state configuration would be populated. From the experimentally measured charge-state distributions, the total fraction of Be-like ions is between 15% and 20%, depending on the exact energy and foil material. However, the Be-like ground-state configuration has a spin of  $J = 0$  and will not contribute to the observed oscillations. In fact, the first excited state of Be-like ions is also a  $J = 0$  state. According to the Boltzmann distribution up to 72% of the Be-like ions will therefore not be relevant for the TDRIV measurement. The higher-lying excited states that account for the other 28% of Be-like ions have non-zero spins. Nevertheless, only two of them have hyperfine fields that could result in an observable frequency within the time frame of the nuclear decay. They represent only 13% and 3% of the Be-like fraction, which corresponds to at most 2.5% and 0.5% of the total number of Ti ions. The former excited state

will be included in the simulations below, while the contribution of the latter is considered to be negligible.

Going further to B-like ions, again mostly the ground state configuration will be populated. Due to the small overall percentage and the expected lower hyperfine fields the B-like ions are not included in the simulations at this time.

The situation for He-like and H-like ions is reversed - the intended exit energy of 7 MeV/A lies below the maximum of the distribution for these charge states. Therefore predominantly the excited atomic states would be populated. However, the GRASP2018 calculations for He-like ions show that the excited states are not expected to be relevant. This is interpreted as being due to the closed-shell nature of the He-like ground state. A large amount of energy is needed to break up the  $2s_{1/2}^2$  electron pair and if the electron pair is broken, the higher-lying electron could easily be stripped, resulting in a H-like ion. Therefore all of the He-like ions are predicted to be in their atomic ground state. As already discussed, the He-like ground state will not contribute any frequency to the  $R(t)$  function as its atomic spin is  $J = 0$ .

Regarding the H-like ions, the GRASP2018 calculations indicate up to four electron configurations that could be populated. As mentioned above, the excited H-like states are expected to be populated more than the atomic ground state. Therefore the Boltzmann distribution is not applicable in the H-like case. The excitation energies of the three excited configurations are only several eV apart and thus a uniform distribution would be more suitable. An assumed fraction of 10% population is assigned to the atomic ground state and a 30% fraction to each of the excited states. However, two of the three excited state configurations have very short lifetimes and decay immediately to the atomic ground state. The second excited state has a longer lifetime and can influence the observed oscillations. This leads to a final population of 70% H-like ground state and 30% H-like excited state. The expected overall amount of H-like ions would be around 7% of the total number of ions from the measured charge-state distributions. Therefore the contributions of the two individual frequencies from H-like states ( $\approx 5\%$  and  $\approx 2\%$ ) would not be very significant.

### 3.3 Simulations

A set of simulations was performed with the TDRIV code to study the influence of each of the aforementioned electron configurations in the final  $R(t)$  function. The simulations were performed assuming an experimental setup consisting of HPGe detectors and the Orsay Particle Scintillator Array (OPSA), described in Chapter 2.5. Two HPGe detector configurations were considered - the JUROGAM 3 array of 24 clover HPGe detectors [115] or an array of 15 co-axial HPGe detectors. Clover detectors are named after their resemblance of a four-leaf clover - they consist of four individual HPGe crystals placed in a common cryostat. Usually, BGO scintillators are placed outside the cryostat to suppress Compton-scattered  $\gamma$  rays. The co-axial HPGe detectors are individual large-volume cylindrical HPGe crystals. The original proposal for the  $^{46}\text{Ti}$  experiment intended to use the combined array of 24 clovers in two rings around  $90^\circ$  and 15 co-axial detectors at backward angles. However, the clover detectors array is a travelling array that moves between the JYFL facility and the ALTO facility of IJCLab, where it is part of the  $\nu$ -ball experimental setup [116]. Hence it is not certain whether the clover detectors would be available at JYFL for performing the experiment. In such case a simulation of the experiment relying solely on the 15 co-axial HPGe detectors was necessary to assess if the experiment would still be viable.

Another important issue that the simulations are useful for is the thickness of the degrader

that has to be used. The Doppler shift of  $\gamma$  rays emitted in flight before (“fast”) and after (“slow”) passing through a thin degrader will be very similar. In this case the “fast” and “slow”  $\gamma$  rays will not be distinguishable in the  $\gamma$ -ray spectra. Then the amplitude of the combined “total” oscillations would be reduced, as was shown in Fig. 1.7. In this regard, the 15 co-axial detectors have an advantage over the 24 clover detectors. The co-axial detectors are placed further away from  $90^\circ$  and would observe a larger Doppler shift and thus better discrimination between “fast” and “slow”  $\gamma$  rays might be possible. If the amplitude of the combined “total” oscillations is too low, a thicker degrader has to be used. Then the larger velocity difference between the two components should allow for them to be separated in the  $\gamma$ -ray spectra and to cleanly select the more sensitive “slow” component.

Regarding the implementation of OPSA in the simulation, again only the outer ring of OPSA was used in the simulations for simplicity. The array was placed at forward angles, 55 mm away from the target/degrader, leading to an angular coverage of  $19.6^\circ < \theta < 25.0^\circ$  for the outer ring.

The initial energy of the  $^{46}\text{Ti}$  beam in the simulation is 390 MeV or about 8.5 MeV/A. The target and degrader foils are similar to those used in the  $^{28}\text{Mg}$  experiment - 4 mg/cm<sup>2</sup>  $^{93}\text{Nb}$  and 1 mg/cm<sup>2</sup>  $^{181}\text{Ta}$ , respectively. The energy of the ions scattered from the target into OPSA is approximately 7 MeV/A with the previously discussed charge-state distribution. This corresponds to a velocity of  $\beta = 0.12 c$  or around 37  $\mu\text{m}/\text{ps}$ . The half-life of the  $2_1^+$  state in  $^{46}\text{Ti}$  is 5.3(2) ps [112] and for the purposes of the simulation the adopted value of the g factor of the  $2_1^+$  state was used.

First, the simulations were performed using the TDRIV analysis program for the 15 co-axial HPGe detectors. As explained in Section 2.3.2, an input file was prepared with all the particle- $\gamma$  combinations. Using the newly added subroutines, 20% of the combinations were assigned as strong and were used in the following simulations. An individual  $R(t)$  function was produced for each electron configuration that was deemed relevant for the simulations, listed in Table 3.5 assuming 50% of all ions are in this configuration. The other half of the ions are considered as fully stripped or with  $J = 0$ . The simulated ratio functions for the relevant electron configurations under these conditions are shown in Fig. 3.13.

**Table 3.5:** Electron configurations considered in the present simulations with their corresponding hyperfine fields and fractions.

Configuration	$B_{HF}$ , kT	Fraction, %
H-like g.s.	184.2	5
H-like exc.s.	23.4	2
Li-like g.s.	20.6	26
Li-like exc.s ( $2p_{1/2}$ )	6.4	6
Li-like exc.s. ( $2p_{3/2}$ )	3.2	3.5
Be-like exc.s.	11.6	2.5
Null	0	55

The H-like ground-state configuration has an extremely high frequency that will result in a sort of “jitter” on top of the Li-like ground-state oscillatory pattern. The H-like excited state has a frequency very close to that of the Li-like ground state. At shorter distances the two frequencies will be in constructive interference, however, after a few periods that will turn to destructive interference. Still, the contribution of this electron configuration is expected to be quite small (2%) and should not significantly reduce the amplitude of the oscillations. The Li-

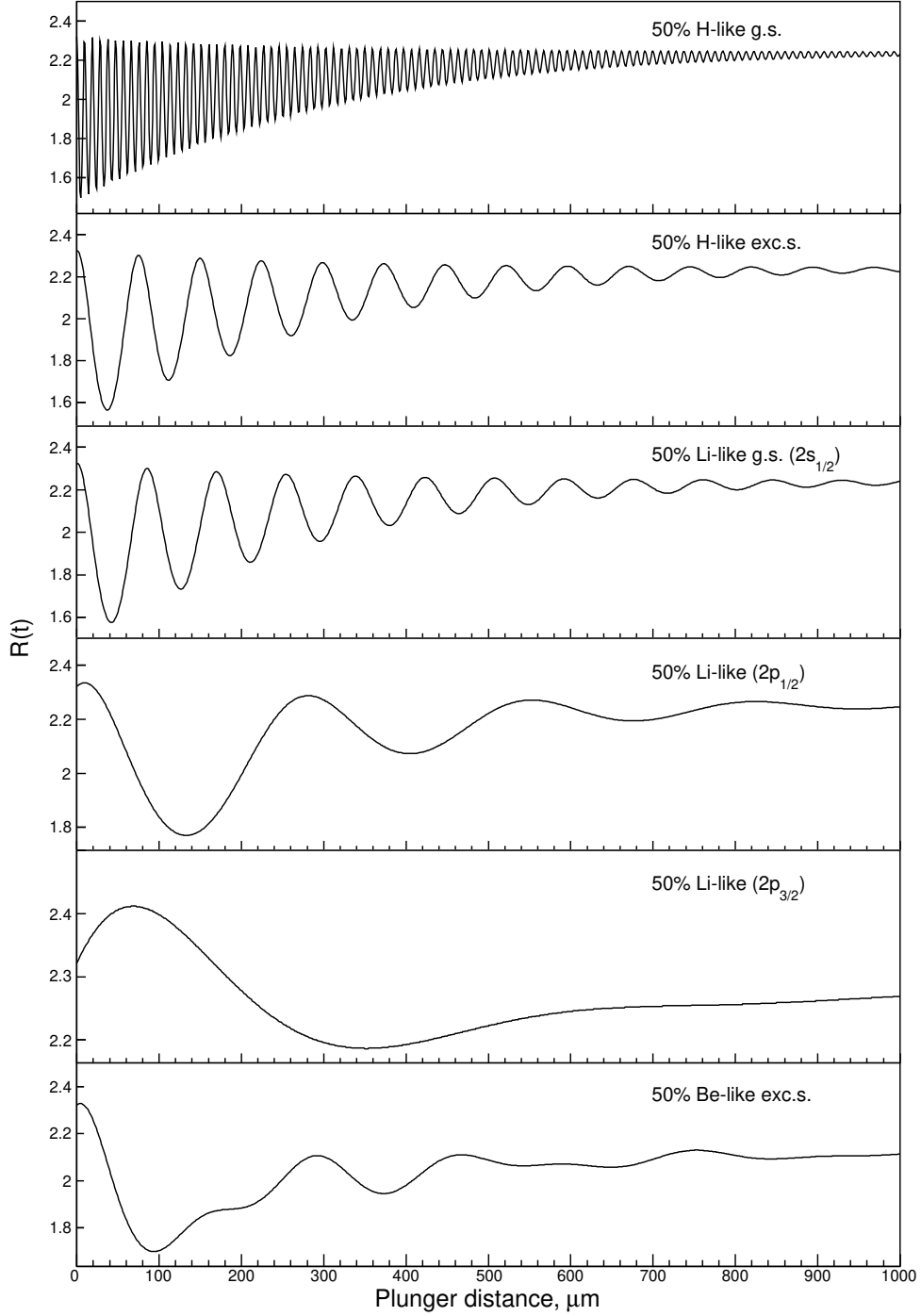


**Figure 3.13:** Simulated  $R(t)$  functions for all considered electron configurations of Ti ions as a function of plunger distance.

like  $2p_{1/2}$  excited state has a lower frequency and should slightly decrease the overall amplitude. On the other hand, the Li-like  $2p_{3/2}$  excited state has a wide maximum in the  $R(t)$  function over the first 200  $\mu\text{m}$  that can severely dampen the most sensitive part of the oscillations. If the relative population of Li-like atomic states follows the Boltzmann distribution, the  $2p_{3/2}$  state (3.5%) will not impact the observed oscillations much. Finally, the Be-like excited-state configuration is also expected to decrease the observed amplitude slightly due to its small fraction (2.5%).

The superposition of all frequencies with their relative fractions results in the  $R(t)$  function shown in Fig. 3.14 for the “slow” and “total” cases. The jitter due to the H-like ground-state

configuration is clearly visible. The observed low-frequency modulation of the maxima is due to the Li-like  $2p_{1/2}$  configuration. The effect of the other configurations with less than 5% fractions is not easily distinguishable by eye. Depending on the level of statistics in the experiment and the uncertainties of the data points, the contribution of the lesser populated configurations could be entirely negligible.

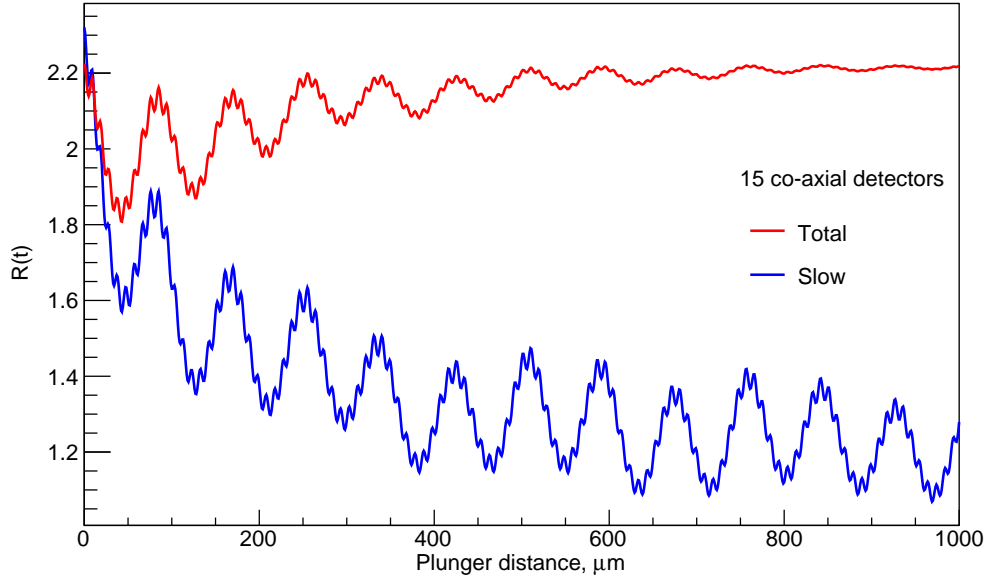


**Figure 3.14:** Simulated  $R(t)$  functions for the “slow” and “total” cases of Ti ions using 15 co-axial HPGe detectors.

Coming back to the comparison of the “slow” and “total” cases, the amplitudes of the two  $R(t)$  functions in Fig. 3.14 were measured to be 32% and 19%, respectively. These values show that while discriminating between the “fast” and “slow” peaks in the  $\gamma$ -ray spectra of the 15 co-axial detectors does provide an improvement in the amplitude, it is not necessarily needed. With appropriately chosen plunger distances at which to collect data and sufficient statistics, a precise  $g$  factor value could be extracted even without separation of the two components.

Finally, another particle- $\gamma$  combinations input file was prepared for the case of the 24 clover detectors. The resulting  $R(t)$  functions for the “slow” and “total” cases are shown in Fig. 3.15. The measured amplitudes of the  $R(t)$  functions are 44% for the pure “slow” component and 28% for the summed “total” case. The increased amplitudes relative to the 15 co-axial HPGe configuration shows the added value of having the 24 clovers in the experimental setup. In addition, the  $\gamma$ -ray efficiency of the clover detectors is at least a factor of 3 larger than that of the 15 co-axial detectors. That roughly translates to a threefold reduction in data taking per plunger distance with the 24 clover detector configuration to achieve the same level of statistics. Hence, a larger overall number of distances can be covered and more accurate fits of the  $R(t)$  function in the final data analysis can be obtained.

The conclusions from the simulations of the  $g(2_1^+, ^{46}\text{Ti})$  TDRIV experiment on Li-like ions are the following. From the detector point of view, the best scenario would be to use the 24 clover detectors, as requested in the proposal, together with the 15 co-axial detectors. Although the clover detectors are around  $90^\circ$ , where the separation of the “fast” and “slow” components would be impossible, the amplitude of the  $R(t)$  function will be sufficient for extracting a  $g$ -factor value in the analysis. With the appropriate choice of initial beam energy and target thickness, the exit energy of the Ti ions scattering into the OPSA particle detector can be adjusted to around 7 MeV/A. The experimentally determined charge-state distribution of the

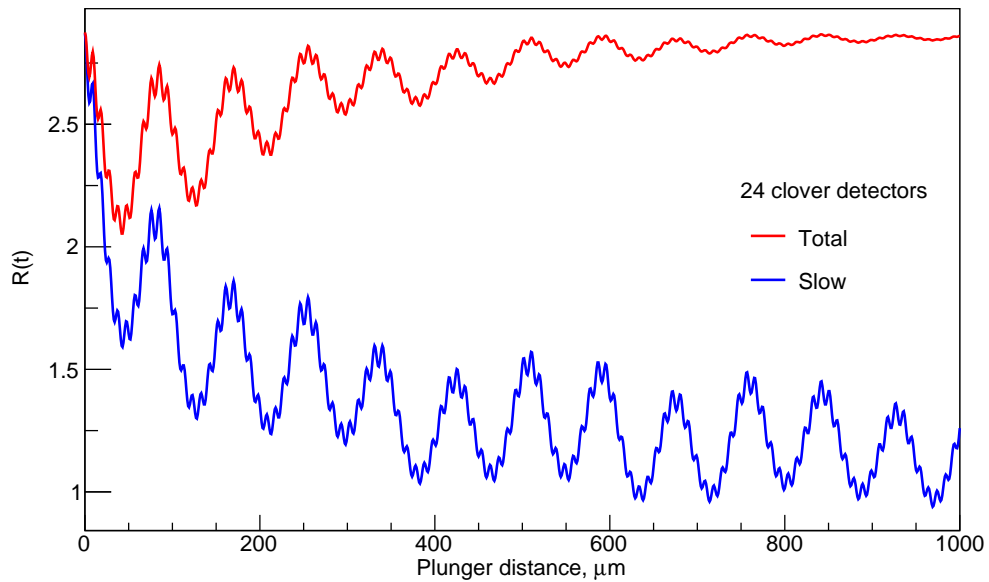


**Figure 3.15:** Simulated  $R(t)$  functions for the “slow” and “total” cases of Ti ions using 24 clover HPGe detectors.

Ti ions shows that the population of electron configurations with frequencies detrimental to the amplitude of the  $R(t)$  function should be almost negligible. These observations show that a high-precision g-factor measurement of the  $2_1^+$  state in  $^{46}\text{Ti}$  could be obtained from the planned TDRIV measurement.



# 4 - Magnetic moments of isomeric states around $^{68}\text{Ni}$

## 4.1 The region around $^{68}\text{Ni}$

The nickel isotopic chain is of great interest for nuclear structure studies as there are three doubly-magic nickel isotopes -  $^{48}\text{Ni}$ ,  $^{56}\text{Ni}$  and  $^{78}\text{Ni}$ . This allows for investigations of many phenomena that occur when going from the stable nickel isotopes towards the neutron-deficient  $^{48}\text{Ni}$  or the neutron-rich  $^{78}\text{Ni}$ . Of particular interest are the evolution of the neutron effective single-particle energies and the magic numbers away from stability, and the interplay between single particle structure and collectivity. Another peculiar case is the  $^{68}\text{Ni}$  isotope located at the  $N = 40$  harmonic oscillator gap between the  $fp$  shell and the  $g_{9/2}$  orbital (see Fig. 4.1). It exhibits some properties typically associated with doubly-magic nuclei and other properties that show no sign of magicity. This sparked multiple lines of research into the region around  $^{68}\text{Ni}$ , some of which will be discussed below.

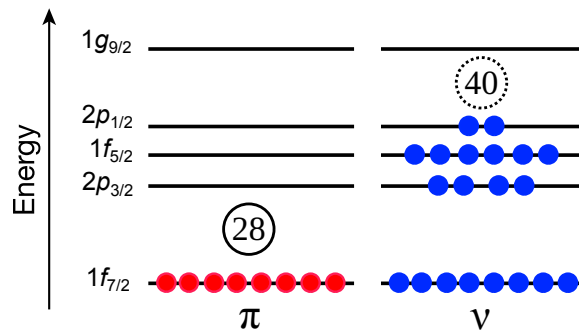


**Figure 4.1:** Schematic representation of the expected ground-state configuration of  $^{68}\text{Ni}$  according to the nuclear shell model with the  $Z = 28$  magic number and the  $N = 40$  sub-shell gap denoted.

The first information about the excited level structure in  $^{68}\text{Ni}$  came from an experiment at the ALTO facility in Orsay by Bernas *et al.* [117]. The study found that the first excited state in this isotope is a  $0^+$  state, rather than a  $2^+$  state as is the case in most even-even isotopes. Other cases in which a  $0^+$  state is below the first  $2^+$  state are  $^{16}\text{O}$ ,  $^{40}\text{Ca}$ , both doubly-magic nuclei. Parallels were also drawn to  $^{90}\text{Zr}$  with a closed  $Z = 40$  harmonic oscillator shell and a closed  $N = 50$  shell, which also has a  $0^+$  first excited state. A follow-up study by Broda *et al.* [118] observed the  $2_1^+$  excited state at just above 2 MeV excitation energy, higher than that in the neighboring Ni isotopes (see Fig. 4.2).

Several years later, a Coulomb-excitation experiment performed at GANIL was able to determine the transition probability to the first  $2^+$  state [119]. The obtained  $B(E2, 0_{g.s.}^+ \rightarrow 2_1^+)$  value of  $255(60) \text{ e}^2\text{fm}^4$  was lower than that in the  $^{66}\text{Ni}$  isotope by around a factor of two. A subsequent Coulomb-excitation study at ISOLDE [120] confirmed the lowering of the  $B(E2)$  value. Both the peak in the  $2_1^+$  excitation energy and the minimum in the  $B(E2, 0_{g.s.}^+ \rightarrow 2_1^+)$  value are signatures of a magic nucleus. These are necessary yet not sufficient conditions for declaring  $N = 40$  a magic neutron number in  $^{68}\text{Ni}$ . Another signature of magicity is a large

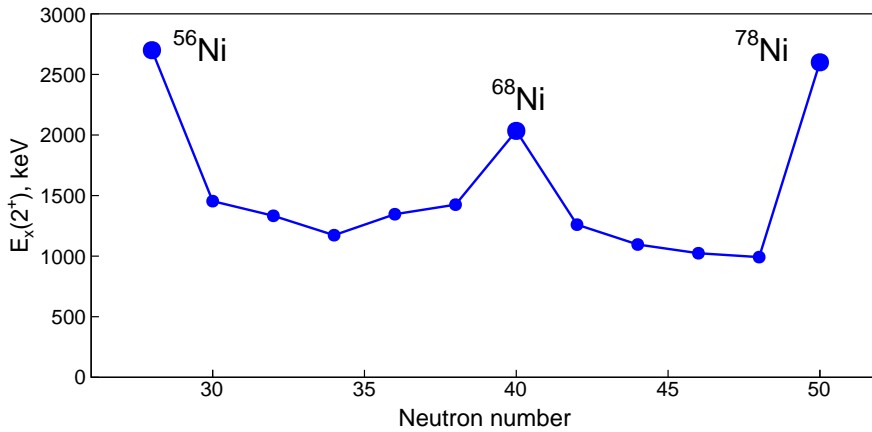


**Figure 4.2:** Excitation energies of the first  $2^+$  states in even-even nickel isotopes showing an increase at  $N = 28$ ,  $N = 40$  and  $N = 50$ .

drop in the two-neutron separation energy  $S_{2n}$  which has been one of the first observables that distinguished the magic numbers in the mid 20<sup>th</sup> century. Precise mass measurements are needed to calculate the  $S_{2n}$  from the binding energy of the isotopes. Two mass measurements in the region showed that there is no evidence of  $N = 40$  being a magic number from  $S_{2n}$  values [121, 122]. Instead, only a small effect of a weak sub-shell closure is observed. One suggestion on how the high excitation energy of the  $2_1^+$  state arises without  $N = 40$  being a magic number was put forward by Grawe *et al.* [123]. The authors propose that in  $^{68}\text{Ni}$ , with the entire  $fp$  shell occupied, a pair of neutrons has to be broken and simultaneously excited to the  $g_{9/2}$  orbital in order to obtain the positive-parity  $2^+$  state. This would artificially inflate the excitation energy simply due to the consideration of the parities of the involved orbitals.

The experimental results also provoked theoretical works on the structure in the  $^{68}\text{Ni}$  region. An in-depth theoretical study was undertaken by Langanke *et al.* [124] using several approaches - QRPA, Shell Model Monte Carlo and large-scale diagonalization shell model. The authors investigated whether the  $B(E2; 0_{g.s.}^+ \rightarrow 2_1^+)$  strength in  $^{68}\text{Ni}$  is small due to its magicity or the value measured by Sorlin *et al.* constitutes only a small part of the total  $B(E2; 0_{g.s.}^+ \rightarrow 2_f^+)$  strength. They performed calculations for the nickel isotopes between  $^{56}\text{Ni}$  and  $^{70}\text{Ni}$  to observe the evolution of the  $B(E2; 0_{g.s.}^+ \rightarrow 2_f^+)$  strength towards the  $N = 40$  sub-shell closure. Their results show that the full  $B(E2; 0_{g.s.}^+ \rightarrow 2_f^+)$  strength in  $^{56}\text{Ni}$ , accumulated entirely in the  $2_1^+$  state, slowly becomes fragmented with the addition of more neutrons. At  $^{68}\text{Ni}$ , the predicted  $B(E2; 0_{g.s.}^+ \rightarrow 2_1^+)$  value is in good agreement with the experimental one, yet it is found to be responsible for less than half of the total  $B(E2)$  strength. The larger part of the  $B(E2)$  strength is found at states above 4 MeV and is attributed to  $1p$ - $1h$  proton excitations above the  $Z = 28$  shell closure. These results are interpreted as a rather small  $N = 40$  gap allowing the excitation of a pair of neutrons to the  $g_{9/2}$  orbital to be more energetically favorable than a single proton excitation across  $Z = 28$ .

These claims can be tested through the measurements of magnetic moments of excited states in and around  $^{68}\text{Ni}$ . Such measurements would be very sensitive to the size of the  $N = 40$  gap and the role of the  $g_{9/2}$  orbital in the region. Ideally, a g-factor measurement of the  $2_1^+$  state in  $^{68}\text{Ni}$  could confirm or deny the purity of the  $(g_{9/2})^2$  configuration suggested by Langanke *et al.*. However, this would require a radioactive ion beam measurement using either the transient field or the TDRIV method due to the short lifetime of the state -  $0.45(7)$  ps [125]. At the time, in the early 2000s, the first TF measurement on a RIB was just performed [43, 126] and the modification of the TDRIV method for RIBs [35] had not been proposed yet. At

the same time, it had been shown that g-factor measurements of isomeric states, populated in projectile-fragmentation reactions, were viable. The first experiment to apply the TDPAD method after fragmentation was targeting exactly the  $^{68}\text{Ni}$  region through the  $9/2^+$  isomer in  $^{67}\text{Ni}$  and the  $13/2^+$  isomer in  $^{69}\text{Cu}$  [127]. The  $9/2^+$  isomer in  $^{67}\text{Ni}$  is a single-particle spin isomer - it decays via an  $M2$  transition to the  $\nu f_{5/2}$  state. Analogous  $9/2^+$  isomers were already known to exist in  $^{63}\text{Ni}$  and  $^{65}\text{Ni}$ . The excitation energy of the isomeric state in the odd nickel isotopes provides the relative energies of the single particle orbits, which is very important for theoretical calculations.

Two dedicated experiments were performed at GANIL to search for isomeric states after fragmentation of the primary beam. The proof-of-concept experiment used a  $^{112}\text{Sn}$  beam on a  $^{nat}\text{Ni}$  target and multiple ns and  $\mu\text{s}$  isomers were discovered in the  $N \approx 50$ ,  $40 < Z < 50$  region [128]. These isomeric states were identified as either seniority isomers from the  $\pi g_{9/2}^n$  configuration or single-particle spin isomers due to the spin difference between the  $\pi g_{9/2}$  and the  $\pi p_{1/2}$  orbitals leading to retarded  $M4$  transitions. The follow-up experiment utilized a  $^{86}\text{Kr}$  beam on a  $^{nat}\text{Ni}$  target to search for analogous isomeric states in the  $Z \approx 28$ ,  $40 < N < 50$  region around  $^{68}\text{Ni}$  where the structure of the orbitals is similar [129]. This study found several isomeric states in neutron-rich Cu, Ni and Fe isotopes, among others. One of the discoveries was that of the expected  $8^+$  seniority isomer in  $^{70}\text{Ni}$  with a  $(\nu g_{9/2})^2$  configuration. Beneath the isomer, the energy of the first  $2^+$  state in  $^{70}\text{Ni}$  was also determined to be 1259 keV. Its excitation energy is much lower than the  $2^+$  state in  $^{68}\text{Ni}$  at 2034 keV, which can be interpreted as a sub-shell closure, albeit weak. In  $^{69}\text{Ni}$  two isomers were found and the first one at low excitation energy was interpreted as a long-lived  $\beta$ -decaying  $1/2^-$  isomer which determines the single particle energy difference between the  $g_{9/2}$  and  $p_{1/2}$  orbitals. The second isomer at higher excitation energy is expected to be the  $17/2^-$   $(\nu g_{9/2})^2$  seniority isomer in  $^{70}\text{Ni}$  coupled to a neutron/hole in  $p_{1/2}$ . Similarly, based on excitation energy a  $19/2^-$  seniority isomer was proposed in  $^{71}\text{Cu}$  with the  $(\nu g_{9/2})^2 \times (\pi p_{3/2})^1$  configuration. These seniority isomers can provide valuable insight into the strength of the  $\nu\nu$  interaction in the region. In a more general view, the information on the role of the  $\nu g_{9/2}$  orbital in the structure of the nickel isotopes and the region around  $^{68}\text{Ni}$  can be accessed through the g factors of the related  $g_{9/2}$  isomeric states.

The first g factor measurement of an isomeric state in this region of the nickel isotopes was that of the  $9/2^+$  state in  $^{63}\text{Ni}$ . The measurement was performed using the TDPAD method after a fusion-evaporation reaction [130]. The obtained value of  $g = -0.269(3)$  is consistent with the corresponding g factors of  $9/2^+$  isomers in Zn and Ge isotopes. Next, the g factor of the  $9/2^+$  state in  $^{65}\text{Ni}$  was measured to be  $g = -0.2962(25)$  by Georgiev *et al.* [131, 132] using the TDPAD method after a transfer reaction. This value agrees perfectly with the effective  $\nu g_{9/2}$  Schmidt limit (-0.2976) implying the extreme single-particle approximation is valid around the  $N = 40$  sub-shell closure already at  $N = 37$ . Curiously, large scale shell model calculations performed for  $^{65}\text{Ni}$  were able to reproduce the experimental result with two different configurations. Both the pure  $\nu g_{9/2}$  configuration, using effective  $g_s^{eff} = 0.7g_s^{free}$  values, and the configurations including proton excitations above  $Z = 28$ , using free-nucleon g factors, were in agreement with the experimental g factor. Although proton excitations across the  $Z = 28$  shell gap seem less likely, a study on the g factors of the  $2_1^+$  states in even- $A$   $^{58-64}\text{Ni}$  isotopes showed that such  $p-h$  excitations are necessary for the shell model calculations to reproduce the experimental values [133]. Going further towards  $^{68}\text{Ni}$ , the first TDPAD measurement after a fragmentation reaction was performed on the  $9/2^+$  state in  $^{67}\text{Ni}$  by Georgiev *et al.* [127]. Just one neutron away from the sub-shell closure one can expect that the value would remain close to the Schmidt limit. However, the obtained value of  $g = |0.125(6)|$  is at least a factor of two off from the Schmidt value and the authors suggest that proton excitations are responsible

for this discrepancy. They perform simple two-state configuration mixing calculations using the approach of Arima and Horie [134]. Assuming a negative sign for the  $g$  factor, they found that a 2% admixture of the  $\pi \left( f_{7/2}^{-1} f_{5/2}^1 \right)_{1+}$  spin-flip configuration to the almost pure  $\nu g_{9/2}$  configuration is enough to explain the deviation from the Schmidt value. These measurements indicate the sensitivity of the  $g$  factors towards the composition of the wave function and the fragility of the  $Z = 28$  shell-gap away from stability.

It is within this context that an experiment to measure the  $g$  factors of the  $19/2^+$  and  $8^+$  seniority isomers in  $^{69,70}\text{Ni}$  using the TDPAD method was performed at Michigan State University (MSU) in 2005. A measurement of the already known  $g$  factor of the  $9/2^+$  isomer in  $^{67}\text{Ni}$  was also performed as a reference to account for any systematic uncertainties. In this Chapter the experimental results for the  $g$  factors of the seniority isomers in  $^{69,70}\text{Ni}$  will be discussed. The measurements of the  $g$  factors of the seniority isomer in  $^{71}\text{Cu}$  and the single-particle  $9/2^+$  isomer in  $^{67}\text{Ni}$  will also be presented.

In later years the region around  $N = 40$  located south of the nickel isotopic chain has also been of great interest for both experiment and theory. The systematics of the excitation energy of the  $2_1^+$  states in neutron-rich Fe and Cr isotopes suggested an onset of deformation [135, 136]. This was confirmed through lifetime measurements of these states in  $^{62,64}\text{Fe}$  [137] and  $^{66}\text{Fe}$  [138]. A sudden increase in the  $B(E2; 2_1^+ \rightarrow 0_{g.s.}^+)$  values was observed between  $^{62}\text{Fe}$  and  $^{64,66}\text{Fe}$ . Theoretical calculations were able to identify that the neutron  $g_{9/2}$  and  $d_{5/2}$  orbitals have to be considered in order to reproduce these trends [139, 137, 140]. An in-depth theoretical study using large-scale shell-model calculations with the LNPS interaction was able to describe very well the known experimental observables for Ni, Fe and Cr isotopes [140]. The occupation of the intruder orbitals  $g_{9/2}$  and  $d_{5/2}$  in the ground state was predicted to increase greatly moving away from  $^{68}\text{Ni}$  towards  $^{66}\text{Fe}$  and even further to  $^{64}\text{Cr}$ . Multi-particle multi-hole excitations to the intruder orbitals drive the emergence of quadrupole collectivity in the Fe and Cr isotopes. Due to the similarities with the nuclear structure around  $^{32}\text{Mg}$ , the region south of  $^{68}\text{Ni}$  has been referred to as the island of inversion around  $^{64}\text{Cr}$ , which is the isotope with the largest predicted deformation. The role of the  $\nu g_{9/2}$  orbital adds to the importance of studying the corresponding excited states in the vicinity. The results from the current experiment on nickel isotopes will be compared with calculations using the LNPS interaction, which has been shown to be successful in this region.

## 4.2 Experimental setup and data taking

The experiment was performed in May-June 2005 at the National Superconducting Cyclotron Laboratory (NSCL) of Michigan State University (MSU), USA. At the time of the experiment, the two existing superconducting cyclotrons - K500 and K1200, had recently been modified to operate in a coupled system. The A1900 fragment separator had been recently constructed and commissioned as an upgrade of the previous A1200 fragment separator. A schematic of the NSCL facility is shown in Fig. 4.3. A set of ECR ion sources provide the initial beam ions to be accelerated by the K500 cyclotron. The accelerated ions are additionally stripped of electrons before being further accelerated by the K1200 cyclotron. The beam ions exiting the K1200 cyclotron impinge on a production target to induce projectile-fragmentation reactions. The species of interest are separated from the unreacted primary beam ions and the various produced secondary beam ions through  $B\rho$  selection in the first half of the A1900 separator. At the mid-point of the separator an energy degrading aluminium “wedge” is placed for isotopic selection. The incoming fragments with different  $Z$  and the same  $B\rho$  values are sepa-

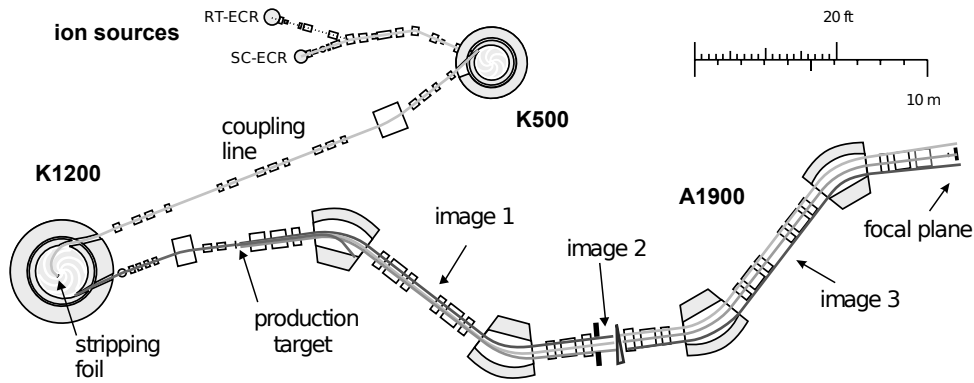


**Figure 4.3:** Schematic representation of the NSCL coupled-cyclotron facility and the A1900 fragment separator taken from Ref. [141].

rated by their different energy losses passing through the wedge. A set of aperture plates (slits) are used for momentum selection of the incoming ions. The second half of the A1900 separator is mirror-symmetric to the first and again provides  $B\rho$  selection. Parallel-Plate Avalanche Counters (PPAC) are present at several points of the separator to provide tracking capabilities of the fragments. After the focal plane of the separator the beam is deviated to one of the several beam lines leading to dedicated experimental setups. The dipole magnet which diverted the beam to the experimental setup used in the current experiment had a bending angle of  $22^\circ$ . This value corresponds to the  $\alpha$  angle from Eq. 1.50, which defines the orientation of the spin alignment relative to the direction of the beam.

The experimental setup used for the TDPAD experiment consisted of a plastic scintillator, a copper implantation host, an electromagnet and four segmented SeGa HPGe detectors [142] in the horizontal plane (see Fig. 4.4). The plastic scintillator had a thickness of 1 mm and provided the “start” signal for a set of four Time-to-Amplitude Converter (TAC) modules, as shown in Fig. 4.5. The signals from the HPGe detectors were sent to Timing Filter Amplifiers (TFA) for shaping via integration and differentiation circuits. The produced signal was then sent to a Constant Fraction Discriminator (CFD) to obtain the time pick-off signal. The CFD output of each HPGe detector supplied the “stop” signal for the respective TAC module. The HPGe detector signals were also sent to spectroscopic amplifiers (SA) before being digitized with Analog-to-Digital Converters (ADC). The data acquisition utilized a particle- $\gamma$  trigger requiring a particle in the plastic scintillator and a  $\gamma$  ray in one of the SeGa HPGe detectors within a selected coincidence window. Both the energy and time information of all registered  $\gamma$  rays was recorded on an event-by-event basis. The energy and timing response of the HPGe detectors was calibrated using standard radioactive sources. This was done both with and without the magnetic field to test its influence on the performance of the detectors. The used magnet provided a magnetic field of 0.504(1) T, measured using a NMR probe. The vertical orientation of the magnetic field could be controlled and it was set to be pointing downward.

In the experiment a primary beam of  $^{76}\text{Ge}^{30+}$  ions at an energy of 130 MeV/A was utilized with an average intensity of 8.5 pA. Multiple tests were performed at the beginning of the experiment to optimize the beam purity, isomeric ratio and momentum selection settings for  $^{67,69,70}\text{Ni}$ . Typically, in the center of the momentum distribution the total yield is the highest, however, the isomeric ratio is at a minimum. In the wing of the momentum distribution the situation is reversed with a reduced overall production and an increased isomeric ratio. As described in Chapter 1.2.1, a positive and negative alignment is expected for ions in the center and the wing of the momentum distribution, respectively. The achieved degree of alignment

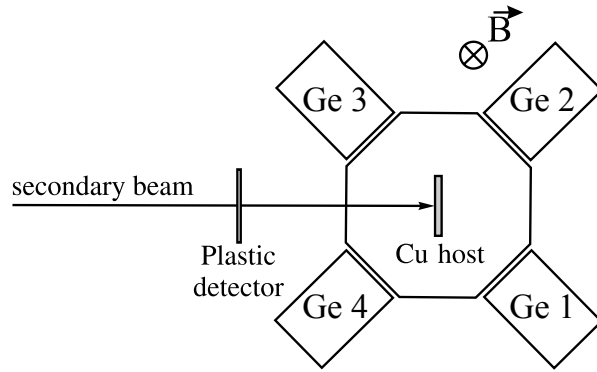


**Figure 4.4:** Schematic of the TDPAD setup used in the experiment at NSCL. The schematic is adapted from Ref. [143] where the same vacuum chamber was used in a TDPAD experiment on  $^{61}\text{Fe}$  with an identical setup at GANIL.

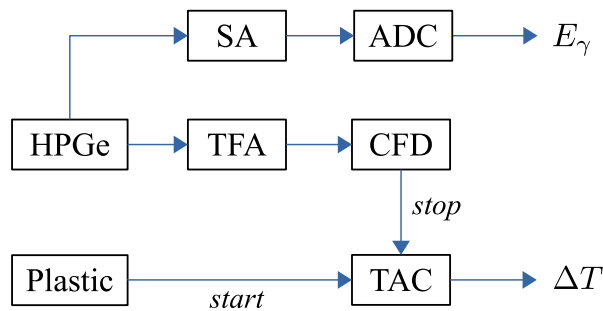


**Figure 4.5:** Schematic of the used electronics modules to obtain the  $\gamma$ -ray energy  $E_\gamma$  and the time difference  $\Delta T$  between the ions passing through the plastic scintillator and the decay of the isomeric state.

is more difficult to predict as it might depend on the primary beam energy to some extent. Experiments at GANIL at primary beam energies around 60 MeV/A on both light [11] and medium mass nuclei [143] have found that the magnitude of the alignment is larger in the wing of the momentum distribution. The study from Ref. [127] also performed at GANIL measured similar magnitudes of the alignment for the center and the wing of the momentum distribution. Another experiment performed at GSI [144] with a primary beam energy of 500 MeV/A showed much larger alignment in the center of the momentum distribution. With the current experiment having been performed at an energy of 130 MeV/A, it was not clear which setting would yield higher alignment. Therefore, the measurements of  $^{67}\text{Ni}$  and  $^{69}\text{Ni}$  were performed both for the wing and the center of the momentum distributions. Due to time constraints the  $^{70}\text{Ni}$  measurement was performed only for the center of the momentum distribution. Out of these measurements only three were deemed as successful with observed oscillations in the experimental  $R(t)$  functions. These are the  $^{67}\text{Ni}$  and  $^{69}\text{Ni}$  measurements in the wing of the momentum distribution and the  $^{70}\text{Ni}$  measurement in the center of the momentum distribution. The momentum selection settings of these three measurements are given in Table 4.1, together with the measured isomeric ratios and estimated production rates of the isotopes of interest. The results obtained for these three data sets are described in the following Section.

**Table 4.1:** The central  $B\rho$  value, the width of the momentum acceptance interval, the estimated production rates and the measured isomeric ratio for the studied isotopes. A beam attenuator was used to reduce the intensity of the secondary  $^{67}\text{Ni}$  beam so that the rates in the plastic scintillator would be below 20 kHz.

Nuclide	Setting	$B\rho$ , Tm	$\Delta p/p$ , %	Production rates, pps/pnA	Isomeric ratio, %
$^{67}\text{Ni}$	Wing	3.658	0.5	12300	25
$^{69}\text{Ni}$	Wing	3.780	0.5	1380	5
$^{70}\text{Ni}$	Center	3.780	1.0	692	3

### 4.3 Analysis

Several ROOT/C++ macros used for the sorting of the data and its TDPAD analysis were provided by G. Georgiev. These codes were updated and modified to be compatible with modern ROOT versions. A random-background subtraction procedure was implemented for the time-difference spectra in the sorting code and will be explained below. A new ROOT/C++ macro was prepared that combined the existing independent TDPAD analysis macros in an easy to use package. An existing Fast Fourier Transform (FFT) macro was implemented, based on the algorithms from Ref. [145]. A new FFT function based entirely on ROOT was also prepared and added to the analysis macro. The results from the two FFT approaches were shown to be identical.

The measurement on  $^{67}\text{Ni}$  will be discussed first, before continuing with the results for  $^{69}\text{Ni}$  and  $^{70}\text{Ni}$ . An attempted measurement on  $^{71}\text{Cu}$  will also be presented, followed by a discussion of all obtained results.

#### 4.3.1 $^{67}\text{Ni}$

A partial level scheme of  $^{67}\text{Ni}$  with the relevant transitions below the  $9/2^+$  isomeric state is shown in Fig. 4.6. The complete  $\gamma$ -ray spectrum from all four HPGe detectors is shown in Fig. 4.7. The spectrum is dominated by the two transitions below the  $9/2^+$  isomer. Transitions originating from beam contaminants ( $^{66}\text{Ni}$ ,  $^{68,69}\text{Cu}$ ,  $^{65}\text{Co}$ ) and their  $\beta$ -decay daughters ( $^{65}\text{Ni}$ ,  $^{65,66,67}\text{Cu}$ ,  $^{66,67,68}\text{Zn}$ ) are also observed. The other notable lines in the spectrum are the 1173 keV and 1332 keV lines from a  $^{60}\text{Co}$  source that was in the vicinity of the experimental setup, the 1461 keV  $^{40}\text{K}$  line and the 846 keV  $2_1^+ \rightarrow 0_{g.s.}^+$  transition from  $^{56}\text{Fe}(n, n'\gamma)$  reactions.

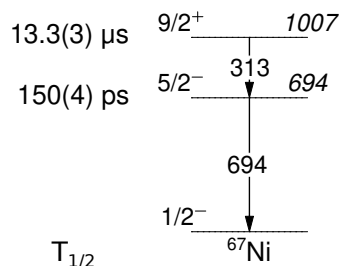


**Figure 4.6:** Partial level scheme of  $^{67}\text{Ni}$  showing the  $9/2^+$  isomeric state and the cascade of two transitions through which it decays to the  $1/2^-$  ground state [146].

Setting an energy gate on the 313-keV transition in the sorting code produces a time-difference spectrum between the plastic scintillator and the HPGe detector. The raw time-difference spectrum for one of the HPGe detectors is shown in Fig. 4.8.

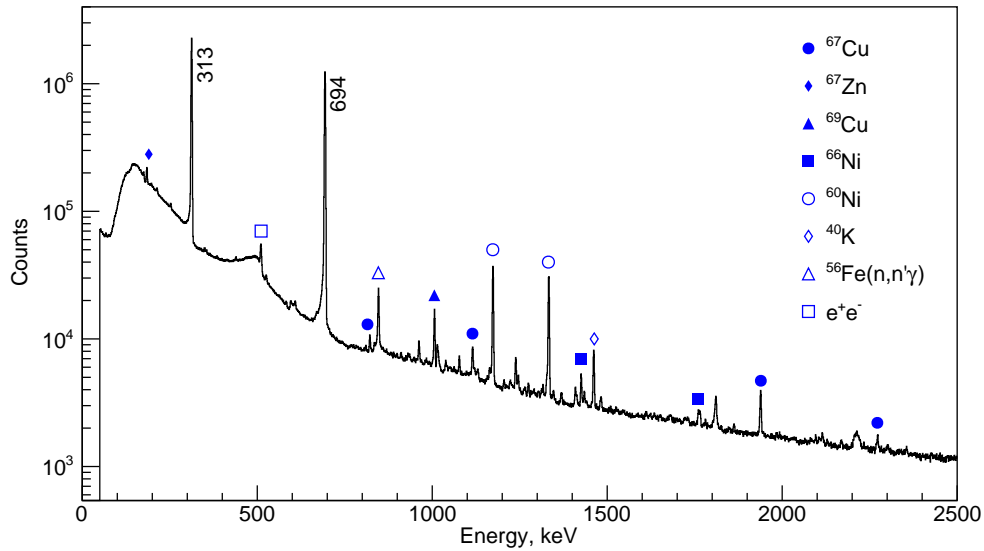


**Figure 4.7:** Total projection of the HPGe detector  $\gamma$ -ray energy spectra with the more intense lines denoted.

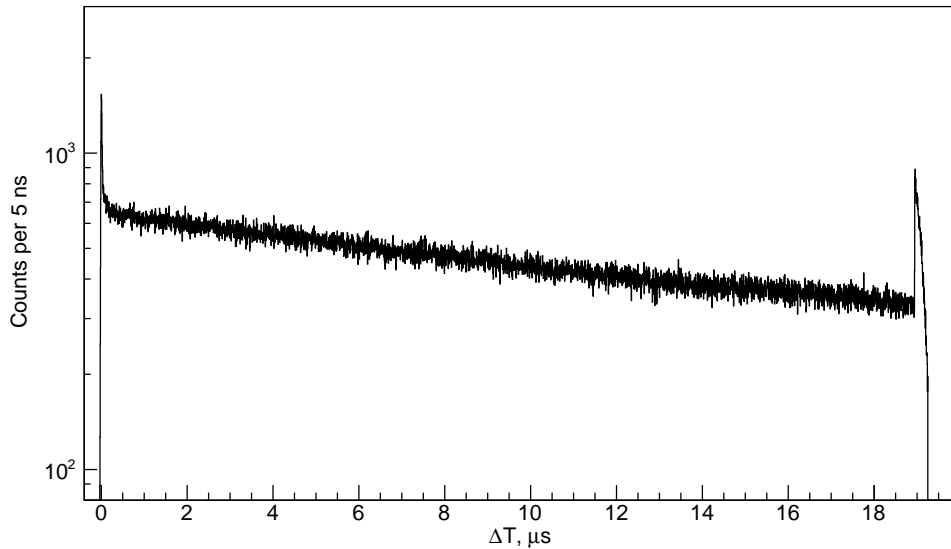


**Figure 4.8:** The full time-difference spectrum after an energy gate on the 313-keV  $\gamma$  ray in a single HPGe detector. Visible are a sharp peak at small time-differences originating from prompt background coincidences, and a discontinuity of the spectrum at the end of the range of the used TAC module.

The used TAC modules for this measurement had a fixed time range of  $20 \mu\text{s}$ , which is less than two half-lives of the isomeric state -  $T_{1/2} = 13.3(2)\mu\text{s}$ . This is seen in Fig. 4.8 as the exponential decrease of intensity cuts off abruptly before having reached the level of random background coincidences. The sharp peak at the beginning of the spectrum is caused by the so-called  $\gamma$ -flash resulting from prompt  $\gamma$  rays and bremsstrahlung from the implantation of the beam. This is easily confirmed by setting an energy gate on the background on either side of the 313-keV line and looking at the corresponding time-difference spectrum. The background contribution beneath the peak of interest can be approximated by taking the averaged time-difference spectrum from background energy gates above and below the peak. The background time-difference spectrum produced in this way is compared with the background-subtracted time-difference spectrum in Fig. 4.9. The background time-difference spectrum exhibits the

same exponential tail as the background-subtracted spectrum. This is due to the Compton-scattering background of the 694-keV transition that is also found underneath the 313-keV line. The background-subtraction procedure slightly decreases the overall statistics and also increases the statistical uncertainty of each data point in the final time-difference spectrum. However, it successfully removes the prompt background coincidences and the contributions from the underlying Compton background. At the same time, the procedure indicates where the fit of the  $R(t)$  function should begin.

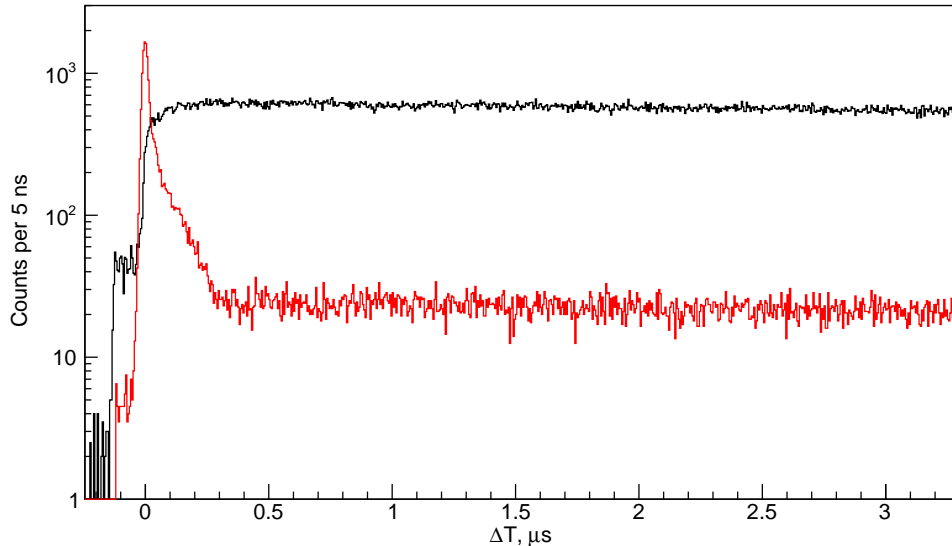


**Figure 4.9:** The time-difference spectrum corresponding to the background underneath the 313-keV peak (red) and the background-subtracted time-difference spectrum for a single HPGe detector. The exponential tail of the background spectrum beyond  $0.5 \mu\text{s}$  is due to the presence of Compton-scattered 694-keV  $\gamma$  rays underneath the 313-keV line which have the same behaviour as the 313-keV  $\gamma$  ray itself.

The lifetime of the isomeric state can be determined by a direct fit of the time-difference spectrum with an exponential function and a linear background. The fit can be applied on the time-difference spectra for both transitions below the isomer as the half-life of the  $5/2^-$  state is negligible compared to the half-life of the  $9/2^+$  isomeric state. The background-subtracted time-difference spectra for both transitions and for all four HPGe detectors were summed. The resulting spectrum is shown in Fig. 4.10 together with the exponential fit of the data. The half-life obtained from the fit is of  $11.5(2) \mu\text{s}$  where the uncertainty is only statistical. The fit results proved to be rather unstable to changes in the fitting range leading to a large systematic uncertainty and the value  $12(4) \mu\text{s}$  is adopted from the current analysis. This volatility of the fit could be attributed to the limitations in the range of the used TAC modules. Due to this the exact level of random background coincidences after the background-subtraction procedure remains unknown and could potentially alter the fit results. The obtained result is in agreement with the adopted value of  $13.3(2) \mu\text{s}$  by Grzywacz *et al.* [129].

Next, the TDPAD  $R(t)$  function from Eq. (1.58) is constructed by first summing the time-difference spectra of the two pairs of opposite HPGe detectors - Ge1 + Ge3 and Ge2 + Ge4. Then, the difference between these two spectra is divided by their sum which produces the final  $R(t)$  function. Typically, the efficiencies of the detectors are not exactly the same and the spectra are multiplied by a coefficient to account for these differences in efficiency. Changing these coefficients only modifies the position of the  $R(t)$  function relative to the  $Y$  axis and not its oscillatory behaviour. The coefficients are manually adjusted until the observed oscillation

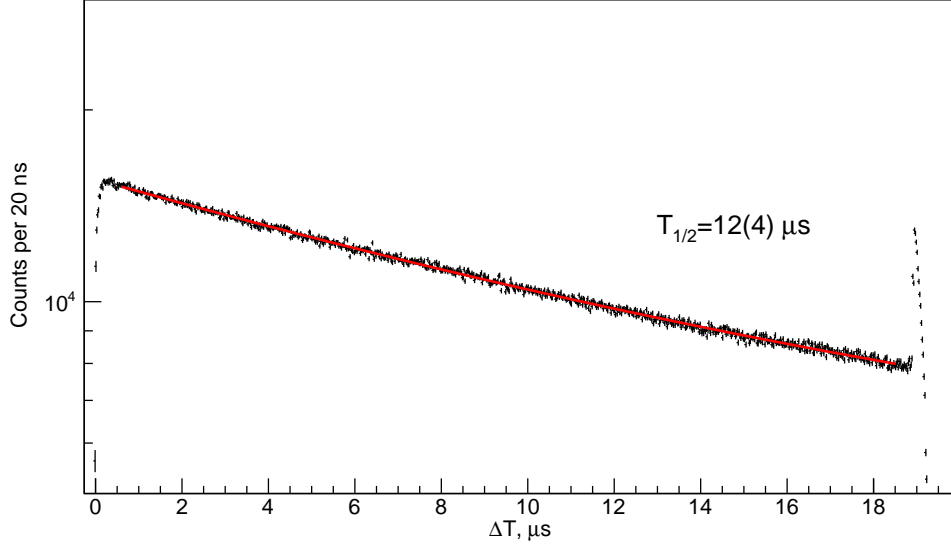


**Figure 4.10:** Exponential fit of the summed time-difference spectra gated on both the 313-keV and 694-keV transitions in all four HPGe detectors.

in the  $R(t)$  function is symmetric around  $Y = 0$ .

After finding the proper efficiency correction coefficients the  $R(t)$  function can be fitted with a cosine function such as Eq. (1.58) to extract the  $g$  factor of the state of interest. The first step is to determine the range in which the  $R(t)$  function should be fitted. As mentioned above, the extent of the prompt background in the time-difference spectra indicates the beginning of the fitting range. The end point of the fitting range can be deduced from the time-difference spectrum by considering when the level of the exponential decay becomes comparable to the background level. Another method to determine the range is to produce alternative  $R(t)$  functions using pairs of neighboring detectors instead of opposite ones. For such  $R(t)$  functions no oscillatory pattern should be observed and instead a horizontal line is expected. Periodic deviations from the horizontal line that are incompatible with random fluctuations would indicate either background contributions or possibly electronics issues. The four detectors can be used to produce two  $R(t)$  functions using the neighboring pairs Ge1 + Ge2 and Ge3 + Ge4, or Ge1 + Ge4 and Ge2 + Ge3. The resulting  $R(t)$  functions can be used to determine some limits to the fitting range of the real  $R(t)$  function. In any case, the approximate upper and lower limits for the fitting range of the  $R(t)$  function should be varied slightly in a series of fits to test the stability of the fit results.

A commonly used approach in the analysis of TDPAD experiments is to also vary the width of the channels in the time-difference spectra by merging several neighbouring channels. Such rebinning of the time-difference spectra can be done for an arbitrary number of neighboring channels. The oscillation in the  $R(t)$  function can become either more or less apparent depending on the used rebinning factors which can influence the fit results for the  $g$  factor. Therefore it is imperative to compare fits of the  $R(t)$  function with different rebinning factors to observe how stable the fit result for the  $g$  factor is to changes in this factor. Fits of the experimental  $R(t)$  function for the 313-keV transition and for several different rebinning factors are shown in Fig. 4.11. The obtained result is  $g = -0.26(2)$  in all cases.

In principle, the result for the  $g$  factor should also be reproduced using the 694-keV transition. However, the fit of the time-difference spectrum for this transition yields a slightly larger value of  $g = -0.29(2)$ , as shown in Fig. 4.12. It is worth noting that in the previous measurement of Georgiev *et al.* [9, 127] the  $R(t)$  function of the 694-keV transition showed no evidence

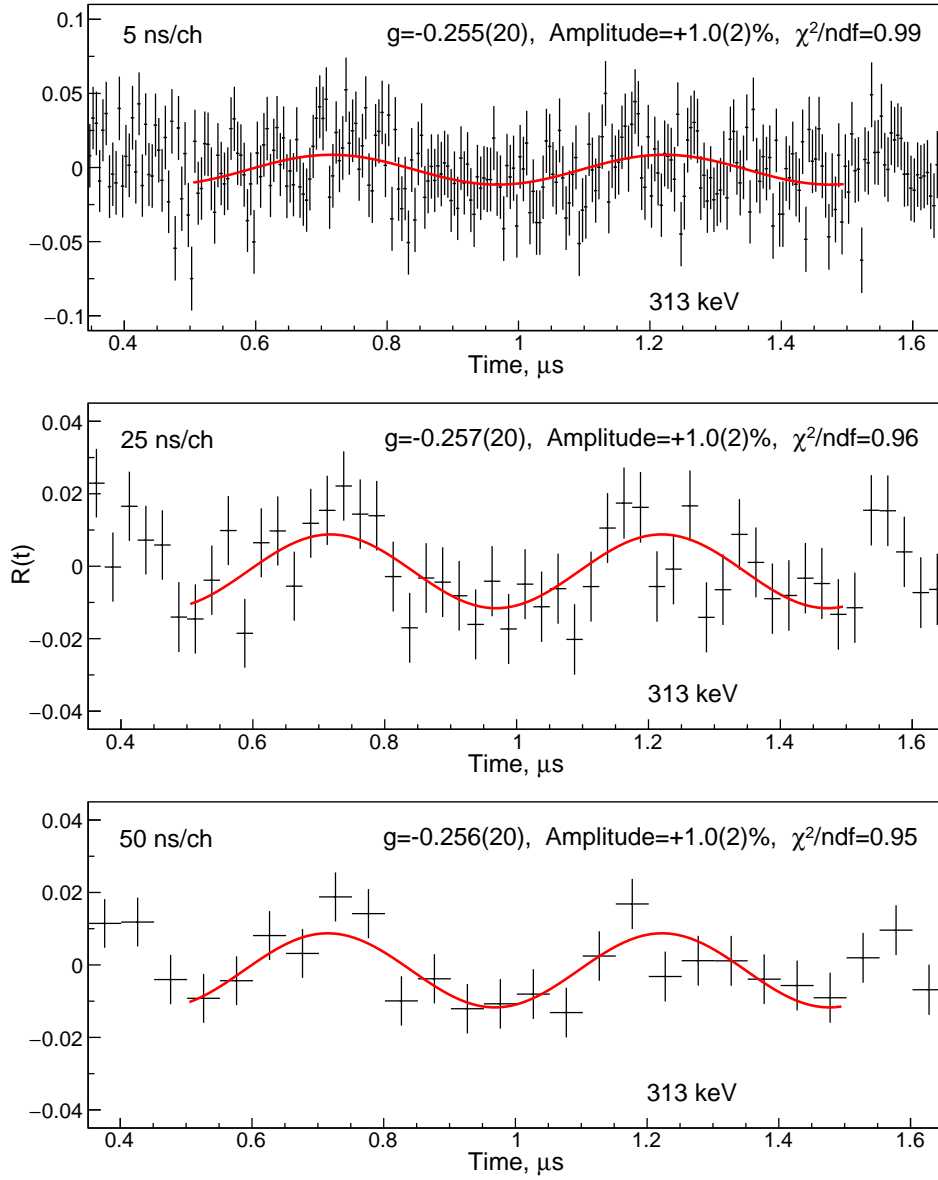


**Figure 4.11:** Fits of the  $R(t)$  function produced using the time-difference spectra after an energy gate on the 313-keV transition with different rebinning factors.

of an oscillation pattern at all.

A consistency check of the results obtained through direct fitting of the data can be achieved by applying the Fast Fourier Transform on the experimental  $R(t)$  function. In essence, the FFT algorithm transforms the time-difference spectrum from the time domain to the frequency domain. Any observed frequencies in the given range of the time-difference spectrum correspond to and are observed as peaks in the resulting magnitude spectrum. In this case, the frequency is the Larmor frequency which is directly related to the  $g$  factor through Eq. 1.14. Therefore, in the current implementation of the FFT algorithms the frequency on the X axis has been scaled by the appropriate constants and factors to yield the absolute  $g$ -factor value corresponding to each frequency.

The FFT results are sensitive to the range of the  $R(t)$  function that is supplied to the algorithm but remain stable to changes in the rebinning factor. The magnitude spectrum obtained from applying the ROOT FFT algorithm on the  $R(t)$  function for the 313-keV transition is presented in Fig. 4.13. The frequency with the highest magnitude corresponds to a  $g$  factor value

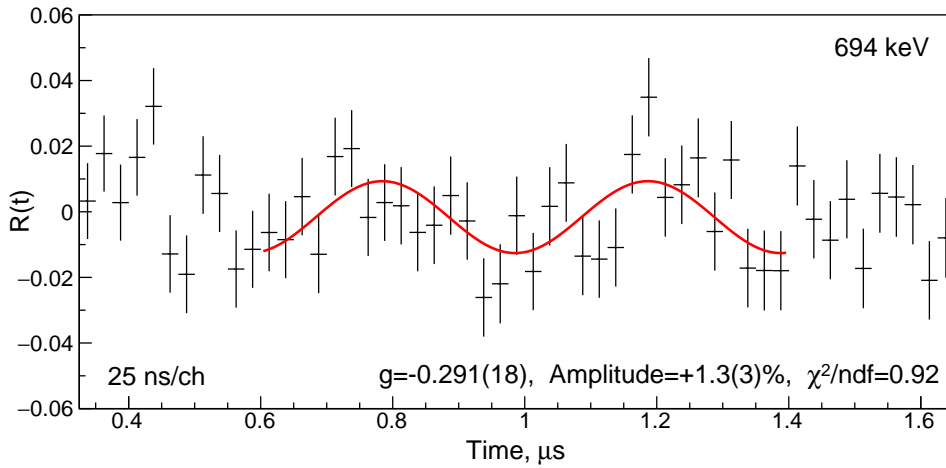


**Figure 4.12:** Fit of the  $R(t)$  function produced using the time-difference spectra after an energy gate on the 694-keV transition.

of  $|g| = 0.27(7)$ . The  $1\sigma$  uncertainty is calculated under the assumption that the frequency peak has an approximately Gaussian shape and  $\text{FWHM} = 2.355\sigma$ . Varying the range of the  $R(t)$  function yielded values within the uncertainty of the given result with some distortions of the peak shape. Nevertheless, even for distorted peak shapes the FWHM remained stable and covered the same range of  $g$ -factor values.

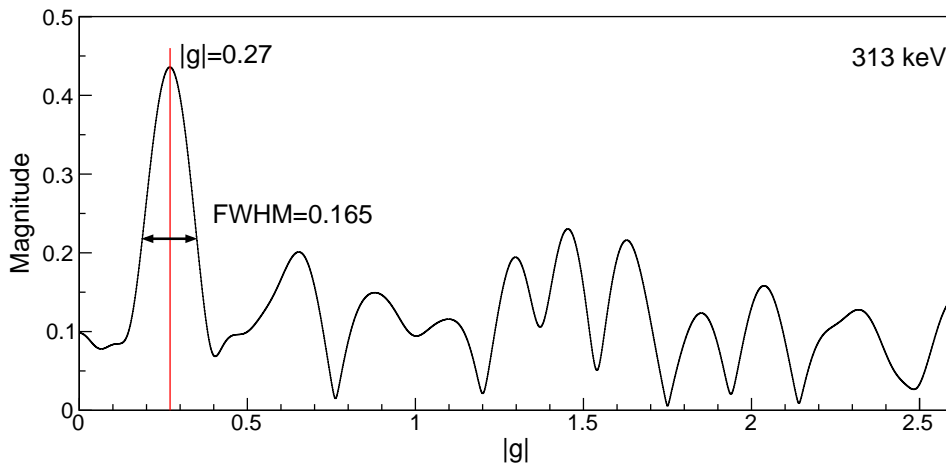


**Figure 4.13:** Magnitude spectrum of the  $R(t)$  function obtained after an energy gate on the 313-keV transition depopulating the  $9/2^+$  isomer in  $^{67}\text{Ni}$ . Each peak in the spectrum corresponds to a frequency that was identified by the FFT algorithm within the supplied range of the  $R(t)$  function. The magnitude of a peak in the spectrum corresponds to the relative strength of the corresponding frequency.

Something to be noted is that the difference in the magnitude of the peak relative to the other frequencies present in the spectrum is approximately a factor of two. For comparison, the magnitude of the main frequency in the FFT analysis in Ref. [127] was a factor of seven above the background. In addition, in Ref. [127] a signal in the magnitude spectrum was only observed for the 313-keV transition and not for the 694-keV transition. The situation was found to be somewhat better in the current data set. Applying the FFT algorithm on the  $R(t)$  function of the 694-keV transition resulted in the magnitude spectrum given in Fig. 4.14. The obtained result of  $|g| = 0.31(8)$  is in agreement with that from the direct fit of the data. The relative magnitude of the main frequency peak and the background peaks is slightly worse than that

for the 313-keV transition. The FFT analysis confirms the direct fitting results, yet it does not resolve the slight discrepancy between 313-keV and the 694-keV g-factor values.

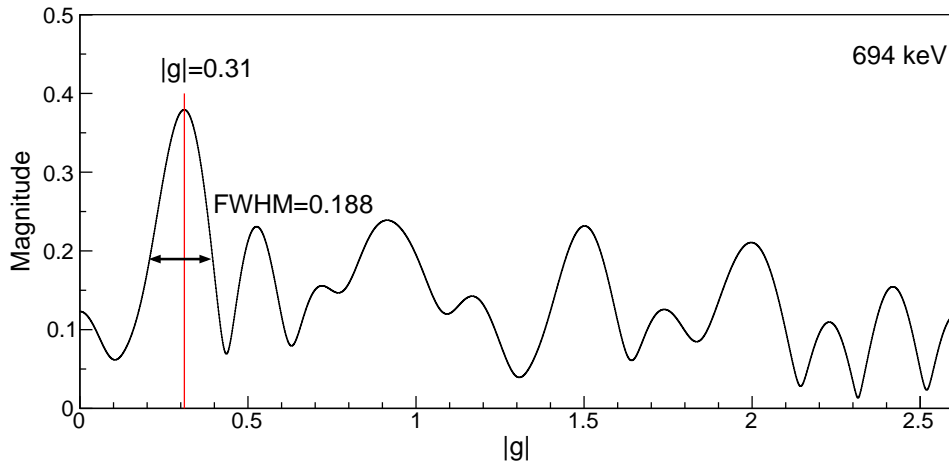


**Figure 4.14:** Magnitude spectrum for the  $R(t)$  function obtained after a gate on the 694-keV transition in  $^{67}\text{Ni}$ .

Finally, in the study of Georgiev *et al.* [127] the  $R(t)$  function was also fitted with an exponentially decreasing cosine function. The exponential decrease of the amplitude was attributed to the relaxation of the crystal lattice of the copper implantation host. A copper host was also used in the MSU experiment therefore an attempt was made to introduce an exponential term in the fit function. The resulting fit of the  $R(t)$  function for the 313-keV transition is shown in Fig 4.15. The obtained g-factor value agrees with the result from the simple cosine function fit. Something to note is that the time-constant of the exponential term is about  $1\mu\text{s}$  and is still consistent with zero. In comparison, the time-constant extracted by Georgiev *et al.* [127] is  $3.8\mu\text{s}$ , considerably larger than the current value.

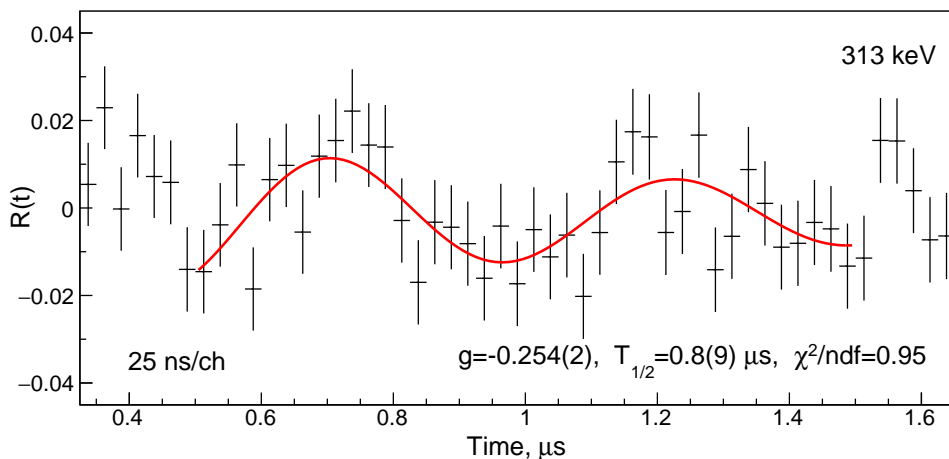


**Figure 4.15:** Fit of the  $R(t)$  function for 313 keV with an exponentially decreasing amplitude.

At the current stage of the analysis we consider the value  $g = -0.26(2)$  from the fit of the  $R(t)$  function obtained after an energy gate on the 313-keV transition as the result for the g factor of the  $9/2^+$  isomer in  $^{67}\text{Ni}$ .

### 4.3.2 $^{69}\text{Ni}$

A partial level scheme of  $^{69}\text{Ni}$  containing the excited states populated after the decay of the  $17/2^-$  isomeric state is shown in Fig. 4.16. The  $\gamma$ -ray energy spectrum for one of the HPGe detectors is presented in Fig. 4.17. No intense lines from beam contamination are observed,  $\gamma$  rays from transitions in the  $\beta$ -decay daughter  $^{69}\text{Cu}$  and grand-daughter  $^{69}\text{Zn}$  are present along with the same background lines ( $^{60}\text{Co}/\text{Ni}$ ,  $^{40}\text{K}$ ,  $^{56}\text{Fe}(n, n'\gamma)$ ).

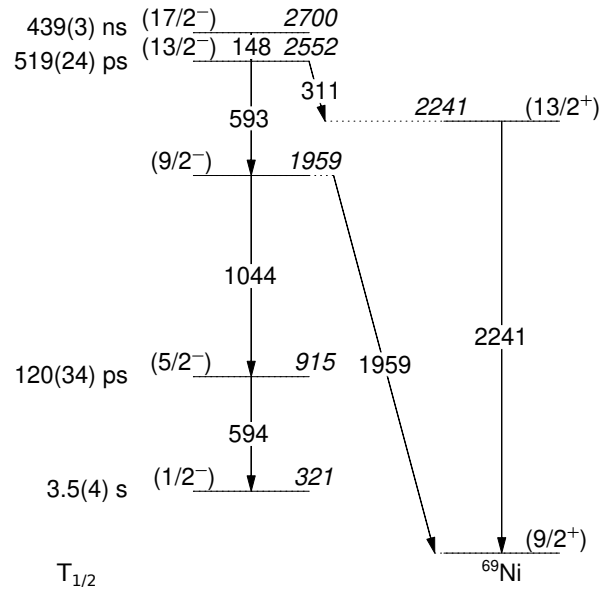


**Figure 4.16:** Partial level scheme of  $^{69}\text{Ni}$  showing the  $17/2^-$  isomeric state and the transitions through which it decays to the  $1/2^-$  isomeric state or the  $9/2^+$  ground state.

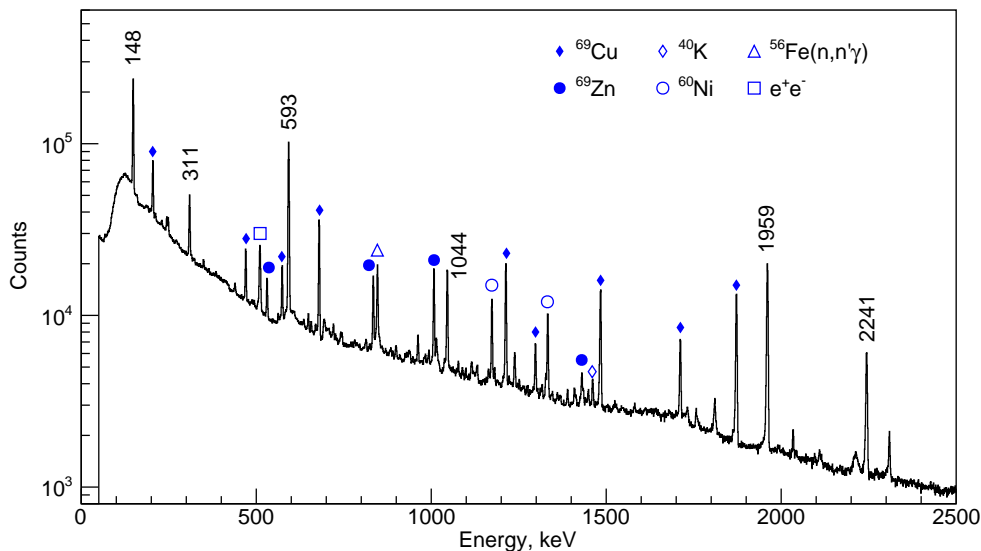


**Figure 4.17:** Total projection of the HPGe detectors  $\gamma$ -ray energy spectra for the  $^{69}\text{Ni}$  data set. The transitions from  $^{69}\text{Ni}$  are denoted with their energies and the other more prominent lines are marked.

The adopted value for the half-life of the  $17/2^-$  isomeric state is  $T_{1/2} = 439(3)$  ns [129] while the lifetimes of all states below the isomer are much lower. Therefore the time-difference spectra for all  $\gamma$ -ray transitions below the isomeric state can be used in the TDPAD analysis. However, out of the observed transitions, only the 148-keV and 593/594-keV transitions proved

to be useful in the analysis. The time-difference spectrum for the 148-keV  $17/2^- \rightarrow 13/2^-$  transition for one of the HPGe detectors is shown in Fig. 4.18. The range of the TAC modules was set at  $5 \mu\text{s}$  as evidenced by the sudden cut-off of the time-difference spectrum. Although less pronounced compared to the  $^{67}\text{Ni}$  case, there is a structure at low time differences due to the prompt background coincidences. Again, the background-subtraction procedure was applied and the resulting time-difference spectrum is shown in Fig. 4.19.

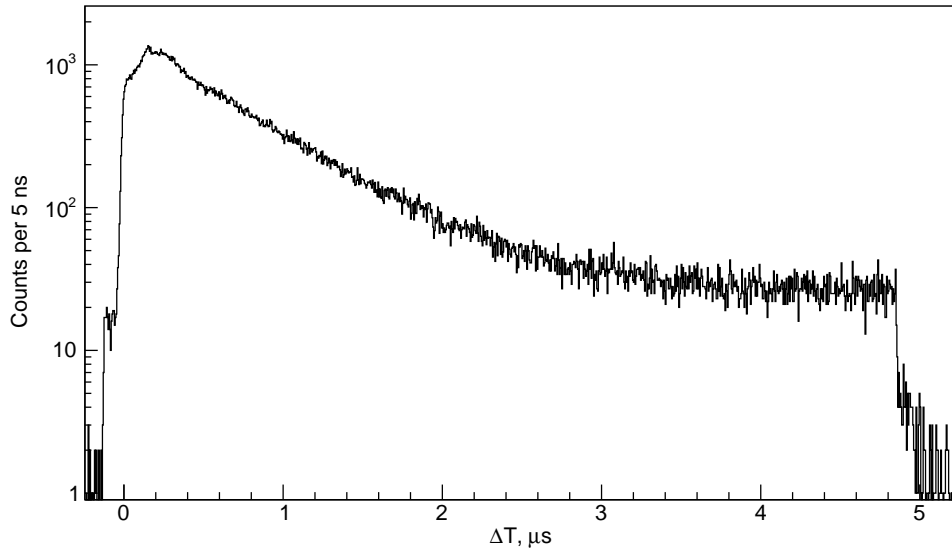


**Figure 4.18:** Time-difference spectrum obtained after a gate on the 148-keV transition in a single HPGe detector.

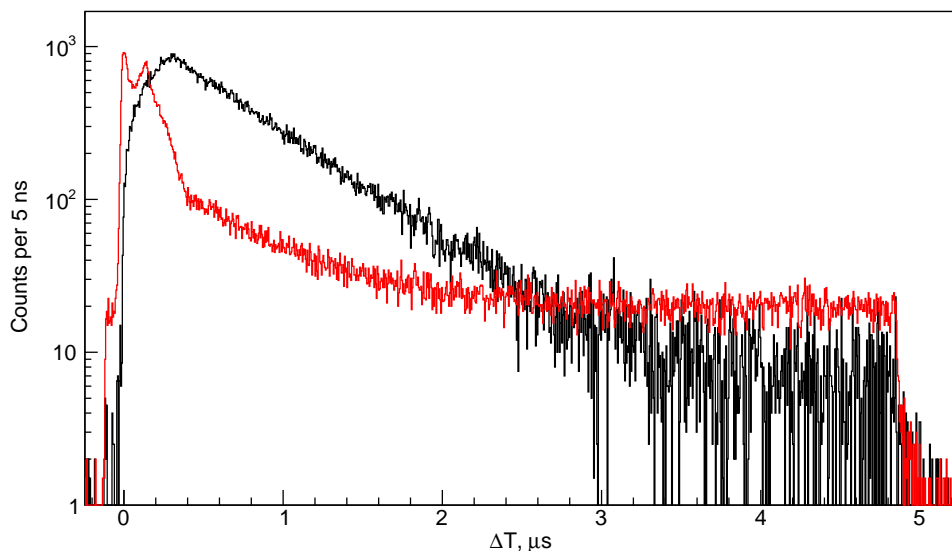


**Figure 4.19:** Comparison of the contribution of the background underneath the 148-keV line to the time-difference spectrum and the background-subtracted time-difference spectrum for a single HPGe detector.

The half-life of the  $17/2^-$  isomeric state was determined to be  $T_{1/2} = 413(4)$  ns with an exponential fit to the time-difference spectrum summed over all  $\gamma$  rays and all four detectors, as shown in Fig. 4.20. The reported uncertainty incorporates both the statistical uncertainty of the fit and the systematic uncertainty from varying the fit range. The obtained value is lower than the adopted value of  $439(3)$  ns [129], however, the fit results are stable to changes in the

fit range. The level of statistics in the current experiment is about three orders of magnitude larger than that in the original study of Ref. [129]. This puts into question the evaluation of the uncertainty of the adopted value as the statistical uncertainty should be much higher than the reported 3 ns uncertainty in Ref. [129].

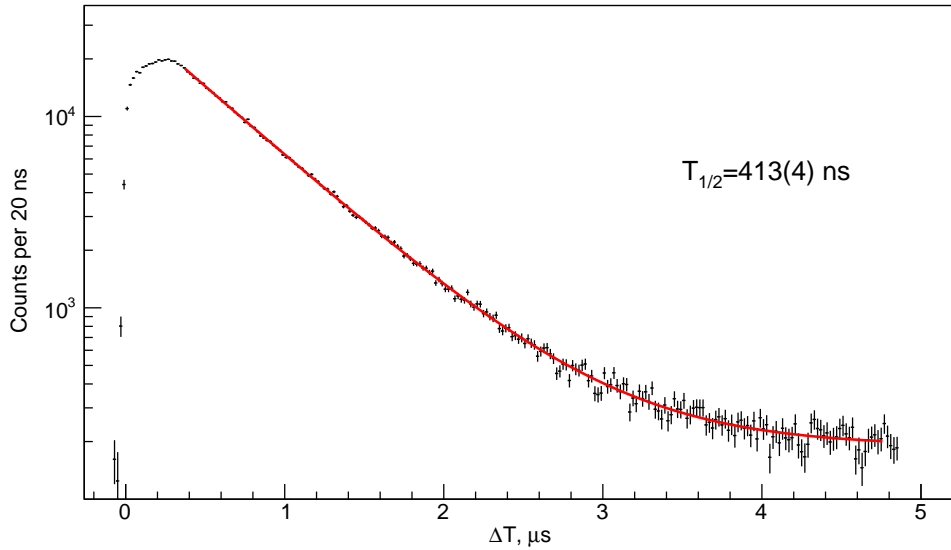


**Figure 4.20:** Exponential fit of the half-life of the  $17/2^-$  isomeric state in  $^{69}\text{Ni}$ .

Following the procedure as explained for the  $^{67}\text{Ni}$  case, multiple experimental  $R(t)$  functions were produced. This was done for both the raw and the background-subtracted time-difference spectra, and for different rebinning factors. The results were found to be stable for the various constructed  $R(t)$  functions. The fitted  $R(t)$  functions for the 148-keV and 593/594-keV transitions are shown in Fig. 4.21 and Fig. 4.22, respectively. The two results are in very good agreement.

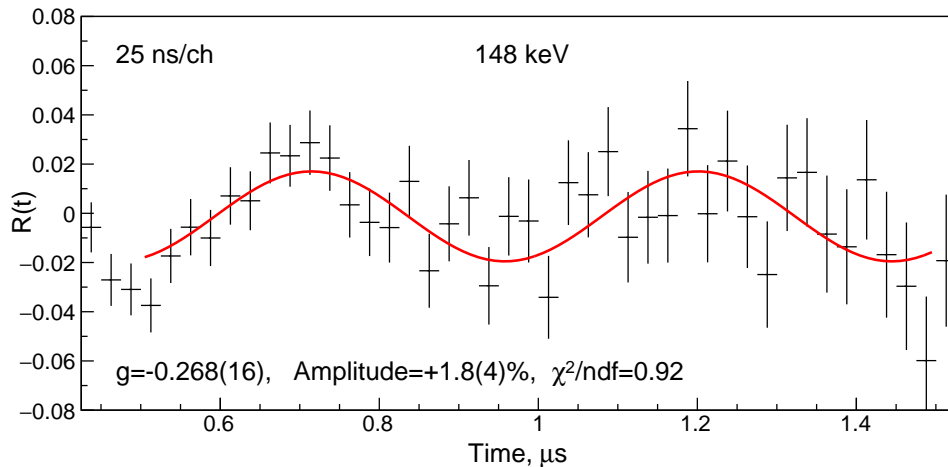


**Figure 4.21:** Fit of the  $R(t)$  function produced using the time-difference spectra after an energy gate on the 148-keV transition in  $^{69}\text{Ni}$ .

The validity of the results from the direct fitting was again tested using the FFT analysis. The magnitude spectrum from the FFT algorithm applied on the 148-keV  $R(t)$  function is presented in Fig. 4.23. The highest frequency peak corresponds to a  $g$  factor of 0.269(57), which agrees very well with the obtained results from the direct fit of the  $R(t)$  function. The centroid of the main frequency peak is very stable to changes in the range of the  $R(t)$  function

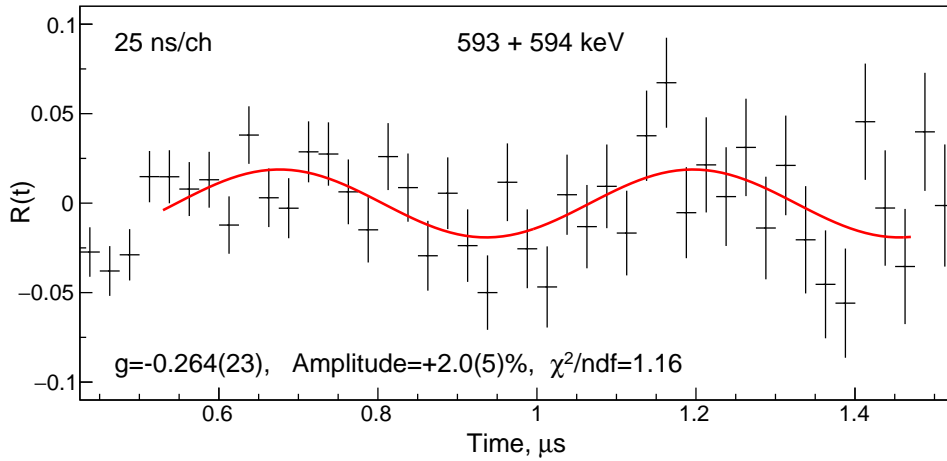


**Figure 4.22:** Fit of the  $R(t)$  function produced using the time-difference spectra after an energy gate on the 593/594-keV transitions in  $^{69}\text{Ni}$ .

on which the FFT algorithm is applied. In magnitude, the peak is about a factor of two above the background frequencies. The observed second peak at higher frequency, corresponding to a  $g \approx 1.5$ , is most likely due to fluctuations in the  $R(t)$  function being interpreted as a high-frequency oscillation. The magnitude spectrum for the 593/594-keV  $R(t)$  function exhibits very similar features, only with a larger width of the main frequency peak.

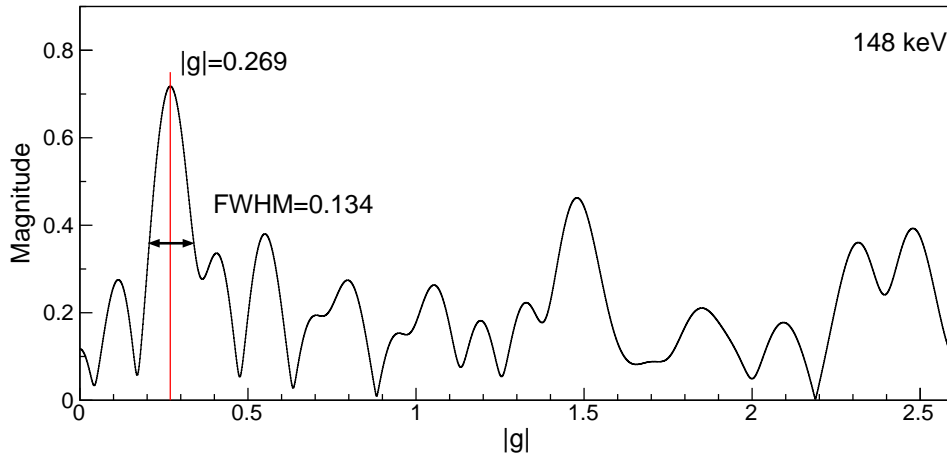


**Figure 4.23:** Magnitude spectrum for the 148 keV  $R(t)$  function obtained for the  $17/2^-$  state in  $^{69}\text{Ni}$ .

With the confirmation from the FFT algorithm, we adopt the value  $g = -0.268(16)$  for the  $g$  factor of the  $17/2^-$  state in  $^{69}\text{Ni}$ .

### 4.3.3 $^{70}\text{Ni}$

The relevant part of the level scheme of  $^{70}\text{Ni}$  is given in Fig. 4.24. The  $\gamma$ -ray energy spectrum from one of the HPGe detectors is shown in Fig. 4.25. One notable observed beam contaminant is  $^{71}\text{Cu}$  which also has a known isomeric state and will be discussed separately in the following Section.

The half-lives of the seniority-multiplet states below the isomer are negligible and all four consecutive  $E2$  transitions to the ground state could in principle be used in the TDPAD analysis. The time-difference spectra obtained for the 183-keV transition is shown in Fig. 4.26.

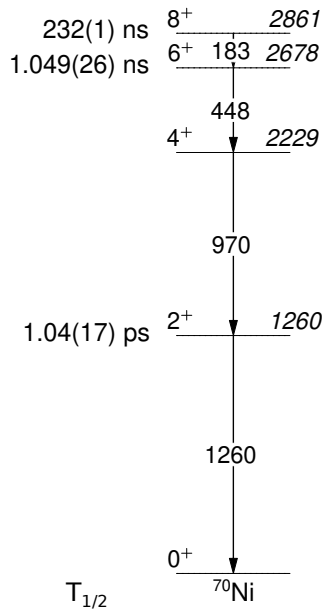


**Figure 4.24:** Partial level scheme of  $^{70}\text{Ni}$  showing the  $8^+$  isomeric state and the cascade of transitions through which it decays to the ground state.

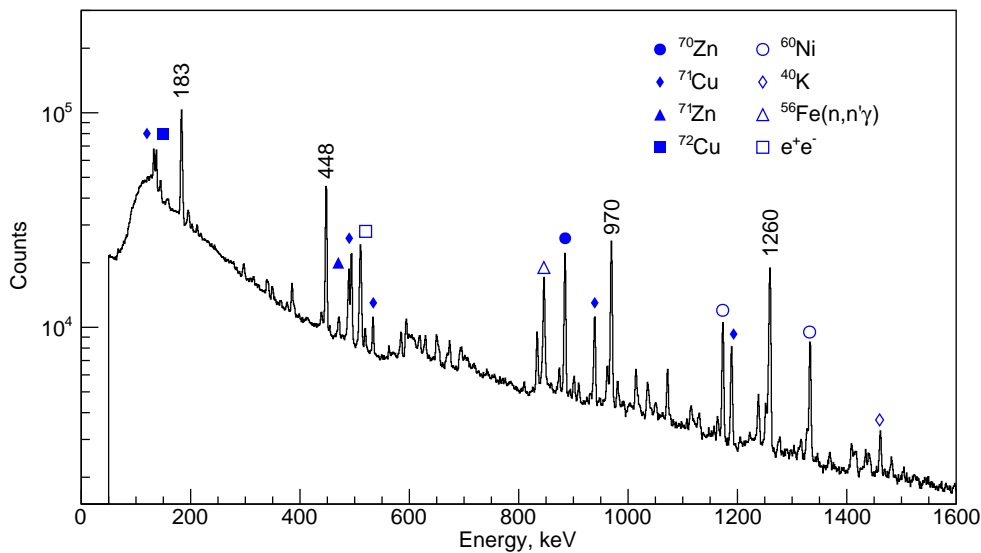


**Figure 4.25:** Total projection of the HPGe detectors  $\gamma$ -ray energy spectra for the  $^{70}\text{Ni}$  data set. The projection is presented up to 1600 keV for better visibility of the relevant part of the spectrum. The transitions from  $^{70}\text{Ni}$  are denoted with their energies and the other more prominent lines are marked.

The background and background-subtracted time-difference spectra for the same transition are shown in Fig. 4.27.

Fitting the exponential decay in the time-difference spectra summed over all four detectors and four  $\gamma$ -ray transitions yielded a half-life of  $T_{1/2} = 231(3)$  ns (see Fig. 4.28). The given uncertainty again considers both the statistical and systematic uncertainties of the performed fit. The present value reproduces exactly the adopted value of 232(1) ns for this half-life [147].

The experimental  $R(t)$  function for the 183-keV transition is presented in Fig. 4.29. The result obtained from the fit was  $g = -0.313(27)$  and it remained very stable to variations in the fit range and the rebinning factor. Due to the relatively low statistics for the higher energy transitions, their respective  $R(t)$  functions were not found to exhibit clear oscillations.

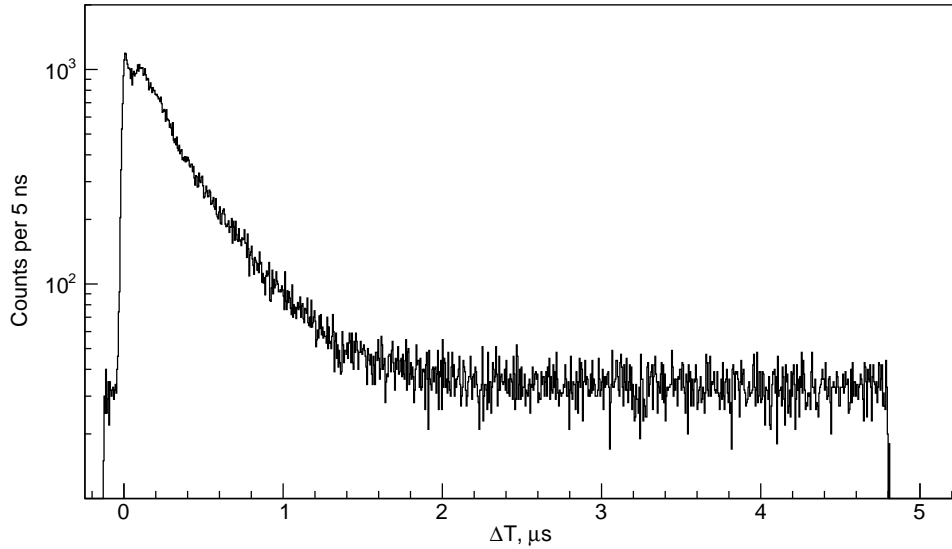


**Figure 4.26:** Raw time-difference spectrum for a single HPGe detector gated on the 183-keV transition.

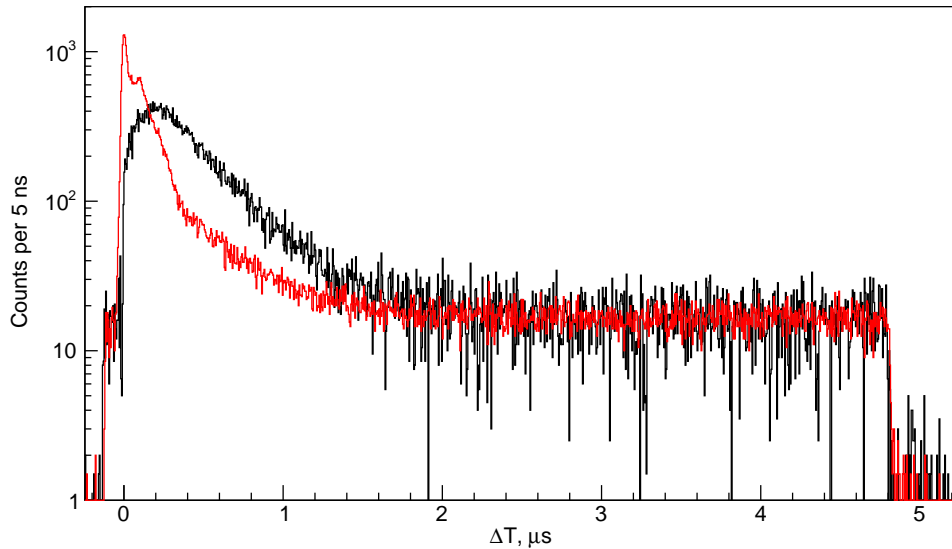


**Figure 4.27:** Comparison of the time-difference contribution of the background underneath the 183-keV line and the background-subtracted time-difference spectrum for a single HPGe detector. The background subtraction procedure was not able to fully remove the constant component of the background.

As for the previous cases, the FFT algorithm was applied on the  $R(t)$  function. The resulting magnitude spectrum is given in Fig. 4.30. The main frequency peak is located at  $|g| = 0.32(10)$  and is in good agreement with the direct fit results. The centroid of the main frequency peak in the magnitude spectrum was quite sensitive to changes in the supplied range of the  $R(t)$  function. Nevertheless, even if shifted, it remained within the uncertainty of the FFT result.

Something to note is that the amplitude of the oscillation from the fit of the  $R(t)$  function for  $^{70}\text{Ni}$  has a negative sign, contrary to those for  $^{67,69}\text{Ni}$ . This is an expected result from the momentum selection for these nuclei - the wing of the momentum distribution for  $^{67,69}\text{Ni}$  vs. the center of the momentum distribution for  $^{70}\text{Ni}$ .

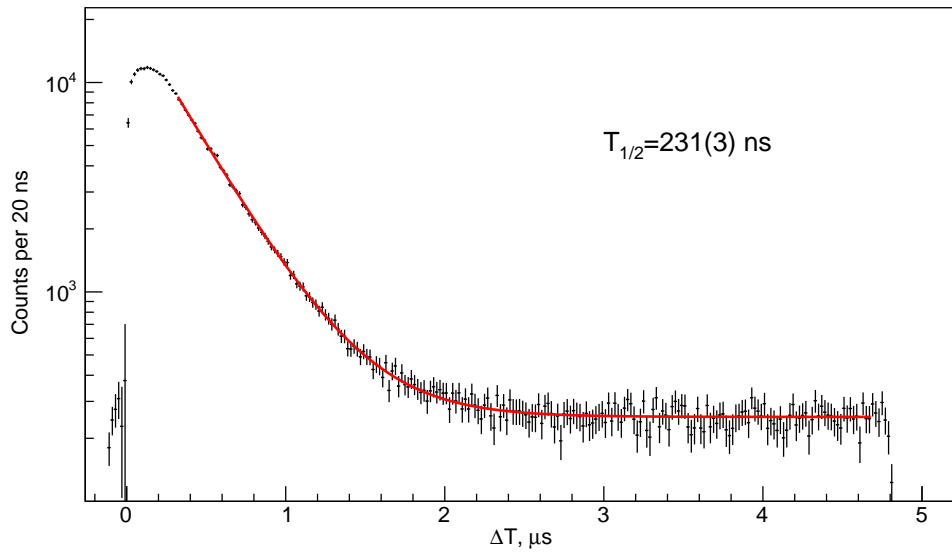


**Figure 4.28:** Exponential fit of the half-life of the  $8_1^+$  isomeric state in  $^{70}\text{Ni}$ .

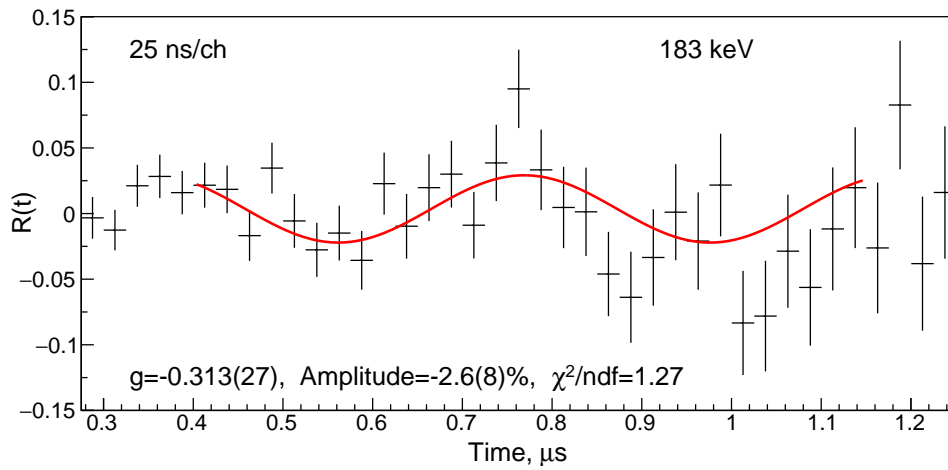


**Figure 4.29:** Fit of the  $R(t)$  function obtained from the time-difference spectra after an energy gate on the 183-keV transition in  $^{70}\text{Ni}$ .

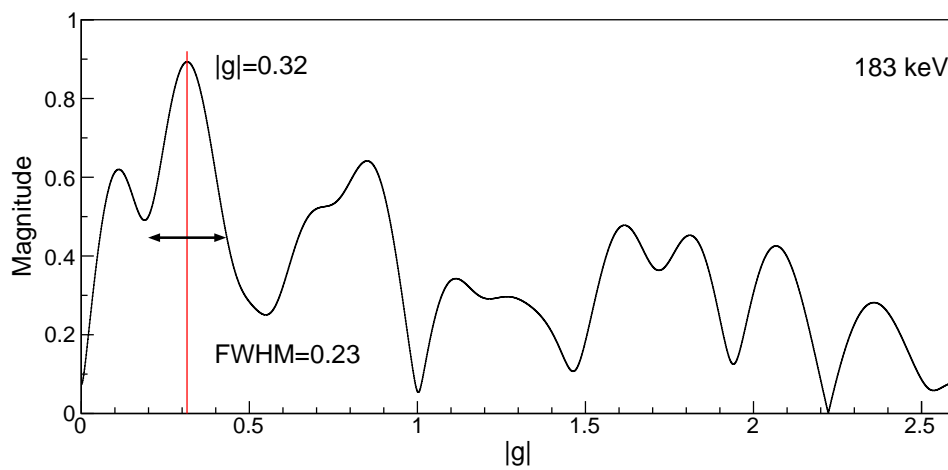


**Figure 4.30:** Magnitude spectrum for the  $R(t)$  function obtained after an energy gate on the 183 keV transition in  $^{70}\text{Ni}$ .

### 4.3.4 $^{71}\text{Cu}$

The presence of  $^{71}\text{Cu}$  in the data for  $^{70}\text{Ni}$  is considered as beam contamination. The  $19/2^-$  isomeric state in  $^{71}\text{Cu}$  was populated in the fragmentation reaction and an attempt was made to measure its g factor. A partial level scheme of  $^{71}\text{Cu}$  is shown in Fig. 4.31.

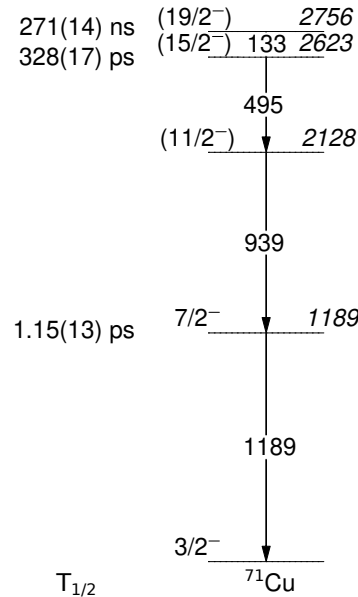


**Figure 4.31:** Partial level scheme of  $^{71}\text{Cu}$  showing the  $19/2^-$  isomeric state and the cascade of transitions with the highest intensity through which it decays to the ground state [148].

The half-life of the isomeric state was measured with an exponential fit to the summed background-subtracted time-difference spectrum from all HPGe detectors and all available  $\gamma$ -ray transitions. The obtained value of  $T_{1/2} = 270(5)$  ns is in agreement with and with a smaller uncertainty than the adopted value of  $271(14)$  ns [148]. The uncertainty of the present value includes the systematic effects of varying the fit range. As can be seen in the HPGe total projection in Fig. 4.25, the 133-keV line is at the top of the Compton continuum background. For this reason the background subtraction procedure is not able to fully account for the structure of the prompt background coincidences.

Multiple  $R(t)$  functions were produced using all of the  $\gamma$ -ray transitions, with and without background subtraction and with different rebinning factors. None of the produced  $R(t)$  functions exhibited well defined oscillations and the fit results were completely unrealistic. The  $R(t)$  functions after a gate on the 133-keV transition is presented in Fig. 4.33. No value for the g factor of the  $17/2^-$  state in  $^{71}\text{Cu}$  could be reliably extracted from the available data.

### 4.3.5 Alignment

The alignment of the spin-oriented ensemble of nuclei can be extracted from the amplitude of the experimental  $R(t)$  function by recalling the detailed expression from Eq. (1.58):

$$R(t, \theta, B) = \frac{3fA_2B_2U_2Q_2}{4 + fA_2B_2U_2Q_2} \cos[2(\theta - \omega_L t - \alpha)]. \quad (4.1)$$

The angular distribution coefficients  $A_2$  can be calculated as the spin-parities of the involved  $\gamma$ -ray transitions are known. If we consider only the  $R(t)$  function obtained for the transition directly depopulating the isomeric state the deorientation coefficients  $U_2$  are equal to unity.

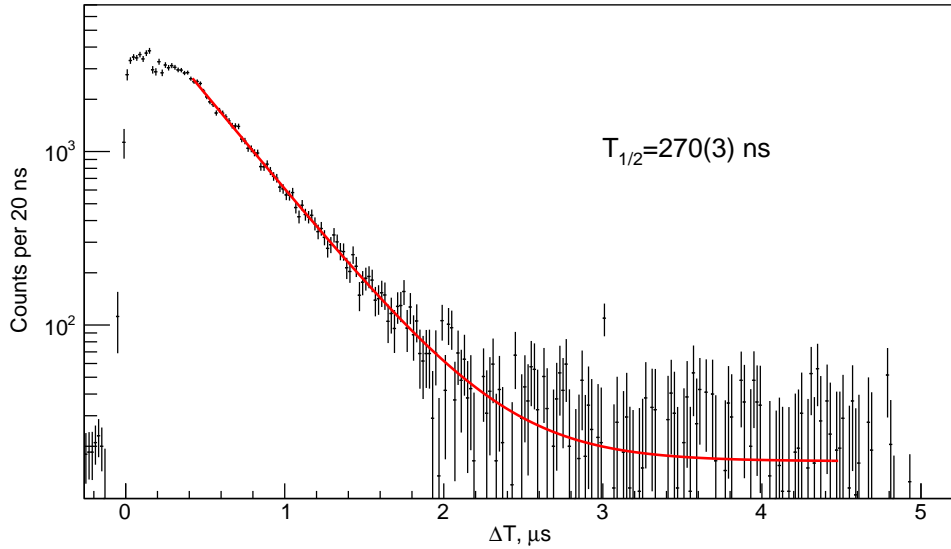


**Figure 4.32:** Exponential fit of the half-life of the  $19/2^-$  state in  $^{71}\text{Cu}$ .

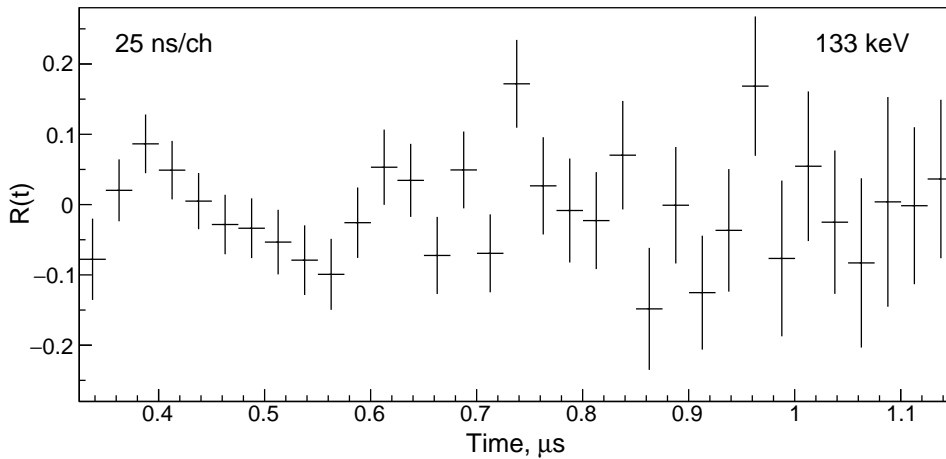


**Figure 4.33:** The  $R(t)$  function obtained from the time-difference spectra after an energy gate on the 133-keV transition in  $^{71}\text{Cu}$ .

The geometrical factor has been calculated to be  $Q_2 = 0.90(2)$  from the known size of the SeGa HPGe detectors and their distance from the implantation host. As described in Chapter 1.2.1, the fraction of nuclei  $f$  that have retained their orientation until implantation is dependent on the charge state of the nuclei. At the beam energies above 100 MeV/A used in the current experiment the secondary beam fragments are expected to be fully stripped. In that case the orientation is fully preserved and  $f = 1$ . In the present experiment the fragments pass through the plastic scintillator before implantation and electron pick-up is estimated to be less than 5% and is neglected in the following calculations. Then, the orientation parameter  $B_2$  can be determined from the amplitude of the  $R(t)$  function. The orientation parameter is linked to the alignment through Eq. (1.31). The results obtained for the alignment of the  $^{67,69,70}\text{Ni}$  nuclei in the current experiment are summarized in Table 4.2.

It should be noted that if we consider the fit with the exponentially decreasing amplitude for  $^{67}\text{Ni}$ , the amplitude at the time of implantation is higher. The amplitude from the fit is  $2.3(1)\%$ , which yields  $B_2 = -0.081(5)$  and alignment  $A = -7.4(5)\%$ . However, the time-constant of the exponential decrease of the amplitude in Fig. 4.15 was consistent with zero. Therefore the increase in the amplitude and in the alignment is likely an overestimation.

**Table 4.2:** The level of alignment determined for the nickel isotopes in the  $^{76}\text{Ge}$  fragmentation reaction.

Nuclide	Transition	Setting	Amplitude, %	$A_2$	$B_2$	Alignment, %
$^{67}\text{Ni}$	$9/2^+ \rightarrow 5/2^-$	Wing	+1.0(2)	-0.433	-0.035(7)	-3.2(7)
$^{69}\text{Ni}$	$17/2^- \rightarrow 13/2^-$	Wing	+1.8(4)	-0.378	-0.083(17)	-7.5(15)
$^{70}\text{Ni}$	$8^+ \rightarrow 6^+$	Center	-2.6(8)	-0.387	+0.105(34)	+5.6(18)

## 4.4 Discussion

### 4.4.1 $^{67}\text{Ni}$

The observed discrepancy between the results obtained in this work and those of Georgiev *et al.* [127] are not fully understood. A short overview of the original measurement at GANIL and the current one at NSCL is given below.

In the first experiment, performed in 1999 at GANIL, the  $^{67}\text{Ni}$  nuclei were produced and spin-oriented in the fragmentation of a primary beam of  $^{76}\text{Ge}$  (61.4 MeV/A) on a  $^9\text{Be}$  target (145 mg/cm<sup>2</sup>) [127]. As mentioned above, this was the first experiment to utilize the TDPAD method following a projectile-fragmentation reaction. As this was an exploratory work, some experimental parameters were not optimized. The  $^{67}\text{Ni}$  secondary beam passed through a 300  $\mu\text{m}$  Si energy-loss detector for particle identification with the  $\Delta E$  vs. Time-of-Flight (TOF) technique. The silicon detector also provided the  $t = 0$  signal for the implantation of the beam nuclei. The  $^{67}\text{Ni}$  ions exiting the thick silicon detector had an energy low enough that a fraction of them ( $\approx 15\%$ ) are expected to be in a H-like ionic state rather than bare nuclei. As in the RIV methods, the hyperfine interaction between the electrons and the nuclear magnetic dipole moment causes a precession of the nuclear spin around the total spin of the ion as it recoils through vacuum. This introduces  $G_k$  attenuation factors to the nuclear spin orientation and leads to an overall loss of alignment. The secondary beam then passed through a stack of aluminium sheets, used as beam-energy degraders, with a total thickness around 250  $\mu\text{m}$ . The ensemble of  $^{67}\text{Ni}$  nuclei exiting each individual sheet of aluminium has an increasing fraction of H-like ions due to the energy losses in each aluminium layer. The passage through each layer of material resets the electron configuration of the ions and the overall loss of spin orientation is multiplicative. The passage through the thick Si detector and the aluminium degraders is estimated to have lead to around 80% loss of the initial spin alignment, which in turn would have resulted in a loss of amplitude of the oscillation in the ratio function. Finally, the beam was implanted in a copper host at the center of the TDPAD experimental setup, located at the first focal plane of the LISE magnetic spectrometer [149]. The setup consisted of three BaF<sub>2</sub> detectors and two HPGe clover detectors in the horizontal plane and an electromagnet, as shown schematically in Fig. 4.34. The three BaF<sub>2</sub> detectors, placed in the optimal detector positions for determining the sign of the g factor, could not be used in the data analysis due to their poor energy resolution. Thus, only the absolute g-factor value  $|g(9/2^+, ^{67}\text{Ni})| = 0.125(6)$  could be extracted from the ratio function obtained from the two HPGe clover detectors, shown in Fig. 4.35. The accuracy of the result can be questioned due to the presence of the issues highlighted above, however, in principle they are expected to only reduce the amplitude of the oscillations and not modify their frequency.

Coming back to the  $^{67}\text{Ni}$  experiment at NSCL, multiple improvements of the experimental setup were implemented compared to the one at GANIL. A thick Si particle detector was used only for beam tuning and was exchanged for a thin plastic scintillator during the data taking.

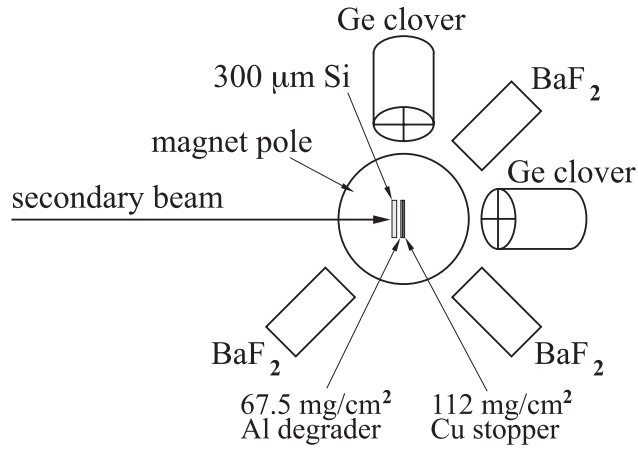


**Figure 4.34:** Schematic of the experimental setup used in the original TDPAD measurement on  $^{67}\text{Ni}$  at GANIL [127].

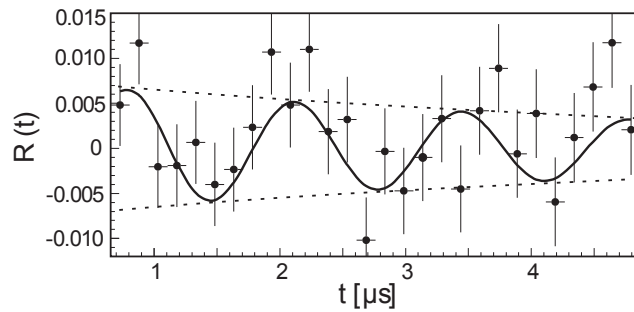


**Figure 4.35:** Experimental ratio function for the  $9/2^+$  isomeric state in  $^{67}\text{Ni}$  obtained in the experiment at GANIL [127]. An exponential decrease of the oscillation amplitude is associated with the relaxation of the copper host.

The fraction of H-like  $^{67}\text{Ni}$  ions after the plastic scintillator is expected to be less than 5%. No aluminium degraders were used in order to preserve the spin alignment until implantation. The detector configuration (see Fig. 4.4) was optimized to be able to determine the sign of the  $g$  factor. One possible issue with the experimental setup was the  $^9\text{Be}$  primary target used for the fragmentation of the  $^{76}\text{Ge}$  beam in the NSCL experiment which had a thickness of  $376 \text{ mg/cm}^2$  ( $\approx 2 \text{ mm}$ ), compared to just  $41 \text{ mg/cm}^2$  ( $\approx 0.22 \text{ mm}$ ) at GANIL. The momentum selection in the wing of the momentum distribution was similar in the GANIL and NSCL experiments for  $^{67}\text{Ni}$  - approximately 2% off from the center of the momentum distribution. However, the use of a thick target is expected to have significantly shifted the center of the momentum distribution and increased the width of the distribution due to energy losses of the primary beam and reactions in different parts of the target. This is thought to have decreased the spin alignment in the selected momentum region leading to a lower observed amplitude of the oscillations. Although this hypothesis could explain the relatively low spin alignment observed in the experiment, it does not provide any clues as to why the observed frequencies in the two measurements differ by a factor of two. From all of the above it becomes clear that both measurements of  $g(9/2^+, ^{67}\text{Ni})$  were problematic in some aspects and neither one can be assumed as “more accurate” than the other.

Regarding the physics interpretation of the obtained results, we performed shell model calculations using the ANTOINE code. The calculations were performed using the JUN45 interaction [150] with a  $^{56}\text{Ni}$  core in the  $fp_{g9/2}$  model space. The result from the calculations using the free-nucleon  $g$  factors predict  $g^{free} = -0.42$ . Using effective spin  $g$  factors with a

quenching factor of 0.75 yields a value of  $g^{eff} = -0.32$ . The wave function of the  $9/2^+$  state is very much fragmented between multiple configurations, listed in Table 4.3. The expected 1p-1h configuration  $\nu \left( p_{3/2}^4 f_{5/2}^6 p_{1/2}^0 g_{9/2}^1 \right)$  comprises just 23% of the total. Another 19% and 16% of the wave function are due to  $3p$ - $3h$  excitations with a neutron pair from the  $f_{5/2}$  being excited to the  $p_{1/2}$  and the  $g_{9/2}$  orbitals, respectively. Further,  $3p$ - $3h$  excitations with the promotion of a pair from the  $p_{3/2}$  to the  $p_{1/2}$  or the  $g_{9/2}$  are both responsible for 8% fractions of the wave function. The rest of the relevant configurations are mostly attributed to  $5p$ - $5h$  excitations.

**Table 4.3:** Wave-function composition for  $^{67}\text{Ni}$  obtained from the shell-model calculations with the JUN45 interaction.

Configuration	Fraction, %
$\nu g_{9/2}^1$	23
$\nu f_{5/2}^{-2} p_{1/2}^2 g_{9/2}^1$	19
$\nu f_{5/2}^{-2} g_{9/2}^3$	16
$\nu p_{3/2}^{-2} f_{5/2}^{-2} p_{1/2}^2 g_{9/2}^3$	9
$\nu p_{3/2}^{-2} p_{1/2}^2 g_{9/2}^1$	8
$\nu p_{3/2}^{-2} g_{9/2}^3$	8
$\nu f_{5/2}^{-4} p_{1/2}^2 g_{9/2}^3$	4
$\nu p_{3/2}^{-2} f_{5/2}^{-2} g_{9/2}^5$	4
$\nu f_{5/2}^{-4} g_{9/2}^5$	2
$\nu p_{3/2}^{-1} f_{5/2}^{-1} g_{9/2}^3$	1
$\nu p_{3/2}^{-2} f_{5/2}^{-4} p_{1/2}^2 g_{9/2}^5$	1

The value obtained using the effective spin g factors  $g^{eff} = -0.32$  is not in agreement with the experimental result from the current work  $g_{exp} = -0.26(2)$ . Interestingly, the shell-model calculations performed in Ref. [127] using the effective spin g factors yielded  $g^{eff} = -0.284$ ,  $g^{eff} = -0.290$  and  $g^{eff} = -0.252$  with the S3V interaction [151], the modified Hjorth-Jensen interaction [152] and with the generalized seniority approach [153], respectively. All of the above values are closer to the experimental result than our JUN45 calculations, with the generalized seniority value in very good agreement with the current result. The different available theoretical values for the g factor of the  $9/2^+$  state in  $^{67}\text{Ni}$  are presented in Table 4.4 and are compared with the two experimental values in Fig. 4.36.

**Table 4.4:** Summary of available calculations for the  $g(9/2^+, ^{67}\text{Ni})$  value. Note that the first two columns use a quenching factor of 0.75, while the latter three calculations, taken from Ref. [127], use a quenching factor of 0.7 for the effective spin g factors. For more details see text and Ref. [127].

	Schmidt limit	JUN45	S3V	Hjorth-Jensen	gen. seniority
Effective	-0.32	-0.32	-0.284	-0.290	-0.252
Free-nucleon	-0.43	-0.42	-0.407	-0.415	

The factor of two difference between the experimental value of  $|g| = 0.125(6)$  from Ref. [127] and the calculations performed for the same publication led the authors to suggest a two-state mixing scenario of the pure  $\nu g_{9/2}$  configuration with a  $1^+$ -excitation of a proton from  $f_{7/2}$  to  $f_{5/2}$ . A 2% contribution from the proton excitation coupled to the  $\nu g_{9/2}$  was found to be enough

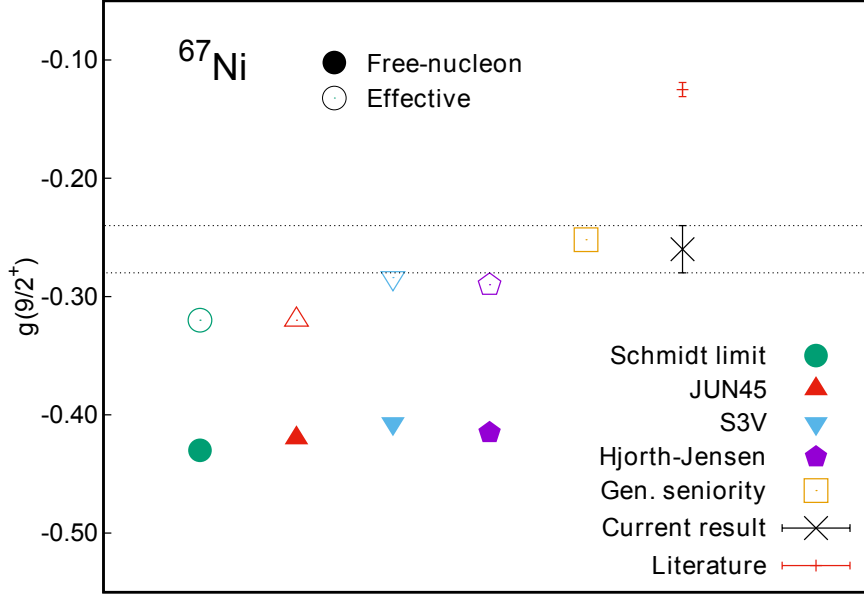


**Figure 4.36:** Experimental values for  $g(9/2^+, {}^{67}\text{Ni})$  from the current work (black) and from Ref. [127] compared with the Schmidt values and calculations with various interactions. Filled symbols denote calculations performed using free-nucleon spin  $g$  factors and empty symbols - calculations with effective spin  $g$  factors. Dotted lines correspond to the  $1\sigma$  uncertainty interval of the experimental result and are drawn to guide the eye.

to reproduce their experimental results. In the newly performed calculations with a  ${}^{56}\text{Ni}$  core proton excitations are prohibited and a larger basis is needed.

In order to put the results for  ${}^{67}\text{Ni}$  in perspective, analogous calculations with ANTOINE and the JUN45 interaction were carried out for the less exotic  ${}^{63}\text{Ni}$  and  ${}^{65}\text{Ni}$ . In both cases the model space was the same as for the  ${}^{67}\text{Ni}$  calculations and only effective spin  $g$  factors were used. The calculations for  ${}^{63}\text{Ni}$  yielded  $g^{eff} = -0.311$  which differs from the experimental result  $g(9/2^+, {}^{63}\text{Ni}) = -0.269(3)$  [130]. The simple  $1p-1h$  excitation of the odd  $f_{5/2}$  neutron to the  $g_{9/2}$  orbital represents the largest component of the wave function at 40%. The other relevant configurations are from  $3p-3h$  excitations with an additional pair of neutrons from  $p_{3/2}$  promoted to either the  $f_{5/2}$  (21%), the  $p_{1/2}$  (11%) or the  $g_{9/2}$  (11%) orbital. Only 2% of the wave function has been assigned to the excitation of the pair of neutrons in  $f_{5/2}$  to either  $p_{1/2}$  or  $g_{9/2}$ . Overall, 81% of the wave function is expected to be in a configuration with a single valence neutron in  $g_{9/2}$ . This gives confidence that the  $9/2^+$  state in  ${}^{63}\text{Ni}$  is a pure  $\nu g_{9/2}$  state.

The results from the  ${}^{65}\text{Ni}$  calculations are very similar. The obtained value  $g^{eff} = -0.313$  is in good agreement with the experimental result  $g(9/2^+, {}^{65}\text{Ni}) = -0.296(3)$  [131]. Again, the excitation of the odd  $f_{5/2}$  neutron to the  $g_{9/2}$  orbital accounts for the largest component of the wave function at 39%. The contribution of additional excitations of a pair of neutrons from the  $p_{3/2}$  has decreased to 30%, while it has increased to 16% for the promotion of pairs from the  $f_{5/2}$ . The overall fraction of the  $\nu(g_{9/2})^1$  configurations in the wave function has slightly decreased to 66% of the total. Therefore the  $9/2^+$  state in  ${}^{65}\text{Ni}$  can still be considered a rather pure  $g_{9/2}$  state.

A comparison can be made with the calculations performed for  ${}^{65}\text{Ni}$  in Ref. [132]. The used valence space included the  $\pi f_{7/2} p_{3/2} f_{5/2} p_{1/2}$  and the  $\nu p_{3/2} f_{5/2} p_{1/2} g_{9/2}$  orbitals. A  ${}^{40}\text{Ca}$  core with 8 protons “frozen” in  $f_{7/2}$  was used to be able to study the influence of proton excitations. The utilized interaction was the interaction from Ref. [139], modified to reproduce the excitation energies of the  $9/2^+$  states in  ${}^{61}\text{Fe}$  and  ${}^{63}\text{Ni}$ . The authors point out that the

experimental value is in very good agreement with the effective Schmidt value for a  $g_{9/2}$  neutron  $g^{eff} = -0.298$ , obtained with a quenching factor of 0.7 for the spin g factors. However, their calculations show that the inclusion of proton excitations across  $Z = 28$  allows for the experimental result to be well reproduced with free-nucleon g factors. Allowing for a total of five  $p-h$  excitations for protons and neutrons the calculations with free-nucleon g factors yielded a value of  $g^{free} = -0.304$ , very close to the experimental one  $g_{exp} = -0.296(3)$ . The authors suggest that this is due to the large valence space of more than one major shell for both neutrons and protons. With such a large valence space it is possible that most of the correlations in the wave function have been taken into account.

The last  $\nu g_{9/2}$  state that can be compared to the  $^{67}\text{Ni}$   $9/2^+$  state is the ground state of  $^{69}\text{Ni}$ . Our ANTOINE calculations yield a value of  $g^{eff} = -0.315$ , which is equal to the predicted value for  $^{67}\text{Ni}$   $g^{eff} = -0.316$ . This is to be expected as the only difference between the two states is that the  $p_{1/2}$  is empty in  $^{67}\text{Ni}$  and full in  $^{69}\text{Ni}$ . Looking into more details, the natural  $0p-0h$  excitation  $\nu(p_{3/2}^4 f_{5/2}^6 p_{1/2}^2 g_{9/2}^1)$  configuration comprises just 30% of the wave function. The other major contributions come from  $2p-2h$  excitations from  $p_{1/2}$  (17%),  $f_{5/2}$  (14%) or  $p_{3/2}$  (12%) to the  $g_{9/2}$  orbital. Unfortunately, the g factor of the  $^{69}\text{Ni}$  ground state has not been experimentally determined yet. The half-life of  $^{69}\text{Ni}$  is 11.4(3) s which should render its magnetic moment accessible to laser spectroscopy methods.

The known experimental g factors of  $g_{9/2}$  states around  $N = 40$  are shown in Fig. 4.37 for Fe, Ni, Zn, Ge and Se isotopes, along with the effective Schmidt limit value. The observed trends for Ge and Zn isotopes show a minimum around  $N = 39$  where the g factors are expected to approach the Schmidt values. The notable exception is exactly the  $^{67}\text{Ni}$  experimental value, which is higher than expected in both the current work and Ref. [127]. Another notable feature is the value for  $^{61}\text{Fe}$  from Ref. [143]. It is higher than the corresponding  $^{63}\text{Ni}$  as the proton  $f_{7/2}$  is not filled and proton excitations play a role. A similar mechanism could be responsible for the discrepancy between our calculations and experimental results for  $^{67}\text{Ni}$ , as was suggested by Georgiev *et al.*, although to a lesser degree. As mentioned above, the use of a  $^{56}\text{Ni}$  core in our calculations prohibits any proton excitations. Therefore more sophisticated calculations will be performed using the LNPS interaction with a  $^{48}\text{Ca}$  core. The results should allow for the importance of protons excitations across  $Z = 28$  to the g factor of the  $9/2^+$  state in  $^{67}\text{Ni}$  to be assessed.

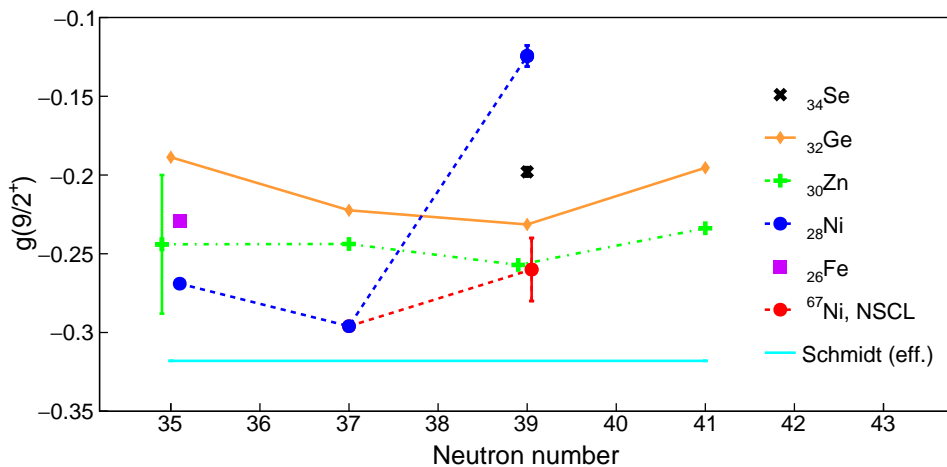


**Figure 4.37:** All measured g factors of  $g_{9/2}$  states in the vicinity of  $^{68}\text{Ni}$  and  $N = 40$ . Most of the experimental uncertainties are not large enough to be visible. The trends visible for Ge and Zn isotopes is not reproduced in the Ni isotopic chain. The sudden change in behaviour at  $^{67}\text{Ni}$  is attributed to proton excitations.

### 4.4.2 $^{69}\text{Ni}$

The obtained experimental value of  $g(17/2^-, ^{69}\text{Ni}) = -0.268(16)$  is compared with theoretical calculations. First, we performed calculations similar to those in the previous Section - using the ANTOINE code with the JUN45 interaction and a  $^{56}\text{Ni}$  core. Then, analogous calculations using the j-coupled code NATHAN were performed by Dr. Kamila Sieja, IPHC Strasbourg. In addition, Dr. Sieja performed ANTOINE calculations using the LNPS interaction [140] and a  $^{48}\text{Ca}$  core. The ANTOINE and NATHAN calculations will be discussed and compared to the expectations of the extreme single-particle model before continuing with the results from the calculations using the LNPS interaction.

The ANTOINE code follows the m-scheme and considers the different configurations in terms of particle-hole excitations. In contrast, the NATHAN code uses a j-coupling scheme and provides the configurations in terms of the number of broken pairs of nucleons. As such, the g factor results from the two codes are equivalent yet their interpretations are complementary. Both codes yield the values  $g^{free} = -0.297$  and  $g^{eff} = -0.223$  with free-nucleon and effective spin g factors, respectively. The wave-function composition for the  $17/2^-$  state in  $^{69}\text{Ni}$  obtained from the ANTOINE calculations is listed in Table 4.5. The calculations indicate that the dominant part of the wave function is the expected  $1p-1h$  excitation configuration  $\nu(p_{1/2}^{-1}g_{9/2}^2)$  at 62%. The various  $3p-3h$  excitations follow with a total of 34%, followed by less than 4% of  $5p-5h$  and higher order excitations.

**Table 4.5:** Wave-function composition for  $^{69}\text{Ni}$  obtained from the shell-model calculations with the JUN45 and LNPS interactions.

JUN45		LNPS	
Configuration	Fraction, %	Configuration	Fraction, %
$\nu p_{1/2}^{-1}g_{9/2}^2$	61	$\nu p_{1/2}^{-1}g_{9/2}^2$	67
$\nu f_{5/2}^{-2}p_{1/2}^{-1}g_{9/2}^4$	11	$\nu f_{5/2}^{-1}g_{9/2}^2$	4
$\nu f_{5/2}^{-1}p_{1/2}^{-2}g_{9/2}^4$	9	$\nu f_{5/2}^{-2}p_{1/2}^{-1}g_{9/2}^4$	4
$\nu p_{3/2}^{-2}p_{1/2}^{-1}g_{9/2}^4$	9	$\pi f_{7/2}^{-2}f_{5/2}^2 \otimes \nu p_{1/2}^{-1}g_{9/2}^2$	4
$\nu p_{3/2}^{-1}f_{5/2}^{-1}p_{1/2}^{-1}g_{9/2}^4$	4	$\pi f_{7/2}^{-1}p_{3/2}^1 \otimes \nu p_{1/2}^{-1}g_{9/2}^2$	3
$\nu p_{3/2}^{-2}f_{5/2}^{-2}p_{1/2}^{-1}g_{9/2}^6$	1	$\pi f_{7/2}^{-1}p_{3/2}^1 \otimes \nu f_{5/2}^{-1}g_{9/2}^2$	3
		$\pi f_{7/2}^{-2}p_{3/2}^2 \otimes \nu p_{1/2}^{-1}g_{9/2}^2$	2
		$\pi f_{7/2}^{-1}f_{5/2}^1 \otimes \nu p_{1/2}^{-1}g_{9/2}^2$	1

Turning to the NATHAN results, again the configuration with the highest contribution is  $\nu(p_{1/2}^{-1}g_{9/2}^2)$  at 62%, as expected. The decomposition in terms of broken pairs yields an 84% fraction of configurations with a single broken pair. This fraction is higher than that for  $1p-1h$  excitations from ANTOINE as the promotion of an additional unbroken pair of neutrons to  $g_{9/2}$  is considered as a  $3p-3h$  excitation, while the number of broken pairs remains one. The configurations with one broken pair correspond to seniority  $\nu = 3$  configurations as there is already one odd valence neutron. A neutron pair from either  $p_{1/2}$  or  $f_{5/2}$  is broken to promote one neutron to the  $g_{9/2}$ . The three unpaired nucleons - two  $g_{9/2}$  neutrons and the neutron hole present in the  $fp$  shell, are coupled to  $J = 17/2^-$  and make a  $\nu = 3$  configuration. In contrast, the  $1/2^-$  state from the  $\nu(g_{9/2})^2$  seniority multiplet also requires one broken pair in the  $fp$  shell, yet the resulting two neutrons in  $g_{9/2}$  are coupled to  $J = 0^+$ , which is a  $\nu = 1$  configuration. Even though the  $\nu(p_{1/2}^{-1}g_{9/2}^2)$  configuration represents such a large fraction, the

rest of the configurations still have an impact on the g factor value. This is seen by comparing the values to the extreme single-particle model predictions for the same  $\nu(p_{1/2}^{-1}g_{9/2}^2)$  configuration -  $g_{s,p}^{free} = -0.325$  and  $g_{s,p}^{eff} = -0.244$ . These values show a 10% difference compared to the JUN45 results. One final point from these calculations are the average occupancies of the orbitals. The results show the occupancies of the  $p_{3/2}$ ,  $f_{5/2}$ ,  $p_{1/2}$  and the  $g_{9/2}$  orbitals to be 3.70, 5.55, 0.91 and 2.83, respectively.

The ANTOINE calculations with the LNPS interaction yielded slightly smaller values -  $g^{free} = -0.273$  and  $g^{eff} = -0.206$ . The experimental value  $g_{exp} = -0.268(16)$  is in agreement with the free-nucleon LNPS result. The obtained fractions of the relevant single-particle configurations are also listed in Table 4.5. The dominant configuration is the expected neutron  $1p-1h$  excitation  $\nu(p_{1/2}^{-1}g_{9/2}^2)$  at 67% with no proton excitations. Every other individual configuration accounts for under 5% of the wave function. These include a total of 9% of the  $\nu(p_{1/2}^{-1}g_{9/2}^2)$  configuration coupled to  $1p-1h$  and  $2p-2h$  proton excitations to the  $p_{3/2}$  or  $f_{5/2}$  orbitals. Another fraction of about 9% is due to neutron excitations with no proton contributions. Considering the total number of excitations, both neutron and proton, there are 71% of  $1p-1h$ , 7% of  $2p-2h$  and 14% of  $3p-3h$  excitations. The average occupancies of the neutron  $p_{3/2}$ ,  $f_{5/2}$ ,  $p_{1/2}$  and  $g_{9/2}$  orbitals are found to be 3.96, 5.73, 1.09 and 2.19. When compared to those from the JUN45 calculations there are clear differences. The main difference is that the occupancy of  $g_{9/2}$  is much lower when proton excitations are considered in the calculations. It also seems that the role of excitations from  $\nu p_{3/2}$  are exaggerated in the JUN45 calculation and are found to be almost negligible in the LNPS calculation. The occupancies of the proton  $f_{7/2}$ ,  $p_{3/2}$ ,  $f_{5/2}$  and  $p_{1/2}$  orbitals are 7.68, 0.15, 0.16 and 0.01, respectively. The protons are equally probable to be excited to  $p_{3/2}$  and  $f_{5/2}$ .

The g-factor results obtained from the calculations with the LNPS interaction show that the experimental result is in agreement with the free-nucleon value, rather than the effective value. An additional LNPS calculation was performed by Dr. Sieja in which the proton excitations were prohibited. The effective spin g factor then becomes  $g^{eff} = -0.242$  and lies relatively close to the experimental value  $g_{exp} = -0.268(16)$ . Thus, the scenario is somewhat similar to that of  $^{65}\text{Ni}$  described in Ref. [132]. The experimental result lies in between the calculated g factors with effective spin g factors and no proton excitations, and the free-nucleon g factor result when proton excitations are considered. The conclusion is therefore the same as for  $^{65}\text{Ni}$  in Ref. [132] - the calculations with the LNPS interaction in the larger valence space seem to have taken into account most, if not all, of the correlations in the wave function. The g-factor values from all performed calculations are listed in Table 4.6 and are compared with the experimental result in Fig. 4.38.

**Table 4.6:** Summary of available calculations for the  $g(17/2^-, ^{69}\text{Ni})$  value. A quenching factor of 0.75 is used for the effective spin g factors in all calculations.

	Schmidt limit	JUN45	LNPS	LNPS (no $\pi$ exc.)
Effective	-0.244	-0.222	-0.206	-0.242
Free-nucleon	-0.325	-0.296	-0.273	

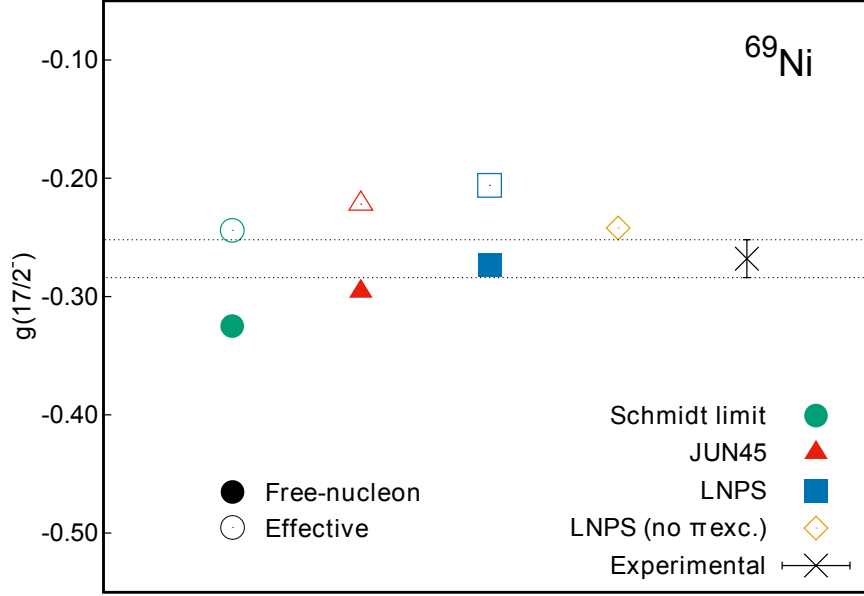


**Figure 4.38:** Experimental result for  $g(17/2^-, {}^{69}\text{Ni})$  from the current work compared with the Schmidt values and calculations with the JUN45 and LNPS interactions.

### 4.4.3 ${}^{70}\text{Ni}$

The experimental result for the g factor of the  $8^+$  state in  ${}^{70}\text{Ni}$  was compared to the same set of theoretical calculations. We performed ANTOINE calculations with the JUN45 interaction ( ${}^{56}\text{Ni}$  core) and Dr. Sieja performed NATHAN calculations with the JUN45 interaction ( ${}^{56}\text{Ni}$  core) and ANTOINE calculations with the LNPS interaction ( ${}^{48}\text{Ca}$  core).

The free-nucleon and effective Schmidt values for the  $\nu(g_{9/2})_{J=8^+}^2$  configuration are  $g^{free} = -0.425$  and  $g^{eff} = -0.319$ , respectively. Almost identical values are obtained through the JUN45 calculations:  $g^{free} = -0.420$  and  $g^{eff} = -0.315$ . The effective values agree well with the experimental one  $g_{exp} = -0.313(27)$ . The natural  $0p-0h$  excitation  $\nu(g_{9/2})^2$  configuration has the largest contribution to the wave function at 43%, with the full list of relevant configurations given in Table 4.7. The other relevant configurations are the  $2p-2h$  excitations to the  $g_{9/2}$  from the  $p_{1/2}$  (16%), the  $f_{5/2}$  (11%) or the  $p_{3/2}$  (11%) orbitals. In total, the  $2p-2h$  excitations make up 47% of the wave function. A minor role is also played by  $4p-4h$  excitations (10%) and the higher order excitations are negligible (<1%).

The decomposition in terms of broken pairs from the NATHAN calculations shows that the wave function is dominated by an 85% fraction of a single broken pair of  $g_{9/2}$  neutrons. This can be interpreted as a very pure  $\nu(g_{9/2})^2$  seniority  $\nu = 2$  configuration. The higher seniority configurations with two (5%), three (10%) and four (<1%) broken pairs are not considered to be very significant. The obtained occupancies of the  $p_{3/2}$ ,  $f_{5/2}$ ,  $p_{1/2}$  and  $g_{9/2}$  orbitals are 3.61, 5.55, 1.49 and 3.34, respectively. An almost equal probability to excite neutrons from any of the three  $fp$ -shell orbitals to the  $g_{9/2}$  is observed.

When compared to the JUN45 results, the g-factor values obtained in the LNPS calculations are significantly smaller:  $g^{free} = -0.345$  and  $g^{eff} = -0.260$ . A comparison between all calculated values for the g factor of the  $8_1^+$  state in  ${}^{70}\text{Ni}$  are shown in Table 4.8 and Fig. 4.39. The configuration with the largest contribution to the wave function is the expected  $0p-0h$  configuration at 66%. The next two configurations with the highest significance are the  $2p-2h$  excitations from the  $p_{1/2}$  (6%) and the  $f_{5/2}$  (6%) to the  $g_{9/2}$ . The remaining 22% of the wave function are divided into a multitude of configurations, most of which below 1% contribution.

**Table 4.7:** Wave-function composition for  $^{70}\text{Ni}$  obtained from shell-model calculations with the JUN45 and LNPS interactions.

JUN45		LNPS	
Configuration	Fraction, %	Configuration	Fraction, %
$\nu g_{9/2}^2$	43	$\nu g_{9/2}^2$	66
$\nu p_{1/2}^{-2} g_{9/2}^4$	16	$\nu p_{1/2}^{-2} g_{9/2}^4$	6
$\nu f_{5/2}^{-2} g_{9/2}^4$	11	$\nu f_{5/2}^{-2} g_{9/2}^4$	6
$\nu p_{3/2}^{-2} g_{9/2}^4$	11	$\pi f_{7/2}^{-2} f_{5/2}^2 \otimes \nu g_{9/2}^2$	4
$\nu f_{5/2}^{-1} p_{1/2}^{-1} g_{9/2}^4$	6	$\pi f_{7/2}^{-1} p_{3/2}^1 \otimes \nu g_{9/2}^2$	2
$\nu f_{5/2}^{-2} p_{1/2}^{-2} g_{9/2}^6$	3	$\pi f_{7/2}^{-2} p_{3/2}^2 \otimes \nu g_{9/2}^2$	2
$\nu p_{3/2}^{-1} p_{1/2}^{-1} g_{9/2}^4$	2	$\pi f_{7/2}^{-1} f_{5/2}^1 \otimes \nu g_{9/2}^2$	1
$\nu p_{3/2}^{-1} f_{5/2}^{-1} g_{9/2}^4$	2		
$\nu p_{3/2}^{-2} p_{1/2}^{-2} g_{9/2}^6$	2		
$\nu p_{3/2}^{-2} f_{5/2}^{-2} g_{9/2}^6$	2		

The relevant proton  $1p-1h$  and  $2p-2h$  excitations account for about 8% of the wave function. Nevertheless, they seem to have a large impact on the  $g$  factor as evidenced by the decrease compared to the Schmidt value. To test this, a second LNPS calculation was performed by Dr. Sieja with effective spin  $g$  factors and no particle-hole excitations for the protons. The resulting value  $g^{eff} = -0.318$  is in very good agreement with our experimental result. Contrary to the  $^{69m}\text{Ni}$  case, it seems that there are still some correlations not fully accounted for since all performed calculations with effective spin- $g$  factors reproduce the experimental result, as visible in Fig. 4.39.

**Table 4.8:** Summary of available calculations for the  $g(8^+, ^{70}\text{Ni})$  value. A quenching factor of 0.75 is used for the effective spin  $g$  factors in all calculations.

	Schmidt limit	JUN45	LNPS	LNPS (no $\pi$ exc.)
Effective	-0.319	-0.315	-0.260	-0.318
Free-nucleon	-0.425	-0.420	-0.345	

Finally, the occupancies of the neutron orbitals are very similar to those of the  $^{69}\text{Ni}$  calculations. An occupancy of 3.96 for the  $p_{3/2}$  indicates the insignificant contribution of neutron excitations from this orbital. The  $f_{5/2}$  and  $p_{1/2}$  with their respective occupancies 5.76 and 1.77 also show that the probability to excite neutrons to  $g_{9/2}$  from either orbital are identical. The 2.44 occupancy of the  $g_{9/2}$  shows that when proton excitations are considered the need for multi-particle-multi-hole excitations to the  $g_{9/2}$  decreases. Looking at the proton orbital occupancies, the  $f_{7/2}$  is largely unchanged at 7.72 and the  $p_{1/2}$  is still negligible at 0.01. However, there is a small change in the higher-lying orbitals, when compared to the  $^{69}\text{Ni}$  calculations. The occupancy of the  $f_{5/2}$  at 0.16 is about 50% higher than that of the  $p_{3/2}$  at 0.11. This could be linked to the fact that the  $f_{7/2}$  and  $f_{5/2}$  are spin-orbit partners and spin-flip excitations become preferential.

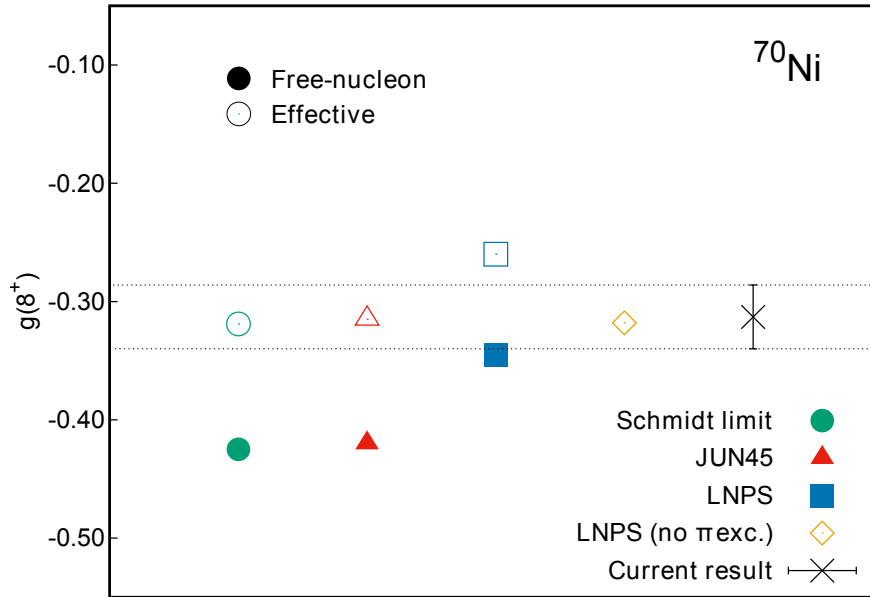


**Figure 4.39:** Experimental result for  $g(8^+, {}^{70}\text{Ni})$  from the current work compared with the Schmidt values and calculations with the JUN45 and LNPS interactions.

#### 4.4.4 ${}^{71}\text{Cu}$

No result could be obtained for the  $g$  factor of the  $19/2^-$  state in  ${}^{71}\text{Cu}$ . Calculations within the extreme single particle model suggest that the  $g$  factor of this state should be close to zero -  $g = +0.06$  and  $g = +0.04$  with effective and free-nucleon  $g$  factors, respectively. Additional calculations with the ANTOINE code, again with a  ${}^{56}\text{Ni}$  core and the JUN45 interaction, also give the same values. In such a case, the strength of the external magnetic field needs to be between 5 and 10 times higher than the one used in the current experiment. Only then the Larmor frequency would be similar to that of the  ${}^{69,70}\text{Ni}$  oscillations and at least one period of the oscillations could be observed in the same time-frame.

# 5 - Summary and outlook

## 5.1 $^{22}\text{Ne}$ , $^{28}\text{Mg}$ and the $N = 20$ island of inversion

The first TDRIV experiment on a radioactive ion beam was performed at ISOLDE, CERN, with the aim to measure the  $g$  factor of the  $2_1^+$  state in  $^{28}\text{Mg}$ . A calibration TDRIV measurement on the  $2_1^+$  state of  $^{22}\text{Ne}$  was also performed to determine the zero-offset distance of the MINIBALL plunger device. The analysis yielded a value for  $g(2_1^+, ^{22}\text{Ne})$  in stark disagreement with the adopted value of Horstman *et al.* [28] from a TDRIV measurement in the 1970s. After a review of the experimental details in Ref. [28] some possible flaws in the assumptions for the charge-state distribution of the ions exiting the target foil were discovered. The possibly erroneous adopted value for  $g(2_1^+, ^{22}\text{Ne})$  made the precise determination of the zero-offset distance impossible, introducing large systematic uncertainties.

Without the suitable calibration  $g$  factor, both the  $^{22}\text{Ne}$  and  $^{28}\text{Mg}$  TDRIV measurements could not yield precise results. The correlation between the two  $g$  factors was considered in order to cancel out the dependence on the zero-offset distance. The resulting correlation plot indicated that the  $g(2_1^+, ^{22}\text{Ne})$  value from Ref. [28] is likely an underestimation. Comparison with shell-model calculations points to a value in between the current result and that of Ref. [28].

To resolve this discrepancy simulations were performed in preparation for a new TDRIV measurement of  $g(2_1^+, ^{22}\text{Ne})$ . A proposal was prepared, submitted and accepted for this measurement to be performed at GANIL. The experimental setup will include the new OPSA particle detector array, which is under development. It is expected that a successful TDRIV experiment on  $^{22}\text{Ne}$  at GANIL would provide an accurate and precise value of  $g(2_1^+, ^{22}\text{Ne})$ . With this value one can immediately extract a value for  $g(2_1^+, ^{28}\text{Mg})$  from the correlation of the two  $g$  factors. The value of  $g(2_1^+, ^{28}\text{Mg})$  obtained in this way will likely be with an uncertainty that would hinder detailed nuclear structure interpretation. Nevertheless, we consider that the  $^{28}\text{Mg}$  measurement has shown that the TDRIV method is applicable to RIBs.

A natural continuation of this study would be to perform TDRIV measurements on the  $2_1^+$  states in  $^{30}\text{Mg}$  and  $^{32}\text{Mg}$  to probe the  $N = 20$  island of inversion. The major difficulty would be to obtain the needed level of statistics in a reasonable amount of beam time. It is expected that when the Facility for Rare Isotope Beams (FRIB) at MSU, USA, becomes fully operational the intensity of a  $^{32}\text{Mg}$  beam would be of the order of  $10^6$  pps. This is similar to the intensity of the  $^{28}\text{Mg}$  beam at HIE-ISOLDE. With the valuable experience obtained from this proof-of-concept measurement the experimental setup can be optimized for a  $^{32}\text{Mg}$  TDRIV measurement. Special care must be taken for the HPGe detectors to be able to handle the inevitable high  $\gamma$ -ray rates from the decay of beam nuclei scattered within the chamber. The particle detector must also be able to perform well with a high rate of incident particle as to not hinder the measurement.

## 5.2 $^{46}\text{Ti}$ and the TDRIV method for higher- $Z$ nuclei

A proof-of-concept experiment for the application of the TDRIV method on Li-like ions is in preparation. The use of Li-like ions will provide an alternative to TDRIV on Na-like ions for nuclei in the  $fp$  shell. The experiment will attempt to measure the  $g$  factor of the  $2_1^+$  state in  $^{46}\text{Ti}$  at JYFL, Finland. An accurate and precise value for this  $g$  factor would render it a suitable calibration point for TF measurements in the region.

A charge-state measurement was performed on the more abundant  $^{48}\text{Ti}$  using the RITU gas-filled recoil separator at JYFL. The charge-state distributions of Ti ions exiting several different target materials at different exit energies of the ions were studied. This was done to optimize the beam energy, target and reset foil materials and thicknesses for the TDRIV measurement. The presence of contaminant nuclei in the beam composition was identified which interfered with the data taking and the following analysis. Nevertheless, charge-state distributions as a function of energy were obtained for Nb and Ta foils and partly for C and Mg foils.

Simulations were performed to establish the feasibility of two possible configurations of HPGe detectors that could be available at the time of the experiment. The relevant electron configurations of the expected ionic species were discussed with their expected relative populations. Taking these experimental parameters, the simulations showed that a detector configuration that includes the 24 clover HPGe detectors would be optimal. However, in case they are not available, the array of 15 co-axial HPGe detectors would still allow for the measurement to be performed at the cost of overall efficiency and a decreased amplitude of the oscillations. A successful TDRIV measurement on Li-like ions would pave the way for future  $g$ -factor measurements on both stable and radioactive isotopes in the  $fp$  shell and above.

Other possible cases to be studied using the TDRIV method on Li-like ions are already being explored. Simulations are ongoing to establish the feasibility of a TDRIV measurement on the  $2_1^+$  states in  $^{72,74}\text{Se}$  at GANIL. The experimental setup would be identical to the one intended for the  $^{22}\text{Ne}$  H-like TDRIV measurement. The SPIRAL1 facility is expected to be able to provide beams in the order of  $10^6$  pps for the radioactive  $^{72}\text{Se}$  with a maximum beam energy of 10 MeV/A. This beam energy would be ideal for such a measurement as the maximum of the Li-like fraction of Se ions is expected to be at around 9 MeV/A. With an atomic number  $Z = 34$ , selenium would be at the upper limit of applicability of the Li-like ions. At higher- $Z$  one has to use Na-like ions and the analysis of such data becomes more complex. In general, it would be preferable to perform several experiments with Li-like ions to gain more understanding of the influence of the atomic state structure for simpler ions before going to higher- $Z$  nuclei with Na-like. However, more data is needed also from experiments on Na-like ions to observe systematic effects that are present. Currently with only one such experiment it is difficult to make conclusions about the proper methods for simulating the atomic state structure and for analysing the experimental data. Therefore, continuing from the successful  $^{56}\text{Fe}$  measurement on Na-like ions at ALTO, a proposal for a  $^{54}\text{Cr}$  measurement on Na-like ions was prepared. The proposal has already been accepted to be performed again at ALTO under very similar experimental conditions to the  $^{56}\text{Fe}$  experiment. When sufficient experience with the TDRIV method on Na-like ions is gained with the easily accessible stable isotopes one could start to explore heavier systems and radioactive isotopes.

### 5.3 The region around $^{68}\text{Ni}$ and g factors of isomeric states

An experiment was performed to measure the g factors of isomeric states in  $^{67,69,70}\text{Ni}$  using the TDPAD method. The states of interest were populated and spin-oriented in a projectile-fragmentation reaction at NSCL, MSU, USA. A moderate degree of spin-alignment was obtained for beam energies around 130 MeV/A with similar values for nuclei in the wing and the center of the momentum distribution. For all isotopes, mainly the  $\gamma$  rays directly depopulating the isomeric state were shown to exhibit a clear oscillatory pattern due to the interaction of the nuclear spin with the external magnetic field. The g factors extracted from the experimental  $R(t)$  functions were compared with shell-model calculations.

The result obtained for the  $9/2^+$  state in  $^{67}\text{Ni}$   $g(9/2^+, ^{67}\text{Ni}) = -0.26(2)$  does not agree with the previous measurement in Ref. [127], however, it is reproduced by some older calculations with effective spin g factors. New calculations with the LNPS interaction will be performed to test the relevance of proton excitations across  $Z = 28$  that were suggested in Ref. [127]. A proposal to re-measure this g factor at GANIL has been submitted. In the proposed measurement a  $^{70}\text{Zn}$  primary beam will be used, instead of  $^{76}\text{Ge}$  as in the previous two experiments which is expected to result in higher spin alignment of the  $^{67}\text{Ni}$  fragments. The obtained g-factor value should definitively resolve the current discrepancy.

For the  $17/2^-$  state in  $^{69}\text{Ni}$ , the experimental value  $g(17/2^-, ^{69}\text{Ni}) = -0.268(16)$  agrees very well with the LNPS interaction predictions using free-nucleon spin g factors. This indicates that the large valence space allows for most of the correlations in the wave function of the state to be accounted for.

The  $^{70}\text{Ni}$  result  $g(8_1^+, ^{70}\text{Ni}) = -0.313(27)$  agrees very well with calculations for effective spin g factors without considering proton excitations. LNPS calculations with proton excitations slightly overestimate the g factor with free-nucleon g factors and underestimate it with effective ones. This could be taken as an indication that the calculations manage to account for a large part of the correlations and a quenching factor between 0.75 and 1 would be more suitable for this case.

Attempts to improve the precision of the results are ongoing in order to further clarify their interpretation.

A measurement of the  $g_{9/2}$  ground-state g factor of  $^{69}\text{Ni}$  would be of interest to compare with the values for  $^{67}\text{Ni}$ . An experiment aimed at the moments and charge radii measurements along the nickel isotopic chain through laser spectroscopy was performed at ISOLDE. The study intended to also measure  $^{69}\text{Ni}$ , however, results have not yet been published. A g-factor measurement on any of the states from the  $g_{9/2}$  seniority multiplet in  $^{68}\text{Ni}$  would also be incredibly valuable to compare with theoretical calculations.

On a more general note, the TDPAD method has been successfully used in multiple experiments to measure the magnetic moments of isomeric states. Since the experiment described in Chapter 4 was performed in 2005 the progress in beam development has been immense. Facilities such as RIKEN, Japan, have provided a wide range of rare isotopic beams that expand the regions of the nuclear chart that are accessible for experiments. In addition, the work of Ichikawa *et al.* [13] introduced the two-step projectile fragmentation process with momentum-dispersion matching that can achieve a higher degree of spin-alignment relative to the single-step projectile fragmentation. This significantly reduces the required experimental time or equivalently the needed level of statistics to observe the oscillations of the  $R(t)$  function, which allows for even more exotic nuclei to be studied. One example is the case of the  $10^+$  isomeric state in  $^{130}\text{Sn}$  for which there is already an accepted proposal at RIKEN. The  $^{130}\text{Sn}$  beam will be produced as a tertiary beam after two-neutron removal from the  $^{132}\text{Sn}$  secondary

beam. The  $10^+$  isomeric state ( $T_{1/2} = 1.6\mu\text{s}$ ) is understood as two coupled  $\nu h_{11/2}$  holes. It is expected to have a g factor consistent with those of  $\nu h_{11/2}$  states in odd- $A$  Sn isotopes which lie close to the effective Schmidt limit. However, the results from an initial TDPAD experiment on this state performed at RIKEN yielded a value much closer to the free-nucleon Schmidt limit, which is unexpected from a theoretical point of view. The new planned measurement will improve on some technical experimental details compared to the previous one and hopefully yield a definitive answer as to the g factor of the  $10^+$  state

Shorter-lived isomeric states in the nanosecond range can also shed light on the structure in the vicinity of  $^{132}\text{Sn}$ . They are inaccessible for the TDPAD method as they would mostly decay in-flight within the mass-spectrometer. Instead the Time-Dependent Perturbed Angular Correlation (TDPAC) method could be used. The idea behind the TDPAC method is the same as for the TDPAD method with the difference that the time-evolution of  $\gamma$ - $\gamma$  angular correlations is observed. These are the correlations between the  $\gamma$  rays populating and depopulating the isomeric state of interest. The use of angular correlation also circumvents the need for initial spin-alignment of the nuclear ensemble as the orientation of the nuclear spin is obtained from the  $\gamma$ - $\gamma$  angular correlations. This allows also for the short-lived isomers to be populated after  $\beta$  decay of the implanted nucleus. So far, the TDPAC method has not been utilized for experiments at RIKEN. A proposal for the first such experiment to be performed at RIKEN was submitted and accepted with the aim to measure the g factor of the  $6^+$  state in  $^{132}\text{Sn}$  ( $T_{1/2} = 20$  ns). This state is expected to have the same structure as the  $8^+1$  isomer ( $T_{1/2} = 2.1\mu\text{s}$ ) -  $\nu f_{7/2}^1 \otimes h_{11/2}^{-1}$ . An attempted TDPAD experiment to directly measure the g factor of the  $8^+$  state was unsuccessful. Therefore, the TDPAC measurement on the  $6^+$  state was proposed as an alternative to access the nuclear structure information of these states. The successful application of the TDPAC method on short-lived isomeric states at RIKEN would open a new avenue of research into nuclear structure in exotic nuclei.

# A - Résumé en Français

Le noyau atomique est un système quantique à plusieurs corps composé de deux types de nucléons : les protons et les neutrons. Le noyau est lié par l'interaction nucléaire forte à courte portée qui agit sur les nucléons à l'échelle du femtomètre. Une description exacte de ce système complexe dépasse nos capacités actuelles. Au lieu de cela, différents modèles théoriques sont utilisés pour expliquer les diverses propriétés observées des noyaux. Ces propriétés sont les énergies de liaison, les rayons nucléaires, les spins et les parités, la structure des niveaux excités, les moments dipolaires magnétiques et quadripolaires électriques, etc.

Peu après le début de l'exploration de la structure nucléaire au 20e siècle, certains comportements systématiques de ces propriétés ont été découverts. Par exemple, on a constaté que les noyaux ayant certains nombres de protons  $Z$  et de neutrons  $N$  avaient des énergies de liaison par nucléon plus élevées que les noyaux voisins. Ces nombres sont appelés nombres « magiques » et correspondent à des enveloppes remplies de protons et de neutrons, à l'instar de la structure de l'enveloppe atomique. De nombreuses propriétés des noyaux peuvent être décrites par le modèle en couches nucléaire grâce au remplissage des orbitales des protons et des neutrons. L'ordre des orbitales du modèle en couches commence à changer lorsque l'on passe à des systèmes nucléaires plus exotiques et instables, c'est à dire des noyaux riches en neutrons, ou déficients en neutrons. Cela peut conduire à la disparition de certains nombres magiques établis et à l'apparition de nouveaux nombres magiques dans certaines régions de la carte des nucléides. Afin de comprendre ces changements dans la structure nucléaire, différents modèles théoriques sont en cours d'élaboration. Leur validité doit être testée par comparaison avec les mesures expérimentales des propriétés nucléaires.

Ces dernières années, les propriétés de ces noyaux exotiques sont devenues expérimentalement accessibles dans les installations à faisceaux radioactifs. L'étude des moments dipolaires magnétiques des états nucléaires constitue un axe de recherche particulier. Le moment magnétique est particulièrement sensible à la nature single particule d'un état nucléaire et peut fournir des informations sur la fonction d'onde nucléaire. La mesure des moments magnétiques permet également d'obtenir des informations sur l'ordre relatif des orbitales du modèle en couches et leur occupation par les nucléons, ce qui constitue un test rigoureux des prédictions théoriques. Les principaux objectifs du travail actuel sont d'obtenir des informations sur la structure nucléaire à partir de mesures du moment magnétique sur des états excités dans des noyaux exotiques et de tester les approches méthodologiques qui permettraient l'étude d'un plus grand nombre de ces noyaux.

Le moment dipolaire magnétique d'un état nucléaire est défini comme le produit du spin nucléaire et du facteur  $g$  de l'état. Différentes méthodes de mesure des moments magnétiques des états nucléaires ont été développées en fonction de la demi-vie de l'état en question et le facteur  $g$  est généralement l'observable expérimentale directe. Dans la présente thèse, les facteurs  $g$  des états isomériques ayant des demi-vies de l'ordre allant de quelques nanosecondes à plusieurs microsecondes ont été déterminés à l'aide de la méthode Time-Dependent Perturbed Angular Distribution (TDPAD), tandis que les facteurs  $g$  des états excités avec des demi-vies de l'ordre de la picoseconde ont été mesurés à l'aide de la méthode Time-Differential Recoil-In-Vacuum (TDRIV).

Le principe général de fonctionnement de la méthode TDPAD repose sur l'interaction d'un

noyau avec un champ magnétique. D'un point de vue semi-classique, le champ magnétique exerce un couple sur le moment dipolaire magnétique, ce qui entraîne une précession des spins nucléaires autour de l'axe du champ magnétique à la fréquence de Larmor. Pour un ensemble de noyaux dont le spin est orienté, l'axe d'orientation précèdera autour de l'axe du champ magnétique avec la même fréquence. À son tour, la distribution angulaire des rayons gamma issus de l'état d'intérêt présente également un comportement oscillatoire lorsque l'axe d'orientation tourne. Par conséquent, la mesure des changements d'intensité des rayons gamma à un angle donné en fonction du temps peut être directement reliée au facteur  $g$  de l'état concerné par le biais de la fréquence de Larmor. Dans la méthode TDPAD, quatre détecteurs HPGe sont généralement placés dans le plan horizontal perpendiculairement les uns par rapport aux autres. Une fonction de rapport oscillatoire est construite à partir des intensités de rayons gamma observées dans ces détecteurs et l'ajustement de la fonction de rapport permet d'obtenir le facteur  $g$  de l'état considéré.

Dans la méthode TDRIV, le noyau du projectile frappe une cible et subit une réaction nucléaire qui alimente et oriente le spin de l'état d'intérêt. Le noyau excité recule hors de la cible dans le vide sous la forme d'un ion. Le champ magnétique hyperfin généré par le nuage d'électrons couple les spins nucléaire et atomique et le spin nucléaire commence à précéder autour du spin total de l'ion avec une fréquence proportionnelle au facteur  $g$  de l'état nucléaire d'intérêt et à l'intensité du champ hyperfin. Le temps d'interaction est défini par la distance entre la cible et une deuxième feuille. La modification de la distance entre les deux feuilles permet d'observer l'évolution de la distribution angulaire perturbée des rayons gamma qui dépeuplent l'état d'intérêt. Habituellement, les noyaux du faisceau diffusé ou les fragments légers de la réaction sont enregistrés dans un détecteur de particules afin d'observer les corrélations angulaires perturbées entre les particules et les rayons gamma. Une fonction de rapport est construite à partir des combinaisons de détecteurs de particules et de rayons gamma les plus sensibles, qui est ensuite ajustée pour extraire le facteur  $g$  de l'état considéré.

La première application de la méthode TDRIV sur un faisceau d'ions radioactifs est rapportée dans la présente thèse. L'expérience a été réalisée dans l'installation HIE-ISOLDE, au CERN, et son objectif était de mesurer le moment magnétique du premier état  $2^+$  dans le  $^{28}\text{Mg}$  afin de tester la faisabilité de la méthode TDRIV avec des faisceaux d'ions radioactifs. La motivation physique de cette mesure était d'étudier la transition vers l'îlot d'inversion autour du  $^{32}\text{Mg}$ . On pensait auparavant que la transition vers l'îlot d'inversion était abrupte et se produisait entre les noyaux  $^{30}\text{Mg}$  et  $^{31}\text{Mg}$ . Cependant, des calculs théoriques plus récents suggèrent une transition plus douce à partir du  $^{28}\text{Mg}$ . Cette hypothèse pourrait être testée grâce aux moments dipolaires magnétiques des premiers états  $2^+$  dans les isotopes pairs du Mg, qui sont particulièrement sensibles à la structure de l'état de particule indépendante et peuvent apporter des éclaircissements sur ce sujet.

L'expérience a eu lieu dans l'installation de détecteurs MINIBALL à HIE-ISOLDE en 2017, en utilisant le réseau de détecteurs HPGe MINIBALL, le détecteur à bandes de silicium double face CD et le dispositif à plunger MINIBALL. L'état excité d'intérêt a été peuplé et orienté en spin dans une réaction d'excitation coulombienne sur une cible de  $^{93}\text{Nb}$  au centre du réseau MINIBALL. Le réseau lui-même se compose de huit clusters triples de détecteurs HPGe à segmentation sextuple utilisés pour enregistrer les rayons gamma qui dépeuplent l'état d'intérêt. Les noyaux des faisceaux diffusés sont enregistrés dans le détecteur CD qui comporte quatre quadrants, chacun segmenté en 16 anneaux concentriques et 24 bandes sectorielles. Le dispositif à plunger contrôle la distance entre la cible et la feuille de réinitialisation pour la mesure TDRIV. Pour étalonner le dispositif à plunger, une mesure TDRIV a été effectuée sur l'état  $2_1^+$  du  $^{22}\text{Ne}$  stable pour lequel le facteur  $g$  est connu dans la littérature avec une très bonne

précision. L'analyse TDRIV avec un facteur  $g$  connu permettrait d'extraire la « distance zéro » du plunger - la distance la plus proche entre la cible et les feuilles de réinitialisation avant qu'elles n'entrent en contact. La distance zéro du plunger est essentielle pour la mesure du  $^{28}\text{Mg}$  et pour toute mesure TDRIV en général. Les données ont été récoltées pour 25 distances de plunger avec le faisceau de  $^{22}\text{Ne}$  et pour 10 distances de plunger avec le faisceau de  $^{28}\text{Mg}$ .

Le principal travail d'analyse a commencé par la correction Doppler des rayons gamma enregistrés pour les données du  $^{22}\text{Ne}$  afin de déterminer les positions exactes des clusters MINIBALL. Après un examen minutieux de tous les paramètres pertinents, des améliorations ont été apportées à la sélection des particules diffusées dans le détecteur CD, ainsi qu'à la géométrie du détecteur CD lui-même. Il en résulte une bonne correction Doppler du pic de 1274 keV de la transition  $2_1^+ \rightarrow 0^+$  du  $^{22}\text{Ne}$ . L'analyse TDRIV des données d'étalonnage du  $^{22}\text{Ne}$  a ensuite été réalisée à l'aide d'un ensemble de sous-programmes Fortran écrits par le professeur A.E. Stuchbery, de l'Australian National University. Ces sous-programmes ont été utilisés pour simuler les corrélations angulaires attendues des particules gamma pour toutes les combinaisons particule-gamma possibles dans l'installation utilisée. Les combinaisons les plus sensibles ont été sélectionnées et les rendements expérimentaux en rayons gamma correspondants ont été utilisés pour construire une fonction de rapport. La fonction a été ajustée par un autre sous-programme en effectuant une recherche de grille  $\chi^2$  sur plusieurs paramètres. Le meilleur fit de la fonction de rapport expérimentale pour  $^{22}\text{Ne}$  a donné un résultat qui n'est pas en accord avec la valeur adoptée dans la littérature. Un examen détaillé de la publication originale de cette valeur adoptée soulève quelques questions quant à sa validité. Les données expérimentales issues des mesures effectuées à l'aide de la méthode du champ transitoire sont également en désaccord avec la valeur de ce facteur  $g$  figurant dans la littérature. Cependant, en raison de la valeur inconnue de la distance zéro du plunger dans la présente mesure, le résultat obtenu peut également souffrir d'incertitudes systématiques importantes. De plus, les calculs théoriques pour le facteur  $g$  de l'état  $2_1^+$  du  $^{22}\text{Ne}$  prédisent une valeur intermédiaire entre le résultat actuel et la valeur adoptée.

Les incertitudes systématiques dans la distance zéro du plunger affectent également l'analyse des données du  $^{28}\text{Mg}$  et conduisent à des incertitudes globales très importantes. La valeur obtenue pour le facteur  $g$  de l'état  $2_1^+$  du  $^{28}\text{Mg}$  est en accord avec les prédictions du modèle en couches dans la couche  $sd$  pure, cependant, l'incertitude empêche de tirer des conclusions fermes. Afin de contourner les effets systématiques liés à la méconnaissance de la distance zéro du plunger, la corrélation entre les facteurs  $g$  du  $^{22}\text{Ne}$  et du  $^{28}\text{Mg}$  a été construite. Le facteur  $g$  du  $^{28}\text{Mg}$  qui correspondrait à la valeur adoptée pour le facteur  $g$  du  $^{22}\text{Ne}$  est significativement plus faible que les prédictions du modèle en couches, ce qui donne des indications supplémentaires que la valeur adoptée pour le facteur  $g$  du  $^{22}\text{Ne}$  est une sous-estimation.

La seule façon d'obtenir une valeur finale pour le facteur  $g$  du  $^{28}\text{Mg}$  à partir de l'ensemble des données actuelles est d'effectuer une mesure indépendante du facteur  $g$  de l'état  $2_1^+$  du  $^{22}\text{Ne}$ . Une telle expérience a été proposée, acceptée et devrait être réalisée au GANIL (France), en 2024. Un nouveau détecteur de particules à base de scintillateurs - le réseau de scintillateurs de particules d'Orsay (OPSA) - est en cours de développement à l'IJCLab en collaboration avec GSI (Allemagne). Le détecteur de particules OPSA est spécialement conçu pour les expériences TDRIV et sera utilisé pour les futures mesures sur le  $^{22}\text{Ne}$ . Des simulations ont été réalisées pour l'expérience proposée au GANIL et montrent qu'il devrait être possible d'obtenir un résultat de haute précision pour résoudre définitivement la divergence observée. Si l'expérience s'avère concluante, un résultat pour le facteur  $g$  de l'état  $2_1^+$  du  $^{28}\text{Mg}$  pourra alors être extrait directement de la courbe de corrélation.

Jusqu'à récemment, les mesures du facteur  $g$  avec la méthode TDRIV ont été principalement

limitées aux noyaux légers jusqu'au Mg en raison de la forte dépendance en  $Z^3$  de la fréquence de précession pour les ions de type H. L'accès à des noyaux plus élevés en  $Z$  avec la méthode TDRIV nécessite l'utilisation d'ions de type Li ou Na. Jusqu'à présent, une seule mesure de ce type a été réalisée pour mesurer le facteur  $g$  de l'état  $2_1^+$  du  $^{56}\text{Fe}$  en utilisant des ions de type Na. Le résultat précis obtenu est très important car il peut être utilisé comme point d'étalonnage pour la plupart des mesures du facteur  $g$  avec la méthode du champ transitoire dans la région. L'un des principaux inconvénients de la méthode du champ transitoire est la nécessité d'une mesure d'étalonnage avec un facteur  $g$  bien connu, et le manque de points d'étalonnage appropriés pour de nombreux isotopes, en particulier dans la couche  $pf$ . Par conséquent, le développement de la méthode TDRIV pour les ions de type Li permettrait d'effectuer des mesures précises du facteur  $g$  jusqu'à  $Z \approx 34$ . Ces valeurs peuvent ensuite être utilisées comme points d'étalonnage pour les futures mesures avec la méthode du champ transitoire. Une expérience de validation du concept TDRIV utilisant des ions de type Li est prévue au JYFL (Finlande), pour mesurer le facteur  $g$  de l'état  $2_1^+$  du  $^{46}\text{Ti}$ . Ce facteur  $g$  a été mesuré précédemment à l'aide de la méthode du champ transitoire, mais il présente une grande incertitude et n'est pas en accord avec plusieurs calculs théoriques. En tant que tel, il servira de bon test pour l'application de la méthode TDRIV aux ions de type Li.

En préparation de la mesure TDRIV, une mesure de l'état de charge a été effectuée au JYFL sur l'isotope  $^{48}\text{Ti}$ , plus abondant, afin d'optimiser les conditions expérimentales pour la future expérience. L'objectif de cette mesure était de déterminer la combinaison du matériau de la feuille cible, du matériau de la feuille de réinitialisation et de l'énergie du faisceau primaire qui maximiserait la fraction d'ions de type Li sortant de la cible lors de l'expérience TDRIV. Pour ce faire, un faisceau de  $^{48}\text{Ti}$  à deux énergies initiales a été envoyé au séparateur de recul RITU. Les matériaux des feuilles à étudier (C, Mg, Nb, Ta) ont été placés dans la chambre de la cible RITU et plusieurs feuilles de Ta de différentes épaisseurs ont été utilisées comme dégradeurs d'énergie du faisceau pour moduler davantage l'énergie du faisceau des ions sortant des feuilles. Les ions de recul ont traversé le séparateur RITU jusqu'au plan focal où une feuille d'au épaisse a été placée. Trois détecteurs à scintillateur ZnS ont été placés à côté de la feuille d'au à près de 90 degrés par rapport à l'axe du faisceau pour enregistrer les taux d'ions Ti diffusés. La modification du champ magnétique de l'aimant dipolaire RITU a permis à différents états de charge des ions Ti d'atteindre le plan focal et a entraîné des changements dans l'intensité des particules diffusées dans les détecteurs ZnS.

Pendant la mesure de l'état de charge, des balayages du champ magnétique ont été effectués pour obtenir l'intensité relative des ions Ti diffusés pour les différents états de charge, pour diverses combinaisons d'énergie de faisceau primaire, de dégradeur Ta et de matériau de feuille à étudier. Une complication inattendue a été la présence de contaminants du faisceau qui n'ont pas pu être identifiés pendant la mesure. Dans le cadre de l'analyse des données obtenues, les états de charge du faisceau de  $^{48}\text{Ti}$  ont été identifiés par comparaison avec les calculs LISE++. Cela a permis d'extraire la distribution des états de charge des ions Ti à différentes énergies de sortie après les feuilles étudiées. Les fractions d'ions de type Li de toutes les distributions disponibles ont été comparées aux prédictions du modèle. D'après ces résultats, il semble plus avantageux d'utiliser des feuilles de Nb ou de Ta dans l'expérience TDRIV et d'avoir une énergie initiale de faisceau telle que l'énergie des ions sortant de la cible soit d'environ 7 MeV/A.

Sur la base de ces informations, des simulations ont été réalisées pour la prochaine mesure TDRIV avec deux configurations de détecteurs possibles - les 24 détecteurs HPGe en trèfle du réseau JUROGAM 3 ou un réseau de 15 détecteurs HPGe coaxiaux. Dans les deux cas, le détecteur de particules OPSA sera utilisé pour la mesure. Les simulations ont montré que la mesure est possible avec les deux configurations de détecteurs et que l'expérience peut être

réalisée dès que le détecteur OPSA sera opérationnel.

Les moments magnétiques des états excités isomériques peuvent également fournir des informations importantes sur la structure nucléaire. Au début des années 2000, de nombreuses études expérimentales sur le  $^{68}\text{Ni}$  ont indiqué que  $N = 40$  est un nombre magique et que le  $^{68}\text{Ni}$  est peut-être un noyau doublement magique. Un exemple particulier est l'énergie d'excitation du premier état  $2_1^+$  dans les isotopes pairs du nickel, qui montre une augmentation pour le  $^{68}\text{Ni}$ , ce qui est typiquement associé à la magie des noyaux. Les études théoriques ont privilégié l'explication alternative selon laquelle l'augmentation de l'énergie d'excitation est due à l'ordre particulier des orbitales du modèle en couches dans la région, qui exige qu'une paire de neutrons soit simultanément excitée vers l'orbitale  $g_{9/2}$  pour former l'état  $2^+$  de parité positive. Ces hypothèses pourraient être testées par des mesures du facteur  $g$  des états excités  $g_{9/2}$  dans la région autour du  $^{68}\text{Ni}$ . Une expérience de ce type a été réalisée au GANIL pour mesurer le facteur  $g$  de l'état isomérique  $9/2^+$  du  $^{67}\text{Ni}$  à la suite d'une réaction de fragmentation d'un faisceau de  $^{76}\text{Ge}$  (61 MeV/A) sur une cible de  $^9\text{Be}$ . Il s'agissait de la toute première mesure du facteur  $g$  par la méthode TDPAD à la suite d'une réaction de fragmentation. Les résultats ont montré une valeur absolue du facteur  $g$  étonnamment faible, qui n'a pas pu être reproduite par les calculs du modèle en couches. Une expérience complémentaire a été réalisée en 2005 à l'installation NSCL de la MSU (Etats-Unis), pour mesurer les facteurs  $g$  de l'isomère  $8^+$  du  $^{70}\text{Ni}$  et de l'isomère  $17/2^-$  du  $^{69}\text{Ni}$ , ainsi qu'une nouvelle mesure du facteur  $g$  de l'isomère  $9/2^+$  du  $^{67}\text{Ni}$ , avec la méthode TDPAD. L'analyse des données obtenues a été réalisée dans le cadre du présent travail.

Dans l'expérience menée au NSCL, un faisceau primaire de  $^{76}\text{Ge}$  (130 MeV/A) a heurté une épaisse cible de  $^9\text{Be}$  pour produire les isotopes d'intérêt dans une réaction de fragmentation du projectile. Les états isomères d'intérêt sont peuplés et orientés par la réaction de fragmentation. Les fragments ont traversé un mince scintillateur en plastique avant d'être implantés dans un hôte en cuivre au centre du dispositif expérimental TDPAD. L'installation comprenait 4 détecteurs SeGa HPGe dans le plan horizontal, et un électro-aimant fournissant un champ magnétique uniforme dans la direction verticale. Les données ont été obtenues avec différents paramètres de sélection de l'impulsion : pour le  $^{67}\text{Ni}$  et le  $^{69}\text{Ni}$ , les fragments se trouvaient dans l'aile de la distribution d'impulsion, tandis que les fragments de  $^{70}\text{Ni}$  étaient au centre de la distribution d'impulsion. Les données obtenues étaient constituées des énergies des rayons gamma enregistrées dans les détecteurs HPGe et de la différence de temps entre les signaux du scintillateur plastique et du détecteur HPGe. Définir une condition sur l'énergie des rayons gamma de la transition dépeuplant l'état isomère d'intérêt produit un spectre de différence de temps montrant la diminution exponentielle de l'intensité des rayons gamma. Le fit de la pente du spectre de différence de temps donne la demi-vie de l'état isomère. Ensuite, en prenant le rapport des spectres de différence temporelle des détecteurs individuels, on obtient la fonction de rapport qui présente un modèle oscillatoire et peut être ajustée pour obtenir le facteur  $g$  de l'état d'intérêt.

L'état isomère  $9/2^+$  du  $^{67}\text{Ni}$  se désintègre jusqu'à l'état fondamental via deux transitions consécutives avec des énergies de 313 keV et 694 keV. La demi-vie de l'état isomère déterminée à partir d'un fit de la décroissance exponentielle des spectres de différence de temps était de 12(4) microsecondes, ce qui est en accord avec la valeur adoptée de 13.3(3) microsecondes. Le fit de la fonction de rapport pour la transition de 313 keV a donné un facteur  $g$  de -0.26(2), qui a été confirmé en utilisant les données de la transition de 694 keV et en appliquant une analyse par transformée de Fourier rapide des fonctions de rapport. La valeur du facteur  $g$  obtenue diffère significativement de celle de la mesure précédente au GANIL:  $g = |0.125(6)|$ . La raison de cet écart n'est pas bien comprise. Les calculs de modèle en couches avec différentes

interactions utilisant les facteurs  $g$  effectifs sont capables de reproduire le résultat actuel, plutôt que la valeur adoptée.

Une procédure similaire a également été suivie pour l'état isomère  $17/2^-$  du  $^{69}\text{Ni}$ . La demi-vie mesurée à partir de la pente du spectre de différence de temps de la transition de 148 keV a donné une valeur de 413(4) nanosecondes, ce qui est en léger désaccord avec la demi-vie de 439(3) nanosecondes de la mesure précédente. Le facteur  $g$  de l'état  $17/2^-$  a été déterminé comme étant de -0.268(16). Le résultat du facteur  $g$  a été parfaitement reproduit par des calculs de modèles en couches utilisant l'interaction LNPS avec les facteurs  $g$  des nucléons libres. Cela suggère que lorsqu'un espace de valence suffisamment grand est utilisé dans les calculs, la plupart des corrélations sont prises en compte et qu'il n'est pas nécessaire d'introduire un facteur de réduction pour les facteurs  $g$ .

Dans le cas de l'état isomère  $8^+$  du  $^{70}\text{Ni}$ , la demi-vie a été déterminée à 231(3) nanosecondes, ce qui est en parfait accord avec la valeur adoptée de 232(1) nanosecondes. Le facteur  $g$  de l'état a été obtenu à partir de la fonction de rapport pour la transition de 183 keV comme étant de -0.313(27). Cette valeur se situe entre les calculs du modèle en couches avec les facteurs  $g$  des nucléons libres et effectifs, montrant que certaines corrélations ne sont peut-être pas entièrement prises en compte.

Au cours de l'expérience, il a été constaté que le  $^{71}\text{Cu}$  était présent comme contaminant dans le faisceau secondaire de  $^{70}\text{Ni}$  et que l'état isomère  $19/2^-$  était peuplé. Une tentative a été faite pour mesurer le facteur  $g$  de cet état en utilisant la transition de 133 keV qui dépeuple cet état. Cependant, aucun comportement oscillatoire n'a été observé dans la fonction de rapport expérimentale. Cela était attendu car les prédictions théoriques suggèrent un facteur  $g$  proche de zéro, ce qui nécessiterait l'application d'un champ magnétique externe beaucoup plus puissant afin d'observer la fréquence de précession avant la désintégration de l'état isomère.

La mesure du facteur  $g$  des états nucléaires excités constitue un défi dans l'étude de la structure nucléaire. En ce qui concerne les facteurs  $g$  des états excités avec des demi-vies de l'ordre de la picosecondes, l'élargissement de la méthode TDRIV à des noyaux à  $Z$  plus élevé et aux faisceaux d'ions radioactifs ouvrira de nombreuses nouvelles possibilités pour les expériences et les résultats de physique futurs. En ce qui concerne les facteurs  $g$  des états isomères, un programme expérimental pour de telles mesures est en cours à RIKEN (Japon), pour les états isomères à longue et à courte demi-vie.

# Bibliography

- [1] E. Tiesinga, P. J. Mohr, D. B. Newell, and B. N. Taylor. Codata recommended values of the fundamental physical constants: 2018. *Rev. Mod. Phys.*, 93:025010, Jun 2021.
- [2] L. D. Landau and E. M. Lifshitz. “*Quantum mechanics: non-relativistic theory*”, volume 3. Elsevier, 2013.
- [3] D. Lee. “Introduction to Nuclear Physics lectures, MSU, USA”, 2021. Last accessed 16 July 2023.
- [4] K. S. Krane. “*Introductory nuclear physics*”. John Wiley & Sons, 1991.
- [5] R. Neugart and G. Neyens. “Nuclear moments”. *The Euroschool Lectures on Physics with Exotic Beams, Vol. II*, pages 135–189, 2006.
- [6] E. Caurier, G. Martínez-Pinedo, F. Nowacki, A. Poves, and A. P. Zuker. “The shell model as a unified view of nuclear structure”. *Rev. Mod. Phys.*, 77:427–488, Jun 2005.
- [7] P. J. Brussaard and P. W. M. Glaudemans. “*Shell-model applications in nuclear spectroscopy*”. North-Holland Publishing Company, Amsterdam, 1977.
- [8] E. Recknagel. “VII.C - Magnetic Moments of Excited States”. In J. Cerny, editor, *Nuclear Spectroscopy and Reactions, Part C*, Pure and Applied Physics Vol. 40, pages 93–141. Elsevier, 1974.
- [9] G. Georgiev. “*Magnetic moments of isomers and ground states of exotic nuclei produced by projectile fragmentation*”. PhD thesis, KU Leuven, 2001.
- [10] J. Hüfner, K. Schäfer, and B. Schürmann. “Abrasion-ablation in reactions between relativistic heavy ions”. *Phys. Rev. C*, 12:1888–1898, Dec 1975.
- [11] K. Asahi, M. Ishihara, T. Ichihara, M. Fukuda, T. Kubo, Y. Gono, A. C. Mueller, R. Anne, D. Bazin, D. Guillemaud-Mueller, R. Bimbot, W. D. Schmidt-Ott, and J. Kasagi. “Observation of spin-aligned secondary fragment beams of  $^{14}\text{B}$ ”. *Phys. Rev. C*, 43:456–460, Feb 1991.
- [12] A. S. Goldhaber. “Statistical models of fragmentation processes”. *Physics Letters B*, 53(4):306–308, 1974.
- [13] Y. Ichikawa, H. Ueno, Y. Ishii, T. Furukawa, A. Yoshimi, D. Kameda, H. Watanabe, N. Aoi, K. Asahi, D. L. Balabanski, et al. “Production of spin-controlled rare isotope beams”. *Nature Physics*, 8(12):918–922, 2012.
- [14] H. Ueno, K. Asahi, H. Izumi, K. Nagata, H. Ogawa, A. Yoshimi, H. Sato, M. Adachi, Y. Hori, K. Mochinaga, et al. “Magnetic moments of  $^{17}\text{N}$  and  $^{17}\text{B}$ ”. *Physical Review C*, 53(5):2142, 1996.
- [15] K. Siegbahn. “Alpha-, Beta-and Gamma-ray Spectroscopy: Volume 1”. *Alpha-, Beta-and Gamma-ray Spectroscopy*, 1, 1965.

- [16] K. Alder and A. Winther. “*Coulomb Excitation: A Collection of Reprints*”. Perspectives in Physics. A Series of Reprint Collections. Academic Press, 1966.
- [17] D. Cline. “Nuclear shapes studied by Coulomb excitation”. *Annual Review of Nuclear and Particle Science*, 36(1):683–716, 1986.
- [18] G. Goldring. “Hyperfine interactions in isolated ions”. In R Bock, editor, *Heavy ion collisions*, volume 3. 1982.
- [19] N. J. Stone, J. R. Stone, and P. Jonsson. “A priori calculations of hyperfine interactions in highly ionized atoms:  $g$ -factor measurements on aligned picosecond states populated in nuclear reactions”. *Hyperfine Interactions*, 197:29–35, 2010.
- [20] P. Jönsson, X. He, C. F. Fischer, and I. P. Grant. “The GRASP2K relativistic atomic structure package”. *Computer Physics Communications*, 177(7):597–622, 2007.
- [21] X. Chen, D. G. Sarantites, W. Reviol, and J. Snyder. “Time-dependent Monte Carlo calculations of recoil-in-vacuum  $g$ -factor data for  $^{122,126,130,132}\text{Te}$ ”. *Phys. Rev. C*, 87:044305, Apr 2013.
- [22] N. J. Stone, A. E. Stuchbery, M. Danchev, J. Pavan, C. L. Timlin, C. Baktash, C. Barton, J. Beene, N. Benczer-Koller, C. R. Bingham, J. Dupak, A. Galindo-Uribarri, C. J. Gross, G. Kumbartzki, D. C. Radford, J. R. Stone, and N. V. Zamfir. “First Nuclear Moment Measurement with Radioactive Beams by the Recoil-in-Vacuum Technique: The  $g$  Factor of the  $2_1^+$  State in  $^{132}\text{Te}$ ”. *Phys. Rev. Lett.*, 94:192501, May 2005.
- [23] B. P. McCormick. “*Calibration of  $2_1^+$  magnetic moments in even-even nuclei around  $Z$  30*”. PhD thesis, Australian National University, 2020.
- [24] C. F. Fischer, G. Gaigalas, P. Jönsson, and J. Bieroń. “GRASP2018 — A Fortran 95 version of the general relativistic atomic structure package”. *Computer Physics Communications*, 237:184–187, 2019.
- [25] T. K. Alexander, G. J. Costa, J. S. Forster, O. Hausser, A. B. McDonald, A. Olin, and W. Witthuhn. “Magnetic Moment of the 97-ps,  $I^\pi = 3^-$  Level in  $^{14}\text{C}$ ”. *Phys. Rev.*, C9:1748, 1974.
- [26] J. Asher, J. R. Beene, M. A. Grace, W. L. Randolph, and D. F. H. Start. “The Nuclear  $g$  Factor of the 397 keV State in  $^{16}\text{N}$ ”. *J. Phys.*, G1:415, 1975.
- [27] R. E. Horstman, J. L. Eberhardt, H. A. Doubt, C. M. E. Otten, and G. Van Middelkoop. “Recoil-distance measurements of  $g$ -factors for  $^{24}\text{Mg}(2_1^+)$  and  $^{20}\text{Ne}(2_1^+)$ ”. *Nuclear Physics A*, 248(2):291–316, 1975.
- [28] R. E. Horstman, J. L. Eberhardt, P. C. Zalm, H. A. Doubt, and G. Van Middelkoop. “Recoil-distance measurements of the  $g$ -factor of  $^{22}\text{Ne}(2_1^+)$ ”. *Nuclear Physics A*, 275(1):237–245, 1977.
- [29] F. A. Beck, T. Byrski, G. J. Costa, and J. P. Vivien. “Magnetic Moment and Lifetime of the First Excited State of Mirror Nuclei  $^{21}\text{Ne}$  and  $^{21}\text{Na}$ ”. *Phys. Rev.*, C16:679, 1977.
- [30] J. Billowes, J. Asher, D. W. Bennett, J. A. G. De Raedt, M. A. Grace, and B. J. Murphy. “The Magnetic Moment of the  $(5 / 2)^-(1.346 \text{ MeV})$  Level in  $^{19}\text{F}$ ”. *J. Phys.*, G9:293, 1983.

- [31] J. Asher, D. W. Bennett, H. A. Doubt, M. A. Grace, T. J. Moorhouse, and B. J. Murphy. “A Precise Measurement of the  $g$  Factor of the 6.13 MeV  $3^-$  State of  $^{16}\text{O}$ ”. *J.Phys.*, G10:1079, 1984.
- [32] A. Dewald, O. Möller, and P. Petkov. “Developing the Recoil Distance Doppler-Shift technique towards a versatile tool for lifetime measurements of excited nuclear states”. *Progress in Particle and Nuclear Physics*, 67(3):786–839, 2012.
- [33] J. M. Allmond, A. E. Stuchbery, D. C. Radford, A. Galindo-Uribarri, N. J. Stone, C. Bakdash, J. C. Batchelder, C. R. Bingham, M. Danchev, C. J. Gross, P. A. Hausladen, K. Lagergren, Y. Larochelle, E. Padilla-Rodal, and C.-H. Yu. “Magnetic moments of  $2_1^+$  states in  $^{124,126,128}\text{Sn}$ ”. *Phys. Rev. C*, 87:054325, May 2013.
- [34] A. E. Stuchbery, J. M. Allmond, A. Galindo-Uribarri, E. Padilla-Rodal, D. C. Radford, N. J. Stone, J. C. Batchelder, J. R. Beene, N. Benczer-Koller, C. R. Bingham, M. E. Howard, G. J. Kumbartzki, J. F. Liang, B. Manning, D. W. Stracener, and C.-H. Yu. “Electromagnetic properties of the  $2_1^+$  state in  $^{134}\text{Te}$ : Influence of core excitation on single-particle orbits beyond  $^{132}\text{Sn}$ ”. *Phys. Rev. C*, 88:051304, Nov 2013.
- [35] A. E. Stuchbery, P. F. Mantica, and A. N. Wilson. “Electron-configuration-reset time-differential recoil-in-vacuum technique for excited-state  $g$ -factor measurements on fast exotic beams”. *Phys. Rev. C*, 71:047302, Apr 2005.
- [36] A. Kusoglu, A. E. Stuchbery, G. Georgiev, B. A. Brown, A. Goasduff, L. Atanasova, D. L. Balabanski, M. Bostan, M. Danchev, P. Detistov, K. A. Gladnishki, J. Ljungvall, I. Matea, D. Radeck, C. Sotty, I. Stefan, D. Verney, and D. T. Yordanov. “Magnetism of an Excited Self-Conjugate Nucleus: Precise Measurement of the  $g$  Factor of the  $2_1^+$  State in  $^{24}\text{Mg}$ ”. *Phys.Rev.Lett.*, 114:062501, 2015.
- [37] A. Kusoglu. “*Nuclear moments and lifetimes of excited states in exotic nuclei*”. PhD thesis, Istanbul University, 2015.
- [38] K.-H. Speidel, O. Kenn, and F. Nowacki. “Magnetic moments and nuclear structure”. *Progress in Particle and Nuclear Physics*, 49(1):91–154, 2002.
- [39] J. L. Eberhardt, R. E. Horstman, P. C. Zalm, H. A. Doubt, and G. Van Middelkoop. “Large transient magnetic fields at high ion velocities in polarized iron”. *Hyperfine Interactions*, 3:195–212, 1977.
- [40] N. K. B. Shu, D. Melnik, J. M. Brennan, W. Semmler, and N. Benczer-Koller. “Velocity dependence of the dynamic magnetic field acting on swift O and Sm ions”. *Phys. Rev. C*, 21:1828–1837, May 1980.
- [41] H. R. Andrews, O. Häusser, D. Ward, P. Taras, R. Nicole, J. Keinonen, P. Skensved, and B. Haas. “Calibration of the transient magnetic field for rare-earth nuclei in iron: Application to  $g$ -factors of high-spin states in  $^{152,154}\text{Sm}$ ”. *Nuclear Physics A*, 383(3):509–529, 1982.
- [42] A. E. Stuchbery. “Transient-field strengths for high-velocity light ions and applications to  $g$ -factor measurements on fast exotic beams”. *Phys. Rev. C*, 69:064311, Jun 2004.

- [43] G. Kumbartzki, J. R. Cooper, N. Benczer-Koller, K. Hiles, T. J. Mertzimekis, M. J. Taylor, K.-H. Speidel, P. Maier-Komor, L. Bernstein, M. A. McMahan, L. Phair, J. Powell, and D. Wutte. “First  $g$  factor measurement using a radioactive  $^{76}\text{Kr}$  beam”. *Physics Letters B*, 591(3):213–219, 2004.
- [44] N. Benczer-Koller, G. J. Kumbartzki, G. Gürdal, C. J. Gross, A. E. Stuchbery, B. Krieger, R. Hatarik, P. O’Malley, S. Pain, L. Segen, C. Baktash, J. Beene, D. C. Radford, C. H. Yu, N. J. Stone, J. R. Stone, C. R. Bingham, M. Danchev, R. Grzywacz, and C. Mazzocchi. “Measurement of  $g$  factors of excited states in radioactive beams by the transient field technique:  $^{132}\text{Te}$ ”. *Physics Letters B*, 664(4):241–245, 2008.
- [45] G. J. Kumbartzki, N. Benczer-Koller, D. A. Torres, B. Manning, P. D. O’Malley, Y. Y. Sharon, L. Zamick, C. J. Gross, D. C. Radford, S. J. Q. Robinson, J. M. Allmond, A. E. Stuchbery, K.-H. Speidel, N. J. Stone, and C. R. Bingham. “Transient field  $g$  factor and mean-life measurements with a rare isotope beam of  $^{126}\text{Sn}$ ”. *Phys. Rev. C*, 86:034319, Sep 2012.
- [46] A. Illana, A. Jungclaus, R. Orlandi, A. Perea, C. Bauer, J. A. Briz, J. L. Egido, R. Gernhäuser, J. Leske, D. Mücher, J. Pakarinen, N. Pietralla, M. Rajabali, T. R. Rodríguez, D. Seiler, C. Stahl, D. Voulot, F. Wenander, A. Blazhev, H. De Witte, P. Reiter, M. Seidlitz, B. Siebeck, M. J. Vermeulen, and N. Warr. “Low-velocity transient-field technique with radioactive ion beams:  $g$  factor of the first excited  $2^+$  state in  $^{72}\text{Zn}$ ”. *Phys. Rev. C*, 89:054316, May 2014.
- [47] A. D. Davies, A. E. Stuchbery, P. F. Mantica, P. M. Davidson, A. N. Wilson, A. Becerril, B. A. Brown, C. M. Campbell, J. M. Cook, D. C. Dinca, A. Gade, S. N. Liddick, T. J. Mertzimekis, W. F. Mueller, J. R. Terry, B. E. Tomlin, K. Yoneda, and H. Zwahlen. “Probing Shell Structure and Shape Changes in Neutron-Rich Sulfur Isotopes through Transient-Field  $g$ -Factor Measurements on Fast Radioactive Beams of  $^{38}\text{S}$  and  $^{40}\text{S}$ ”. *Phys. Rev. Lett.*, 96:112503, Mar 2006.
- [48] A. E. Stuchbery, A. D. Davies, P. F. Mantica, P. M. Davidson, A. N. Wilson, A. Becerril, B. A. Brown, C. M. Campbell, J. M. Cook, D. C. Dinca, A. Gade, S. N. Liddick, T. J. Mertzimekis, W. F. Mueller, J. R. Terry, B. E. Tomlin, K. Yoneda, and H. Zwahlen. “Shell structure underlying the evolution of quadrupole collectivity in  $^{38}\text{S}$  and  $^{40}\text{S}$  probed by transient-field  $g$ -factor measurements on fast radioactive beams”. *Phys. Rev. C*, 74:054307, Nov 2006.
- [49] E. Fiori. “Measurement of the magnetic moment of the  $2^+$  state of  $^{72}\text{Zn}$  via extension of the high-velocity transient-field method”. PhD thesis, Université Paris-Sud 11, 2010.
- [50] E. Fiori, G. Georgiev, A. E. Stuchbery, A. Jungclaus, D. L. Balabanski, A. Blazhev, S. Cabaret, E. Clément, M. Danchev, J. M. Daugas, S. Grevy, M. Hass, V. Kumar, J. Leske, R. Lozeva, S. Lukyanov, T. J. Mertzimekis, V. Modamio, B. Mougnot, F. Nowacki, Yu. E. Penionzhkevich, L. Perrot, N. Pietralla, K. Sieja, K.-H. Speidel, I. Stefan, C. Stodel, J. C. Thomas, J. Walker, and K. O. Zell. “First  $g(2^+)$  measurement on neutron-rich  $^{72}\text{Zn}$ , and the high-velocity transient field technique for radioactive heavy-ion beams”. *Phys. Rev. C*, 85:034334, Mar 2012.
- [51] C. Thibault, R. Klapisch, C. Rigaud, A. M. Poskanzer, R. Prieels, L. Lessard, and W. Reisdorf. “Direct measurement of the masses of  $^{11}\text{Li}$  and  $^{26-32}\text{Na}$  with an on-line mass spectrometer”. *Physical Review C*, 12(2):644, 1975.

- [52] X. Campi, H. Flocard, A. K. Kerman, and S. Koonin. “Shape transition in the neutron rich sodium isotopes”. *Nuclear Physics A*, 251(2):193–205, 1975.
- [53] C. Détraz, M. Langevin, D. Guillemaud, M. Epherre, G. Audi, C. Thibault, and F. Touchard. “Mapping of the onset of a new region of deformation: the masses of  $^{31}\text{Mg}$  and  $^{32}\text{Mg}$ ”. *Nuclear Physics A*, 394(3):378–386, 1983.
- [54] F. Touchard, J. M. Serre, S. Büttgenbach, P. Guimbal, R. Klapisch, M. de Saint Simon, C. Thibault, H. T. Duong, P. Juncar, S. Liberman, et al. “Electric quadrupole moments and isotope shifts of radioactive sodium isotopes”. *Physical Review C*, 25(5):2756, 1982.
- [55] C. Détraz, D. Guillemaud, G. Huber, R. Klapisch, M. Langevin, F. Naulin, C. Thibault, L. C. Carraz, and F. Touchard. “Beta decay of  $^{27-32}\text{Na}$  and their descendants”. *Physical Review C*, 19(1):164, 1979.
- [56] D. Guillemaud-Mueller, C. Detraz, M. Langevin, F. Naulin, M. de Saint-Simon, C. Thibault, F. Touchard, and M. Epherre. “ $\beta$ -decay schemes of very neutron-rich sodium isotopes and their descendants”. *Nuclear Physics A*, 426(1):37–76, 1984.
- [57] T. Motobayashi, Y. Ikeda, K. Ieki, M. Inoue, N. Iwasa, T. Kikuchi, M. Kurokawa, S. Moriya, S. Ogawa, H. Murakami, et al. “Large deformation of the very neutron-rich nucleus  $^{32}\text{Mg}$  from intermediate-energy Coulomb excitation”. *Physics Letters B*, 346(1-2):9–14, 1995.
- [58] N. Fukunishi, T. Otsuka, and T. Sebe. “Vanishing of the shell gap in  $N = 20$  neutron-rich nuclei”. *Physics Letters B*, 296(3):279–284, 1992.
- [59] B. V. Pritychenko, T. Glasmacher, P. D. Cottle, M. Fauerbach, R. W. Ibbotson, K. W. Kemper, V. Maddalena, A. Navin, R. Ronningen, A. Sakharuk, et al. “Role of intruder configurations in  $^{26,28}\text{Ne}$  and  $^{30,32}\text{Mg}$ ”. *Physics Letters B*, 461(4):322–328, 1999.
- [60] V. Chisté, A. Gillibert, A. Lepine-Szily, N. Alamanos, F. Auger, J. Barrette, F. Braga, M. D. Cortina-Gil, Z. Dlouhy, V. Lapoux, et al. “Electric and nuclear transition strength in  $^{30,32}\text{Mg}$ ”. *Physics Letters B*, 514(3-4):233–239, 2001.
- [61] S. Michimasa, Y. Yanagisawa, K. Inafuku, N. Aoi, Z. Elekes, Zs. Fülöp, Y. Ichikawa, N. Iwasa, K. Kurita, M. Kurokawa, et al. “Quadrupole collectivity in island-of-inversion nuclei  $^{28,30}\text{Ne}$  and  $^{34,36}\text{Mg}$ ”. *Physical Review C*, 89(5):054307, 2014.
- [62] O. Niedermaier, H. Scheit, V. Bildstein, H. Boie, J. Fitting, R. von Hahn, F. Köck, M. Lauer, U. K. Pal, H. Podlech, R. Repnow, D. Schwalm, et al. ““Safe” Coulomb Excitation of  $^{30}\text{Mg}$ ”. *Phys. Rev. Lett.*, 94:172501, May 2005.
- [63] O. Niedermaier. “*Low-Energy Coulomb Excitation of the Neutron-Rich Mg Isotopes  $^{30}\text{Mg}$  and  $^{32}\text{Mg}$* ”. PhD thesis, University of Heidelberg, 2005.
- [64] M. Seidlitz, D. Mücher, P. Reiter, V. Bildstein, A. Blazhev, N. Bree, B. Bruyneel, J. Ced-erkäll, E. Clement, T. Davinson, et al. “Coulomb excitation of  $^{31}\text{Mg}$ ”. *Physics Letters B*, 700(3-4):181–186, 2011.
- [65] B. Fernández-Domínguez, B. Pietras, W.N. Catford, N.A. Orr, M. Petri, M. Chartier, S. Paschalis, N. Patterson, J.S. Thomas, M. Caamaño, T. Otsuka, A. Poves, N. Tsunoda,

- N.L. Achouri, J.-C. Angélique, N.I. Ashwood, A. Banu, B. Bastin, R. Borcea, J. Brown, F. Delaunay, S. Franchoo, M. Freer, L. Gaudefroy, S. Heil, M. Labiche, B. Laurent, R.C. Lemmon, A.O. Macchiavelli, F. Negoita, E.S. Paul, C. Rodríguez-Tajes, P. Roussel-Chomaz, M. Staniou, M.J. Taylor, L. Trache, and G.L. Wilson. “Re-examining the transition into the  $N = 20$  island of inversion: Structure of  $^{30}\text{Mg}$ ”. *Physics Letters B*, 779:124–129, 2018.
- [66] N. Tsunoda, T. Otsuka, N. Shimizu, M. Hjorth-Jensen, K. Takayanagi, and T. Suzuki. “Exotic neutron-rich medium-mass nuclei with realistic nuclear forces”. *Phys. Rev. C*, 95:021304, Feb 2017.
- [67] E. Caurier. Computer code ANTOINE, 1989.
- [68] B. A. Brown and W. A. Richter. “New “USD” Hamiltonians for the sd shell”. *Physical Review C*, 74(3):034315, 2006.
- [69] W. A. Richter, S. Mkhize, and B. A. Brown. “sd-shell observables for the USDA and USDB Hamiltonians”. *Physical Review C*, 78(6):064302, 2008.
- [70] T. Otsuka, M. Honma, T. Mizusaki, N. Shimizu, and Y. Utsuno. “Monte Carlo shell model for atomic nuclei”. *Progress in Particle and Nuclear Physics*, 47(1):319–400, 2001.
- [71] E. Caurier and F. Nowacki. Compture code NATHAN, 1997.
- [72] B. P. McCormick, A. E. Stuchbery, T. Kibédi, G. J. Lane, M. W. Reed, T. K. Eriksen, S. S. Hota, B. Q. Lee, and N. Palalani. “Probing the  $N = 14$  subshell closure:  $g$  factor of the  $^{26}\text{Mg}(2_1^+)$  state”. *Physics Letters B*, 779:445–451, 2018.
- [73] ISOLDE Logos, Layouts and Templates. <http://isolde.web.cern.ch/isolde-logos-layouts-and-templates>.
- [74] V. I. Mishin, V. N. Fedoseyev, H.-J. Kluge, V. S. Letokhov, H. L. Ravn, F. Scheerer, Y. Shirakabe, S. Sundell, O. Tengblad, ISOLDE Collaboration, et al. “Chemically selective laser ion-source for the CERN-ISOLDE on-line mass separator facility”. *Nuclear Instruments and Methods in Physics Research Section B: Beam Interactions with Materials and Atoms*, 73(4):550–560, 1993.
- [75] V. N. Fedoseyev, G. Huber, U. Köster, J. Lettry, V. I. Mishin, H. Ravn, and V. Sebastian. “The ISOLDE laser ion source for exotic nuclei”. *Hyperfine Interactions*, 127:409–416, 2000.
- [76] E. Kugler. “The ISOLDE facility”. *Hyperfine interactions*, 129(1-4):23–42, 2000.
- [77] F. Ames, J. Cederkäll, T. Sieber, and F. Wenander. “*The REX-ISOLDE Facility: Design and Commissioning Report*”. CERN, 2005.
- [78] Y. Kadi, Y. Blumenfeld, W. Venturini Delsolaro, M. A. Fraser, M. Huyse, A. Papageorgiou Koufidou, J. A. Rodriguez, and F. Wenander. “Post-accelerated beams at ISOLDE”. *Journal of Physics G: Nuclear and Particle Physics*, 44(8):084003, jun 2017.
- [79] J. Eberth, G. Pascovici, H. G. Thomas, N. Warr, D. Weisshaar, D. Habs, P. Reiter, P. Thirolf, D. Schwalm, C. Gund, H. Scheit, M. Lauer, P. Van Duppen, S. Franchoo,

- M. Huyse, R. M. Lieder, W. Gast, J. Gerl, and K. P. Lieb. “MINIBALL A Ge detector array for radioactive ion beam facilities”. *Progress in Particle and Nuclear Physics*, 46(1):389–398, 2001.
- [80] P. A. Butler, J. Cederkäll, and P. Reiter. “Nuclear-structure studies of exotic nuclei with MINIBALL”. *Journal of Physics G: Nuclear and Particle Physics*, 44(4):044012, mar 2017.
- [81] A. N Ostrowski, S. Cherubini, T. Davinson, D. Groombridge, A. M. Laird, A. Musumarra, A. Ninane, A. di Pietro, A. C. Shotter, and P.J. Woods. “CD: A double sided silicon strip detector for radioactive nuclear beam experiments”. *Nuclear Instruments and Methods in Physics Research Section A: Accelerators, Spectrometers, Detectors and Associated Equipment*, 480(2):448–455, 2002.
- [82] A. Boukhari. “*Study of the nuclear spin-orientation in incomplete fusion reactions. Measurement of the magnetic moment of the  $2^+$  states in  $^{22}\text{Ne}$  and  $^{28}\text{Mg}$* ”. PhD thesis, Université Paris-Saclay, 2018.
- [83] O.B. Tarasov and D. Bazin. “LISE++: Radioactive beam production with in-flight separators”. *Nuclear Instruments and Methods in Physics Research Section B: Beam Interactions with Materials and Atoms*, 266(19):4657–4664, 2008. Proceedings of the XVth International Conference on Electromagnetic Isotope Separators and Techniques Related to their Applications.
- [84] D. P. Rosiak. “*Coulomb excitation of doubly-magic  $^{132}\text{Sn}$  at HIE-ISOLDE and development of escape-suppression shields for the MINIBALL spectrometer*”. PhD thesis, Universität zu Köln, 2018.
- [85] G. Schiwietz and P. L. Grande. “Improved charge-state formulas”. *Nuclear Instruments and Methods in Physics Research Section B: Beam Interactions with Materials and Atoms*, 175-177:125–131, 2001. Twelfth International Conference of Ion Beam Modification of Materials.
- [86] K.-H. Speidel, S. Schielke, J. Leske, J. Gerber, P. Maier-Komor, S. J. Q. Robinson, Y. Y. Sharon, and L. Zamick. “Experimental  $g$  factors and  $B(E2)$  values in Ar isotopes: Crossing the  $N = 20$  semi-magic divide”. *Physics Letters B*, 632(2):207–211, 2006.
- [87] M. Frosini, T. Duguet, J.-P. Ebran, B. Bally, T. Mongelli, T. R. Rodríguez, R. Roth, and V. Soma. “Multi-reference many-body perturbation theory for nuclei: II. Ab initio study of neon isotopes via PGCM and IM-NCSM calculations”. *The European Physical Journal A*, 58(4):63, 2022.
- [88] A. Magilligan and B. A. Brown. “New isospin-breaking “USD” Hamiltonians for the sd shell”. *Phys. Rev. C*, 101:064312, Jun 2020.
- [89] M. B. Bennett, C. Wrede, B. A. Brown, S. N. Liddick, D. Pérez-Loureiro, D. W. Bardayan, A. A. Chen, K. A. Chipps, C. Fry, B. E. Glassman, C. Langer, N. R. Larson, E. I. McNeice, Z. Meisel, W. Ong, P. D. O’Malley, S. D. Pain, C. J. Prokop, H. Schatz, S. B. Schwartz, S. Suchyta, P. Thompson, M. Walters, and X. Xu. “Isospin Mixing Reveals  $^{30}\text{P}(p, \gamma)^{31}\text{S}$  Resonance Influencing Nova Nucleosynthesis”. *Phys. Rev. Lett.*, 116:102502, Mar 2016.

- [90] B. A. Brown and W. D. M. Rae. “The Shell-Model Code NuShellX@MSU”. *Nuclear Data Sheets*, 120:115–118, 2014.
- [91] J. B. Marion and F. C. Young. “*Nuclear Reaction Analysis (Graphs and Tables)*”. North-Holland Publishing Company, 1968.
- [92] R. Böhm, R. Keitel, W. Klinger, W. Witthuhn, W. L. Randolph, and E. Matthias. “The magnetic moment of the first  $2^+$  state in  $^{22}\text{Ne}$ ”. *Zeitschrift für Physik A Atoms and Nuclei*, 278:133–137, 1976.
- [93] G. Burgunder, O. Sorlin, F. Nowacki, S. Giron, F. Hammache, M. Moukaddam, N. de Séréville, D. Beaumel, L. Caceres, E. Clément, G. Duchêne, J. P. Ebran, B. Fernandez-Dominguez, F. Flavigny, S. Franchoo, J. Gibelin, A. Gillibert, S. Grévy, J. Guillot, A. Lepailleur, I. Matea, A. Matta, L. Nalpas, A. Obertelli, T. Otsuka, J. Pancin, A. Poves, R. Raabe, J. A. Scarpaci, I. Stefan, C. Stodel, T. Suzuki, and J. C. Thomas. “Experimental Study of the Two-Body Spin-Orbit Force in Nuclei”. *Phys. Rev. Lett.*, 112:042502, Jan 2014.
- [94] J. Ljungvall, G. Georgiev, S. Cabaret, N. Karkour, D. Linget, G. Sedes, R. Chevrier, I. Matea, M. Niikura, M.-D. Salsac, and B. Sulignano. “The Orsay Universal Plunger System”. *Nuclear Instruments and Methods in Physics Research Section A: Accelerators, Spectrometers, Detectors and Associated Equipment*, 679:61–66, 2012.
- [95] J. Simpson, F. Azaiez, G. de France, G. Fouan, J. Gerl, R. Julin, W. Korten, P. J. Nolan, B. M. Nyako, G. Sletten, and P. M. Walker. “The EXOGAM array: A radioactive beam gamma-ray spectrometer”. *Acta Physica Hungarica New Series-Heavy ion*, 11:159–188, 2000.
- [96] P. Petkov, C. Müller-Gatermann, D. Werner, A. Dewald, A. Blazhev, C. Fransen, J. Jolie, S. Ohkubo, and K. O. Zell. “New lifetime measurements for the lowest quadrupole states in  $^{20,22}\text{Ne}$  and possible explanations of the high collectivity of the depopulating  $E2$  transitions”. *Physical Review C*, 100(2):024312, 2019.
- [97] N. J. Stone. “Table of Recommended Nuclear Magnetic Dipole Moments: Part II, Short-Lived States”. *INDC (NDS)–0816*, 2020.
- [98] M. C. East, A. E. Stuchbery, S. K. Chamoli, A. N. Wilson, H. L. Crawford, J. S. Pinter, T. Kibédi, and P. F. Mantica. “ $g$  factor of the first excited state in  $^{56}\text{Fe}$  and implications for transient-field calibration in the Fe region”. *Phys. Rev. C*, 79:024303, Feb 2009.
- [99] R. Ernst, K.-H. Speidel, O. Kenn, A. Gohla, U. Nachum, J. Gerber, P. Maier-Komor, N. Benczer-Koller, G. Kumbartzki, G. Jakob, L. Zamick, and F. Nowacki. “Shell structure of Ti and Cr nuclei from measurements of  $g$  factors and lifetimes”. *Phys. Rev. C*, 62:024305, Jul 2000.
- [100] K.-H. Speidel, R. Ernst, O. Kenn, J. Gerber, P. Maier-Komor, N. Benczer-Koller, G. Kumbartzki, L. Zamick, M. S. Fayache, and Y. Y. Sharon. “Core polarization in the light of new experimental  $g$  factors of  $fp$  shell,  $N = 28$ , isotones”. *Physical Review C*, 62(3):031301, 2000.
- [101] S. Wagner, K.-H. Speidel, O. Kenn, R. Ernst, S. Schielke, J. Gerber, P. Maier-Komor, N. Benczer-Koller, G. Kumbartzki, Y.Y. Sharon, and F. Nowacki. “New measurement

- of the  $g$  factor of the  $^{54}\text{Cr}(2_1^+)$  state and its shell model interpretation”. *Phys. Rev. C*, 64:034320, Aug 2001.
- [102] M. C. East, A. E. Stuchbery, S. K. Chamoli, J. S. Pinter, H. L. Crawford, A. N. Wilson, T. Kibédi, and P. F. Mantica. “Relative  $g$ -factor measurements in  $^{54}\text{Fe}$ ,  $^{56}\text{Fe}$ , and  $^{58}\text{Fe}$ ”. *Phys. Rev. C*, 79:024304, Feb 2009.
- [103] M. J. Taylor, N. Benczer-Koller, G. Kumbartzki, T. J. Mertzimekis, S. J. Q. Robinson, Y. Y. Sharon, L. Zamick, A. E. Stuchbery, C. Hutter, C. W. Beausang, et al. “Competing core and single particle excitations in the  $2_1^+$  state in  $^{44}\text{Ca}$ ”. *Physics Letters B*, 559(3-4):187–192, 2003.
- [104] S. Schielke, K.-H. Speidel, O. Kenn, J. Leske, N. Gemein, M. Offer, Y. Y. Sharon, L. Zamick, J. Gerber, and P. Maier-Komor. “First measurement and shell model interpretation of the  $g$  factor of the  $2_1^+$  state in self-conjugate radioactive  $^{44}\text{Ti}$ ”. *Physics Letters B*, 567(3-4):153–158, 2003.
- [105] H. Koivisto, J. Ärje, R. Seppälä, and M. Nurmi. “Production of titanium ion beams in an ECR ion source”. *Nuclear Instruments and Methods in Physics Research Section B: Beam Interactions with Materials and Atoms*, 187(1):111–116, 2002.
- [106] M. Leino, J. Äystö, T. Enqvist, P. Heikkinen, A. Jokinen, M. Nurmi, A. Ostrowski, W. H. Trzaska, J. Uusitalo, K. Eskola, et al. “Gas-filled recoil separator for studies of heavy elements”. *Nuclear Instruments and Methods in Physics Research Section B: Beam Interactions with Materials and Atoms*, 99(1-4):653–656, 1995.
- [107] J. Konki. “Discovery of the new isotopes  $^{240}\text{Es}$  and  $^{236}\text{Bk}$  and in-beam spectroscopic studies of  $^{244}\text{Cf}$ ”. PhD thesis, University of Jyväskylä, 2017.
- [108] I. Lazarus, E. E. Appelbe, P. A. Butler, P. J. Coleman-Smith, J. R. Cresswell, S. J. Freeman, R. D. Herzberg, I. Hibbert, D. T. Joss, S. C. Letts, R. D. Page, V. F. E. Pucknell, P. H. Regan, J. Sampson, J. Simpson, J. Thornhill, and R. Wadsworth. “The GREAT triggerless total data readout method”. *IEEE Transactions on Nuclear Science*, 48(3):567–569, 2001.
- [109] P. Rahkila. “Grain—A Java data analysis system for Total Data Readout”. *Nuclear Instruments and Methods in Physics Research Section A: Accelerators, Spectrometers, Detectors and Associated Equipment*, 595(3):637–642, 2008.
- [110] J. F. Ziegler and J. P. Biersack. “*The Stopping and Range of Ions in Matter*”. Springer US, Boston, MA, 1985.
- [111] V. S. Nikolaev and I. S. Dmitriev. “On the equilibrium charge distribution in heavy element ion beams”. *Physics Letters A*, 28(4):277–278, 1968.
- [112] S.-C. Wu. “Nuclear Data Sheets for  $A = 46$ ”. *Nuclear Data Sheets*, 91(1):1–116, 2000.
- [113] H. A. Doubt. *Annals of Israel Phys. Soc.*, 1:537, 1977.
- [114] Y. C. Lin, W. A. Little, G. D. Sprouse, and P. D. Bond. “Velocity dependence of atomic state populations in highly stripped atoms”. *Hyperfine Interactions*, 4(1-2):105–109, 1978.

- [115] J. Pakarinen, J. Ojala, P. Ruotsalainen, H. Tann, H. Badran, T. Calverley, J. Hilton, T. Grahn, P. T. Greenlees, M. Hytönen, et al. “The JUROGAM 3 spectrometer”. *The European Physical Journal A*, 56:1–8, 2020.
- [116] M. Lebois, N. Jovančević, D. Thisse, R. Canavan, D. Étasse, M. Rudigier, and J. N. Wilson. “The  $\nu$ -ball  $\gamma$ -spectrometer”. *Nuclear Instruments and Methods in Physics Research Section A: Accelerators, Spectrometers, Detectors and Associated Equipment*, 960:163580, 2020.
- [117] M. Bernas, Ph. Dessagne, M. Langevin, J. Payet, F. Pougheon, and P. Roussel. “Magic features of  $^{68}\text{Ni}$ ”. *Physics Letters B*, 113(4):279–282, 1982.
- [118] R. Broda, B. Fornal, W. Królas, T. Pawłat, D. Bazzacco, S. Lunardi, C. Rossi-Alvarez, R. Menegazzo, G. de Angelis, P. Bednarczyk, J. Rico, D. De Acuña, P. J. Daly, R. H. Mayer, M. Sferrazza, H. Grawe, K. H. Maier, and R. Schubart. “ $N = 40$  Neutron Subshell Closure in the  $^{68}\text{Ni}$  Nucleus”. *Phys. Rev. Lett.*, 74:868–871, Feb 1995.
- [119] O. Sorlin, S. Leenhardt, C. Donzaud, J. Duprat, F. Azaiez, F. Nowacki, H. Grawe, Zs. Dombrádi, F. Amorini, A. Astier, D. Baiborodin, M. Belleguic, C. Borcea, C. Bourgeois, D. M. Cullen, Z. Dlouhy, E. Dragulescu, M. Górska, S. Grévy, D. Guillemaud-Mueller, G. Hagemann, B. Herskind, J. Kiener, R. Lemmon, M. Lewitowicz, S. M. Lukyanov, P. Mayet, F. de Oliveira Santos, D. Pantalica, Yu.-E. Penionzhkevich, F. Pougheon, A. Poves, N. Redon, M. G. Saint-Laurent, J. A. Scarpaci, G. Sletten, M. Stanoiu, O. Tarasov, and Ch. Theisen. “ $^{68}\text{Ni}_{40}$ : Magicity versus Superfluidity”. *Phys. Rev. Lett.*, 88:092501, Feb 2002.
- [120] N. Bree, I. Stefanescu, P. A. Butler, J. Cederkäll, T. Davinson, P. Delahaye, J. Eberth, D. Fedorov, V. N. Fedosseev, L. M. Fraile, S. Franchoo, G. Georgiev, K. Gladnishki, M. Huyse, O. Ivanov, J. Iwanicki, J. Jolie, U. Köster, Th. Kröll, R. Krücken, B. A. Marsh, O. Niedermaier, P. Reiter, H. Scheit, D. Schwalm, T. Sieber, J. Van de Walle, P. Van Duppen, N. Warr, D. Weisshaar, F. Wenander, and S. Zemlyanoy. “Coulomb excitation of  $^{68}\text{Ni}_{40}$  at “safe” energies”. *Phys. Rev. C*, 78:047301, Oct 2008.
- [121] C. Guénaut, G. Audi, D. Beck, K. Blaum, G. Bollen, P. Delahaye, F. Herfurth, A. Kellerbauer, H.-J. Kluge, J. Libert, D. Lunney, S. Schwarz, L. Schweikhard, and C. Yazidjian. “High-precision mass measurements of nickel, copper, and gallium isotopes and the purported shell closure at  $N = 40$ ”. *Phys. Rev. C*, 75:044303, Apr 2007.
- [122] S. Rahaman, J. Hakala, V.-V. Elomaa, T. Eronen, U. Hager, A. Jokinen, A. Kankainen, I. D. Moore, H. Penttilä, S. Rinta-Antila, et al. “Masses of neutron-rich Ni and Cu isotopes and the shell closure at  $Z = 28, N = 40$ ”. *The European Physical Journal A*, 34:5–9, 2007.
- [123] H. Grawe, M. Górska, C. Fahlander, M. Palacz, F. Nowacki, E. Caurier, J. M. Daugas, M. Lewitowicz, M. Sawicka, R. Grzywacz, et al. “Experimental approach towards shell structure at  $^{100}\text{Sn}$  and  $^{78}\text{Ni}$ ”. *Nuclear Physics, Section A*, 704:211C–222C, 2002.
- [124] K. Langanke, J. Terasaki, F. Nowacki, D. J. Dean, and W. Nazarewicz. “How magic is the magic  $^{68}\text{Ni}$  nucleus?”. *Physical Review C*, 67(4):044314, 2003.
- [125] E. A. McCutchan. “Nuclear Data Sheets for  $A = 68$ ”. *Nucl. Data Sheets*, 113:1735–1870, 2012.

- [126] N. Benczer-Koller, G. Kumbartzki, J. R. Cooper, T. J. Mertzimekis, M. J. Taylor, L. Bernstein, K. Hiles, P. Maier-Komor, M. A. McMahan, L. Phair, et al. “First  $g$ -factor measurement using a radioactive  $^{76}\text{Kr}$  beam”. *The European Physical Journal A-Hadrons and Nuclei*, 25:203–304, 2005.
- [127] G. Georgiev, G. Neyens, M. Hass, D. L. Balabanski, C. Bingham, C. Borcea, N. Coulier, R. Coussement, J. M. Daugas, G. De France, et al. “ $g$  Factor measurements of  $\mu\text{s}$  isomeric states in neutron-rich nuclei around  $^{68}\text{Ni}$  produced in projectile-fragmentation reactions”. *Journal of Physics G: Nuclear and Particle Physics*, 28(12):2993, 2002.
- [128] R. Grzywacz, R. Anne, G. Auger, D. Bazin, C. Borcea, V. Borrel, J. M. Corre, T. Dörfler, A. Fomichov, M. Gaelens, et al. “Identification of  $\mu\text{s}$ -isomers produced in the fragmentation of a  $^{112}\text{Sn}$  beam”. *Physics Letters B*, 355(3-4):439–446, 1995.
- [129] R. Grzywacz, R. Béraud, C. Borcea, A. Emsallem, M. Glogowski, H. Grawe, D. Guillemaud-Mueller, M. Hjorth-Jensen, M. Houry, M. Lewitowicz, et al. “New Island of  $\mu\text{s}$  Isomers in Neutron-Rich Nuclei around the  $Z = 28$  and  $N = 40$  Shell Closures”. *Physical review letters*, 81(4):766, 1998.
- [130] W. Müller, H. H. Bertschat, H. Haas, B. Spellmeyer, and W.-D. Zeitz. “Magnetic hyperfine interaction studies of isolated Ni impurities in Pd and Pd-Pt alloys”. *Physical Review B*, 40(11):7633, 1989.
- [131] G. Georgiev, I. Matea, D. L. Balabanski, J. M. Daugas, F. de Oliveira Santos, S. Franchoo, F. Ibrahim, F. Le Blanc, M. Lewitowicz, G. Lo Bianco, et al. “ $g$ -factor measurement of the  $9/2+$  isomeric state in  $^{65}\text{Ni}$ ”. *Journal of Physics G: Nuclear and Particle Physics*, 31(10):S1439, 2005.
- [132] G. Georgiev, I. Matea, D. L. Balabanski, J. M. Daugas, F. de Oliveira Santos, S. Franchoo, F. Ibrahim, F. Le Blanc, M. Lewitowicz, G. Lo Bianco, et al. “ $g$ -factor of the  $9/2+$  isomeric state in  $^{65}\text{Ni}$  from transfer reaction”. *The European Physical Journal A-Hadrons and Nuclei*, 30:351–356, 2006.
- [133] O. Kenn, K.-H. Speidel, R. Ernst, J. Gerber, P. Maier-Komor, and F. Nowacki. “Measurements of  $g$  factors and lifetimes of low lying states in  $^{58-64}\text{Ni}$  and their shell model implications”. *Physical Review C*, 63(6):064306, 2001.
- [134] A. Arima and H. Horie. “Configuration mixing and magnetic moments of odd nuclei”. *Progress of Theoretical Physics*, 12(5):623–641, 1954.
- [135] M. Hannawald, T. Kautzsch, A. Wöhr, W. B. Walters, K.-L. Kratz, V. N. Fedoseyev, V. I. Mishin, W. Böhmer, B. Pfeiffer, V. Sebastian, et al. “Decay of neutron-rich Mn nuclides and deformation of heavy Fe isotopes”. *Physical review letters*, 82(7):1391, 1999.
- [136] O. Sorlin, C. Donzaud, F. Nowacki, J. C. Angélique, F. Azaiez, C. Bourgeois, V. Chiste, Z. Dlouhy, S. Grévy, D. Guillemaud-Mueller, et al. “New region of deformation in the neutron-rich  $^{60}_{24}\text{Cr}_{36}$  and  $^{62}_{24}\text{Cr}_{38}$ ”. *The European Physical Journal A-Hadrons and Nuclei*, 16:55–61, 2003.
- [137] J. Ljungvall, A. Görgen, A. Obertelli, W. Korten, E. Clément, G. De France, A. Bürger, J.-P. Delaroche, A. Dewald, A. Gadea, et al. “Onset of collectivity in neutron-rich Fe isotopes: Toward a new island of inversion?”. *Physical Review C*, 81(6):061301, 2010.

- [138] W. Rother, A. Dewald, H. Iwasaki, S. M. Lenzi, K. Starosta, D. Bazin, T. Baugher, B. A. Brown, H. L. Crawford, C. Fransen, et al. “Enhanced quadrupole collectivity at  $N = 40$ : The case of neutron-rich Fe isotopes”. *Physical Review Letters*, 106(2):022502, 2011.
- [139] E. Caurier, F. Nowacki, and A. Poves. “Large-scale shell model calculations for exotic nuclei”. *The European Physical Journal A*, 15:145–150, 2002.
- [140] S. M. Lenzi, F. Nowacki, A. Poves, and K. Sieja. “Island of inversion around  $^{64}\text{Cr}$ ”. *Phys. Rev. C*, 82:054301, Nov 2010.
- [141] D. J. Morrissey, B. M. Sherrill, M. Steiner, A. Stolz, and I. Wiedenhoever. “Commissioning the A1900 projectile fragment separator”. *Nuclear Instruments and Methods in Physics Research Section B: Beam Interactions with Materials and Atoms*, 204:90–96, 2003.
- [142] W. F. Mueller, J. A. Church, T. Glasmacher, D. Gutknecht, G. Hackman, P. G. Hansen, Z. Hu, K. L. Miller, and P. Quirin. “Thirty-two-fold segmented germanium detectors to identify  $\gamma$ -rays from intermediate-energy exotic beams”. *Nuclear Instruments and Methods in Physics Research Section A: Accelerators, Spectrometers, Detectors and Associated Equipment*, 466(3):492–498, 2001.
- [143] I. Matea, G. Georgiev, J. M. Daugas, M. Hass, G. Neyens, R. Astabatyan, L. T. Baby, D. L. Balabanski, G. Bélier, D. Borremans, et al. “Magnetic Moment of the Fragmentation-Aligned  $^{61}\text{Fe}$  ( $9/2^+$ ) Isomer”. *Physical review letters*, 93(14):142503, 2004.
- [144] W. D. Schmidt-Ott, K. Asahi, Y. Fujita, H. Geissel, K. D. Gross, T. Hild, H. Irnich, M. Ishihara, K. Krumbholz, V. Kunze, et al. “Spin alignment of  $^{43}\text{Sc}$  produced in the fragmentation of 500 MeV/u  $^{46}\text{Ti}$ ”. *Zeitschrift für Physik A Hadrons and Nuclei*, 350:215–219, 1994.
- [145] B. P. Flannery, W. H. Press, S. A. Teukolsky, and W. Vetterling. “Numerical recipes in C”. *Press Syndicate of the University of Cambridge, New York*, 24(78):36, 1992.
- [146] Huo Junde, Huang Xiaolong, and J.K. Tuli. “Nuclear Data Sheets for  $A = 67$ ”. *Nuclear Data Sheets*, 106(2):159–250, 2005.
- [147] G. Gürdal and E. A. McCutchan. “Nuclear Data Sheets for  $A = 70$ ”. *Nucl. Data Sheets*, 136:1–162, 2016.
- [148] Khalifeh Abusaleem and Balraj Singh. “Nuclear Data Sheets for  $A = 71$ ”. *Nuclear Data Sheets*, 112(1):133–273, 2011.
- [149] R. Anne and A. C. Mueller. “LISE 3: a magnetic spectrometer—Wien filter combination for secondary radioactive beam production”. *Nuclear Instruments and Methods in Physics Research Section B: Beam Interactions with Materials and Atoms*, 70(1):276–285, 1992.
- [150] M. Honma, T. Otsuka, T. Mizusaki, and M. Hjorth-Jensen. “New effective interaction for  $f_5pg_9$ -shell nuclei”. *Phys. Rev. C*, 80:064323, Dec 2009.
- [151] J. Sinatkas, L. D. Skouras, D. Strottman, and J. D. Vergados. “Shell-model calculations in the  $A = 80 - 100$  mass region: I. A study of the  $N = 50$  nuclei”. *Journal of Physics G: Nuclear and Particle Physics*, 18(8):1377, aug 1992.

- [152] M. Hjorth-Jensen, T. T. S. Kuo, and E. Osnes. “Realistic effective interactions for nuclear systems”. *Physics Reports*, 261(3):125–270, 1995.
- [153] O. Monnoye, S. Pittel, J. Engel, J. R. Bennett, and P. Van Isacker. “Odd-mass nickel isotopes in a generalized-seniority approach”. *Phys. Rev. C*, 65:044322, Apr 2002.